

Optimization of gasification process and waste heat recovery for power and distilled water production

Doctoral Thesis

By

Rohtash Goswami

(2017MEZ0028)

Department of Mechanical Engineering

Submitted

in the partial fulfillment of the requirements of the degree

of

Doctor of Philosophy

to the



Indian Institute of Technology Ropar

Rupnagar 140001, India

December 2023

© Indian Institute of Technology Ropar- 2023
All rights reserved.



INDIAN INSTITUTE OF TECHNOLOGY ROPAR, PUNJAB, INDIA

CANDIDATE'S DECLARATION

I hereby certify that the work presented in this thesis, titled “**Optimization of gasification process and waste heat recovery for power and distilled water production**” in partial fulfillment of the requirements for the award of the degree of Doctor of Philosophy and submitted to Department of Mechanical Engineering, IIT Ropar, is an authentic record of my own work carried out during the period January 2018 to September 2023 under the supervision of Dr. Ranjan Das and Dr. Sayantan Ganguly.

The content presented in this thesis has not been submitted elsewhere for the award of any degree.

(Mr. Rohtash Goswami)

Date: December 18, 2023

This is to certify that the above statement made by the candidate is correct to the best of my knowledge. The Ph.D. Viva-Voce examination of Mr. Rohtash Goswami, Research Scholar, has been held on December 18, 2023.

(Dr. Ranjan Das)

(Dr. Sayantan Ganguly)

Date: December 18, 2023

ACKNOWLEDGEMENTS

My first and foremost words of gratitude shall go to my parents, my daughters and wife who are the ones behind every achievement of my life, let alone my doctoral programme's research work. It is their unremitting support and encouragement that has made possible for me to shatter clouds of negativity and despair in my mind and move forward to overcome every obstacle that showed up in my life.

Next, my gratitude and thank go to my supervisors, Dr. Ranjan Das and Dr. Sayantan Ganguly for completing of this research work by providing guidance on time to time. It was because of their insightful suggestions that I was able to refine my every single work to the level that is required for publishing in the academic community. Further, I would like to say thank to my Ph.D. doctoral committee members Dr. Navin kumar, Dr. Himanshu Tyagi, Dr. Rakesh Kumar Maurya and Dr. Bibhu Prasad Padhy for evaluating and giving the valuable remarks in my research work. I also gratefully acknowledge the financial support provided by Science & Engineering Research Board (SERB), Department of Science & Technology (DST), Govt. of India under the sponsored project EEQ/2016/000073 and other research facilities provided by IIT Ropar.

Finally, I would express my thankfulness to my colleagues: Mr. Gaurav Singh, Mr. Adityabir Singh, Mr. Abhishek Kumar, and Mr. Sunirmit Verma. The humorous discussions that I had with them at regular intervals in the lab, along with the brief and relaxing strolls to the canteen to pause the boredom of the day's routine were quite useful to retain my work's momentum going. Eventually, I thank God for helping me in getting me through all the difficulties.

(Rohtash Goswami)

ABSTRACT

Two major issues concerning the world presently are the depletion of fossil fuels due to an increase in energy requirements and global warming mostly caused by the rejection of flue gases (waste heat) to the atmosphere. In many developing countries, people are still using biomass inefficiently for heating and cooking purposes which causes an indoor air pollution and diseases to people. Now, one of the major arising issues for the environment is stubble burning (combustion process) in the field and many other places. Many industries are still using biomass for power generation through combustion process which causes environment pollution as well as global warming. Additionally, most of the industries, automobiles, power plants and combustion engines produce waste heat (WH) caused by inefficient use of fossil fuels and dump into the atmosphere. This WH represents about 20-50% of the fuel energy consumed by a conversion system and is capable for sustainable energy use. For intense, an amount of 440 TWh/year is released by the industrial sector of the United States (US) as reported by the Department of Energy, the US while India releases about 160 TWh/year from cement, iron and steel industries only. Further, the availability of fresh drinking water is also a universal problem because the quantity of freshwater available is only about 2.5% of the total quantity and the remaining is saline water. The increase in population and subsequently the decrease in freshwater arise the major attention of researchers towards it. Reverse Osmosis/RO (membrane-based) to produce fresh drinking water has limited output and also it is driven by the power consuming pump. It is such an extensive energy process that it requires about 10,000 tons of fossil fuel every year to produce 1000 m³ of fresh water per day. These concerns motivate the researchers to develop more efficient and clean energy technologies. This work is aimed at the assessment of effective energy (heat and power) and fresh drinking water production from the renewable energy as well as WH sources through the development of efficient systems. This study is carried out fully experimentally on the various developed systems and performance parameters have been analyzed. Based on the research gaps identified in the literature survey, the present work has been accomplished in the following steps.

The first study (chapter-3) reveals the energy cogeneration study of locally available biomass red mulberry (*Morus Rubra*) and other biomasses (dried grass, leaves and dead branches) in a 10 kW

downdraft biomass gasifier (power plant). The optimal operating condition of a gasifier is obtained by performing experiments at variable equivalence ratios (ER), and by analyzing the characteristics of syngas (produced) along with gas composition, calorific value (CV) and cold gas efficiency (η_{cg}). Before processing various biomasses for gasification, the potential capability of these biomasses was analyzed by determining higher heating value (HHV), ultimate (C-Carbon, H-Hydrogen, N-Nitrogen, S-Sulphur and O-Oxygen) and proximate (moisture content/MC, ash content/AC, volatile matters/VM and fixed carbon/FC) analyses. The characterization of gasification end products including bio-oil and bio-char have been done by gas chromatography and Fourier-transform infrared techniques. Furthermore, the economic analysis (electricity generation cost and payback period) of the biomass gasification-based power plant of various capacities (10 kW, 500 kW and 1000 kW) are assessed. The outcomes of this study specified that the various biomasses mentioned above are capable in producing thermal energy and power within the substantial range (15.58-18.36 MJ/kg) of HHV. The ultimate and proximate analyses show that red mulberry biomass is relatively superior to other biomass reported in the published literature, while dried grass, leaves and dead branches are also comparable with others. The maximum values of CV and η_{cg} are obtained as 5.846 MJ/m³ and 68.45%, respectively for red mulberry biomass at the optimum ER of 0.296. The economic analysis indicated that the electricity production cost (Rs.4.34/kWh or 0.055 USD/kWh) and payback period (3.12 years) are minimum for the largest capacity plant i.e., 1000 kW.

In the second study (chapter-4), use of biomass energy as an external heat source for the heat recovery system (HRS) to produce continuous and long-term electric power generation aimed at end-use applications. This study is carried out in three stages to accomplish the objective.

In the first stage, the electrical power is generated from the WH of biomass energy driven engine-generator using two thermoelectrical generators (TEGs)-thermosyphon-based HRSs. The proficiency of the TEGs-thermosyphon-based HRS is recognized for power generation by performing the experiments at variable conditions of heat source water temperature (T_s) and thermosyphon filling ratio (TFR). The performance is analyzed by measuring the different electrical parameters such as open circuit voltage (V), short circuit current (I_s) output power (P_o) and conversion efficiency of TEG (η_{TEG}). The effort is made to charge a 12 V, 7 Ah uninterruptible power source (UPS) battery for end-use applications. The results showed that

the maximum values of V , I_s , P_o and η_{TEG} are found as 17.12 V, 0.152 A, 0.615 W and 2.218% respectively at the maximum T_s of 87 °C and an optimum TFR of 0.496. It has been realized that this HRS is able to charge a 12 V, 7 Ah UPS battery and found a minimum value of I_s as 0.118 A to charge it.

In the second stage, these two TEGs-thermosyphon-based HRSs are installed in a salt gradient solar pond (SGSP) for power generation since the literature study found on this system are performed either theoretically or electrically at the simulated conditions. The performance of HRSs has been investigated by carrying out the experiments for 40 days under the actual weather conditions. Before installing them, the capability of a fabricated SGSP is examined for storing the solar energy through measuring the profiles of key thermal and electrical parameters such as temperature, specific heat (c_{sw}), thermal (k_{sw}) and electrical conductivity (EC) of salt water along with the thermal efficiency of SGSP (η_{SGSP}). The results indicated that the SGSP is able to store a high amount of solar energy in its lower convective zone (LCZ) with 6.06% of η_{SGSP} . It has been found that this thermosyphon-based HRS is not able to generate the minimum required output to charge a 12 V, 7 Ah UPS battery at the maximum achievable temperature gradient obtained in SGSP (ΔT_{LU}) due to the involvement of various thermal resistances (a total of nine) in the heat flow. The maximum V of 1.44 is obtained corresponding to a heat source (here LCZ i.e. T_{LCZ}) temperature of 49.99 °C. Further, it is also suggested that an external heat source is mandatory to meet the same that can be fulfilled by the WH of biomass based engine-generator of a gasifier. Subsequently, the biomass energy required to produce the enough output is computed theoretically under certain conditions and found that 15.60 kg of biomass is needed corresponding to a minimum obtained average (over a day) ΔT_{LU} of 7.0 °C for charging a UPS battery. Moreover, the economic analysis is also performed in order to viability of the proposed system (a SGSP combined with a 10 kW gasifier) and found that this system can replace the conventional power generation from diesel with a significant amount of profit.

In the third stage, a new TEGs-array-based HRS is developed for the effective power generation from SGSP through minimizing the thermal resistances. This new HRS is integrated with a small capacity SGSP (proposed system) which is firstly operated by the solar energy under actual weather conditions and then externally heated by the WH of biomass based engine-generator of a 10 kW gasifier at variable conditions of an engine load (W_L) and frequency (f) levels. Before integration of a new HRS with the SGSP, a study is carried out to analyze the capability of

fabricated small capacity SGSP for recovering and storing the WH of an engine-generator. The results revealed that this SGSP has efficiently recovered the WH with a significant range (0.75-0.77) of effectiveness and a high η_{SGSP} of 47.73%. The outcomes of the proposed system when operated by the solar energy explored that this new HRS has generated much higher (9.19 times) output compared to the TEGs-thermosyphon-based (1.44 V at 49.99 °C) and found a maximum V of 7.97 V corresponding to 43.36 °C of T_{LCZ} . But this output is still not enough and also it doesn't remain constant due to the intermittency of solar energy over the day and unavailability during the night. Therefore, the proposed system is further operated by the WH of biomass engine-generator for constant power generation and obtained the maximum V , I_s , P_o and η_{TEG} as 81.62 V, 0.272 A, 7.483 W and 4.63% respectively at 68.04 °C (T_{LCZ}), 3 kW (W_L) and 51 Hz (f). This high performance is obtained due to upgrading in HRS along with the cooling system where seven thermal resistances (out of total nine) have been totally eliminated with the aid of an array-based system and the remaining two are minimized by using a high thermal conductive material (copper). A 12 V, 80 Ah heavy-duty battery is successfully charged from the P_o of TEGs-array-based HRS and the minimum I_s required to charge this battery is recognized as 0.155 A under the given conditions. Therefore, the TEGs-array-based HRS has effectively generated the power from heat sources, however it has been realized that pumps are required when it was connected with the SGTSD. Thus, to make it more effective for power generation without using pumps, a proposal of arrangement has been suggested in which the TEGs-array-based HRS can be applied directly to WH available at high temperature via common rail waste heat pipe and then the leftout low temperature WH can be stored in SGSP. A demonstration study has been carried out to validate the concept of direct connection of TEGs-array-based HRS with the WH of biomass engine-generator. The results showed that this proposed HRS has produced 12-14 times more performance than the TEGs-thermosyphon-based HRS when operated under similar temperature limit and obtained V , I_s and P_o of 74.78 V, 0.261 A and 4.93 W respectively.

In the third study (chapter-5), the use of biomass energy as an external heat source (WH) for water desalination using a developed distillation system. Therefore, a new wick and copper-finned distillation system (CFDS) is fabricated which is driven by the WH of biomass based engine-generator. The performance of proposed CFDS is analyzed in the form of an amount of distilled water (m_d) produced at variable operating conditions of waste heat inlet temperature ($T_{WH, inl.}$),

glass inclination angle (θ_g) and height of basin water (H_{bw}). Furthermore, the response surface-based correlations (linear and quadratic) are also developed using BBD, ANOVA as well as regression methods and the accuracy or goodness of generated correlations is checked by the coefficient of determination (R^2). The deviation in the response parameter (m_d) is analyzed in terms of input factors ($T_{WH, in}$, θ_g and H_{bw}) through main effect, interaction, surface and contour plots along with the percentage contribution of each input factor (linear, square and 2-way interaction). The outcomes of this study indicated that the maximum value of m_d is obtained as 2.407 kg at 321.53 °C, 45° and 0.08 m of $T_{WH, in}$, θ_g and H_{bw} respectively. The employment of wick and fins in the distillation system has a positive effect on the yield of m_d and increased the productivity from 2.054 kg to 2.407 kg with 17.18% improvement at the optimal conditions of input parameters. It can be suggested that the highest level of $T_{WH, in}$ is always preferred to obtain a large value of m_d , but the moderate levels of θ_g and H_{bw} provide maximum performance for the same. It has been realized that each factor has its certain influence on m_d , but H_{bw} and $T_{WH, in}$ are found to be the most dominant factors over θ_g . The quadratic correlation has been found to be in good agreement with the experimental values with a maximum error of 12.03%.

LIST OF PUBLICATIONS

Dr. S. Ganguly was included as joint supervisor in December 2019, so, papers which were communicated before did not involve his name.

Journals

- [J1] Goswami R, Das R. Energy cogeneration study of red mulberry (*Morus rubra*)-based biomass. *Energy Sources, Part A: Recovery, Utilization, and Environmental Effects*. 2020; 42(8): 979-1000.
- [J2] Goswami R, Das R. Waste heat recovery from a biomass heat engine for thermoelectric power generation using two-phase thermosyphons. *Renewable Energy*. 2020; 148: 1280-91.
- [J3] Goswami R, Das R. Experimental analysis of a novel solar pond driven thermoelectric energy system. *Journal of Energy Resources Technology*. 2020; 142(12): 121302.
- [J4] Goswami R, Das R, Ganguly S, Lamba R. Waste heat recovery from the biomass-driven engine for effective power generation using a new array-based system: An experimental study. *Sustainable Energy Technologies and Assessments*. (Status: Under review).
- [J5] Goswami R, Das R, Ganguly S. Waste heat recovery from the biomass engine for desalination using a new wick and finned distillation system. *Renewable Energy*. (Status: Under review).
- [J6] Goswami R, Das R, Ganguly S. Harvesting of thermal energy for effective power generation using a new array-based heat recovery system: An experimental study. (Status: Under preparation).

Conference Proceedings

- [C1] Goswami R, Das R. Investigation of thermal and electrical performance in a salt gradient solar pond. 2nd International Conference on New Frontiers in Engineering, Science & Technology (NFEST-2019), 18-22 February, 2019, NIT Kurukshetra, India, Journal of Physics: Conference Series, IOP Publishing. 2019; 1240: 012111.
- [C2] Goswami R, Das R, Ganguly S. Economic and feasibility study of biomass-based electric power generation. 15th Regional Conference on Energy Engineering (RCEnE) and 13th International Conference on Thermofluids 2022, 25-26 October, 2022, Gadjah Mada University, Yogyakarta, Indonesia (Status: presented).
- [C3] Goswami R, Das R, Ganguly S. Experimental investigation on electric power generation by harvesting biomass waste heat using thermoelectric array. International Recent Trends in Engineering, Advanced Computing & Technology, Conference (RETREAT), 28-29 November, 2022, Jeddah, Saudi Arabia. (Status: presented).
- [C4] Goswami R, Das R, Ganguly S. Performance analysis of salt gradient thermal storage device driven by waste heat. International Conference on Electrical, Computer, Communications and Mechatronics Engineering (ICECCME'23), 19-21 July, 2023, Tenerife-Canary Islands, Spain (Status: presented).
- [C5] Goswami R, Das R, Ganguly S. Zero waste production technology investigating through gasification process and characterization of its byproducts (biochar/bio-oil). The 9th International Symposium on Hydrogen Energy, Renewable Energy and Materials (HEREM 2023), 13-14 October, 2023, Bangkok, Thailand (Status: presented).

Book Chapters

- [B1] Goswami R, Verma S, Das R. Energy production through gasification of waste biomass in Punjab region. International Conference on Emerging trends in Mechanical Engineering-2018 (ICETME-2018), 20-22 November, 2018, SRIT, Ananthapuramu, Andhra Pradesh, India. [Springer book chapter: Emerging Trends in Mechanical Engineering], Springer 2020; 529-537.

TABLE OF CONTENTS

Contents

| | |
|---|-----|
| ACKNOWLEDGEMENTS | i |
| ABSTRACT | ii |
| LIST OF PUBLICATIONS | vii |
| NOMENCLATURE | xxv |
| 1 Introduction | 1 |
| 1.1 Motivation | 1 |
| 1.2 Gasifier | 2 |
| 1.3 Types of gasifier | 3 |
| 1.3.1 Updraft gasifier | 3 |
| 1.3.2 Downdraft gasifier | 4 |
| 1.3.3 Crossdraft gasifier | 4 |
| 1.3.4 Bubbling fluidized bed gasifier | 5 |
| 1.3.5 Circulating fluidized bed gasifier | 6 |
| 1.3.6 Dual fluidized bed gasifier | 7 |
| 1.3.7 Entrained flow gasifier | 7 |
| 1.4 Biomass-based power plant | 9 |
| 1.5 Potential components for recovery of waste heat | 10 |
| 1.5.1 Heat recovery steam generator | 11 |
| 1.5.2 Thermoelectric generator | 11 |
| 1.5.3 Phase change materials | 14 |
| 1.5.4 Salinity gradient solar pond | 15 |
| 1.5.5 Active distillation system | 16 |
| 2 Literature review | 18 |

| | | |
|---------|---|----|
| 2.1 | History of the gasification process | 18 |
| 2.1.1. | <i>Literature survey on the performance of gasifier using different biomass: International status</i> | 19 |
| 2.1.2. | <i>Literature survey on the performance of gasifier using different biomass: National status</i> | 26 |
| 2.2 | Management and recovery of waste heat | 32 |
| 2.2.1 | <i>Literature survey on the recovery of waste heat from the gasifier for various applications: International status</i> | 33 |
| 2.2.2 | <i>Literature survey on the recovery of waste heat from the gasifier for various applications: National status</i> | 41 |
| 3 | Energy production from sustainable biomass through gasification and its economic analysis | 47 |
| 3.1 | Energy cogeneration study of the red mulberry (Morus Rubra)-based biomass..... | 47 |
| 3.1.1 | <i>Experimental setup details</i> | 47 |
| 3.1.2 | <i>Experimental procedure</i> | 52 |
| 3.1.3 | <i>Biomass characterization</i> | 53 |
| 3.1.4 | <i>Results and discussion</i> | 55 |
| 3.1.4.1 | <i>Equivalence ratio</i> | 56 |
| 3.1.4.2 | <i>Gas composition and calorific value</i> | 56 |
| 3.1.4.3 | <i>Cold gas efficiency and gas production rate</i> | 60 |
| 3.1.4.4 | <i>Flame quality</i> | 61 |
| 3.1.4.5 | <i>Comparison of performance</i> | 62 |
| 3.1.4.6 | <i>Characteristics of bio-oil and biochar</i> | 67 |
| 3.1.4.7 | <i>Analysis of zero waste production technology</i> | 70 |
| 3.1.4.8 | <i>Uncertainty analysis</i> | 72 |
| 3.1.5 | <i>Summary</i> | 73 |

| | | |
|---------|--|----|
| 3.2 | Energy production from the sustainable waste biomass (dried grass, leaves and dead branches) | 74 |
| 3.2.1 | <i>Characterization of biomass</i> | 74 |
| 3.2.2 | <i>Results and discussion</i> | 76 |
| 3.2.2.1 | <i>Gas composition</i> | 76 |
| 3.2.2.2 | <i>Calorific value and cold gas efficiency</i> | 77 |
| 3.2.3 | <i>Summary</i> | 78 |
| 3.3 | Economic and feasibility study of biomass-based electric power generation..... | 78 |
| 3.3.1 | <i>Energy scenario in India</i> | 78 |
| 3.3.1.1 | <i>Energy potential status of biomass</i> | 79 |
| 3.3.1.2 | <i>Trend of electricity demand</i> | 80 |
| 3.3.2 | <i>Economic analysis</i> | 80 |
| 3.3.2.1 | <i>Capital cost</i> | 81 |
| 3.3.2.2 | <i>Electricity generation cost</i> | 82 |
| 3.3.2.3 | <i>Payback Period and Feasibility</i> | 85 |
| 3.3.3 | <i>Summary</i> | 87 |
| 4 | Use of biomass for effective power generation | 89 |
| 4.1 | Waste heat recovery from the biomass engine using the TEGs-thermosyphon-based HRS 89 | |
| 4.1.1 | <i>Experimental setup details</i> | 89 |
| 4.1.2 | <i>Experimental procedure</i> | 91 |
| 4.1.3 | <i>Principle, specifications and performance parameters of thermoelectric generator</i> | 93 |
| 4.1.4 | <i>Results and discussion</i> | 95 |
| 4.1.4.1 | <i>Variations of average waste heat temperature</i> | 96 |
| 4.1.4.2 | <i>Variation of source and sink temperatures</i> | 97 |
| 4.1.4.3 | <i>Maximum open circuit voltage</i> | 98 |

| | | |
|-----------|--|-----|
| 4.1.4.4 | <i>Variation of open circuit voltage and short circuit current.....</i> | 99 |
| 4.1.4.5 | <i>Variation of power output and conversion efficiency of TEG</i> | 99 |
| 4.1.4.6 | <i>Variations of dimensionless figure of merit</i> | 101 |
| 4.1.4.7 | <i>Charging of a 12 V, 7 Ah UPS battery.....</i> | 101 |
| 4.1.4.8 | <i>Comparison of theoretical and experimental parameters</i> | 103 |
| 4.1.4.9 | <i>Uncertainty analysis</i> | 105 |
| 4.1.5 | <i>Summary</i> | 107 |
| 4.2 | <i>TEGs-thermosyphon-based HRS operated by the stored energy of SGSP</i> | 107 |
| 4.2.1 | <i>Investigation of thermal and electrical performance in a SGSP</i> | 108 |
| 4.2.1.1 | <i>Experimental setup.....</i> | 108 |
| 4.2.1.2 | <i>Calculation of thermal efficiency and various parameters of SGSP</i> | 110 |
| 4.2.1.3 | <i>Results and discussion</i> | 111 |
| 4.2.1.4 | <i>Summary</i> | 115 |
| 4.2.2 | <i>TEGs-thermosyphon-based HRS installed in a SGSP</i> | 116 |
| 4.2.2.1 | <i>Experimental methodology</i> | 116 |
| 4.2.2.2 | <i>Results and discussion</i> | 118 |
| 4.2.2.3 | <i>External energy required in SGSP for charging a UPS battery</i> | 124 |
| 4.2.2.4 | <i>Economic analysis</i> | 126 |
| 4.2.2.4.1 | <i>Capital cost</i> | 126 |
| 4.2.2.4.2 | <i>Operating cost.....</i> | 128 |
| 4.2.2.4.3 | <i>Electricity generation cost</i> | 129 |
| 4.2.2.4.4 | <i>Payback period and feasibility.....</i> | 129 |
| 4.2.2.5 | <i>Uncertainty analysis</i> | 130 |
| 4.2.2.6 | <i>Summary</i> | 131 |

| | | |
|-----------|--|-----|
| 4.3 | Experimental study on the developed TEGs-array-based HRS operated by a SGSP driven by waste heat | 132 |
| 4.3.1 | <i>Performance analysis of a SGSP</i> | 133 |
| 4.3.1.1 | <i>Experimental setup details</i> | 133 |
| 4.3.1.2 | <i>Materials and methods</i> | 135 |
| 4.3.1.2.1 | <i>Effectiveness of exhaust pipe</i> | 136 |
| 4.3.1.2.2 | <i>Thermal efficiency of SGSP</i> | 137 |
| 4.3.1.3 | <i>Results and discussion</i> | 137 |
| 4.3.1.3.1 | <i>Calorific value of syngas</i> | 137 |
| 4.3.1.3.2 | <i>Waste heat temperature at inlet and outlet of a SGSP</i> | 138 |
| 4.3.1.3.3 | <i>Effectiveness of exhaust/waste heat pipe</i> | 139 |
| 4.3.1.3.4 | <i>Maximum temperature achieved in LCZ, NCZ and UCZ of SGSP</i> | 140 |
| 4.3.1.3.5 | <i>Transient change of temperature profile corresponding to elevation from bottom</i> 141 | |
| 4.3.1.3.6 | <i>Temperature gain in LCZ</i> | 141 |
| 4.3.1.3.7 | <i>Thermal storage capacity and efficiency of SGSP</i> | 142 |
| 4.3.1.4 | <i>Summary</i> | 143 |
| 4.3.2 | <i>Performance analysis of the developed TEGs-array-based HRS integrated with SGSP</i> 144 | |
| 4.3.2.1 | <i>Experimental setup details</i> | 144 |
| 4.3.2.2 | <i>Experimental procedure</i> | 148 |
| 4.3.2.3 | <i>Thermal resistances between heat source (LCZ) and hot side of TEGs</i> | 149 |
| 4.3.2.4 | <i>Results and discussion</i> | 152 |
| 4.3.2.4.1 | <i>Average solar radiation, LCZ and ambient temperatures</i> | 152 |
| 4.3.2.4.2 | <i>Maximum LCZ temperature in SGSP</i> | 153 |
| 4.3.2.4.3 | <i>Open circuit voltage and short circuit current</i> | 154 |

| | | |
|------------|--|-----|
| 4.3.2.4.4 | <i>Transient variation of waste heat temperature</i> | 155 |
| 4.3.2.4.5 | <i>Transient variation of LCZ temperature</i> | 156 |
| 4.3.2.4.6 | <i>Variation of temperature gradient across TEG</i> | 157 |
| 4.3.2.4.7 | <i>Variation of open circuit voltage and short circuit current.....</i> | 158 |
| 4.3.2.4.8 | <i>Variation of output power and conversion efficiency</i> | 160 |
| 4.3.2.4.9 | <i>Comparison of thermal resistances</i> | 162 |
| 4.3.2.4.10 | <i>Charging a 12 V, 80 Ah heavy-duty battery.....</i> | 164 |
| 4.3.2.4.11 | <i>Uncertainty analysis.....</i> | 165 |
| 4.3.2.5 | <i>Expansion of present system</i> | 166 |
| 4.3.2.6 | <i>Summary</i> | 168 |
| 4.3.3 | <i>Performance analysis of the developed TEGs-array-based HRS directly operated from the waste heat.....</i> | 169 |
| 4.3.3.1 | <i>Experimental setup and procedure</i> | 169 |
| 4.3.3.2 | <i>Results and discussion</i> | 171 |
| 4.3.3.2.1 | <i>Performance comparison between conventional and proposed system</i> | 171 |
| 4.3.3.2.2 | <i>Effect of sink/cold water temperature</i> | 172 |
| 4.3.3.2.3 | <i>Performance under various combinations of the series structure</i> | 174 |
| 4.3.3.2.4 | <i>Uncertainty analysis</i> | 176 |
| 4.3.3.3 | <i>Summary</i> | 176 |
| 5 | <i>Use of biomass gasification for desalination.....</i> | 177 |
| 5.1 | <i>Performance and response surface analysis of a new wick and finned distillation system</i> | 178 |
| 5.1.1 | <i>Experimental setup details.....</i> | 179 |
| 5.1.1.1 | <i>Experimental procedure.....</i> | 182 |
| 5.1.1.2 | <i>Variable input factors and different measuring parameters.....</i> | 182 |
| 5.1.2 | <i>Methodology</i> | 183 |

| | | |
|---------|--|-----|
| 5.1.2.1 | <i>Box-Behnken design method</i> | 183 |
| 5.1.2.2 | <i>Regression analysis and correlations</i> | 185 |
| 5.1.2.3 | <i>Analysis of variance and coefficient of determination or R^2</i> | 186 |
| 5.1.3 | <i>Results and discussion</i> | 187 |
| 5.1.3.1 | <i>Mass of distilled/pure water</i> | 188 |
| 5.1.3.2 | <i>Transient variation of distilled water and temperatures for waste heat, fins, moist air and basin water</i> | 190 |
| 5.1.3.3 | <i>Effect of fins and wick</i> | 192 |
| 5.1.3.4 | <i>Performance ratio and productivity of distilled water</i> | 194 |
| 5.1.3.5 | <i>Properties of distilled/pure water</i> | 196 |
| 5.1.3.6 | <i>Response surface analysis</i> | 198 |
| 5.1.3.7 | <i>Uncertainty analysis</i> | 206 |
| 5.1.4 | <i>Summary</i> | 207 |
| 6 | <i>Conclusions and future scope</i> | 207 |
| | REFERENCES..... | 213 |

LIST OF FIGURES

| | |
|--|--------|
| Figure 1.1: Different processes involved in the gasifier to produce syngas | 2 |
| Figure 1.2: A schematic diagram representing different types of gasifier..... | 3 |
| Figure 1.3: Principle of (a) updraft, (b) downdraft and (c) crossdraft fixed bed gasifiers..... | 4 |
| Figure 1.4: Schematic layout of a bubbling fluidized bed gasifier | 5 |
| Figure 1.5: Diagram of a circulating fluidized bed gasifier..... | 6 |
| Figure 1.6: Principle of a dual fluidized bed gasifier..... | 7 |
| Figure 1.7: Principle of an entrained flow gasifier | 8 |
| Figure 1.8: A layout representing various components in the biomass-based power plant..... | 9 |
| Figure 1.9: Schematic of a heat recovery steam generator | 11 |
| Figure 1.10: Illustration of a thermoelectric generator | 12 |
| Figure 1.11: Schematic diagram of the two-phase closed thermosyphon | 14 |
| Figure 1.12: Diagram of a typical salinity gradient solar pond | 16 |
| Figure 1.13: Schematic of an active distillation system | 17 |
| Figure 3.1.1: (a) Schematic layout and (b, c) actual photograph of a 10 kW downdraft biomass gasifier | 49 |
| Figure 3.1.2: (a, b) Biomass cutter, (c, d) Syngas analyzer, (e) Moisture meter, (f) Anemometer | 51 |
| Figure 3.1.3: Biomass (<i>Morus rubra</i>) used in the present work, (a) green tree, (b) partially dry tree, (c) mulberry fruit, (b) dead mulberry tree wood chips | 52 |
| Figure 3.1.4: Variation of gas composition and calorific value with time for each experiment at varying biomass consumption rate, (a) 9.0 kg/hr, (b) 9.5 kg/hr, (c) 10.0 kg/hr, (d) 10.5 kg/hr, (e) 11.0 kg/hr, (f) 11.5 kg/hr, (g) 12.0 kg/hr, (h) 12.5 kg/hr, (i) 13 kg/hr | 57 |
| Figure 3.1.5: Variation of average CV with ER for each experiment | 58 |
| Figure 3.1.6: Variation of cold gas efficiency with time for each experiment with varying biomass consumption rate, (a) 9.0 kg/hr, (b) 9.5 kg/hr, (c) 10.0 kg/hr, (d) 10.5 kg/hr, (e) 11.0 kg/hr, (f) 11.5 kg/hr, (g) 12.0 kg/hr, (h) 12.5 kg/hr, (i) 13 kg/hr | 59 |
| Figure 3.1.7: Variation of average cold gas efficiency with equivalence ratio for each experiment | 61 |

| | |
|---|--------|
| Figure 3.1.8: Variation of gas production rate with equivalence ratio for each experiment | 61 |
| Figure 3.1.9: Flame of syngas at various ERs | 62 |
| Figure 3.1.10: Comparisons of CV with various biomass available in the published literature | 62 |
| Figure 3.1.11: Comparisons of η_{cg} with different biomass available in the published literature | 63 |
| Figure 3.1.12: Comparisons of HHV with other biomass available in the published literature | 64 |
| Figure 3.1.13: Comparison of ultimate analysis of red mulberry wood biomass with the biomass available in literature | 65 |
| Figure 3.1.14: Comparison of proximate analysis of red mulberry wood biomass with biomass available in literature | 66 |
| Figure 3.1.15: GC-MS test spectrum results at various peak for bio-oil | 68 |
| Figure 3.1.16: FT-IR spectroscopy test spectrum results for biochar | 69 |
| Figure 3.1.17: Analysis of zero waste production technology through different applications of products (syngas, biochar and bio-oil) | 70 |
| Figure 3.2.1: Specimens of dried grass, leaves and dead branches used for gasification (a, b, c) as raw biomass and their powdered form for characterization (d, e, f) respectively | 75 |
| Figure 3.2.2: Gas composition at various reduction chamber temperatures ($^{\circ}\text{C}$) for gasification of (a) dried grass, (b) leaves and (c) dead branches | 77 |
| Figure 3.2.3: Calorific value of gas at various temperatures of reduction chamber ($^{\circ}\text{C}$) for dried grass, leaves, and dead branches | 78 |
| Figure 3.3.1: Inefficient use of biomass for (a) cooking and (b) agriculture purposes | 79 |
| Figure 3.3.2: Energy potential of different biomass in India [Kumar et al. 2010] | 80 |
| Figure 3.3.3: Trend of electricity demand in India [Kumar et al. 2010] and [Laha et al. 2020] | 80 |
| Figure 3.3.4: Capital cost per kW for different capacities power plant | 82 |
| Figure 3.3.5: Payback period of various capacities power plant | 87 |
| Figure 4.1.1: Details of the experimental setup with block diagram | 90 |
| Figure 4.1.2: Schematic diagram of (a) a two-phase closed thermosyphon and (b) the network of resistances offered in the heat flow | 92 |

| | |
|--|-----|
| Figure 4.1.3: Circuit diagram for measuring the output current and voltage at variable external load resistance | 92 |
| Figure 4.1.4: (a) Schematic diagram of a TEG (b) top internal view and (c) side view of TEG used | 94 |
| Figure 4.1.5: Profile of average waste heat temperature at various ER..... | 96 |
| Figure 4.1.6: Transient variation of source and sink temperatures..... | 97 |
| Figure 4.1.7: Variation of maximum open circuit voltage obtained at various TFR for thermosyphon 1 and 2..... | 98 |
| Figure 4.1.8: Variation of V and I_s for thermosyphons (a) 1 and (b) 2 | 99 |
| Figure 4.1.9: Variation of output current and power for thermosyphons (a) 1 and (b) 2 | 100 |
| Figure 4.1.10: Variation of heat conversion efficiency with T_h | 100 |
| Figure 4.1.11: Variation of dimensionless figure of merit with ΔT_{TEG} | 101 |
| Figure 4.1.12: Real life use of fully charged UPS battery for various applications | 102 |
| Figure 4.1.13: Comparison of model and experiment results for thermosyphons (a) 1 and (b) 2 | 105 |
| | |
| Figure 4.2.1: Experimental setup details of a SGSP | 109 |
| Figure 4.2.2: (a) Transient variations of temperatures and average solar radiation and (b) maximum UCZ temperature | 112 |
| Figure 4.2.3: Transient variation of salt concentration across H_{SGSP} | 112 |
| Figure 4.2.4: Transient variation of electrical conductivity across H_{SGSP} | 113 |
| Figure 4.2.5: Transient variation of TDS across H_{SGSP} | 113 |
| Figure 4.2.6: Transient variation of thermal conductivity of salt water across H_{SGSP} | 114 |
| Figure 4.2.7: Transient variation of density of salt water across H_{SGSP} | 114 |
| Figure 4.2.8: Transient variation of specific heat of salt water across H_{SGSP} | 115 |
| Figure 4.2.9: Details of the experimental setup and its block diagram..... | 117 |
| Figure 4.2.10: Variations of (a) maximum and (b) average values of ΔT_{LU} and V | 119 |
| Figure 4.2.11: Variations of maximum and minimum values (a) S and T_a , (b) T_{LCZ} and T_{UCZ} .. | 120 |
| Figure 4.2.12: Variation of maximum temperature in NCZ | 121 |
| Figure 4.2.13: Variations of average values of S , T_a , T_{LCZ} and T_{UCZ} | 121 |

| | |
|--|-----|
| Figure 4.2.14: Variation of V corresponding to S with time (a) first day (b) 18th day (c) last day | 122 |
| Figure 4.2.15: Variation of heat storage capacity of SGSP during the operational days | 124 |
| Figure 4.2.16: Proposed system of SGSP for power generation from TEGs | 125 |
| Figure 4.2.17: Biomass requirement corresponding to the average temperature gradients..... | 126 |
| | |
| Figure 4.3.1: (a) Photograph and (b) block diagram of the experimental setup | 134 |
| Figure 4.3.2: Schematic of a SGSP with various notations | 136 |
| Figure 4.3.3: (a) Photograph of measured CV from analyzer and (b) CV of syngas measured for all run | 138 |
| Figure 4.3.4: Effectiveness of exhaust pipe for all experiments..... | 140 |
| Figure 4.3.5: Maximum temperature attained in LCZ, NCZ and UCZ of SGSP | 140 |
| Figure 4.3.6: Transient change of temperature profile within SGSP corresponding to elevation from bottom | 141 |
| Figure 4.3.7: Temperature gain in LCZ for all experiments..... | 142 |
| Figure 4.3.8: (a) Thermal storage capacity and (b) thermal efficiency of SGSP for all experiments | 143 |
| Figure 4.3.9: (a) Photograph and (b) block diagram describing about the first part of the experimental setup | 146 |
| Figure 4.3.10: (a-d) Experimental setup and (e) schematic of the proposed HRS | 148 |
| Figure 4.3.11: (a) Wiring connection for measuring the output power of TEGs and (b) photo of TEG module used | 149 |
| Figure 4.3.12: (a) Schematic and (b) actual photograph of the array-based HRS | 150 |
| Figure 4.3.13: Thermal resistances between LCZ and hot side of TEGs | 150 |
| Figure 4.3.14: Deviation in average (over a day) solar radiation, LCZ and ambient temperatures during the entire experiments..... | 153 |
| Figure 4.3.15: (a) Variation of maximum LCZ temperature in a day during the entire experiments and (b) the profile of LCZ temperature on the day (15 th) of maximum attained temperature.... | 154 |
| Figure 4.3.16: Open circuit voltage and short circuit current during the steady-state condition | 155 |
| Figure 4.3.17: Transient variation of waste heat temperature at engine loads of (a) 1 kW and (b) 3 kW under different operating frequencies | 156 |

| | |
|--|-----|
| Figure 4.3.18: Transient variation of LCZ temperature at engine loads of (a) 1 kW and (b) 3 kW under different operating frequencies and ambient conditions | 157 |
| Figure 4.3.19: Variation of temperature gradient across TEG at engine loads of (a) 1 kW and (b) 3 kW under the ambient temperatures of 11.77 °C and 12.46 °C respectively | 158 |
| Figure 4.3.20: Variation of open circuit voltage, and short circuit current with ΔT_{TEG} at engine loads of (a) 1 kW and (b) 3 kW under different ambient conditions and fixed operating f of 51 Hz | 159 |
| Figure 4.3.21: Output current and power profiles of TEG varying with output voltage for engine load of (a) 1 kW and (b) 3 kW at different LCZ and cold water temperatures | 160 |
| Figure 4.3.22: Variation of conversion efficiency of TEG with LCZ temperature at (a) 1 kW and (b) 3 kW loads | 161 |
| Figure 4.3.23: Schematic representation of thermal resistances for (a) TEGs-thermosyphon-based HRS (conventional system) and (b) TEGs-array based HRS (proposed) | 163 |
| Figure 4.3.24: Charging a 12 V, 80 Ah heavy-duty battery from the output power of TEGs | 165 |
| Figure 4.3.25: Expansion of proposed system (a) front view and (b) top view | 168 |
| Figure 4.3.26: (a) Photograph and (b) block diagram of the experimental setup | 171 |
| Figure 4.3.27: Comparisons of open circuit voltage and short circuit current | 172 |
| Figure 4.3.28: Profile of output current and power at a heat source temperature of 55 °C | 172 |
| Figure 4.3.29: Effect of cold water temperature on open circuit voltage under (a) pool water and (b) flow water cooling arrangements | 174 |
| Figure 4.3.30: Performance under various combinations of the series structure; (a) 1 set of 92 series-connected TEGs, (b) 2 sets (each set has 46 TEGs) of series-connected TEGs in parallel, and (c) 4 sets (each set has 23 TEGs) of series-connected TEGs in parallel | 175 |
| Figure 4.3.31: Variation of output current and power at maximum heat source temperature (80 °C) | 176 |
| | |
| Figure 5.1.1: (a) Photograph and (b) schematic of experimental setup displaying various parts | 181 |
| Figure 5.1.2: Schematic of the CFDS displaying various measuring parameters (a) sectional side view and (b) sectional top view | 183 |
| Figure 5.1.3: Graphically representation of ANOVA method for linear | 187 |
| Figure 5.1.4: Variation of m_d with (a) Θ_g and (b) H_{bw} | 189 |

| | |
|--|-----|
| Figure 5.1.5: Transient variation of (a) $T_{WH, inl.}$ and $T_{WH, outl.}$, (b) T_{f1} , T_{f3} and T_{f5} , (c) T_{bw} and T_{ma} , and (d) m_d at optimal working conditions | 192 |
| Figure 5.1.6: Mass of distilled water, m_d obtained at different accessibility of fins and wick | 193 |
| Figure 5.1.7: Effect of fins on m_d through evaporation of high energy water molecules | 193 |
| Figure 5.1.8: (a) Structure of cold water flow over glass' surface without wick and (b) effects of wick on m_d through condensation of water vapours | 194 |
| Figure 5.1.9: Measured values of SC, EC and TDS for (a) seawater and (b) distilled/pure water | 197 |
| Figure 5.1.10: Main effects of individual input factors ($T_{WH, inl.}$, θ_g and H_{bw}) on the experimental output (m_d) | 200 |
| Figure 5.1.11: Interaction effect of various input factors ($T_{WH, inl.}$, θ_g and H_{bw}) on the experimental output (m_d) | 201 |
| Figure 5.1.12: Surface plots that show the combined effect of any two input factors (a) $T_{WH, inl.}$ and θ_g , (b) $T_{WH, inl.}$ and H_{bw} and (c) θ_g and H_{bw} with keeping one factor constant (centre level) at a time on the predicted m_d | 203 |
| Figure 5.1.13: Contour plots that display the different ranges of obtained m_d at various the combination of any two input factors (a) $T_{WH, inl.}$ and θ_g , (b) $T_{WH, inl.}$ and H_{bw} and (c) θ_g and H_{bw} . | 204 |
| Figure 5.1.14: Contribution of various factors (linear, square and 2-way interaction of $T_{WH, inl.}$, θ_g and H_{bw}) in the predicted response parameter (m_d) | 205 |
| Figure 5.1.15: Comparison of correlation and experimental results for m_d along with error between them | 206 |

LIST OF TABLES

| | |
|--|-----|
| Table 3.1.1: Computation of ER for gasification at different air flow rates and biomass consumptions | 56 |
| Table 3.1.2: Identified compounds in the bio-oil with chemical formulas | 69 |
| Table 3.1.3: Identified functional groups in the biochar corresponding to different wavenumber | 70 |
| Table 3.1.4: Uncertainties in proximate analysis, HHV, SAFR and others quantities at optimum ER | 72 |
| Table 3.2.1: Proximate analysis of dried grass, leaves and dead branches | 76 |
| Table 3.2.2: Ultimate analysis and HHV estimated by correlations | 76 |
| Table 3.3.1: Capital costs of different capacities power plant (gasification-based) in present scenario of India | 81 |
| Table 3.3.2: Various parameters involved in electricity generation costs (Rs./kWh) from various capacities power plant | 84 |
| Table 3.3.3: Profit in electricity costs from various capacities of biomass-based power plant | 86 |
| Table 4.1.1: Properties of Bi_2Te_3 semiconductor materials used for TEGs | 93 |
| Table 4.1.2: Comparison of V per ΔT_{TEG} for one TEG with the previous published literature | 105 |
| Table 4.1.3: Uncertainty analysis of various parameters | 106 |
| Table 4.2.1: Uncertainty analysis of various measuring parameters | 131 |
| Table 4.3.1: Properties of salt/saline water (fluid) stored in SGSP | 135 |
| Table 4.3.2: Experiments run under different conditions | 135 |
| Table 4.3.3: Waste heat temperatures at inlet and outlet of a SGSP for all run | 139 |
| Table 4.3.4: Thermal resistances offered between heat source and TEG's hot side for conventional and proposed systems | 163 |
| Table 4.3.5: Comparison of equivalent thermal resistance, $R_{t, \text{eq}}$, with the published literature | 164 |

| | |
|---|-----|
| Table 4.3.6: Uncertainties assessment of different measuring quantities | 166 |
| Table 4.3.7: Uncertainties associated with various measuring parameters | 176 |
| Table 5.1.1: Comparison between CCD and BBD | 184 |
| Table 5.1.2: Design levels of various operating input factors | 184 |
| Table 5.1.3: Design sets of experiments based on the three levels BBD | 185 |
| Table 5.1.4: Comparisons of PR and productivity of m_d under working conditions of different parameters | 196 |
| Table 5.1.5: Properties of seawater, distilled water and BIS maximum limit | 198 |
| Table 5.1.6: Experimental outcomes for the mass of distilled water under the different design set of run | 199 |
| Table 5.1.7: Goodness of correlations for the mass of distilled water as response parameter | 202 |
| Table 5.1.8: Uncertainty analysis of various measured values | 206 |

NOMENCLATURE

| | |
|---------------------------|--|
| a | Side of thermosyphon, m |
| $A_{b, LCZ}$ | Bottom area of LCZ, m ² |
| $A_{cont.}$ | Crossectional area of source container, m ² |
| $A_{s, cond.}$ | Surface area of condenser section, m ² |
| $A_{s, evap.}$ | Surface area of evaporator section, m ² |
| $A_{s, LCZ}$ | Total surface area of LCZ, m ² |
| $A_{t, SGSP}$ | Top area of SGSP, m ² |
| A_{wall} | Array wall surface area, m ² |
| b_o, b_1, b_2 and b_3 | Coefficient values |
| c_{bw} | Specific heat of basin water, J/(kg·K) |
| C | Carbon percentage in biomass |
| CH_4 | Methane |
| c_{LCZ} | Specific heat of LCZ water, J/(kg·K) |
| $C_{min.}$ | Minimum heat capacity between waste heat and salt water, J/K |
| CO | Carbon monoxide |
| CO_2 | Carbon dioxide |
| C_v | Contribution of a input/governing factor |
| c_{water} | Specific heat of pure water, J/(kg·K) |
| $c_{wf, l}$ | Specific heat of liquid working fluid, J/(kg·K) |
| c_{WH} | Specific heat of flue gases (waste heat), J/(kg·K) |
| $d_{eq.}$ | Equivalent diameter of flow passage through HRS, m |
| $D_{cont.}$ | Diameter of source container, m |
| D_e | Equivalent diameter of thermosyphon, m |
| f | Engine frequency, Hz |
| h | Convective heat transfer coefficient, W/(m ² ·K) |
| H | Hydrogen percentage in biomass |

| | |
|----------------------------------|--|
| H_2 | Hydrogen |
| H_2O | Water |
| H_{bw} | Height of the basin water, m |
| h_{fg} | Latent heat of evaporation for water, J/kg |
| $h_{fg, wf}$ | Latent heat of evaporation for working fluid, J/kg |
| H_{LCZ} | Height of LCZ, m |
| H_{SGSP} | Height of SGSP, m |
| $H^* = H_{bw} / [H_{bw}]_{max.}$ | Dimensionless basin water height |
| I_o | Output current, A |
| I_s | Short circuit current, A |
| $k_{cop.}$ | Thermal conductivity of copper sheet, W/(m·K) |
| K_e | Equivalent thermal conductance, W/K |
| k_{LCZ} | Thermal conductivity of LCZ water, W/(m·K) |
| k_n | Thermal conductivity of n-type semiconductor material, W/(m·K) |
| k_p | Thermal conductivity of p-type semiconductor material, W/(m·K) |
| k_{sw} | Thermal conductivity of salt water, W/(m·K) |
| k_{water} | Thermal conductivity of pure water, W/(m·K) |
| $k_{wf, l}$ | Thermal conductivity of liquid working fluid, W/(m·K) |
| l | Length of array-based HRS, m |
| L | Length of flow passage in array HRS, m |
| $L_{cond.}$ | Length of condenser section, m |
| $L_{evap.}$ | Length of evaporator section, m |
| m_b | Mass of biomass required, kg |
| M_C | Molecular mass of carbon, kg/kmol |
| m_d | Mass of distilled/pure water, kg |
| $m_d^* = m_d / m_{d, max.}$ | Dimensionless amount of distilled water produced |

| | |
|-------------------|--|
| $\dot{m}_{f,LCZ}$ | Mass flow rate of LCZ water passes through array-based HRS, kg/s |
| M_H | Molecular mass of hydrogen, kg/kmol |
| m_{LCZ} | Mass of LCZ water, kg |
| m_{N_2} | Mass of stoichiometric Nitrogen compound, kg/kg of fuel |
| M_{N_2} | Molecular mass of N_2 , kg/kmol |
| m_{NCZ} | Mass of NCZ water, kg |
| m_{O_2} | Mass of stoichiometric Oxygen compound, kg/kg of fuel |
| M_{O_2} | Molecular mass of O_2 , kg/kmol |
| M_{SW} | Molecular mass/weight of salt water, kg/mol |
| m_S | Mass of source water, kg |
| M_S | Molecular mass of sulphur, kg/kmol |
| M_{water} | Molecular mass/weight of pure water, kg/mol |
| m_{WH} | Mass of flue gases (waste heat) (over period of 1 hour), kg |
| n | Number of input factors |
| $n_{couples}$ | Number of series-connected couples in a TEG |
| N_o | Number of observed data points |
| N | Nitrogen percentage in biomass |
| O | Oxygen percentage in biomass |
| p | Number of level |
| $P_{atm.}$ | Atmospheric pressure, N/m ² |
| P_o | Output power, W |
| P_v | Vacuum pressure, mm of Hg |
| $P_{vap.}$ | Vapour pressure, N/m ² |
| q_i | Number of observations completed at the i_{th} level |
| $Q_{act.}$ | Actual heat transfer to saline water of SGSP, J |
| Q_b | Required biomass energy, MJ |
| Q_{CFDS} | Heat energy supplied to CFDS, J |
| $\dot{Q}_{cont.}$ | Rate of heat supplied to source container, W |

| | |
|--------------------|--|
| $\dot{Q}_{evap.}$ | Rate of heat supplied at evaporator section, W |
| Q_{LCZ} | Heat stored in LCZ, J |
| $Q_{max.}$ | Maximum possible heat transfer to SGSP, J |
| Q_{SGSP} | Heat storage capacity of SGSP, MJ |
| \dot{Q}_{TEG} | Rate of heat energy supplied to TEG, W |
| r | Number of independent variable |
| R^2 | Coefficient of determination |
| R_E | External load resistance in the circuit, Ω |
| R_o | Number of central points |
| R_T | Total internal electrical resistance for a TEG, Ω |
| $R_{t, cond.}$ | Array wall conduction resistance, $^{\circ}\text{C}/\text{W}$ |
| $R_{t, conv.}$ | Convection resistance in array-based HRS, $^{\circ}\text{C}/\text{W}$ |
| $R_{t, e}$ | Equivalent thermal resistance for thermosyphon-based HRS, $^{\circ}\text{C}/\text{W}$ |
| $R_{t, eq.}$ | Equivalent thermal resistance for array-based HRS respectively, $^{\circ}\text{C}/\text{W}$ |
| $R_{t, fb, evap.}$ | Film boiling resistance at evaporator section, $^{\circ}\text{C}/\text{W}$ |
| $R_{t, fc, cond.}$ | Film condensation resistance at the condenser section, $^{\circ}\text{C}/\text{W}$ |
| $R_{t, max.}$ | Maximum thermal resistance, $^{\circ}\text{C}/\text{W}$ |
| $R_{t, pb, evap.}$ | Pool boiling resistance at evaporator section, $^{\circ}\text{C}/\text{W}$ |
| $R_{t, w, cond.}$ | Thermosyphon wall conduction resistance at condenser section, $^{\circ}\text{C}/\text{W}$ |
| $R_{t, w, evap.}$ | Thermosyphon wall conduction resistance at evaporator section, $^{\circ}\text{C}/\text{W}$ |
| s | Measured value |
| \bar{s} | Mean of ε number of data points |
| S | Solar radiation intensity, W/m^2 |
| $S_{avg.}$ | Average (over a day) solar radiation incident, W/m^2 |
| $S_{max.}$ | Maximum solar radiation incident, W/m^2 |
| $S_{min.}$ | Minimum solar radiation incident, W/m^2 |
| $S_{T, avg.}$ | Average of total solar radiation incident over the exposure time period, W/m^2 |

| | |
|--|---|
| S_u | Sulphur percentage in biomass |
| t | Time, minutes or hours |
| $T^* = \frac{T_{WH, inl.}}{[T_{WH, inl.}]_{max.}}$ | Dimensionless temperature |
| T_a | Ambient temperature, °C |
| $T_{a, avg.}$ | Average (over a day) temperatures of ambient, °C |
| T_{bw} | Temperature of basin water, °C |
| T_C | Sink/cold water temperature, °C |
| $T_{Ch, avg.}$ | Average temperature of cold and hot sides of TEG, °C |
| T_{CW} | Cold water temperature, °C |
| T_f | Temperature of fin, °C |
| T_h | Hot side temperature of TEG, °C |
| T_{LCZ} | Temperature of LCZ, °C |
| $T_{LCZ, avg.}$ | Average (over a day) temperature of LCZ respectively, °C |
| $T_{LCZ, max.}$ | Maximum temperature of LCZ respectively, °C |
| $T_{LCZ, out.}$ | Temperature of LCZ water at the outlet of array-based HRS, °C |
| T_{NCZ} | Temperature of NCZ, °C |
| T_{ma} | Temperature of moist air, °C |
| $T_{NCZ, max.}$ | Maximum temperature of NCZ, °C |
| T_s | Source water temperature, °C |
| T_{UCZ} | Temperature of UCZ, °C |
| $T_{UCZ, avg.}$ | Average (over a day) temperature of UCZ, °C |
| $T_{UCZ, max.}$ | Maximum temperature of UCZ, °C |
| $T_{UCZ, min.}$ | Minimum temperature of UCZ, °C |
| T_{WH} | Waste heat temperature, °C |
| $T_{WH, avg.}$ | Average temperature of waste heat, °C |
| $T_{WH, in}$ | Waste heat temperature at inlet of SGSP, °C |
| $T_{WH, inl.}$ | Waste heat temperature at inlet of CFDS, °C |
| $T_{WH, out}$ | Waste heat temperature at outlet of SGSP, °C |

| | |
|-----------------|--|
| $T_{WH, outl.}$ | Waste heat temperature at outlet of CFDS, °C |
| u | Velocity of flowing LCZ water through array-based HRS, m/s |
| v | Independent input factors |
| V | Open circuit voltage, V |
| $V_{max.}$ | Maximum open circuit voltage, V |
| V_o | Output voltage, V |
| \dot{V}_{WH} | volume flow rate of waste heat, m ³ /s |
| w | Width of array-based HRS, m |
| W_L | Engine load, kW |
| X_C | Mass fraction of carbon component in biomass |
| X_H | Mass fraction of hydrogen component in biomass |
| X_S | Mass fraction of sulphur component in biomass |
| Y_{N_2} | Volume fraction of N ₂ compound in air |
| Y_{O_2} | Volume fraction of O ₂ compound in air |
| Z_{fb} | Figure of merit for film boiling, K ⁻¹ |
| Z_{pb} | Figure of merit for pool boiling, K ⁻¹ |
| z | Independent variable |
| ZT | Dimensionless figure of merit for TEG |
| $\frac{dT}{dt}$ | Rate of rise in temperature, K/s |

Greek symbols

| | |
|------------------|--|
| α_e | Equivalent Seebeck coefficient, $\mu V/K$ |
| α_n | Seebeck coefficient of n-type semiconductor material, $\mu V/K$ |
| α_p | Seebeck coefficient of p-type semiconductor material, $\mu V/K$ |
| $\delta_{cop.}$ | Thickness of copper sheet, m |
| ΔT_{bw} | Temperature rise of basin water before evaporation, °C |
| ΔT_{LCZ} | Temperature gain within LCZ, °C |
| ΔT_{LU} | Temperature gradient between LCZ and UCZ at particular instant of time, °C |

| | |
|------------------------------|--|
| $\Delta T_{LU, \text{avg.}}$ | Average (over a day) temperature gradient between LCZ and UCZ, °C |
| $\Delta T_{LU, \text{max.}}$ | Maximum temperature gradient between LCZ and UCZ, °C |
| $\Delta T_{LU, \text{req.}}$ | Required minimum critical/threshold temperature gradient, °C |
| ΔT_{TEG} | Temperature gradient across TEG, °C |
| ΔT_{WH} | Temperature gradient of waste heat across SGSP, °C |
| ε | Number of data points taken |
| ϕ | Measuring parameter/dependent variable of interest |
| η_{cg} | Cold gas efficiency, % |
| η_{e} | Conversion efficiency of engine-generator, % |
| η_{p} | Efficiency of waste heat pipe, % |
| η_{SGSP} | Thermal efficiency of SGSP, % |
| η_{TEG} | Conversion efficiency of TEG, % |
| μ_{LCZ} | Viscosity of LCZ water, N·S/m ² |
| μ_{water} | Viscosity of pure water, N·S/m ² |
| $\mu_{\text{wf}, l}$ | Viscosity of liquid working fluid, N·S/m ² |
| Θ_{g} | Glass inclination angle, degree |
| ρ_{LCZ} | Density of LCZ water, kg/m ³ |
| ρ_{n} | Electrical resistivity of n-type semiconductor material, $\mu\text{V/K}$ |
| ρ_{p} | Electrical resistivity of p-type semiconductor material, $\mu\text{V/K}$ |
| ρ_{salt} | Density of salt, kg/m ³ |
| ρ_{sw} | Density of saline water, kg/m ³ |
| ρ_{water} | Density of pure water, kg/m ³ |
| $\rho_{\text{wf}, l}$ | Density of working fluid in liquid form, kg/m ³ |
| $\rho_{\text{wf}, v}$ | Density of working fluid in vapour form, kg/m ³ |
| ρ_{WH} | Density of waste heat, kg/m ³ |
| σ | Standard deviation |
| γ | Aspect ratio, m ⁻¹ |
| ψ | Response parameter |
| $\overline{\psi}$ | Grand mean of all observed data points |

Abbreviations

| | |
|-------------------------------------|--|
| <i>AAFR</i> | Actual air-fuel ratio |
| <i>AC</i> | Ash content |
| <i>ANOVA</i> | Analysis of variance |
| <i>BBD</i> | Box-Behnken design |
| <i>Bi₂Te₃</i> | Bismuth Telluride |
| <i>CCD</i> | Central composite design |
| <i>CFDS</i> | Copper finned distillation system |
| <i>CGE</i> | Cold gas efficiency |
| <i>CV</i> | Lower Calorific value |
| <i>DAQ</i> | Data acquisition system |
| <i>DFE</i> | Degree of freedom for error |
| <i>DFI</i> | Degree of freedom for a input/governing factor |
| <i>EC</i> | Electrical conductivity |
| <i>EPDM</i> | Ethylene Propylene Diene Monomer |
| <i>ER</i> | Equivalence ratio |
| <i>ESS</i> | Error sum of squares |
| <i>FC</i> | Fixed carbon |
| <i>GI</i> | Galvanized iron |
| <i>HHV</i> | Higher heating value |
| <i>HRS</i> | Heat recovery system |
| <i>IC</i> | Internal combustion |
| <i>LCZ</i> | Lower convective zone |
| <i>MC</i> | Moisture content |
| <i>MSS</i> | Mean sum of squares |
| <i>NCZ</i> | Non-convective zone |
| <i>Nu</i> | Nusselt number |
| <i>ORC</i> | organic Rankine cycle |
| <i>Pr</i> | Prandtl number |

| | |
|-------------|--------------------------------|
| <i>PR</i> | Performance ratio |
| <i>Re</i> | Reynolds number |
| <i>SAFR</i> | Stoichiometric air-fuel ratio |
| <i>SC</i> | Salt concentration |
| <i>SGP</i> | Specific gas production |
| <i>SGSP</i> | Salt gradient solar pond |
| <i>TDS</i> | Total dissolved solids |
| <i>TEG</i> | Thermoelectric generator |
| <i>TFR</i> | Thermosyphon filling ratio |
| <i>TSS</i> | Total sum of squares |
| <i>UCZ</i> | Upper convective zone |
| <i>UPS</i> | Uninterruptible power source |
| <i>VM</i> | Volatile matters |
| <i>WH</i> | Waste heat |
| <i>XLPE</i> | Cross linked polyethylene foam |

CHAPTER 1

INTRODUCTION

This chapter presents some basic aspects of biomass gasification along with potential components for waste heat recovery such as thermosyphon, thermoelectric generator, solar pond and active distillation system. In particular, the working principle of different types of gasifier and other supplementary components are discussed in details along with their features, utility and practical applications under various working conditions. The content presented in this chapter will help the reader to understand the working/utilization of each component of the experimental setup in processing out the complete work and their practical applications.

1.1 Motivation

With fast decline of fossil fuels (non-renewable sources) and growing energy demand, it is essential to discover alternative energy sources in order to develop sustainable, clean, efficient and renewable energy-based technologies. Mostly used energy source after coal, petroleum and natural gas is biomass which contributes about 14% of the global primary energy consumption [Saxena et al. 2009]. Biomass is a renewable energy source and is derived from plants, waste from forests, agriculture and the industrial sectors. In contrast to fossil fuels, biomass doesn't contribute to the addition of carbon dioxide (CO₂) to the environment and it is cheap, easily as well as abundantly available almost all over the world [Sheth and Babu 2009; Antar et al. 2021]. In India, more than 65% of the total population live in villages where people are still using biomass in fired cookstove for their energy needs (heating and cooking purposes). This fired cookstove is based on combustion process which has low conversion efficiency and emits many harmful gases that pollute the indoor air quality causing diseases to people. The work in the thesis addresses this issue by producing useful energy in an efficient manner through WH recovery techniques. The purpose is to lower the emissions with high energy generation from the inefficiently used locally biomass. There are mainly three conversion routes available to extract the useful energy from the biomass: (i) Biochemical, (ii) Thermochemical and (iii) Mechanical [Kumar et al. 2015]. In comparison to

other conversion routes, the gasification technology via thermochemical conversion process/route is found to be the most efficient way of energy production from the biomass. The system in which gasification process occurs is known as gasifier. This technology has many ecological advantages such as higher energy conversion efficiency, effective energy utilization with almost negligible waste production and very low emission [Basu 2006; Tezer et al. 2022]. However, the performance of gasifier depends upon many factors such as its design, air input flow rate, gasification temperature, type of feeding fuel, category of the gasifier, and many more. In order to understand the principle of gasifier, characteristics of gasification process, uses and limitations of different kinds of gasifier, the details are provided in the below texts.

1.2 Gasifier

A gasifier converts the carbonaceous fuel into combustible gases (known as syngas) through the gasification technique. There are mainly four processes involved in the gasifier to produce syngas namely: (i) Drying, (ii) Pyrolysis, (iii) Combustion and (iv) Reduction as described in Figure 1.1. In the drying process, the moisture content (MC) present in the raw biomass gets evaporated into vapour form when it is heated at a temperature range of 100-150 °C. In the pyrolysis process, the

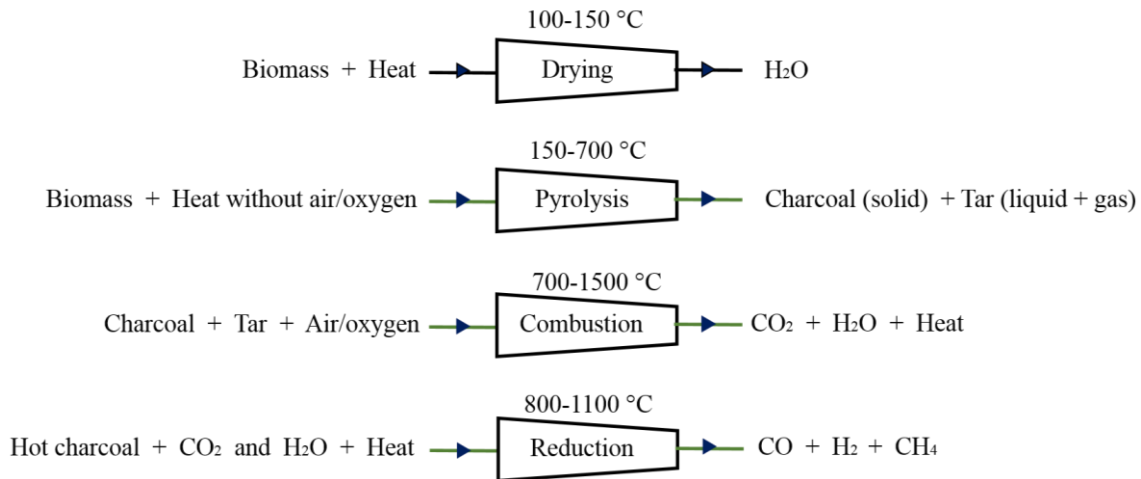


Figure 1.1: Different processes involved in the gasifier to produce syngas

raw biomass is heated in the absence of air within the temperature range of 150-700 °C that breaks down it into charcoal (solid) and tar (liquid and gas). The combustion process is the only exothermic process among all which provides heat to drying, pyrolysis and reduction directly or indirectly by internal heat exchange. The combustion process produces CO₂, water (H₂O) vapours and heat when charcoal as well as tar react with the air/oxygen at a high temperature (800-1200

°C). The reduction process is the reverse of combustion in which oxygen gets removed from the products (CO_2 and H_2O) at a temperature of 650-900 °C to produce combustible gases such as carbon monoxide (CO), hydrogen (H_2) and methane (CH_4) [Baruah and Baruah 2014; Diyoke et al. 2018].

1.3 Types of gasifier

Gasifiers are generally categorized into three types: (a) fixed bed gasifier, (b) fluidized bed gasifier and (c) entrained flow gasifier as revealed in Figure 1.2. The fixed bed gasifier is the simplest form of gasifier used for 10 kW to 10 MW [Basu 2010] capacity power plants and applies the traditional method for gasification of biomass. It is further classified into three kinds: (i) updraft (countercurrent) gasifier, (ii) downdraft (co-current) gasifier and (iii) crossdraft gasifier.

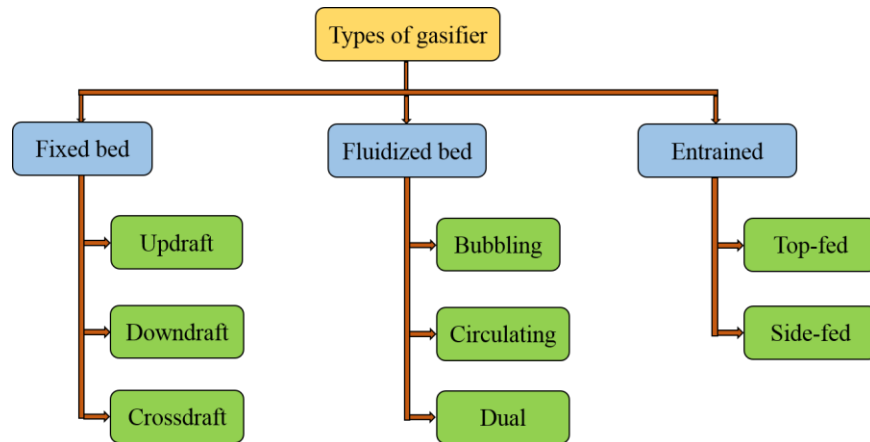


Figure 1.2: A schematic diagram representing different types of gasifier

1.3.1 Updraft gasifier

An updraft gasifier is the oldest form of gasifier. In this gasifier, the biomass fuel is fed from the top of reactor, while air (as gasifying agent) enters from the bottom and flows in the upward direction as revealed in Figure 1.3 (a). The syngas along with tars and volatile matters produced in the reactor exit from the top after passing through the biomass (low temperature zone) that do not allow the tars to further decompose. Therefore the product (syngas) leaving the gasifier would be contaminated with a significant amount of tars. This high quantity of tars in the syngas is not desirable for internal combustion (IC) engines. However, an updraft gasifier has some major advantages like ease to use, high proportion of charcoal burn out, high conversion efficiency and low temperature of leaving syngas due to the exchange of internal heat. It is mostly used for the

gasification of coal and non-volatile fuels like charcoal, but impractical to produce clean syngas from the volatile fuels (biomass) [Reed and Das 1988; Luo et al. 2018].

1.3.2 Downdraft gasifier

In the downdraft gasifier, both gasifying agent and biomass enter from the top of the reactor as sketched in Figure 1.3 (b) and the syngas generated in the reactor exits from the bottom at high temperatures of about 900 °C -1000 °C. Thus, the syngas contains a lower amount of tars compared to an updraft gasifier, but has higher amount of particulate content. The syngas generated from a downdraft gasifier is suitable for IC engines but needs to be cooled at room temperature before usage. This is the most successful developed design of gasifier for the production of low tar syngas from the gasification of high volatile fuels (biomass) [Reed and Das 1988; Luo et al. 2018].

1.3.3 Crossdraft gasifier

A downdraft gasifier is the lightest gasifier in which air enters at a very high velocity through a nozzle and moves across the reactor via bed of char as shown in Figure 1.3 (c). This generates a very high temperature in a small controlled volume of bed that leads to a fastest response time and a production of low tar content in the syngas which is required for IC engines. However, the formation of slag and insulation on the wall of gasifier occurs due to ash depositing on the mild steel construction material of the gasifier. Also, nozzle as well as grate require refractory alloys and cooling system (air/water-cooled). Further, a specific size of fuel is also required for smooth and proper operation of the crossdraft gasifier [Luo et al. 2018].

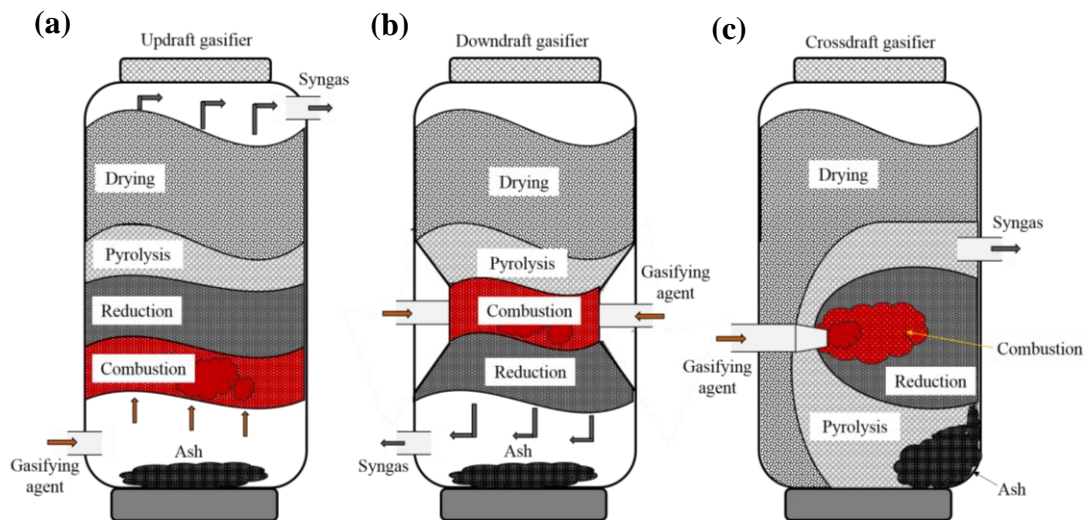


Figure 1.3: Principle of (a) updraft, (b) downdraft and (c) crossdraft fixed bed gasifiers

A fluidized bed gasifier uses the non-consumable bed material which gets fluidized by the gasifying agent to provide an excellent mixing of air and fuel, high heat capacity of chamber, and helps in controlling gasification temperature and create an isothermal behavior. In this gasifier, high velocity gasifying agent enters through a grate from the bottom of the reactor and the small sized particles of bed material above the grate levitate to form the fluidized bed. The reduction chamber or bed zone exhibits a uniform temperature distribution because of proper mixing of air and fuel. The syngas generated from the gasification process exits at the top of the reactor. The fluidized bed gasifier is appropriate for moderate capacities range (5 MW-100 MW) and mainly classified into three types: (i) bubbling fluidized bed gasifier, (ii) circulating fluidized bed gasifier and (iii) dual fluidized bed gasifier [Reed and Das 1988; Motta et al. 2018].

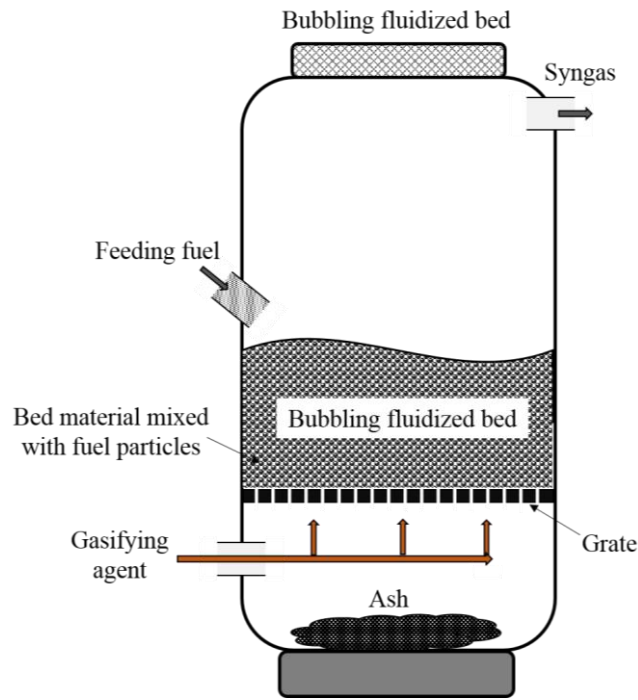


Figure 1.4: Schematic layout of a bubbling fluidized bed gasifier

1.3.4 Bubbling fluidized bed gasifier

A bubbling fluidized bed gasifier (Figure 1.4) is characterized by appropriate (moderate) fluidization velocities and the gas bubbles formed in the reactor are accountable for proper mixing of gasifying agent and fuel. In this gasifier, the gasifying agent is supplied at high velocity from the bottom and the bed containing fine grained bed material (0.5-1.0 mm of particles size) moves upward to form the bubbling fluidized bed. The gasification temperature remains almost uniform in the chamber within 800 °C-900 °C and the generated syngas with a low tar content and high

temperature withdrawals from the reactor at the top. This type of gasifier has presented many featured characteristics such as generation of low tar content gas, high carbon conversion efficiency and ability to process heterogeneous fuel. However, the problem of agglomeration in the gasification zone occurs during the operation [Hofbauer and Materazzi 2019; Hanchate et al. 2021].

1.3.5 Circulating fluidized bed gasifier

In circulating fluidized bed gasifier (Figure 1.5), the entering of gasifying agent at high velocity creates a fast fluidized bed and the whole reactor is filled with the fast fluidization bed materials (0.2 mm-0.5 mm of particles size) by its expansion. The particles leaving from the top of the reactor are separated by a cyclone and resent back to the gasification chamber. Therefore, the bed material as well as char are circulated between cyclone separator and chamber. The benefit of particle separator is that the residence time of fuel particles in the reactor gets extended and carbon loss is decreased. A uniform temperature distribution is attained throughout the reactor. The properties of a fast fluidized bed is similar as those of bubbling fluidized bed, however, the power/cross-sectional area is much greater for a circulating fluidized bed reactor that makes it more favorable for large-scale units [Hofbauer and Materazzi 2019].

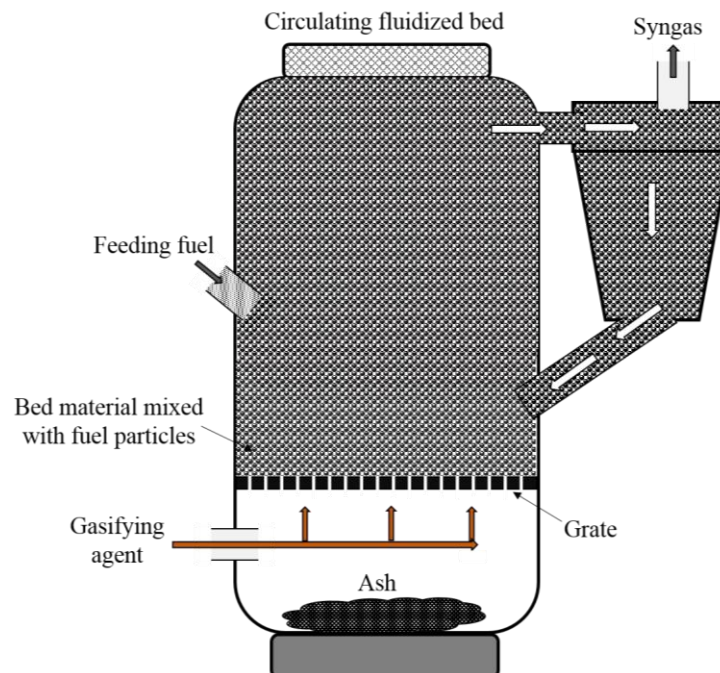


Figure 1.5: Diagram of a circulating fluidized bed gasifier

1.3.6 Dual fluidized bed gasifier

A dual fluidized bed gasifier as shown in [Figure 1.6](#) is comprised of two different fluidized beds (bubbling and circulating) in which the first reactor is used for pyrolysis process and the second is employed for combustion process. The first fluidized bed acts as a pyrolysis reactor and it is heated with the circulated bed material having high temperature that is supplied from the second reactor. The char delivered from the first reactor gets burnt and provide heat to the bed material. The bed material plays a key role in transporting the heat and acts as a heat transfer medium. A dual fluidized bed gasifier has many performance characteristics such as its flexibility in fuel feeding, constant reactor temperature, high heat transfer rates and production of nitrogen-free syngas [[Pissot et al. 2020](#); [Hanchate et al. 2021](#)].

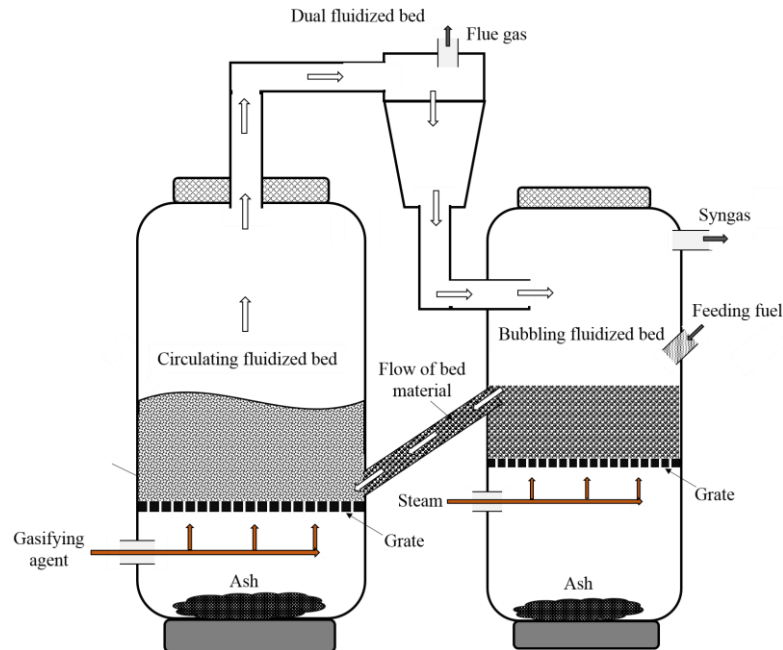


Figure 1.6: Principle of a dual fluidized bed gasifier

1.3.7 Entrained flow gasifier

In an entrained flow gasifier ([Figure 1.7](#)), the gasifying agent/steam oxygen and fine coal are fed co-currently in the reactor. This leads to entraining of coal particles by the gasifying agent when they travel in the reactor through dense medium. It is operated at very high temperature (1800-1990 °C) and pressure with enormous turbulent flow in the reactor that cause fast fuel conversion. The reaction rate of gasification process is very high that allows few seconds of residence time and produces syngas having high efficiency of carbon conversion (98-99.5%). An entrained flow gasifier has the ability to produce clean and tar-free syngas by handling any type of coal feedstock.

However, the high gasification/operating temperature melts the coal ash to form inert slag and the syngas exits with a high sensible heat that needs to be recovered to increase the efficiency of the system. This type of gasifier is suitable for large units with capacities range of 50 MW-1000 MW and classified into two parts: (i) top-fed entrained gasifier and (ii) side-fed entrained gasifier [Ratafia-Brown et al. 2002; Phillips 2006; Basu 2010].

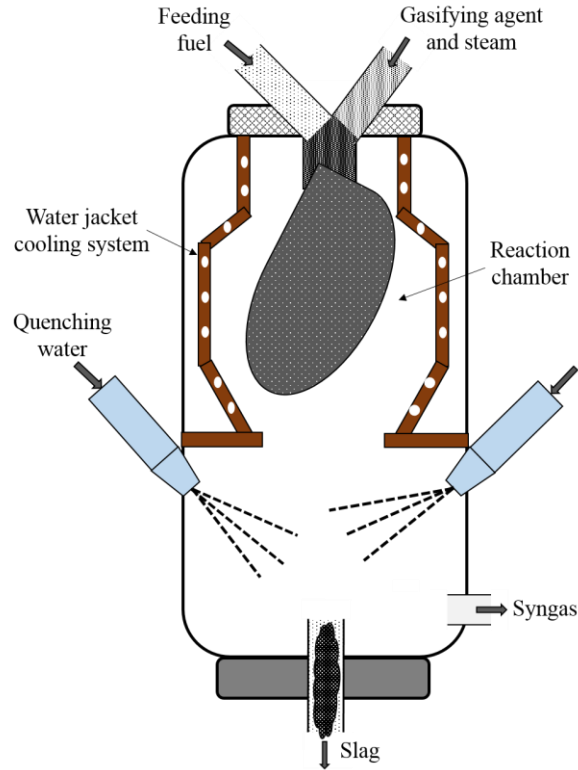


Figure 1.7: Principle of an entrained flow gasifier

In the top-fed entrained gasifier, the jet form of fine fuel particles and gasifying agent enter from the top of the reactor. The produced syngas exits the reactor at the side of bottom section and slag is deposited at the bottom [Molino et al. 2018]. In the side-fed entrained gasifier, the gasifying agent and powdered fuel are supplied from the side-lower section of reactor through nozzles and achieves a proper mixing of feeding fuel with the agent. The produced syngas is taken out from the top of reactor, whereas the formed slag is left at the bottom of the reactor [Molino et al. 2018].

Among all types of gasifiers, the downdraft gasifier is found to be most promising/friendly-used gasifier for pilot-scale experiments, low tar content, flexible operational capacities and feeding fuels. Additionally, the syngas produced from this gasifier can also be directly used for IC engines to generate power. Therefore, the downdraft gasifier is most successful for thermal energy

and power generation under variable conditions and has been currently used for co-generation (thermal energy and power) study of this work through optimizing the gasification process to lower the emissions. Further, the viability of this biomass-based gasification power plant under variable capacities has been also performed through an economic analysis. The system of the power plant to generate the co-generation (thermal energy and power) has been explained in the next paragraph.

1.4 Biomass-based power plant

The biomass-based power plant mainly consists of (i) Gasifier, (ii) Filters, (iii) Cooling tower and (iv) Engine generator (genset) as presented in [Figure 1.8](#). As described earlier, a gasifier produces syngas when biomass fuel is heated at a high temperature in the presence of a limited quantity of oxygen/air [\[Balat et al. 2009\]](#). The gasifier comprises of many parts such air blower, heater, reactor with ash tank. The purpose of an air blower is to supply the air from ambient to the place where reactions occur. The biomass stored in the gasifier is ignited from the heater for thermochemical conversion. The produced syngas gets collected in a tank from which biochar in the form of ash is stowed at bottom (ash tank) while syngas is remained above it. Filters are useful to get clean gas through various methodology such as whirling action, absorption and sieving. The generated syngas has high temperature and needs to be cooled that is accomplished using the cooling tower with the aid of water pump and cooling fan. Then, the syngas is delivered to the engine where chemical energy of the syngas is converted into mechanical power through the combustion process that drives the engine generator to produce electrical power [\[Puig-Arnavat et al. 2010\]](#).

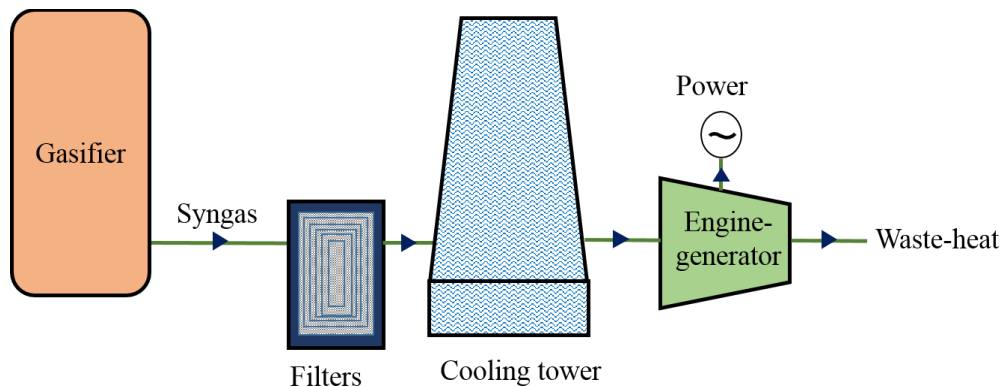


Figure 1.8: A layout representing various components in the biomass-based power plant

Since most of the engines have a limited conversion efficiency of 25-30%, therefore, the remaining energy gets released in the ambient as coolant and flue gases or waste heat (WH) [Jadhao and Thombare 2013]. WH is considered to be a potential form of energy source and it is available in the form of thermal energy that represents about 20-50% of the total fuel energy consumed [Elsaid et al. 2020; Forman et al. 2016]. To overcome the WH related issue, two approaches have been realized: first is to develop more efficient engines that are presently available and second is efficient recovery of WH for useful energy production. Instead of making more efforts to develop efficient engines which seems to be a difficult challenge, it is relatively easier and effective to recover the WH for useful energy production to enhance the system's efficiency [Aghaali and Angstrom 2015; Loni et al. 2021].

1.5 Potential components for recovery of waste heat

The WH is generally available at high temperatures and can be recovered for further useful applications. In India, the annual growth rate of population (1.58%) has significantly increased the energy demand over the last few decades. In 1991-92, the electricity demand in India was only 231 TWh which has escalated up to 725 TWh in 2009-10 with a growing rate of 27.44 TWh/year. The growing rate was found to be increased with time and expected to reach 91.40 TWh/year with a projected demand of 2531 TWh in 2031-32 [Laha et al. 2020]. This concern needs developing an efficient power generation technique in a sustainable manner through waste heat recovery. Further, the availability of fresh drinking water is also a universal problem because the quantity of freshwater available is only about 2.5% of the total quantity and the remaining is saline water. The increase in population and subsequent decrease in freshwater attract major attention of researchers towards this direction. Reverse Osmosis/RO (membrane-based) technique to produce fresh drinking water has limited output and also it is driven by power consuming aspects. It is such an extensive energy process that it requires about 10,000 tons of fossil fuel every year to produce 1,000 m³ of fresh water per day. These concerns motivate to develop more efficient and clean energy technologies. The work presented in this thesis also covers these problems and an attempt has been made for power as well as fresh drinking water production from the WH using suitable components [Jadhao and Thombare 2013]. There are many potential components available which could be tried based on their capability, uses, suitability and limitations that have been described in the following sections.

1.5.1 Heat recovery steam generator

The heat recovery steam generator is a combined system used to recover the WH for steam generation. It consists of different segments such as evaporator, superheater, economiser and steam drum as presented in Figure 1.9. The superheater is located in the route of hottest WH upstream of the evaporator and the economiser is employed downstream of the evaporator in the coolest regime of WH [Muniandy et al. 2022]. The WH is recovered to enhance the overall efficiency by generating the steam which can be used either for process heating/drying in the industry or to drive a steam turbine for electricity generation. The evaporator section is used to convert the water into steam through the boiling process and then it is delivered to the steam drum where the saturated steam is separated from the water. This separation process is accomplished in two steps via a combination of gravity and mechanical work before it gets supplied to the superheater. Further, the WH rises its temperature beyond the saturation temperature and produces superheated steam which is then sent to a steam turbine for power generation. On the other hand, the economiser preheats the feedwater delivered to the evaporator and improves the efficiency of steam generation [Jouhara et al. 2018].

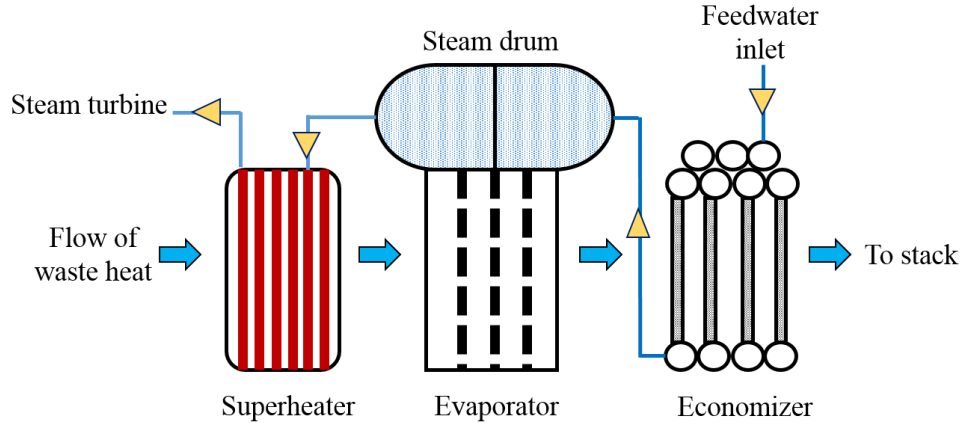


Figure 1.9: Schematic of a heat recovery steam generator

1.5.2 Thermoelectric generator

Thermoelectric generator (TEG) is a kind of heat engine that converts the available energy from the heat source into electric power directly through Seebeck effect. It is made by two types (“p-type” and “n-type”) of semiconductor materials as exposed in Figure 1.10, thus the thermo-physical properties of semiconductor materials play an important role on the performance of the TEG [Zheng et al. 2013]. Various types of materials (Bi_2Te_3 , Zn_4Sb_3 , PbTe , CoSb_3 , SiGe ,

$\text{Bi}_2\text{Se}_{0.3}\text{Te}_{2.7}$, etc) can be used for the TEG, but Bismuth Telluride (Bi_2Te_3) materials are commonly preferred because of their low costs and availability. The charge carriers for P-type and N-type semiconductor materials are holes (positively-charged) and electrons (negatively-charged) respectively. On the top/upper side of the TEG, a discrete junction is made by P and N-type semiconductor materials through an electrically conductive material and above which a ceramic substrate is attached. On the bottom/lower side of the TEG, the electrically conductive materials are attached individually below both P and N-type semiconductors and another substrate (ceramic) of same type connects these conductive materials. Heat energy from the source is delivered at the hot side of TEG and it is released at the cold side of the TEG. When heat energy from the source is provided, holes present in P-type semiconductor move into N-type semiconductor, while electrons travel from N-type to P-type semiconductor. Therefore, a potential difference is created across the TEG that produces voltage as well as current. TEG has many favorable features that make it more attractive for useful energy production. The most favorable is that it doesn't contain any moving parts during the operation of power production. This makes the TEG more reliable, increases its working life and declines the operational as well as maintenance costs. Since, the power production from the TEG is through Seebeck effect, it doesn't contribute in the environmental pollution and is eco-friendly in usage. Also, TEG is manufactured with compact

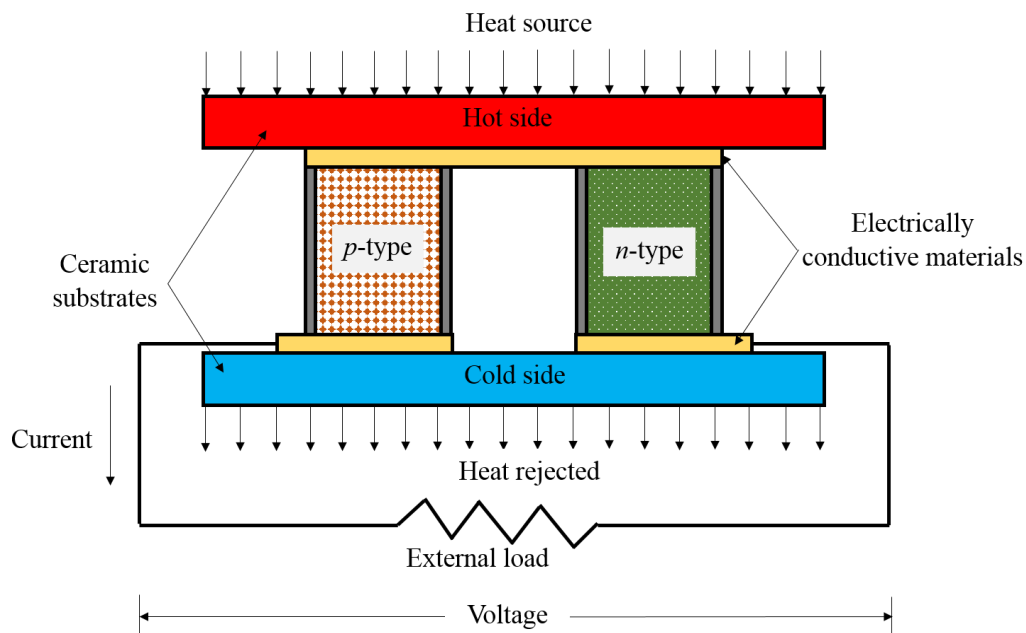


Figure 1.10: Illustration of a thermoelectric generator

size and light weight that allows it to utilize in a wide variety of places without any space constraints [Pourkiaei et al. 2019]. TEGs can be used for power generation by recovering the WH using a heat exchanger such as thermosyphon. TEGs are imposed on the condenser part (outer surface) of thermosyphon and converts the heat energy into electricity directly via Seebeck effect.

A thermosyphon is a closed-loop heat pipe which is used to transfer the heat energy from one place to another via boiling and condensation processes [Kim et al. 2018]. It is also known as two-phase closed thermosyphon and consists of three sections: (i) evaporator, (ii) adiabatic and (iii) condenser as revealed in Figure 1.11. The function of lower section (evaporator) is to evaporate the working fluid by absorbing heat from a heat source. The middle section (adiabatic) acts as an insulation against the surface heat losses while the upper section transfers the heat to the required place called condenser. The performance of thermosyphon depends upon many working parameters such as the properties of working fluid, thermosyphon filling ratio (TFR), aspect ratio, physical properties of thermosyphon material, working (heat source) temperature and vacuum pressure [Kumar et al. 2018]. Thermosyphon is filled with the working fluid for functioning of its heat transfer from evaporator to condenser section. The different kinds (water, acetone, methanol, ethanol, R-134a, R-123, etc.) of working fluids can be used based on their specific characteristics such as latent heat of vaporization, boiling point, thermal conductivity, kinematic viscosity, surface tension, thermal stability and compatibility with working materials, The working fluid with low viscosity and thermal stability, high latent heat of vaporization and surface tension is desirable for effective heat transfer. Mostly, water is preferred as working fluid in the thermosyphon [Gedik 2016]. TFR is the ratio of volume of the working fluid contained in the thermosyphon to the volume of the evaporator section. To get a maximum performance of the thermosyphon, it should be operated at an optimum TFR. The higher values of operating temperature and vacuum pressure are required for the thermosyphon that provide maximum heat transfer at the condenser section [Noie 2005]. The process of thermosyphon starts with the transferring of heat energy from the heat source to the working fluid at evaporator section where it gets evaporated under the condition of high vacuum pressure. The vapours move in the upward direction and passing through the adiabatic section where no heat transfer occurs. Thereafter, reaching to the condenser section, vapours release their latent heat and get condensed in the form of water. The condensed water falls down at the bottom section (evaporator) through gravity affect and this process repeats again continually with the availability of heat source [Louahlia-Gualous et al. 2017].

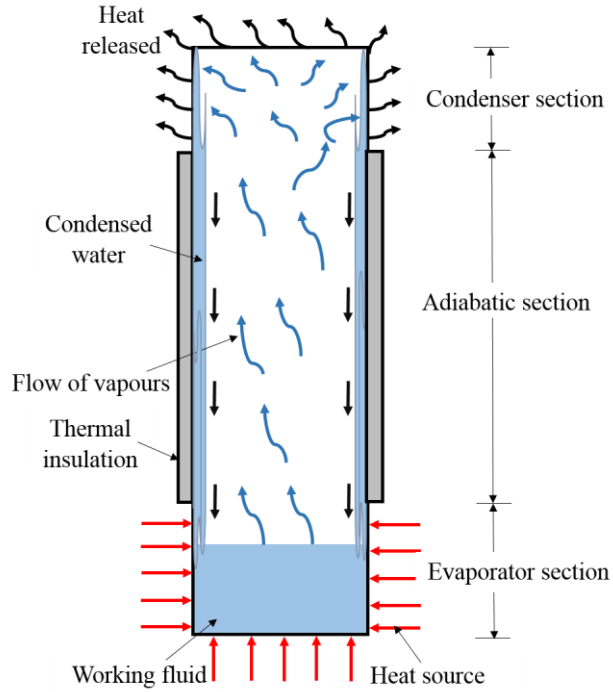


Figure 1.11: Schematic diagram of the two-phase closed thermosyphon

1.5.3 Phase change materials

Thermal energy storage is an appropriate method to store the WH in the materials for later usage. The materials used in the latent heat storage systems are known as phase change materials and their capacities depend upon the storing/releasing of heat during the transition of phase from one to another [Cabeza et al. 2020]. The storage of latent heat via phase change materials has many advantages such as high heat storage capacity, almost isothermal phase conversion and chemical stability [Faraj et al. 2020]. Phase change materials are classified into three categorizes based on the phase transition state: solid–solid, solid–liquid and liquid–gas. Solid-solid phase change materials have inherent drawbacks of slight/small transition latent heat and high cost, in spite of their low change in volume. Liquid-gas phase change materials reveal greater latent heat of vaporization, but their high change in volume during phase transformation restricts their utilization in thermal energy storage systems. Solid-liquid transition displays a low latent heat compared to liquid-gas form, but it gives a smaller change in volume (about 10% or less) and is more convenient. Therefore, solid-liquid phase change materials are mostly used and favorable in various thermal energy storage systems [Rashidi et al. 2020]. The working principle of solid–liquid phase change materials is that when the external temperature rises, the phase change material absorbs the heat up to its melting point and starts to melt until it is completely transformed into

liquid phase. When the external temperature declines, the phase change material discharges the previously stored heat and returns again to the solid phase [Wong-Pinto et al. 2020]. The solid-liquid phase change materials should have the following properties to be considered as suitable thermal energy storage media: high latent heat capacity, melting point closed to the utilization temperature, high specific heat per unit low vapour pressure, low corrosion effect, chemical stability, volume and mass, non-toxicity, low volume change during phase transformation, low supercooling and segregation, high thermal conductivity, environment friendly, and availability with low cost. The WH can be recovered by two methods using phase change materials: direct and indirect techniques. In the direct method, WH is directly applied to the thermal storage systems containing phase change materials, while in the indirect method, a distinct heat transfer fluid is used to recover the WH and then it is allowed to circulate through the thermal storage systems via heat pipes [Omara et al. 2021].

1.5.4 Salinity gradient solar pond

A salinity gradient solar pond (SGSP) is a heat energy storage system used to store thermal energy by heating water through resisting/suppressing the convective heat loss offered by a halocline effect [Weinberger 1964]. It comprises of three different zones: (i) upper convective zone (UCZ), (ii) non-convective zone (NCZ) and (iii) lower convective zone (LCZ) as described in Figure 1.12. The LCZ contains the saturated salt water (maximum salt concentration) it stores the thermal energy in it at a high temperature. The salt concentration varies in NCZ along its height (in increasing order from top to bottom) that acts as an insulator to the convection heat loss through a carefully maintained salinity gradient in it. Although, a small amount of heat is lost from the LCZ to the UCZ via convection-free NCZ by virtue of heat conduction, the UCZ is the coldest zone among them with lowest salt concentration (equivalent to normal water) because it continuously loses its heat to the ambient via convection, evaporation and radiation [Ganguly et al. 2017]. An SGSP is capable of storing high thermal energy up to 80 °C depending on the operating conditions [Nakoa et al. 2015]. The thermal performance of an SGSP depends on many characteristics such as the chemical properties of fluid, amount of fluid stored, physical properties of pond and ambient conditions [Karakilcik et al. 2013]. An SGSP has the ability to work day and night since it can store the thermal energy for long duration (weeks and months) even in the night also [Ganguly et al. 2019]. Moreover, it can also be easily used anywhere such as in hilly and remote areas where solar radiations are accessible. SGSPs are extensively used for desalination of water [Lu et al.

2001], electric power production [Singh et al. 2011], mechanical power generation [Tchanche et al. 2011] and several more [Rabl and Nielsen 1975].

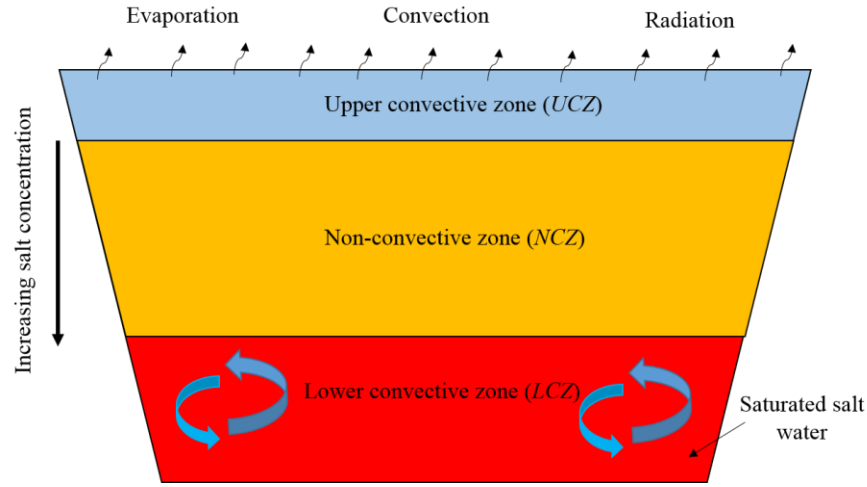


Figure 1.12: Diagram of a typical salinity gradient solar pond

1.5.5 Active distillation system

Desalination is a water purification technique used to produce fresh and clean water by removing salt and other impurities from it. It is mainly classified into two categories: (i) Reverse Osmosis/RO (membrane-based) and (ii) solar still (distillation-based). RO removes salt and other impurities by passing water through series connected semi-permeable membranes. A pump is used to pressurize the water against membrane surface that leads to salt-depleted water across it and releases clean water at the low pressure side. This technique has scaled down the size of system to make it suitable for portable applications, but still challenges are associated with high power consumption and requirement of more energy or power while feeding high salinity water [Ahmed et al. 2021]. Distillation system mainly consists of a basin (contains impure water or seawater) and glass cover (acts as a condenser). The seawater present in the basin evaporates from the solar energy and vapours move in an upward direction. The vapours condense at the internal surface of cooled glass cover and leaving the clean/pure water [Singh et al. 2021]. In comparison to RO, distillation system is simple to construct (locally available materials can be used), needs low maintenance and proves to be cost-effective along with its suitability for remote areas where the shortage of pure water is a major problem and availability of solar radiation is high [Singh et al. 2019]. The distillation system operated by only solar radiation is known as passive distillation system which has a very small output because it operates at low temperatures. Also, the problem occurs during the operation

of passive distillation system due to intermittent nature of solar radiation. Therefore, an active distillation system (Figure 1.13) is preferred to use in which thermal energy can be additionally supplied by some external heat source to increase the evaporation rate and productivity of the system [Nougriaya et al. 2021].

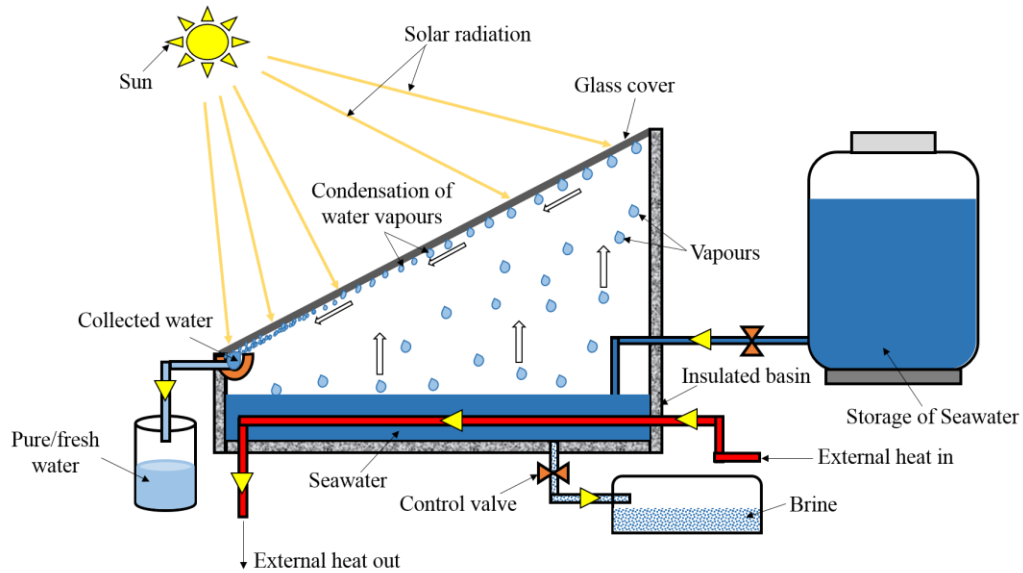


Figure 1.13: Schematic of an active distillation system

Based on the above discussion, it is realized that many locally waste biomass like dried grass, red mulberry, leaves available around the region of the current research is not explored in many energy generation/gasification-related aspects. This is imperative as the quality of syngas and other matter related to a biomass sample is dependent on the prevailing weather condition. Next to transform waste heat energy from gasification system, it has been found that the TEGs could play a key role in small-scale power generation from the WH through utilization of heat transfer using thermosyphons or any other device. SGSPs can be used for efficiently recovering the WH and can store the thermal energy for these applications. Further, WH can be utilized for water desalination by appropriate design of active distillation systems for addressing the issue of pure/potable water. Therefore, these all above opportunities have been tried for power and pure water production. All of these contribute towards the rationale of performing the current research.

CHAPTER 2

LITERATURE REVIEW

This chapter starts with highlighting the history of gasification process at international (outside India) and national (within India) levels. The first part of this chapter covers a brief summary of several published research articles describing the performance of gasifier using different biomasses at both international and national levels. Furthermore, the management and recovery of waste heat for various applications is pointed to enhance the efficiency of the system. The second part of this chapter covers a brief summary of various published research articles at international and national levels focused on the waste heat recovery for different applications. Finally, the objectives are proposed based on the research gaps identified through the literature survey and presented in the last section of this chapter.

2.1 History of the gasification process

The process of gasification was first invented by the two countries of Europe i.e. England and France during the year 1798. Initially, syngas or producer gas was produced within a control volume producer system in which charcoal and peat were used as feeding fuel and the viability of syngas for heating and power was soon recognized [Siwal et al. 2020]. During the World War I and II, generators driven by the syngas to power trucks, buses and industrial machines were used when the required fuel supply was not enough. All over the world, an estimated 90,00,000 vehicles were running on the syngas at that time. After the World War II, fossil fuels (petroleum)-based reliable and cheap technology was developed which gradually declined the utilization of syngas due to lack of strategic inputs and availability of cheaper fossil fuels. Due to hike in petroleum prices and the energy crisis in many countries during 1975, contemporary interest has risen again in the gasification process [Rajvanshi 1986]. This opens various scopes for improvement in the gasification process and exploring different waste biomass for useful energy production. Here, the international (outside India) and national (within India) status of various important research

findings (literature survey) on the gasification process (performance of gasifier) using different kinds of biomass are described.

2.1.1. Literature survey on the performance of gasifier using different biomass: International status

[Schoeters et al. 1989] studied the optimization study of a fluidized-bed downdraft gasifier by varying different input parameters such as the reactor temperature, air factor and the properties of feedstock fuels. Cacao hulls, pellets (*Euphorbia tirucalli*) and wood chips were used as fuel in the gasifier. The maximum values of calorific value (CV), cold gas efficiency (CGE) and gas yield of syngas were obtained as 5.7 MJ/m³, 60% and 6.5 kg/kg of fuel, respectively.

[Wang et al. 1992] conducted an experimental study to measure the properties of syngas produced from a fluidized bed gasifier. Various input parameters like equivalence ratio (ER), the residence time of gas, temperature and steam-biomass ratio were varied to get the maximum output and solid wood biomass was used as a feedstock fuel. It was observed that the gasification process was improved with longer residence time and higher temperature.

[Narvaez et al. 1996] used a pilot-scale bubbling fluidized-bed gasifier to investigate the gasification process of pine sawdust biomass under diverse variable input factors. The quality of syngas was analyzed by varying bed temperature of gasifier (750-850 °C), ER (0.20-0.45), H/C ratio in fuel and biomass mixed with calcined dolomite (2-5% by wt) as feeding fuel. Among all input parameters, the ER was found to be most effective in gasification for the yield of tar, gas composition and CV. The optimum value of ER was found in the range of 0.25 to 0.30.

[Fletcher et al. 1998] developed two mathematical models to optimize the design of a gasifier for avoiding slagging through the tracking of particles within the reactor. The flowfield calculations were accomplished by applying a differential Reynolds stress model and standard k- ϵ model. For this purpose, the sawdust and chopped cotton gin trash were considered as biomass fuel for the gasifier. The results showed that compared to standard k- ϵ model, differential Reynolds stress model provides better results and performed fine.

[Pan et al. 2000] carried out experiments on a fluidized-bed gasifier to study the characteristics of syngas in terms of CV and gas production rate operated under the atmospheric pressure. Various experiments were performed using blending of two fuels (pine chips and low-grade/refuse coal). The results showed that the most appropriate blending was found with at least 20% and 40% pine chips for low-grade and refuse coal respectively. The maximum CV (4750 kJ/m^3) and gas production rate ($3.20 \text{ m}^3/\text{kg}$) were achieved for pine chips/refuse coal and pine chips/low-grade coal respectively.

[Zainal et al. 2001] reported the performance of a downdraft biomass gasifier through an equilibrium model. The influence of MC in the wood biomass and gasification zone temperature on the CV of syngas were observed. Outcomes indicated that the CV decreases with an increment of the MC and the gasification temperature. The hydrogen/ H_2 and methane/ CH_4 contents in syngas were increased almost linearly, while carbon monoxide/ CO was linearly decreased with an increase in the MC.

[Zainal et al. 2002] investigated the gasification process by varying the ER using furniture wood and wood chips as biomass fuel in a downdraft biomass gasifier. The effect of ER on the CV, composition and production rate of syngas was experimentally analyzed. The results explored that the maximum output of the gasifier was obtained at an optimum ER of 0.38. The specific fuel consumption and CGE were found as 2 kg/kWh and 80% respectively.

[Mathieu and Dubuisson 2002] developed a numerical model to analyze the effect of air temperature, oxygen factor, operating pressure, etc. on the performance parameters of a gasifier in which solid wood was considered as a supplied fuel. The results revealed that the enrichment in oxygen levels enhances the performance under a certain temperature limit, and preheating of air beyond the critical temperature was no longer efficient.

[Lv et al. 2004] studied the performance of a fluidized bed gasifier by varying different input parameters include gasification temperature, ER, steam to biomass ratio and particle size of the biomass. Experiments were performed by using the pine sawdust biomass with a size range of 0.2-

0.9 mm. The results indicated that yield and CV of syngas were found in the range of 1.43-2.57 m³/kg and 6741-9143 kJ/m³ respectively.

[Hanaoka et al. 2005] investigated the performance of a fixed bed downdraft gasifier when Japanese oak and Japanese red pine bark were used as feeding fuel. Experiments were carried out to study the effect of cellulose, xylan, and lignin components of woody biomass on the gasification when operated at atmospheric pressure and 1173 K of temperature. Results indicated that carbon conversion efficiencies obtained for cellulose, xylan, and lignin were 97.9%, 92.2%, and 52.8% respectively.

[Yang et al. 2006] used the high temperature of air (up to 1473 K) in an updraft fixed bed gasifier to examine the gasification process. The performance was evaluated by using wood pellets as a feeding fuel. It was found that high temperature and oxygen concentration of the gasifying agents resulted in a higher gasification rate, gas composition and CV of the gas.

[Mahishi and Goswami 2007] developed a model based on the thermodynamic equilibrium to estimate the composition of syngas and the influence of pressure, temperature, ER etc. on the yielding of the gas composition. For this study, solid wood was considered as a fuel in the gasifier. It was found that the maximum production of gas composition in terms of hydrogen occurred at a gasification temperature of 1000 K and ER of 0.1 (optimum conditions).

[Gao and Li 2008] carried out a theoretical study to analyse the behavior of pyrolysis and reduction zones in a fixed bed biomass gasifier at various heating temperatures. Douglas fir bark was considered as biomass fuel for the gasifier. Their gasification model predicted time and spatial variations of temperature field and producer gas concentration. Their numerical analysis was based on the 4th order Runge–Kutta for simulating the pyrolysis zone, and finite differencing for the reduction zone. From this investigation, it was found that methane content increased up to 11.16% at the eighth minute during the process and remained 10.83% at the end of the reaction.

[Velez et al. 2009] experimentally investigated the co-gasification of biomass and Colombian coal in a fluidized bed gasifier operated at atmospheric pressure. The coal was blended with rice husk,

sawdust and coffee husk biomass in different proportions (6-15% by weight). Experiments were performed at different mixture ratios of air/blend and steam/blend to get high CV syngas for power production. Outcomes of experiments revealed that the presence of biomass in the blending slightly decreases the energy efficiency of process and the generated syngas was found to be rich in H_2 (15%) and CO (11%).

[Compoy et al. 2010] performed an experimental study on a 100 kW_{th} bubbling fluidized bed gasifier to obtain the maximum performance parameters and low tar content in the gas. The wood pellet was introduced in the gasifier to run the experiments at various operating conditions. Results showed that optimum stoichiometric ratio and CGE are 0.3 and 70% respectively. Also, the tar content in the gas was reduced three times under the given conditions.

[Ojolo and Orisaleye 2010] designed and developed a downdraft gasifier (laboratory scale) to produce 4 kW of mechanical power when operated under two modes (natural and forced draft). Experiments were conducted on the designed gasifier by using the two types of biomass: palm kernel shells and wood shaving. The results showed that the burning capacity rate for this gasifier is 4 kg/h under forced draft mode.

[Olgun et al. 2011] developed and constructed a bench-scale downdraft fixed bed biomass gasifier to analyze its performance. For that purpose, various kinds of fuel biomass like olive pomace, wood chips and hazelnut shells were used in the gasifier. This study revealed that the maximum CV (5.5 MJ/m³) of syngas was found at 0.35 of optimum ER when wood chips was used as a feeding fuel.

[Umeki et al. 2012] examined the performance of an updraft biomass gasifier using the high-temperature steam via a numerical model. The wooden chips-based biomass was considered as a feedstock fuel and the influence of different input parameters such as fuel feeding rate, steam temperature, the diameter of particle, etc. on the gas composition was analyzed. The outcomes of the model showed that with an increase in steam temperature, H_2 fraction also increased, while a declined trend was found for CO fraction.

[Kim et al. 2013] demonstrated the gasification of wood biomass fuel in an air-blown bubbling fluidized bed gasifier. The biomass feeding rate and flow rate of the gasifying agent were varied to examine the performance of a gasifier in terms of gasification temperature, CV and gas composition. The results highlighted that the maximum CV of syngas was 5.7 MJ/m³.

[Guo et al. 2014] conducted an experimental study on an air-blown pilot-scale circulating fluidized bed gasifier for power production. The performance (tar yield and gas composition) of the gasifier system was investigated using herb residue fuel through varying the biomass feed rate, ER and steam/biomass ratio. The findings of the experimental study revealed that the maximum CV of syngas is 6.0 MJ/m³ at 0.23-0.43 range of steam/biomass ratio.

[James et al. 2015] studied the effect of two input parameters (air flow rate and types of biomass) on the performance of an updraft gasifier by varying the ER in the range of 0.21 to 0.29. To execute this study, three different kinds of biomass fuel such as agriculture residue, wood chips and perennial grass were used for the gasifier. The outcomes of the study revealed that among all three biomass, the highest CV of syngas was obtained for the wood chips biomass and varying of ER had no much effect on the gas composition.

[Zheng et al. 2016] carried out an experimental study on a fixed bed biomass gasifier (bench-scale) for the gasification of polyethylene and bamboo biomass. The performance (CV and composition of syngas) of the gasifier was investigated at varying input parameters including gasification temperature, ER, steam/biomass ratio and presence of calcium oxide. The results indicated that with the presence of calcium oxide, the CV of syngas was increased from 5.81 MJ/m³ to 17.33 MJ/m³ (bamboo) and 10.52 MJ/m³ to 12.18 MJ/m³ (polyethylene).

[Jangsawang 2017] conducted experiments with wood residue biomass in an updraft gasifier to investigate CGE and CV of syngas to be used for the dryer. The gasifier was operated continuously for 30 hours to investigate the performance of the system. The average CGE, CV and drying temperature of the dryer were found as 84.97%, 4.66 MJ/m³ and 170 °C, respectively.

[Susastriawan et al. 2018] fabricated a pilot-scale downdraft biomass gasifier (throat-less) and experiments were conducted to analyze the propagation front, temperature profile of reactor, CGE of gasifier, composition and CV of syngas. The gasification process was examined using wood sawdust and rice husk biomass by varying ER in the range of 0.15-0.25. The maximum value of CV (3.21 MJ/m^3) and CGE (76.90%) was obtained at an optimum ER of 0.2 for rice husk and the same (2.18 MJ/m^3 and 76.90%) was found at an optimum ER of 0.15 for blended biomass.

[Li et al. 2019] carried out modeling and experimental study on a biomass gasifier to find out maximum conversion efficiencies (cold gas and power). Relation between engine and the gasifier was mainly highlighted. To investigate the same, redwood pellets and woodchips were supplied as fuel in the gasifier. The results of the study revealed the maximum cold gas and power efficiency as 80.8% and 9.0% respectively for woodchips. The fractions of energy output, involving electricity and waste heat were found between 43.0–54.6% and 40.0–60.4%, respectively.

[Nguyen et al. 2020] conducted an experimental work on a bubbling fluidized gasifier (pilot scale) using torrefied woodchips as a biomass fuel in order to produce hydrogen. The performance of the gasifier system was evaluated at various operating conditions such as steam/biomass ratio, gasification temperature and ER. The outcomes of the experimental investigation presented that the maximum content and yield of hydrogen production are 48.41% and $0.039 \text{ m}^3/\text{h}$ respectively at an optimum value (1.2) of steam/biomass ratio.

[Martinez et al. 2020] investigated the performance of an 18 kW fixed bed gasifier (pilot scale) for power generation. The effect of different fine sizes of corncobs biomass fuel on the output performance characteristics of the system was analyzed experimentally under three loading conditions (4 kW, 8 kW and 12 kW) of generator. The results indicated that CGE of the gasifier system was found in the range of 33.7-37.0%.

[Awais et al. 2021] examined the effect of ER on the various outcome parameters (composition, yield and CV of syngas, CGE and tar content) for a downdraft biomass gasifier. Experiments were performed by using two types of biomass, namely sugarcane bagasse and coconut shells. The

maximum values of performance parameters for sugarcane bagasse and coconut shells were obtained at the optimum ER of 0.22 and 0.29, respectively.

[Quintero-Coronel et al. 2022] used an updraft gasifier to study the co-gasification of biomass and coal at different ER in the range of 0.26 to 0.34. The palm kernel shell as a biomass was blended with high volatile bituminous coal in different proportions (75, 80 and 100% by volume). The results showed H_2/CO ratio in the range of 0.57–0.59 for 70% biomass, 0.49–0.51 for 85% biomass and 0.42–0.46 for 100% biomass.

[He et al. 2022] investigated the gasification process of citrus peel and pine sawdust biomasses using a fixed bed gasifier to analyze the effects of various key factors on its performance. The outcomes showed that the yield of H_2 and CGE for citrus peel biomass was 34.35 mol/kg and 66.30%, respectively and it exhibited higher performance than that of pine sawdust. The reactivity of citrus peel biomass was also found higher than pine sawdust and it took only 100 minutes to complete its gasification process.

[Kaydouh and Hassen 2022] performed a thermodynamic simulation study on the co-gasification of plastic waste mixed with biomass as a feeding fuel using HSC Chemistry Software. By varying the plastic-to-biomass fraction, the performance was determined in terms of CV, CGE and yield of syngas. The simulated results presented that the CV increases from 21 to 25 MJ/kg when plastic-to-biomass fraction varies from 1 to 5. The yield of H_2 and CV of syngas were found lowered when CO_2 was used as a gasifying agent due to the reversal of water gas shift reaction.

For combined heat and power production, [HajiHashemi et al. 2023] conducted experimental and simulation studies on the biomass gasification using a pilot-scale gasifier and ASPEN Plus software, respectively. The experiments were performed at two power loads (7 and 10 kW) of engine and pomegranate wood chips were used as a fuel for the gasifier. The outcomes revealed that the concentrations of H_2 (21.5%) and CO (30.08%) in syngas were higher at 7 kW power load than those (H_2 -13.35% and CO-13.76%) at 10 kW. Kinetic simulation results indicated good agreement with the experimental outcomes with absolute error of 8.91% and 1.98% for H_2 and CO, respectively.

[Zhou et al. 2023] carried out an experimental study on biomass gasification in a batch reactor gasifier using CO₂ as a gasifying agent with rice husk as the pilot fuel. The influences of different input parameters such as residence time, rate of CO₂ supplied and gasification temperature on the yield of syngas were examined. Experimental outcomes disclosed that with the rise of gasification temperature from 700 to 900 °C, the yield of syngas increases from 23.53 to 50.24 mol/kg.

[Gu et al. 2023] experimentally analyzed the steam gasification process of citrus peel biomass in a fixed bed gasifier using kaolin catalyst with different Ni concentrations. They investigated the influence of Ni/kaolin on the characteristics of syngas. The results revealed that the carbon conversion efficiency and yield of H₂ were 84.54% and 36.79 mmol/g, respectively at the optimum loading (10% by weight) of Ni.

2.1.2. Literature survey on the performance of gasifier using different biomass: National status

In India, the work on biomass gasification started in early 1980s [Kulkarni and Saluja 1987] that introduced the national programme on demonstrating the technology based on the gasification process. The first phase of the programme was mainly focused to drive the diesel engine generator for water pumping purpose which was run by the biomass gasifier of small scale type. In the early 1990s, the second phase was originated on the gasification technology for emphasising the power generation and development of market-oriented gasifiers with large capacities. Many research programme on gasification technology were initiated by the MNES (Ministry of Non-conventional Energy Sources) in five different institutes. Out of these five institutes, Indian Institute of Technology Bombay and Indian Institute of Science Bangalore played an important role by developing the gasifier test facilities and gasifiers for power generation respectively. In 2004, being the first large project grounded on 100% syngas systems, three gasifiers having a total power capacity of 250 kW were commissioned at Coimbatore, Tamil Nadu [Bhattacharya and Jana 2009].

[Parikh et al. 1989] reported the performance of a downdraft biomass gasifier in which two types of engines (direct and indirect) were operated by the syngas-cum-diesel dual fuel mode. The study was conducted by using Subabool (*Leucaena leucocephala*) as a biomass fuel and the improvement

in the maximum power capacity was found up to 4.5 kW by varying the volume of the gas cooling-cleaning system.

[Ganesh et al. 1992] carried out gasification and combustion characteristics of rice husk biomass via thermogravimetric analysis for understanding the carbon conversion. Various experiments were performed at different atmospheres of nitrogen, CO₂, steam and air when operated under variable temperature conditions. The findings of this study revealed that an incomplete carbon conversion of biomass occurs above 700 °C while complete conversion of carbon was found at lower temperatures.

[Mukunda et al. 1994] presented the experimental results of a 100 kW biomass gasifier which was operated at different engine loads (33%, 55% and 100% of the rated capacity). Experiments were performed by feeding the wood chips as a fuel in the gasifier. The maximum value of the CGE was obtained at 79.2% at 55% of the rated capacity, but variation of the load had no effect on tar content and particulate levels.

[Bhattacharya et al. 1999] experimentally studied a two-stage gasification process for producing the low tar syngas by varying the air flow rate. Wood chip was used as a feeding fuel for the gasifier to analyze the performance parameters. It was observed that with an increase in secondary air flow rate, keeping primary as constant, there was a decrease in the tar content, CO₂ and H₂ concentration, whereas an increasing trend was found for CO. The tar content in syngas was found in the range of 19-34 mg/m³ with the two-stage gasification.

[Babu and Sheth 2003] used equilibrium modelling to determine the effect of various design parameters (steam-air ratio, preheating and oxygen enrichment of air) of a downdraft biomass gasifier on the composition and CV of syngas. The analysis of the gasification process was done by considering the solid wood as a fuel for the gasifier. The obtained results showed that the reaction temperature, composition and CV of syngas were increased with an increase in oxygen fraction and the same decreased with the steam-air ratio.

[Sivakumar et al. 2006] revealed the performance of the reduction chamber of a downdraft biomass gasifier by varying the design of a choke plate in terms of the number of nozzles, diameter and inclination angle of the nozzle. The study was conducted by applying a computational fluid dynamics method in which wood was considered as a feedstock fuel. The design of a choke plate with 6 nozzles and a 15° inclination angle had provided the maximum performance for the gasifier.

[Saravanakumar et al. 2007] used an updraft fixed bed gasifier to investigate the gasification of long stick woody biomass. The experiments were performed using a 10 kW_{th} capacity gasifier by varying air/fuel ratio. The gasifier was continuously run for 5 hours with a biomass feeding rate of 9-10 kg/h and 401-1195 K of temperature limits. The outcomes revealed that CGE for the long stock woody biomass was 73%.

[Panwar et al. 2009] performed an experimental study on a 180 kW_{th} downdraft biomass gasifier to analyze the outcomes in terms of gas composition, CV of gas and CGE. Its suitability for baking operation was highlighted in the study. The babul wood (*Prosopis juliflora*) was utilized as a feedstock fuel for the gasifier. The maximum values of gas composition, CV and CGE were obtained as CO-19.3%/H₂-15.1%/CH₄-1.35%, 5.07 MJ/m³ and 74% respectively. They highlighted that 6.5 kg of petroleum gas can be replaced by 38 kg of wood on hourly basis.

[Roy et al. 2010] checked the performance assessment of a downdraft biomass gasifier through an equilibrium modeling. For this study, the biomass fuels used for the gasifier were cow dung and sawdust. The use of cow dung as a feeding fuel was not found feasible but could be used as a binder with the woody biomass. The results of the study showed that CV of syngas and CGE decreased with an increase in the fraction of cow dung.

[Dasappa et al. 2011] presented the operational experience of a 100 kW downdraft biomass gasifier in which the system was operated for 1000 hours of continuous run. The experimental analysis was completed by using solid wood as a biomass fuel for the gasifier. The overall specific fuel consumption and biomass to electricity conversion efficiency were observed as 1.36 kg/kWh and 18%, respectively.

[Senapati and Behera 2012] carried out an experimental study on an entrained flow biomass gasifier for power generation. The performance of the gasifier (CGE, CV, reactor temperature and tar content) was investigated using coconut coir dust biomass as a feedstock fuel with 40 kg/h of average feeding rate. The outcomes of the investigation indicated that the highest values of CGE, reactor temperature, tar content and CV of syngas were obtained as 87.6%, 976-1100 °C, 23.6 g/m³ and 7.86 MJ/m³ respectively.

[Raman and Ram 2013] reported the performance improvement of a theoretically designed and developed 75 kW gasifier via changing of ash removal method and applying a heat exchanger. This study was conducted by considering solid wood as the biomass fuel. It was observed that the improvement made in the ash removal method increased the CGE from 75% to 88.4%. The specific biomass/fuel consumption rate and fuel to power conversion efficiency were found as 1.18 kg/kWh and 18%, respectively.

[Kumar and Randa 2014] experimentally evaluated the performance of a downdraft biomass gasifier in the form of ER, gas production rate, CGE, CV and composition of syngas. The gasification process was achieved by supplying the chir pine needle (Leaf) biomass fuel in the gasifier. The biomass consumption rate was increased with an increased in the air flow rate, while the same was decreased with an increased in the MC. The optimum ER was found as 0.251 at which the maximum values of performance parameters were observed.

[Vivek et al. 2015] conducted an experimental study on a 2 kW capacity biomass gasifier for power generation application. The performance of the biomass gasifier was analyzed using Jatropha seed cake as the feedstock fuel. The results of the study indicated that CV of the syngas as 600 kcal/m³ (2.51 MJ/m³) along with the generated output voltage of approximately 180-200 V and current of 3.0-3.5 A.

[Singh and Sekhar 2016] carried out theoretical and experimental studies on a downdraft biomass gasifier (capacity of 50 kW_{th}) in which the feedstock fuel was prepared by blending two biomasses (coconut shells and rubber seed shells) in four different proportions (coconut: rubber seed) such as

100:0, 90:10, 70:30 and 90:10. The maximum values of the gas composition, CV of syngas and CGE were obtained when the ER was maintained between 0.2 and 0.3.

To analyze the feasibility of the system used for the process heating of green leaves, [Ayyadurai and Kandasamy 2017] investigated the performance of a pilot-scale biomass gasifier having a capacity of 150 kW_{th}. Experiments were done by using forest firewood biomass having MC of around 35%. Compared to the conventional firing system, the wood firing rate in this system was achieved 15% more and the charging rate of a green leaf was increased by 15.6%.

[Suyambazhahan 2018] studied the gasification process of the coconut shells in a fluidized bed gasifier for power generation application. The influence of the steam/biomass ratio (in the range of 0-2.6) on the performance parameters of the gasifier was experimentally examined. The results showed that the maximum performance values of gas yield, carbon conversion efficiency and CV of syngas as 1.32 m³/kg, 86% and 5 MJ/m³, respectively.

An experimental study on a lab-scale bubbling bed biomass gasifier having a capacity of 40 kW_{th} was conducted by [Bharath et al. 2018]. Both air and steam were used as gasifying agents. The performance of a biomass gasifier was investigated using the blending of two fuels: rice husk (with 22% ash) and coal (with 36% ash). The outcomes of the study indicated that the CGE and the CV of syngas as 78% and 5.4 MJ/m³ respectively, when rich husk was blended with 75%.

[Ram et al. 2019] presented a detailed analysis on a dual fired biomass gasifier in which the properties of produced syngas were improved by supplying the steam along with air as gasifying agent. The analysis was experimentally performed by using wood as a fuel for the gasifier. The study has been analyzed to improve the flammable portion of syngas by supplying the air-steam as gasifying agent to lead the high combustion temperature in IC engine. The results showed that the maximum value of gas yield, CV of syngas and CGE as 2.85 m³/kg, 6.33 MJ/m³ and 86.29% respectively. The CV of syngas produced from the air-steam gasification was enriched by 44%.

[Mahapatro and Mahanta 2020] carried out the gasification process on a lab-scale pressurized circulating fluidized bed gasifier (operated under a pressure range of 1 to 4 bar) to investigate the

performance of the system in terms of the composition of syngas, CV of the syngas, CGE and carbon conversion efficiency. To examine that, three kinds of feedstock fuel such as coal, rice husk and sawdust were utilized in the gasifier. When increased the pressure from 1 to 4 bar, CGE for rice husk, coal and sawdust was also increased by 34%, 51% and 61% respectively while CV of syngas was increased by 12% for coal and sawdust.

[Murugan and Sekhar 2021] investigated the gasification process via CFD modelling as well as experimentally in terms of CV, ER, CGE and yield of syngas. The suitability of gasification process was performed by using locally available Tamarind shell as a fuel for the gasifier. The results of this study indicated that the optimum ER is 0.30, where maximum values of parameters were obtained. At this ER, CV, yield of syngas and CGE were attained as 5.76 MJ/m³, 1.95 m³/kg and 78.23%, respectively.

For the production of energy-rich products like syngas, bio-char and bio-oil, [Pawar and Panwar 2022] examined the gasification of wheat straw biomass. The performance of the gasifier was analyzed at four different temperatures (350°C, 400°C, 450°C and 500°C) of the reactor. The results of the study presented that the maximum conversion efficiency (wheat to bio-char) and the higher heating value (HHV) of bio-char as 30% and 23 MJ/kg respectively.

[Dutta et al. 2022] performed an experimental study on a downdraft biomass gasifier for power generation application. The performance of gasifier was analyzed in terms of composition and CV of the syngas at different ER (within the range of 0.3-0.4) using sawdust pallet and tree waste biomass as feedstock fuels. The experimental results indicated that the average CV of syngas as 4.19 MJ/m³.

[Pandey et al. 2022] performed an experimental study on the autothermal downdraft gasifier using air-CO₂ or oxygen-enriched air-CO₂ as gasifying agents. The effect of varying concentrations of CO₂ (0-45% by volume) and oxygen (21-35% by volume) on the gasification of pellets (sawmill and agriculture waste-based) was investigated. The results exposed that the yield of CO in the syngas increases with air-CO₂ gasification compared to air gasification that leads to a higher CV.

If the oxygen concentration increases from 21% to 35% while keeping CO₂ as a constant (30%), the concentration of CO rises from 23.96 to 31.37%.

[Sapariya et al. 2023] investigated the gasification process of three different biomasses, namely, groundnut shell, bagasse and wooden shavings using a fluidized bed gasifier. The CFD analysis was performed for the selected biomass in order to find the feasible ER (0.3). The experimental outcomes presented that a high CV of syngas can be obtained at higher gasification temperature and maximum CV of 4.21 MJ/m³ was found for groundnut shell biomass at 600 °C of gasification temperature.

[Murugan et al. 2023] conducted an experimental study for the gasification of leafy biomass using a downdraft gasifier. The experiments were performed at various ERs and its effect on syngas composition, CV and gasification temperature was analyzed. The results indicated that the maximum CV is 4.23 MJ/m³ at an optimum ER of 0.23 with a gas yield of 1.1 m³/kg. Corresponding to this optimum ER, the concentrations of CO, H₂ and CH₄ were observed as 19.29%, 10.31% and 2.23%, respectively.

A wide variety of biomass can be used for the gasification process, but there are many scopes of exploring locally available biomass for energy production, as based on the location, chemical compositions of biomass varies. Further, use of syngas for power generation emits flue gases at high temperatures that can be used for useful applications.

2.2 Management and recovery of waste heat

Every country in the world produces a significant amount of WH and discharges into the atmosphere that causes environmental pollution and global warming. According to the Department of Energy, the United States/US generates a total WH of 440 TWh/year out of 2462 TWh/year consumed energy by the industrial sector. The amounts of WH generated from cement, iron and steel industries by India and China are 160 TWh/year and 1398 TWh/year, respectively [Elsaid et al. 2020; Abdelkareem et al. 2022]. This causes considerable energy loss to the ambient and creates the pollution and other problems that need to be effectively utilized for useful applications. The literature survey on the recovery of waste heat from the gasifier has been performed next.

2.2.1 Literature survey on the recovery of waste heat from the gasifier for various applications: International status

[Demirbas 2005] proposed a cogeneration system consisting of a biomass gasifier and a gas turbine for power and heat generation. A heat exchanger was used for recovering WH of the engine to produce hot water or steam which was further utilized for electricity production. This cogeneration system was found to be a promising technology for heat and power production with 15-25% less fuel requirement for the same amount of energy generation.

[Wang et al. 2009] carried out a simulation study using an ECLIPSE process simulator for a trigeneration system (heating, cooling and electricity) made up of an IC engine, a gasifier, an absorption refrigerator and a heat recovery system (HRS). In this system, WH generated from the engine was first recovered for space heating and hot water applications, thereafter it was used to operate the absorption refrigerator. The results indicated that the system was able to reform lignite and biomass (low-quality fuels) into clean hydrogen fuel through absorption enhanced reforming unit.

[Pavlas et al. 2010] proposed a system of process integration for the case study of industrial use in which the syngas produced from the gasifier was cooled using a low temperature scrubber maintained by a refrigeration cycle. WH generated from the syngas-driven engine was used for heating of water to dry the biomass or preheating of boiler feed water. The power generated from the engine was found 454 kW and its efficiency was increased by 20% with an extensive cleaning of syngas by the refrigeration cycle.

[Kalina 2011] presented a theoretical model (based on the thermodynamic equilibrium approach) for a distributed generation plant system consisting of a biomass gasifier, an IC engine and an organic Rankine cycle (ORC). The performance of the system was analyzed for three different configurations of the system with utilization of WH for air preheating to be supplied for the gasification process. The minimum and maximum efficiency of the configuration system were obtained as 23.6% and 28.3%, respectively.

[Jimenez et al. 2012] proposed a combined system of heat and power in which WH of an engine driven by a biomass gasifier was utilized to dry the biomass feedstock. The proposed design system is developed for supplying heat and power to the people of villages in Cuba to meet the energy need. The economic analysis of the designed system was also performed and found a low cost of electricity.

For combined heat and power generation applications, [Chutichai et al. 2013] introduced a flowsheet model of an integrated system comprising of a biomass gasifier and proton exchange membrane fuel cell. The performance of the integrated system was evaluated at variable input parameters and WH was recovered for producing power to enhance the efficiency of the system. The outcomes of the study revealed the power conversion efficiency of an integrated system as 22%, that reached 51% when a waste HRS was considered.

Using ECLIPSE software, [Huang et al. 2013] conducted modelling and simulation study on a combined system (an ORC and a biomass gasifier) for heat and power generation. In this system, WH from the syngas-driven engine was employed for the heating purpose. The performance of the combined system was analyzed through techno-economic and environmental basis. The results of the simulation study showed that the overall efficiency of the combined system reaches up to 76% and 81% for willow chip and miscanthus biomass fuels, respectively.

[Wang et al. 2014] recovered WH of a biomass gasifier to produce power using the TEGs by placing it at various locations on the surface of the reactor. The performance of the biomass gasifier was examined through a simulation model using the Fire Dynamics Simulator. The obtained outcomes showed that a power density of 857 W/m^2 can be achieved by the TEGs when the temperature difference across it was maintained at 140°C .

[Puig-Arnavat et al. 2014] developed a theoretical model of a trigeneration configuration system (comprised of a biomass gasifier, an IC engine and an absorption chiller) for heating, cooling and power generation applications. In this system, the heat recovered during the cooling of syngas was used to heat water for the district heating and cooling system. The overall and equivalent energy efficiencies were found highest for the configuration in which steam (to feed a double effect absorption chiller) was produced from WH at of an engine by using HRS.

To generate power by using Bi_2Te_3 made TEGs sandwiched between the heating collector plate and the plate combined with a cooling pipe, [Ma et al. 2015] recovered the WH of a biomass gasifier. The tar content in catalytic reactor was removed by using dolomite and the gastifier temperature was found 623-773 K. This study was conducted experimentally and it was found that the maximum power output is 6.1 W along with 193.1 W/m^2 of power density.

[Wang et al. 2015] proposed a combined system of a biomass gasifier, an IC engine, a heat pipe exchanger, and an absorption heater/chiller to generate power, heating and cooling effects. The exergy and energy analyses were conducted for three different seasons: winter, summer and transitional. WH produced from the gasification process was supplied to an absorption chiller/heater through a heat exchanger for producing heating and cooling effects. Exergy and energy efficiencies during winter, summer and transitional seasons were found as 12.51%, 6.23%, 13.79% and 37.77%, 50.0%, 36.95%, respectively.

To meet the household energy demand of 100 kW, [Chutichai and Arpornwichanop 2015] presented a system in which a biomass gasifier was integrated with a proton-exchange membrane fuel cell for the combined heat and power generation. The system is theoretically examined with considering two main operational issues: recovery of WH and response to deviation in power/heat ratio. WH produced from the biomass processing and the proton-exchange membrane fuel cell was utilized for water heating and space heating aimed at household applications. The results of the study revealed that the stack efficiency of the proton-exchange membrane fuel cell falls in the range of 47-57%, while efficiency for the combined heat and power system was found as 68-93%.

[Nisamaneenate et al. 2015] investigated the performance of a modular biomass gasifier (fixed bed) with a thermal transfer unit using peanut shells biomass. The syngas generated from the gasification process was passed through a thermal transfer unit to release the heat for the drying and pyrolysis processes. The performance of the system was studied in terms of gas flow rate, CGE, gas composition, specific gas production rate and biomass consumption rate. The optimum

value of air flow rate was found as 3.06 m³/hour, where the maximum composition and yield of syngas were generated.

[Nwokolo et al. 2016] conducted a study on the recovery of surface WH from a cyclone attached with a downdraft biomass gasifier for the drying of timber and water steaming purposes using a water (cold) casing around the cyclone. The outcomes indicated that a downward decrease in the temperature profile of the cyclone occurs, and it was also found that a significant amount of lost energy (665893.07 kcal) occurs from the surface of the cyclone.

For an integrated system of a multi-stage biomass gasifier and a heat treatment furnace of steel industry, [Gunarathne et al. 2016] developed a theoretical model based on ASPEN Plus software. The HRS was integrated for recovering WH at low (400 °C) as well as high temperatures (700 °C). In this system, the hot syngas was cooled down by passing it through the heat recovery boiler to produce saturated steam, while on other hand, flue gases or WH from the furnace was used to generate superheated steam to be supplied as gasifying agent. By employing the HRS, the efficiency of an integrated system was improved via harvesting 2/3 of the total available WH.

[Kuo and Wu 2016] examined the performance of a co-generation (heat and power) system made of a biomass gasifier and an ORC for power generation by recovering WH. ASPEN Plus-based thermodynamic model was formulated for the system and efficiencies (exergy and energy) were analyzed by blending of biomass (raw and torrefied) and coal. The flue gas as WH from the combustion of syngas was used to produce steam for an ORC. From the results, the power generated with 40% torrefied biomass and 60% coal fuel feeding was increased by 8.43%, compared to 40% raw biomass and 60% coal.

For combined heat and power generation, [Elsner et al. 2017] reported numerical and experimental studies on a biomass gasifier equipped with a gas cleaning system integrated with an engine-generator system. The numerical study was conducted to identify the places of available WH in the system and showcased a new heat recovery method for further applications. The parametric study of the system and economic analysis of the process were performed under steady and

unsteady state conditions. The heat released during the cooling of syngas was used for air preheating by using a coiled heat exchanger and gas CV of 4.45 MJ/m^3 was found.

To produce heat and power, [Ozgoli 2017] carried out the modelling and simulation studies on an energy-efficient system comprising of a biomass gasifier, an air bottoming cycle and a gas turbine. A novel approach has been used for the proposed combined system to alleviate restrictions on power generation from the biomass gasification-gas turbine systems. The WH generated from the syngas driven gas turbine was employed to dry the biomass fuel in a dryer. The outcomes presented that the energy efficiency of the proposed system was 58.9%.

To produce power, syngas, cooling effect, heating load, oxygen and hydrogen, [Boyaghchi et al. 2018] introduced a multi-generation system consisting of a biomass gasifier, a proton exchange membrane electrolyzer and an ejector refrigeration loop assisted with a dual ORC. A theoretical model was developed to analyze economic, thermodynamic and environmental performances based on elitist non-dominated sorting-based genetic algorithm. WH released by the hot syngas was used to heat the organic working fluid flowing through an ORC by heat exchangers. Results revealed that the impact on the environment per unit exergy and cost of hydrogen get improved by 34.58% and 49.18%, respectively.

[Zhang et al. 2018] evaluated the performance of a hybrid system (1000 liters anaerobic digester and a 10 kW biomass gasifier) for the treatment of waste solid organic to produce energy. The overall energy efficiency of the system was increased by harvesting WH of biomass gasification to be delivered for the anaerobic digestion process. The results of study revealed that the CV of mixed gas (biogas and syngas) is around 16-54% greater than the CV of syngas.

[Islam and Dincer 2018] developed an ASPEN PLUS simulation model to analyze the performance of the gasification process (for syngas production) combined with waste HRS via energy and exergy approaches. WH from the flue gases and hot syngas was used to generate steam for the gasification process by using four heat exchangers. The results indicated that the trend of exergy and energy efficiencies for cold gas is decreasing with increase in the temperature of the combustion chamber.

[Li et al. 2019] conducted theoretical and experimental studies on a system consisting of a biomass gasifier combined with an engine generator and a unit of WH recovery to produce power. WH from the gasifier and exhaust of an engine was utilized to dry the biomass feedstock (redwood pellets and woodchips). The experimental results showed that maximum values of CGE and power generation efficiency as 80.8% and 19.0%, respectively for the woodchips biomass, whereas the same were found as 75.0% and 16.4%, respectively for the redwood pellets.

For power generation application, [Khanmohammadi et al. 2019] proposed a thermodynamic model to recover WH of an integrated system consisting of a gas turbine (externally fired) and a biomass gasifier. The performance of three HRSs was evaluated by placing them at different locations in the system. The first law efficiency of the integrated system was 17.11% (with an improvement of 0.35%) by supplying the total heat of stack to HRS and the same escalated to 17.93% when HRS was placed on the condenser section.

[Wu et al. 2020] developed a thermodynamic model for a hybrid system made up of a biomass gasifier, a fuel cell (solid oxide), an engine (homogeneous charge compression ignition) and a HRS in which WH from the engine was used to preheat air and water with the aid of heat exchangers. The performance of system was comprehensively evaluated through multiple approaches including exergy, exergoeconomic, energy and environmental analyses. From the theoretical results, the overall exergy and energy efficiencies of the hybrid system were observed as 51% and 68%, respectively.

[Yuksel et al. 2020] presented a multi generation plant system equipped with a waste HRS that included a biomass gasifier, a solid oxide fuel cell, an ORC combined with an ejector refrigerator system and a distillation unit. The system was examined for the production of power, freshwater, hydrogen, cooling and heating effect through a developed simulation model. The steam as a gasifying agent was generated from the water by recovering the heat dissipated during the cooling of the syngas. The exergetic and energetic effectiveness of the system were observed as 52.83% and 56.17%, respectively.

[Ruya et al. 2020] introduced a theoretical model for a hydrogen generation system consisting of a gasifier, a furnace, an absorber and a reformer. WH released during the cooling of syngas was used to produce low pressure steam through a heat exchanger. The results showed that with the implementation of a HRS, the system efficiency increases from 5 to 8%.

Using ASPEN Plus tool, [Ishaq et al. 2020] analyzed the performance of a multi generation system for electricity, hot water and hydrogen production through modelling and simulations. The system consisted of a biomass gasifier, a proton exchange membrane electrolyzer, an ORC and HRSs. WH was utilized to generate the steam for gasification process using a heat exchanger. The overall exergy and energy efficiencies of the system were observed as 32.78% and 58.03%, respectively.

To generate power by using TEGs, [Zoghi et al. 2021] harvested WH of a regenerative gas turbine system that was driven by a hybrid heat source comprising of a biomass gasifier and a solar power tower. The performance of the multi generation configuration system for generating power, hydrogen, heating, and cooling was analyzed through modelling. The results of the study indicated that with recovery of WH from the gas turbine system, the exergy efficiency increases by 9%.

[Georgousopoulos et al. 2021] presented techno-economic and thermodynamic performances of a system in which an ORC recovered WH from the three different heat recovery units equipped with a biomass gasifier. The cycle was optimized to maximize the efficiency of the plant by recovering WH from various heat recovery units. Heat dissipated in the cooling of syngas was consumed to produce steam by using a heat recovery steam generator. The outcomes revealed that the efficiency of the system improves by 2.81% when WH from the syngas was recovered.

[Sun et al. 2021] conducted an experimental study on a desiccant dehumidification unit operated from WH of a biomass gasifier through the usage of a HRS. WH from the syngas driven IC engine was applied to produce hot water provided for the regeneration process. The maximum coefficient of performance for the regeneration system was found as 1.34% corresponding to 86.5% of WH utilization ratio.

[Cao et al. 2021] proposed a system made of a biomass gasifier, a closed cycle gas turbine, an ORC and an absorption refrigeration cycle. WH from the system was utilized for power generation. The optimization of system was examined by developing a genetic algorithm-based model. WH from the syngas combustion chamber was used for air preheating and steam generation by using heat exchangers. The results showed that a total of 11.2% enhanced exergy efficiency can be obtained through optimization of the system.

[Mehrpooya et al. 2022] developed a computational model for a hybrid system comprising of various components such as a gasifier, a thermo-photovoltaic cell and a hydrogen generation unit. The optimal design of a hybrid system and an economic analysis were performed for the production of methanol, hydrogen and power. WH was used for air preheating and steam generation to be useful in the gasification process. With the implementation of the HRS, the overall efficiency of the hybrid system was raised by 3.5% and reached up to 68.17%.

Using grey wolf optimizer algorithm, [Musharavati et al. 2022] investigated the multi objective optimization of a system comprising of a biomass gasifier, a heat exchanger, a gas turbine, a combustion chamber, a compressor and a desalination unit. WH produced from the hot syngas was used to heat compressed air and generate steam. The findings of the study indicated the generated freshwater and power as 38.6 kg/s and 5127 kW, respectively at the optimized level.

[Awais et al. 2022] experimentally examined the performance of a 24 kW capacity downdraft biomass gasifier for power generation. The performance was evaluated in terms of gasification efficiency, temperature profile in the reactor, yielding of syngas, ER and tar content. WH from the surface of the reactor was recovered using glass tube collectors to pretreat the gasifying agents consisting of air and mixture of air-steam. The maximum yielding of syngas during the gasification process was found as 3.14 m³/kg for bagasse (sugarcane) and coconut shells biomass.

By recovering the WH carried away with ash after the gasification process, [Huang et al. 2023] presented an experimental study on the drying of biomass (peanut shells, straw and woody debris). The steel-made ball was used as spherical heat carrier and the effect of its temperature on the dewatering of biomass (containing 40% moisture) using a mixture-drying device was analyzed.

The outcomes indicated that the biomass dewatering rate (drying thermal efficiency) was 25.87% (59.22%), 19.86% (53.01%) and 35.57% (71.74%) for straw, woody debris and peanut shells, respectively at the optimum spherical heat carrier temperature of 400 °C, 350 °C and 450 °C, respectively.

[Osat et al. 2023] performed the exergy, energy, technological, exergoeconomic and environmental assessments of a combined system comprising of a biomass gasifier, a solar subsystem, a HRS, a regeneration subsystem and a power generation unit (Rankine cycle). The WH during cooling of syngas was recovered for heating of air to be supplied at the power generation unit via regeneration and solar subsystems. The obtained results confirmed that the maximum energy efficiency and the fuel cost rate for the combined system were 4.29% and 67.66 USD/hour, respectively.

2.2.2 Literature survey on the recovery of waste heat from the gasifier for various applications:

National status

[Srinivas et al. 2009] developed a thermodynamic model to examine the performance of a biomass gasifier in terms of gas composition, CV of syngas, gasification temperature and exergy efficiency. The power was generated from the combustion of syngas in a gas turbine and WH produced was delivered to a heat recovery steam generator to produce steam for the gasification process. The CV of syngas and exergy efficiency were found to be high at a lower value of relative air-fuel ratio and steam-fuel ratio.

For power and cooling applications, [Srinivas et al. 2011] introduced a system in which a biomass gasifier was integrated with a vapor absorption refrigeration cycle and a gas turbine. A thermochemical model was formulated to examine performance of the gasifier system and the effect of various input parameters on the output was analyzed. Thermal energy recovered from WH was applied to the cooling unit to evaporate ammonia from the mixture present in the generator. The results showed that as compared to a single vapor absorption refrigeration system, the cogeneration efficiency of the combined system increases by 0.9 %.

[Raman and Ram 2013] demonstrated the performance of a downdraft biomass gasifier involving a capacity of 75 kW. The efficiency of the system was increased by introducing a heat exchanger to recover the waste heat of hot syngas for air preheating to be supplied in the gasifier. The gas production efficiency was enhanced by applying an improved method of ash removal. The results of this study indicated that by adopting an improved method of ash removal, the CGE increases from 75.0 % to 88.4 % along with fuel to power conversion efficiency of 18 %.

[Bhattacharya and Dey 2014] proposed a system consisting of a biomass gasifier, a bottoming cycle power plant and a chiller unit. An IC engine was powered by the syngas and WH generated was used to generate the steam to be supplied for the bottoming power cycle. The efficiency of the integrated biomass gasification combined cycle was obtained in the range of 43-45% as compared to 22-25% for the conventional plant systems.

[Chattopadhyay et al. 2016] simulated the performance of a combined power and refrigeration plant driven by a biomass gasifier. The generated syngas was burnt through a combustor heat exchanger duplex to heat the air running the gas turbine. The WH was used to produce steam by using a heat recovery steam generator for driving the refrigeration cycle. The outcomes presented that maximum power conversion efficiency of 30 % for the gas turbine between 8-10 of pressure ratio, and maximum fuel saving energy ratio of 53% at pressure ratio of 9 was found.

For the off-grid areas of India, [Ray et al. 2017] proposed a polygeneration system containing a biomass gasifier, a solar photovoltaic cell, a vapor absorption cooling cycle and an ethanol generation unit for producing power, ethanol and cooling effect. The linear programming based theoretical model was formulated using MATLAB software to analyze the performance and optimization of the system. WH produced from a gas turbine after generating the power was then used to operate the vapor absorption chiller system. The outcomes revealed that polygeneration system was able to significantly reduce CO₂ emission as compared to diesel engine generator system.

To generate thermoelectric power, [Angeline et al. 2017] carried out an experimental study on TEGs for recovering WH produced from the gasification of biomass. The system was examined

at variable operating temperatures and loading conditions. The results of the experimental study explored that the maximum power and conversion efficiency from a hybrid system of TEGs are 8.94 W and 2.5%, respectively at 200 °C of temperature gradient across the TEGs.

[[Rather and Tripathi 2018](#)] presented a hybrid system comprising of a biomass gasifier combined with a HRS and a cold storage unit (vapor absorption system) for the applications of heating, cooling and electricity production. A case study of Jammu and Kashmir State was presented in which WH coming from the exhaust of an engine was delivered to the HRS for heating and cooling effects. The observations of the study showed that along with the power generation of 50 kW from the engine, WH was also found sufficient to run the vapor absorption system.

[[Roy et al. 2018](#)] performed thermodynamic analysis for a combined system consisting of a biomass gasifier, a solid oxide fuel cell system, an indirectly heated air turbine and two-staged compression and intercooling supercritical CO₂ powered cycle. The influence of various input parameters such as pressure ratio of an air turbine and current density of the fuel cell on the output power and overall efficiency was examined through a developed model. In this system, WH was used to heat the gas for driving the CO₂ power cycle. The outcomes indicated that the overall efficiency of the combined system was in the range of 30-55%.

For generating power and cooling effect via a combined system, [[Parvez 2019](#)] developed an entropy generation model based on the second law analysis. The combined system consisted of a biomass gasifier, a gas turbine, a steam turbine, an absorption refrigeration cycle and an ejector cooling system equipped with a HRS. To produce steam, WH generated from the combustion of syngas in the gas turbine was delivered to a heat recovery steam generator. The observations of the study pointed that the first and second law efficiencies of the combined system can be raised by 6.22% and 3.21%, respectively.

[[Roy et al. 2019](#)] proposed a hybrid system for the power generation application, and the techno-economic analysis of system was examined through a developed theoretical model. The hybrid system was made of an indirectly heated air turbine, a biomass gasifier and a supercritical CO₂ power cycle. The gas heated by WH was used to operate the supercritical CO₂ power cycle. The

outcomes showed that the maximum first law efficiency of the proposed system is 51% at 2000 A/m² of current density and 1123 K of cell temperature.

[Chattopadhyay and Ghosh 2020a] introduced a combined system comprising of a biomass gasifier and a vapor absorption refrigeration cycle to produce power and cooling effects. The syngas produced from the gasification of biomass was supplied to the gas turbine for generating power and the remaining WH was utilized to produce hot water for the driven of vapor absorption cycle. The electrical power was stored in a Lithium-ion battery system and storage capacity of about 250 kWh was found.

[Roy et al. 2020] carried out an optimization study for a combined system consisting of a biomass gasifier, a solid oxide fuel cell and a gas turbine through response surface methodology. A regression model was used to examine the performance of the system in the form of exergy efficiency, levelized cost of energy and exergy. WH was passed through a HRS to generate steam for further application. The findings of study revealed that exergy efficiency, levelized cost of energy and exergy were 46.58%, 0.0454 \$/kWh and 0.0657 \$/kWh, respectively at the optimum conditions.

For heat and power generation, [Chattopadhyay and Ghosh 2020b] investigated the techno-economic performance of a combined system made of a gas turbine, an ammonia-water vapor absorption refrigeration unit and a biomass gasifier. A theoretical model was developed for the combined system in which WH was used to drive the vapor absorption cycle by producing hot water from it. The results presented that the combined system was able to produce 100 kW power along with cooling effect of 33-115 ton.

For producing cooling effect and electricity, [Rathor and Sahoo 2021] proposed a hybrid system containing a biomass gasifier (50 kW capacity) combined with a cold storage unit (vapor absorption cooling system) and a solar driven Scheffler dishes (4 nos.). After generating the electricity from the syngas operated engine, WH from the exhaust was used to operate the vapor absorption system. The hybrid system was performed for the design of an automated process working under the different intensities of solar radiation and ambient conditions. The results

exposed that the maximum coefficient of performance for the cooling system was 0.6 at 85.91 °C of generator temperature.

[Tripathi et al. 2022] developed a combined system consisting of a biomass gasifier, a reformer fuel cell unit, a HRS and a homogeneous charge compression ignition engine. WH of engine was utilized to provide the thermal energy for process system of electricity generation. The feasibility of the system was examined via exergy, energy, environmental and exergoeconomic analyses. The outcomes revealed that electrical, total energy and exergy efficiencies were 50.5%, 68.7% and 51.6%, respectively. Also, the combined system was found superior to reduce the CO₂ emission by 62.4% and 47.7% when compared to coal and petroleum-driven plants, respectively.

Via thermo-economic and environmental explorations, [Samanta and Roy 2023] performed a theoretical study on a hybrid system of power generation that involved a biomass steam gasifier, a heated air turbine unit, a molten carbonate fuel cell, a HRS, and a Rankine cycle. In this system, the WH recovered from hot syngas was used to heat the fuel to be supplied at the boiler of the organic Rankine turbine. Further, a multi-objective optimization was also carried out through the response surface methodology in order to determine the operating conditions where the hybrid system provided maximum exergy efficiency. The results of the study indicated that the hybrid system is capable of generating 1.3 MW of power with 54.5% of energy efficiency at the optimum conditions, while the cost of electricity generation and exergy efficiency were found as 0.0993 USD/kWh and 47.46%, respectively.

For combined power and cooling generation, [Parvez et al. 2023] introduced a theoretical model to study a hybrid system via energy, exergy and environmental examinations. This hybrid system consisted of a fluidized bed gasifier, a gas turbine, a heat recovery steam generator, a steam turbine and a vapour absorption refrigeration unit. The WH of biomass driven gas turbine was recovered for steam generation in a heat recovery steam generator, and then this steam was supplied to the steam turbine for power generation. Further, the exit WH from the steam generator was delivered to a generator of vapour absorption refrigeration cycle for cooling effect. The outcomes explored that the best thermodynamic energy and exergy efficiencies were obtained as 37.6 % and 35.9 %, respectively.

From the literature review, some key research objectives can be identified based on the varieties of biomass used for the gasification process, where the study of biomass gasification using locally available waste biomass such as dried grass, red mulberry, leaves etc. is not explored. This is important because, the quality of syngas and other matter related to a biomass sample is governed by the prevailing weather condition. Further, it has been found that waste heat has been utilized for different applications like power generation, steam production etc. but the attempt of using thermosyphon-based HRS with an effective manner is not explored. Additionally, the study on the use of waste heat for desalination is not examined extensively in past research and can be used more effectively for large pure water production with a novel design of distillation system. Therefore, based on these research gaps, some objectives are identified for the scope of present research work and these are given below,

- I. The first objective is “Optimization of gasification process using various locally sustainable biomass (red mulberry, dried grass, leaves and dead branches) and its economic analysis”. The purpose of this objective is to produce useful energy (thermal energy and power) from inefficiently used local biomass through the optimizing the gasification process. Further, the focus will be to examine the viability of such system under different capacities by an economic analysis.
- II. The second objective is “Waste heat recovery for effective power generation using the development of HRS”. The main motivation of this objective is develop a novel design of HRS for effectively harvesting the waste heat of the system to generate thermoelectric power. Further, the focus will also be to analyze the optimum conditions of the HRS for maximum power generation.
- III. The last objective is “Use of waste heat for water desalination in an effective manner through a novel distillation system”. The purpose of this objective is to develop a new type of distillation system based on the waste heat of biomass gasification unit for large-scale water production. Additional purpose is to develop the correlations between various response and input parameters to analyze their inter-dependence in the studied system.

CHAPTER 3

*ENERGY PRODUCTION FROM SUSTAINABLE BIOMASS THROUGH GASIFICATION AND ITS ECONOMIC ANALYSIS

*This chapter covers into three stages. The first stage reveals about the energy cogeneration study of inefficiently used locally available biomass i.e. red mulberry (*Morus Rubra*) using a 10 kW downdraft biomass gasifier. Further, the various sustainable waste biomass (dried grass, leaves and dead branches) are investigated for useful energy production in second stage and finally in the last stage the feasibility of such gasifier power plant for different capacities are analyzed through economic analysis in present scenario of India.*

This chapter addresses the emission issues from biomass combustion process through gasification process and exploring the locally available biomass for efficient energy (heat and power) production. Further, the feasibility of this gasification-based power plant under various capacities has been also conducted to address the economically installation of different scaled systems. The purpose of this work is to produce effective energy production through optimizing the gasification process in a 10 kW downdraft gasifier. The characterization of feeding fuels has been carried out before using them for gasification and experiments were performed at variable input conditions. The outcomes have been measured and analyzed to obtain the optimum conditions for the present gasification process.

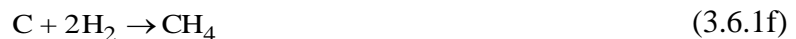
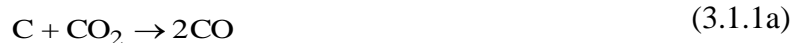
3.1 Energy cogeneration study of the red mulberry (*Morus Rubra*)-based biomass

3.1.1 Experimental setup details

An Enersol made fixed bed downdraft biomass gasifier system or power plant (Model No.: ESB-R10) of 10 kW capacity is used for the study as shown in [Figure 3.1.1](#): (a) Schematic layout and (b, c) actual photograph of a 10 kW downdraft biomass gasifier. The gasifier system consists of (i) hopper with blower and heater, (ii) reduction chamber, (iii) gas collector and ash tank, (iv)

* Content presented in this chapter can be found in the publications J1, B1 and C2

filters (cyclone, charcoal, sawdust and cotton), (v) cooling tower integrated with pump and water tank, (vi) gas flow meter, (vii) gas analyzer, (viii) engine generator (genset), and (ix) control panel. As indicated, the setup is primarily used to drive an engine for power generation. Additionally, a burner is also provided for the purpose of process heating, domestic cooking or other similar applications. The gasifier has four different zones from top to bottom: (1) drying, (2) pyrolysis (3) combustion, and (4) reduction. The blower is used to supply air from the environment to the gasifier. An auxiliary heater operated by a battery that is charged during part-load operation of the engine is used between the blower and the hopper. The heater is used to ignite the biomass present in the gasifier by burning of small sized dry furniture waste. A wood cutter [Figure 3.1.2 (a, b)] is used to cut the biomass in small pieces. A hopper is used to store the biomass fuel where drying of biomass occurs in the upper part within the temperature range of 100-150 °C where all moisture evaporates. Next, the thermal decomposition of biomass occurs in the absence of oxygen in the pyrolysis zone that is located below the drying zone. Here cellulose, poly-cellulose, and lignin present in the biomass are converted into solid, liquid and gas. Solid phase is referred as charcoal, whereas, liquid and gaseous phases are collectively known as tar. The tar and moisture thus generated move further downwards in the biomass gasifier to enter the combustion zone. Here, the outlet of air pipe from the blower is located that discharges air in this zone. When tar and moisture pass through the combustion zone, tar is cracked and charcoal comes in contact with the combustion zone to become hot reactive charcoal that in turn reacts with oxygen of the supplied air to produce CO₂ and heat. Next, the hot reactive charcoal reacts with water vapours and CO₂ in the reduction zone to produce flammable gases such as CO, H₂, and CH₄ known as syngas. Gasification of charcoal with carbon dioxide, steam, oxygen and hydrogen are shown below,



The hot reactive char in the reduction zone is supported by grate with holes that rotates about the shaft axis connected to gear mechanism run by a motor located at the bottom of the gasifier. A gas collector is attached below the reduction chamber followed by an ash tank. As the grate rotates,

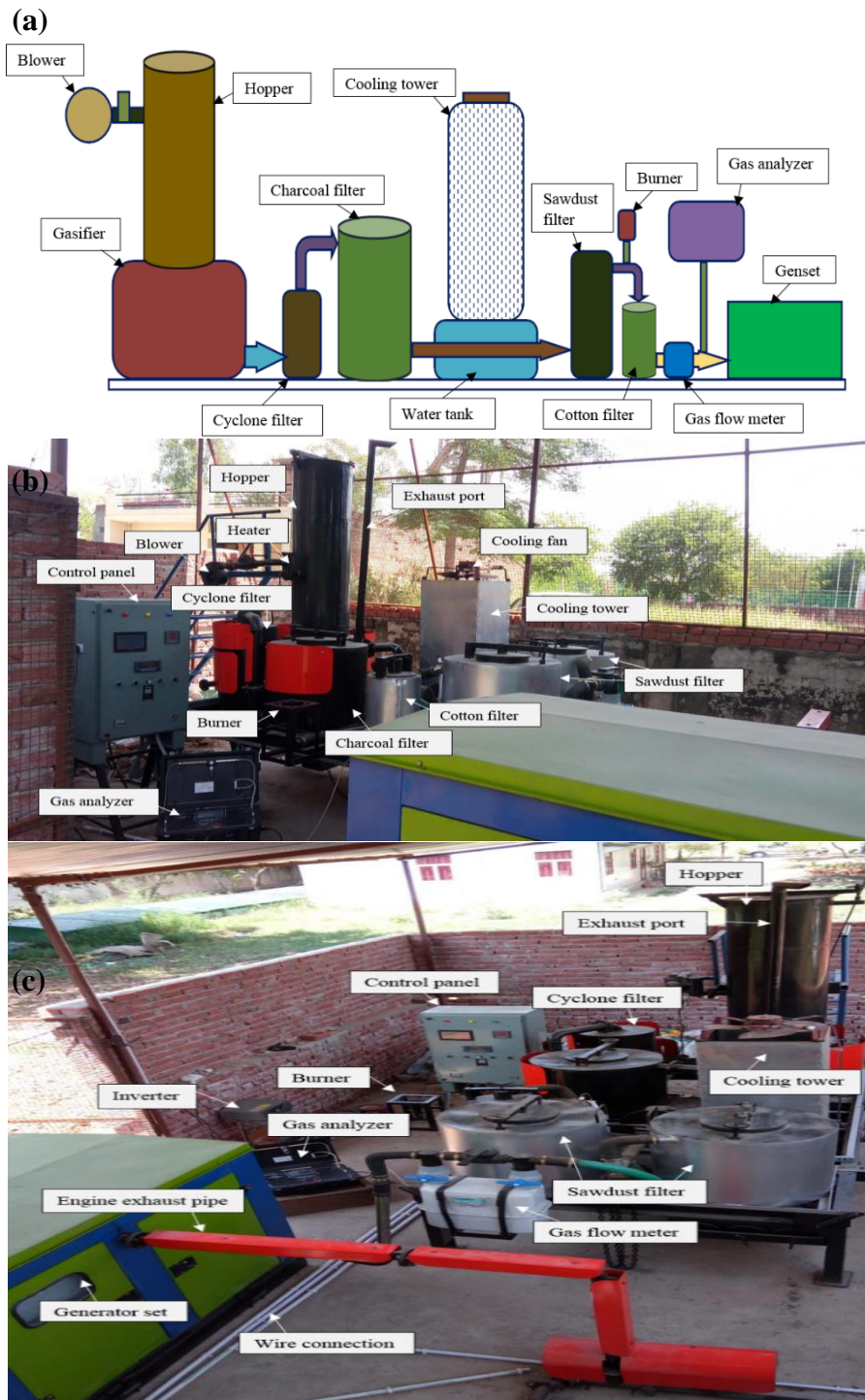


Figure 3.1.1: (a) Schematic layout and (b, c) actual photograph of a 10 kW downdraft biomass gasifier

syngas is collected in the gas collector and ash falls down through the holes of the grate into the ash tank. There is a small opening in the reduction chamber joined with the exhaust port for removal of initial smoke. The movement of grate is very important because it makes homogenous mixture in the reduction zone to improve the gas quality and break the harmful clinker into small pieces so that there is no disturbance in the flow of gas and the problem of chocking and jamming of grate is eliminated. After gasification, gas is fed to the cyclone filter. The cyclone filter removes dust from the syngas due to whirling (or rotating) action of gas from the top to the bottom. After the syngas exits from the cyclone filter, it enters into a charcoal filter. Charcoal is filled upto half the height of charcoal filter and is used to remove impurities like moisture content, tar, and ash from gas by absorption. Thereafter, syngas enters into the water tank where three parallel pipes are used to increase the heat transfer rate by increasing the surface area. These are connected through a common pipe at start and end points. An induced draft cooling tower is used for water cooling and circulation. The cooling of syngas condenses any water vapor present in the syngas and the liquid is removed through an opening. Secondly, cooling also prevents pre-ignition and knocking in the engine. The cooled syngas then enters into sawdust filters to remove additional small impurities from the gas. They are cylindrical in shape and half filled with small sized paddy straw. A burner is connected through pipe between two sawdust filters. The gas flow rate to the burner is regulated by a variable frequency drive blower. Next, the syngas enters into the cotton filter where cotton cloth removes the dust that emerges from the sawdust filter and clean syngas is produced. The syngas then passes through the gas flow meter that measures the quantity of gas entering into the engine. For the measurement of gas composition and CV, a small side valve is placed before the engine for supplying pure cooled syngas to the gas analyzer [Figure 3.1.2 (c, d)].

The generated cooled and refined syngas runs the engine to produce electricity that in turn is supplied to the control panel where all running equipments (motor, fan and water pump) are operated. The control panel is connected through thermocouple wires at different points of the gasifier system to display the temperatures on digital temperature indicator. The inverter battery system is placed for backup power and is charged during the experiments from the power of genset. The calibration of gas analyzer is done by using zero and span gases through the procedure as follows [AMB Electronic System 2018]: Initially, zero gas that contain 0% concentration of each component i.e., CO, CO₂, CH₄ and H₂ is passed through the gas analyzer and then the concentrations of CO, CO₂, CH₄ and H₂ from the analyser were recorded. The zero gas is passed

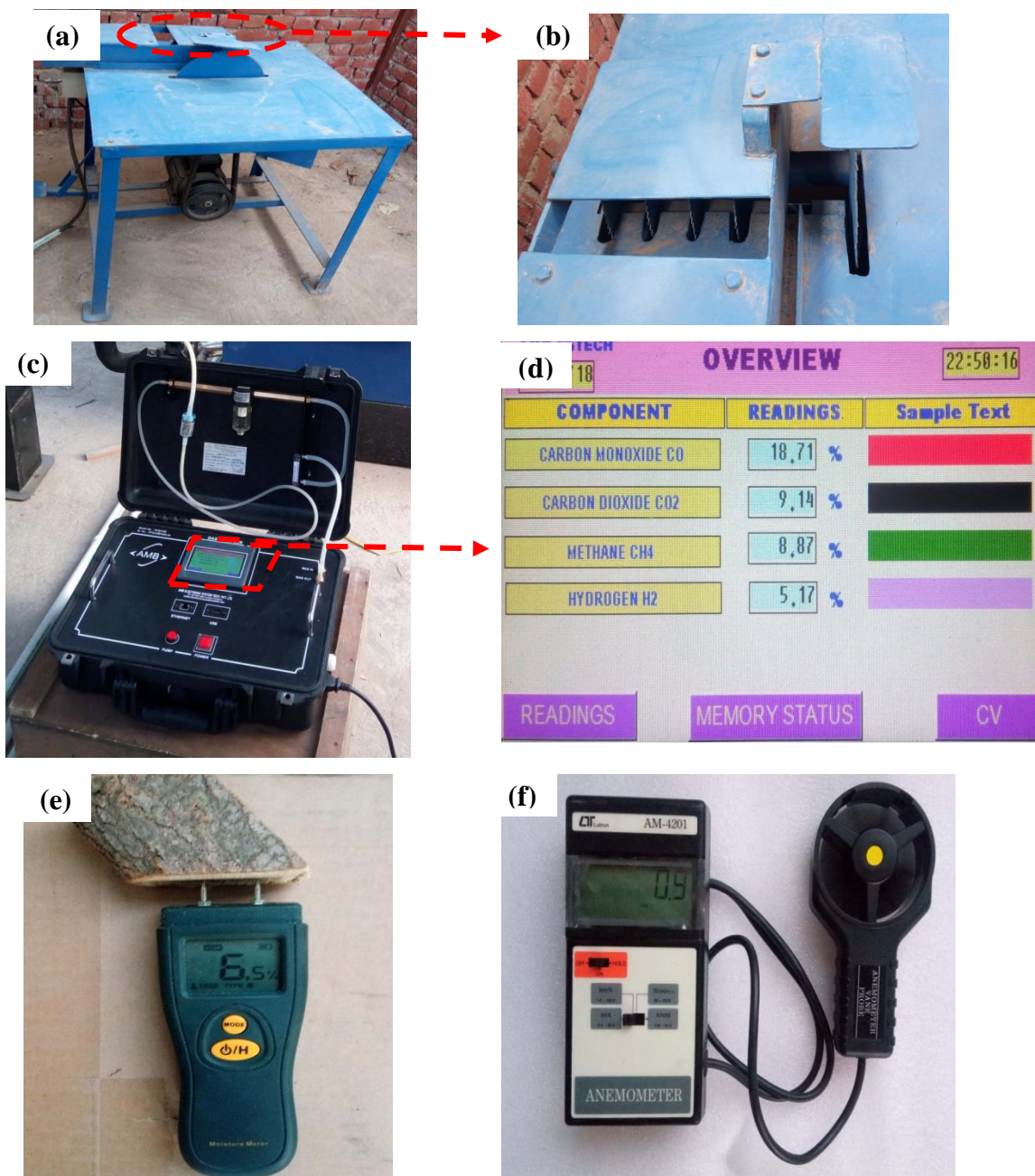


Figure 3.1.2: (a, b) Biomass cutter, (c, d) Syngas analyzer, (e) Moisture meter, (f) Anemometer

until the concentrations of all components (i.e., CO, CO₂, CH₄ and H₂) read zero. Thereafter, span gas containing 20.03%, 30.00%, 6.02% and 40.13% of CO, CO₂, CH₄ and H₂, respectively has been passed through analyzer and the concentrations of CO, CO₂, CH₄ and H₂ are recorded from the analyzer. The recorded concentration of each component is ensured to be same as that of concentration in span gas.

3.1.2 Experimental procedure

Originally, the water tank was occupied up to some suitable limit and the gas control valve is shut to prevent any leak. It was safeguarded that the valve positioned ahead of the engine is also shut such that the early smoke generated does not get inside the combustion zone. The reduction chamber was occupied with char for effortless ignition of biomass that is refilled by consecutive processes. The MC of biomass was assessed with the aid of a digital moisture meter (Figure 3.1.2e). Subsequently, the hopper gate was unlocked and a fixed amount of biomass was physically supplied within the hopper, and afterwards, the gate was locked. Succeedingly, 50/100 g small-sized and dried biomass was supplied on the heating port and the relevant gate was locked. The heater was controlled via a switch situated on the control panel of the generator that was functioned with the aid of a battery. After switching on the control panel, the heater switch was pushed for 40/50 s. The purpose of the heater was to kindle a small-sized wood biomass via resistance heating. When the initial smoke begins to emerge out from the heater port through very small leakage,

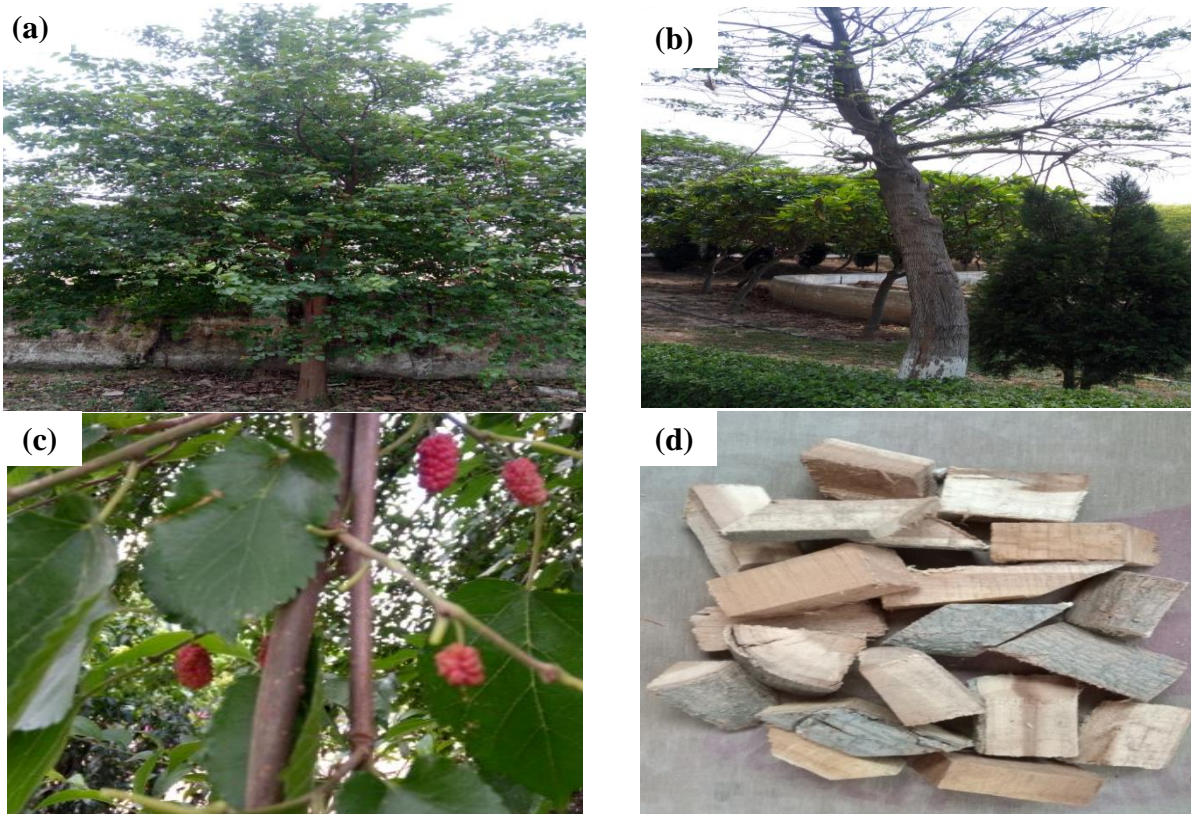


Figure 3.1.3: Biomass (*Morus rubra*) used in the present work, (a) green tree, (b) partially dry tree, (c) mulberry fruit, (d) dead mulberry tree wood chips

the blower is switched on to initiate the combustion of the small amount of biomass in the hopper. The air flow rate is measured by a vane type anemometer (Figure 3.1.2f). The heat generated by this combustion process is carried downwards by the blower to the combustion chamber for initial ignition of biomass in the combustion zone of the gasifier. The flue gases produced in this zone move upwards to trigger the series of gasification consisting of drying, pyrolysis, combustion and reduction. Now the exhaust port connected to the reduction chamber is opened to remove the smoke. After the warm-up time, the syngas is generated. As the gas production starts, the exhaust port of the reduction chamber is closed. To check the flame quality, the gas control valve of the burner is opened. Thereafter, gas control valve of the generator is opened. The power generated from the genset is supplied to the control panel. The temperature reading, gas composition, and the higher CV are recorded at intervals of ten minutes. The sample gas coming out of the side valve is analyzed with the gas analyzer. Each experiment is carried out for one hour. Biochar produced is removed after each experiment.

3.1.3 Biomass characterization

As highlighted previously, that the biomass used in the current study consist of dead wood twigs of red mulberry (*Morus rubra*) tree (details presented in Figure 3.1.3) that is extensively found in the Northern India. The solid biomass is first converted into powdered form and then it is used for the analysis. The chemical constituents (C-Carbon, H-Hydrogen, N-Nitrogen, S-Sulphur, and O-Oxygen) of the biomass was described by the ultimate analysis of biomass, while, MC, ash content (AC), volatile matters (VM), and fixed carbon (FC) were expressed by proximate analysis as per ASTM D121 [ASTM 2009] and [Lenka 2016]. The compositions of C, H, N, S, and O in present biomass (*Morus rubra*) were found as 45.03%, 6.16%, 0.27%, 0.02% and 40.75%, respectively. The HHV is calculated as 18.36 MJ/kg by empirical formula indicated below [Yin 2011],

$$\text{HHV (MJ/kg)} = 0.2949\text{C} + 0.8250\text{H} \quad (3.1.2)$$

The ultimate analysis of present biomass is carried out by CHNS-O elemental analyzer (Model No. Flash 2000). For ultimate analysis, powdered biomass was first dropped into combustion reactor to initiate a strong exothermic reaction where temperature around 1800°C is attained. The products of combustion were next conveyed crossways the reactor. Nitrogen oxides and sulphur trioxides formed during the process are reduced to elemental Nitrogen and Sulphur dioxide, and excess Oxygen is retained. Thereafter, the gas mixture flows into the gas chromatographic column

where the separation takes place. The removed gases are passed to a thermal conductivity detector that generates electrical signals, which after processing provide the C, H, N, and S_u percentages contained in the biomass sample. For the measurement of Oxygen content, the biomass sample is first weighed in a silver container and stored in an auto sampler. It is then dropped into the reactor to undergo instant pyrolysis and the products cross the adsorption filter, where halogenated compounds are hold. The gaseous mixture flows into the chromatographic columns where carbon monoxide/CO is separated from the other gases. The remaining gaseous mixture is then again conveyed to the thermal conductivity detector to yield the O percentage.

Proximate analysis is carried out by testing two samples of the biomass each weighing 3 g. One of the samples is used to compute VM and MC through air dry process, whereas the other one is used for determining AC via oven dry process. Proximate analysis is done using hot air oven, muffle furnace, ceramic crucible, desiccators, and weighing machine. For each of the two samples, two replicates are carried out. MC involves the water vapor that affects the heating value of biomass and can be determined by using standard oven dry method [Singh et al. 2013]. The sample is prepared in the form of very small size chips of solid biomass. The prepared sample is air-dried in the local environment. The sample of the prepared biomass weighing 3 g is kept in the hot air oven at 105 °C. Next, oven dried sample of biomass is cooled at room temperature in the desiccators so that the sample do not regain moisture from the environment. Then the MC of the sample is calculated using Eq. (3.1.3) on wet basis [Singh et al. 2013],

$$MC (\%) = \frac{\text{Weight (crucible + air dried sample)} - \text{Weight (crucible + oven dried sample)}}{\text{Weight (air dried sample)}} \times 100 \quad (3.1.3)$$

The MC of biomass is evaluated by averaging the values of two replicates and computed as 7.01%. Next, AC of the biomass is evaluated that involves Calcium, Ferrous carbonate, Magnesium, Phosphorous, and sand with clay [Lenka 2016]. The oven-dried biomass sample is burned in the muffle furnace at 575°C and thereafter cooled to evaluate the AC on dry basis using Eq. (3.1.4) [Singh et al. 2013],

$$AC (\%) = \frac{\text{Weight (crucible + residue)} - \text{Weight (crucible)}}{\text{Weight (oven dried sample)}} \times 100 \quad (3.1.4)$$

The AC of sample biomass is calculated as 2.21% by averaging the values of two replicates. VM is that portion of fuel which volatiles rapidly when the biomass is heated at high temperature [Lenka 2016]. The sample of air dried biomass of 3 g is taken in the pre-weighed lid-closed

alumina crucible and heated in the muffle furnace at 925 °C. Then the crucible is removed from muffle furnace and cooled in air. The VM is calculated on dry basis as below [Singh et al. 2013],

$$\text{VM (\%)} = \text{Loss in weight of crucible and biomass (\%)} - \text{MC (\%)} \quad (3.1.5)$$

The VM is found as 78.13% by averaging the values of the two replicates. Finally, the FC is calculated on dry basis as 12.65% using Eq. (3.1.6) [Singh et al. 2013],

$$\text{FC (\%)} = 100 - [\text{VM (\%)} + \text{AC (\%)} - \text{MC (\%)}] \quad (3.1.6)$$

Stoichiometric air-fuel ratio (SAFR) is the ratio of the mass of air (kg) required for complete combustion to 1 kg of biomass and it is calculated as [Dion et al. 2013],

Mass of stoichiometric Oxygen compound (m_{O_2}) required for 1 kg of fuel:

$$m_{O_2} \left[\frac{\text{kg}}{\text{kg of fuel}} \right] = X_C \left(\frac{M_{O_2}}{M_C} \right) + \frac{X_H}{4} \left(\frac{M_{O_2}}{M_H} \right) + X_{S_u} \left(\frac{M_{O_2}}{M_{S_u}} \right) - X_O \quad (3.1.7)$$

Mass of stoichiometric Nitrogen compound (m_{N_2}) required for 1 kg of fuel:

$$m_{N_2} \left(\frac{\text{kg}}{\text{kg of fuel}} \right) = m_{O_2} \left(\frac{Y_{N_2} M_{N_2}}{Y_{O_2} M_{O_2}} \right) \quad (3.1.8)$$

$$\text{SAFR} \left[\frac{\text{kg}}{\text{kg of fuel}} \right] = m_{O_2} + m_{N_2} \quad (3.1.9)$$

where, the significance of various components is indicated in the nomenclature.

3.1.4 Results and discussion

A downdraft biomass gasifier powering a 10 kW engine-generator has been used to study the sungas generated when dried branches of dead red mulberry (*Morus rubra*) wood is used as a fuel. Experiments are performed to study the characteristics of syngas, conversion efficiency and flame quality corresponding to various in ER. The average values (taken over three replicates) of all performance parameters are presented in plots along with standard error. A standard error shows the precision in the measurement value and it is function of estimated population standard deviation (σ) and the number of data points (ε) taken. Let $s_1, s_2, s_3, \dots, s_\varepsilon$ are the measured values for ε number of data points. Then, a standard error is calculated by using Eq. (3.1.10) as reported in [Brown 1982],

$$\text{Standard error} = \frac{\sigma}{\sqrt{\varepsilon}} \quad (3.1.10)$$

The value of σ is calculated by using Eq. (3.1.11) [Brown 1982],

$$\sigma = \sqrt{\frac{\sum_{i=1}^{\varepsilon} (s_i - \bar{s})^2}{\varepsilon - 1}} \quad (3.1.11)$$

where, \bar{s} represents the mean of ε number of data points. This standard error is applicable to all experimental measuring values of current research work provided in this thesis.

3.1.4.1 Equivalence ratio

ER is defined as the ratio of actual air-fuel ratio (AAFR) to SAFR i.e. $ER = AAFR/SAFR$ [Sheth and Babu 2009]. The operating conditions of the gasifier are based on the optimum ER which varies in the range 0.217 to 0.350 as shown in Table 3.1.1. The optimum ER is obtained where CV and efficiency are maximum.

Table 3.1.1: Computation of ER for gasification at different air flow rates and biomass consumptions

| Experiment No. | Actual air flow rate (kg/hr) | SAFR (kg/kg of fuel) | Biomass consumption rate (kg/hr) | AAFR (kg/kg of fuel) | ER |
|----------------|------------------------------|----------------------|----------------------------------|----------------------|-------|
| 1 | 10.67 | 5.459 | 9.0 | 1.185 | 0.217 |
| 2 | 11.86 | 5.459 | 9.5 | 1.248 | 0.228 |
| 3 | 13.24 | 5.459 | 10.0 | 1.324 | 0.242 |
| 4 | 15.63 | 5.459 | 10.5 | 1.488 | 0.272 |
| 5 | 16.94 | 5.459 | 11.0 | 1.540 | 0.282 |
| 6 | 18.64 | 5.459 | 11.5 | 1.620 | 0.296 |
| 7 | 20.14 | 5.459 | 12.0 | 1.678 | 0.307 |
| 8 | 22.66 | 5.459 | 12.5 | 1.812 | 0.331 |
| 9 | 24.89 | 5.459 | 13.0 | 1.914 | 0.350 |

3.1.4.2 Gas composition and calorific value

Air flow rate influences the composition of the syngas. Air contains Oxygen causing combustion of biomass and the varying amount of the supply air flow rate controls the degree of combustion

◇: Carbon monoxide, □: Carbon dioxide, Δ: Methane, x: Hydrogen, o: Calorific value

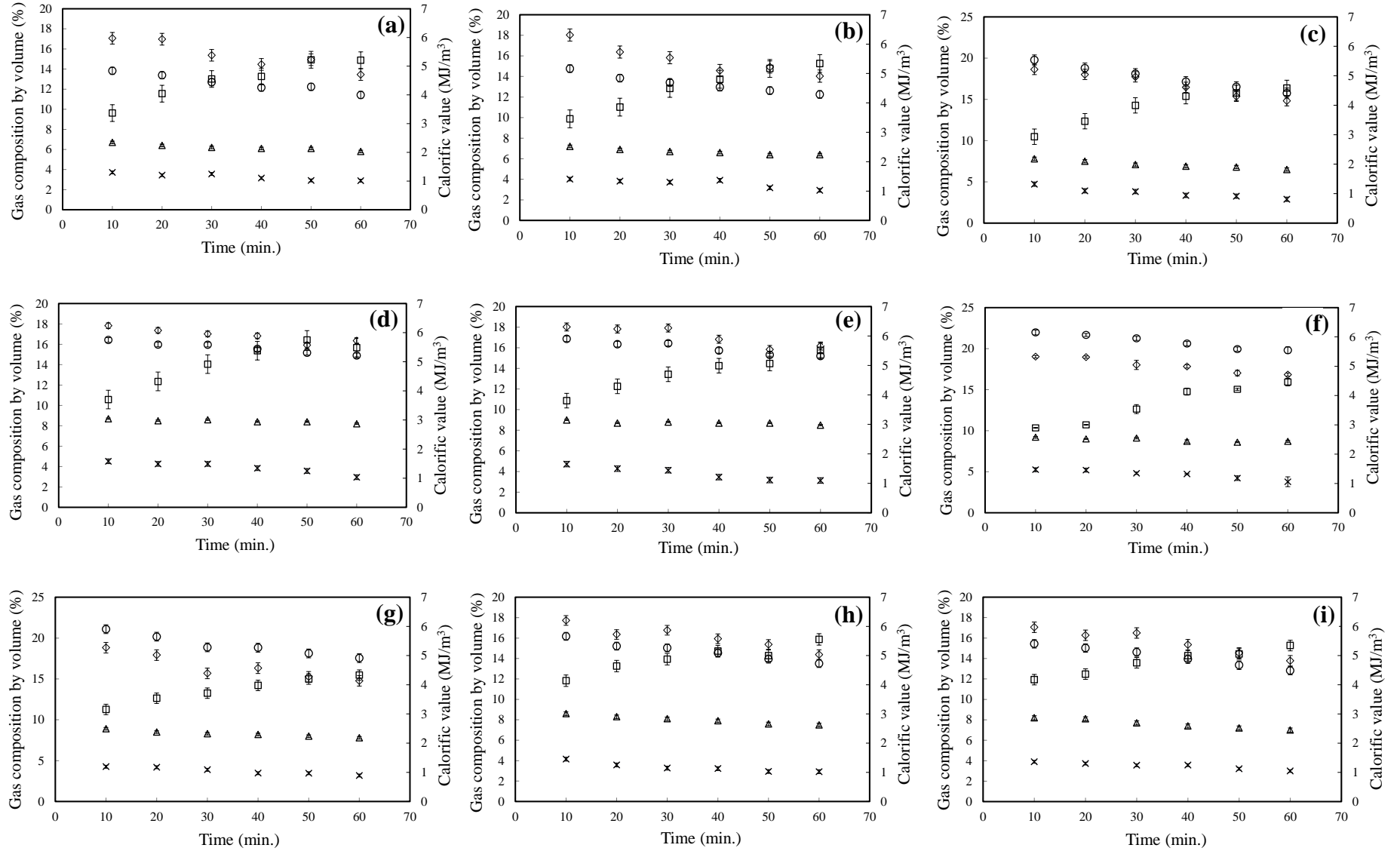


Figure 3.1.4: Variation of gas composition and calorific value with time for each experiment at varying biomass consumption rate, (a) 9.0 kg/hr, (b) 9.5 kg/hr, (c) 10.0 kg/hr, (d) 10.5 kg/hr, (e) 11.0 kg/hr, (f) 11.5 kg/hr, (g) 12.0 kg/hr, (h) 12.5 kg/hr, (i) 13 kg/hr

which in turn, affects the gasification temperature. The energy content of the syngas decreases when the degree of combustion is excessive. This is because a part of combustible matter is utilized during the combustion itself owing to excessive Oxygen content. Figure 3.1.4 shows the variation of gas composition and CV with time for each experiment. It has been observed that generally CO_2 content increases, whereas CO content decreases with time. However, the decrement in H_2 and CH_4 composition is found to be marginal than CO. Initially, air to fuel ratio is low and with time this ratio increases due to decrease in fuel quantity and increase in air flow rate. The insufficient Oxygen (low air to fuel ratio) during initial periods causes partial combustion of biomass that results in high CO and low CO_2 , whereas, an opposite trend is observed during the later phase. Water vapours react with charcoal, CO and CH_4 in the reduction chamber to produce H_2 . However, if there is a decrease in the water vapor with time due to its more consumption (in the reduction zone) than its production (because of decrease in the biomass content, it releases less water vapour from drying zone), it may lead to decrease in H_2 content. It is already highlighted earlier that the formation of CH_4 depends on Carbon in hot charcoal, CO, and H_2 contents. However, amongst them, the presence of H_2 is vital for the establishment of CH_4 gas. As the H_2 composition slightly reduces with time, so, the composition of CH_4 too reduces as time progresses.

The CV of the producer depends upon the individual CVs of CO, CH_4 and H_2 . As highlighted earlier that the concentrations of CO, CH_4 , and H_2 decrease with time, consequently, CV of the syngas also decreases with time.

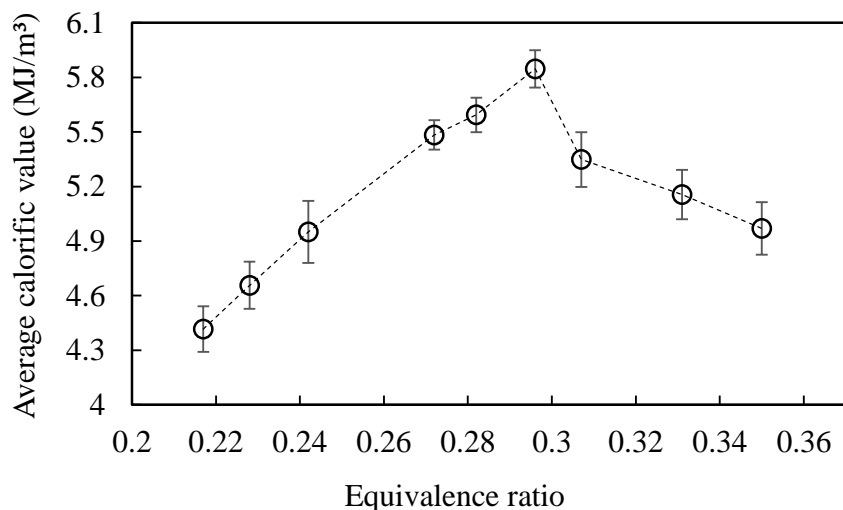


Figure 3.1.5: Variation of average CV with ER for each experiment

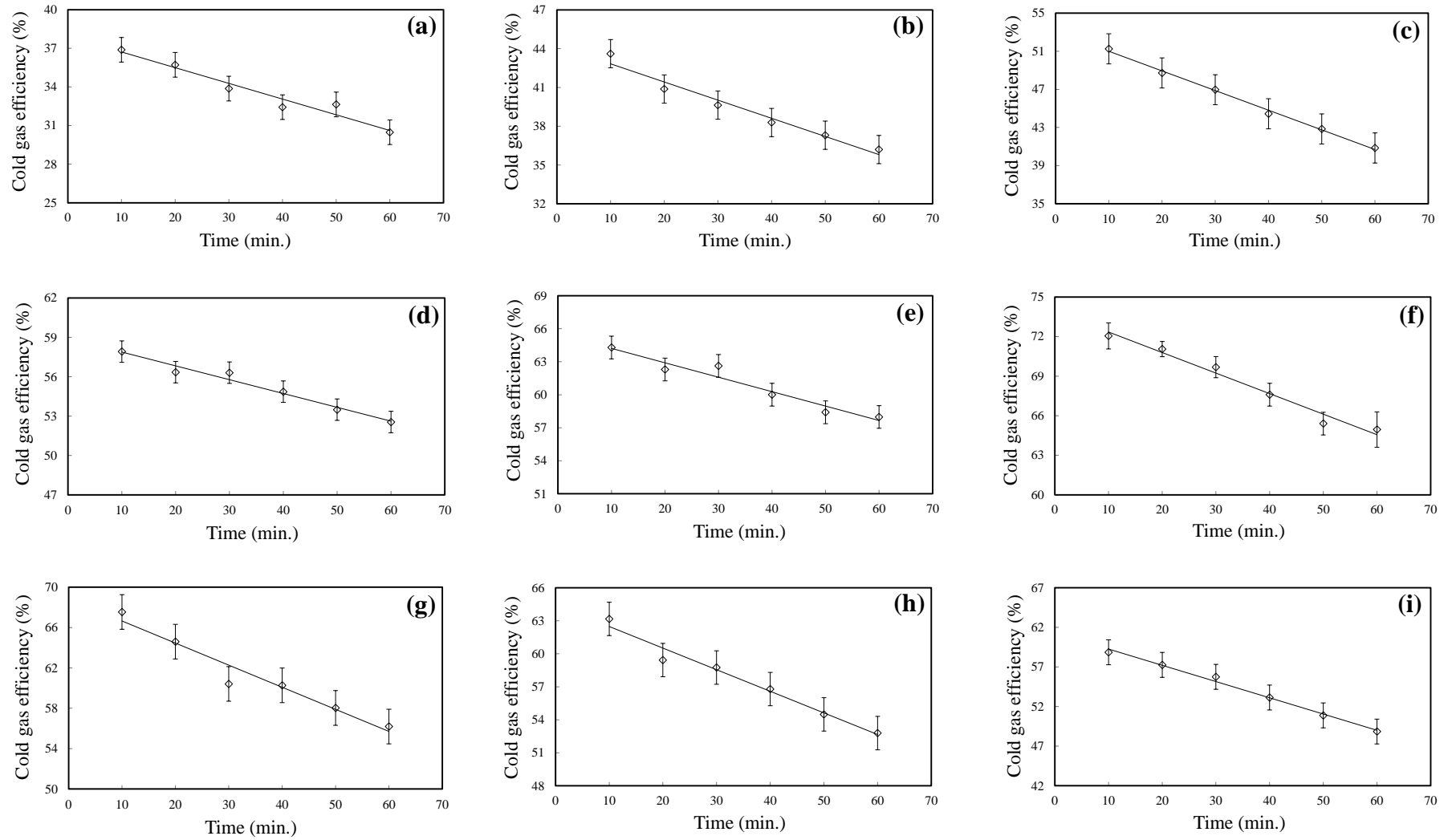


Figure 3.1.6: Variation of cold gas efficiency with time for each experiment with varying biomass consumption rate, (a) 9.0 kg/hr, (b) 9.5 kg/hr, (c) 10.0 kg/hr, (d) 10.5 kg/hr, (e) 11.0 kg/hr, (f) 11.5 kg/hr, (g) 12.0 kg/hr, (h) 12.5 kg/hr, (i) 13 kg/hr

It is well-known that the nominal ER for wood gasification in a downdraft gasifier occurs within the domain of 0.25 to 0.35 [Dutta and Baruah 2014]. Figure 3.1.5 depicts the trends of mean CV of syngas with respect to ER. It is envisioned that CV upsurges with surge in ER and touches maximum (5.846 MJ/m³) for 0.296 ER. Past this, CV drops with additional growth in ER. This nature may be elucidated as follows. Small values of the ER creates imperfect gasification of biomass resulting in the unnecessary char creation and creation of inferior quality gas. As ER rises, desired gasification of biomass occurs till the optimal point is acquired where the gasification develops to optimal level, and so, the CV of syngas gets maximized. Furthermore, intensification of the ER consequences in whole combustion which results in extreme generation of CO₂ at the expense of CO, CH₄ and H₂. At the optimized ER, the maximal values of CO, CH₄ and H₂ were found as 19.02%, 9.20% and 5.25%, respectively.

3.1.4.3 Cold gas efficiency and gas production rate

The cold gas efficiency (η_{cg}) is a function of CV of gas, specific gas production (SGP) and the HHV of biomass used as defined below [Sheth and Babu 2009],

$$\eta_{cg} (\%) = \frac{[CV \text{ of syngas (MJ/m}^3\text{)}] \times [SGP \text{ (m}^3\text{/kg)}]}{HHV \text{ of biomass (MJ/kg)}} \times 100 \quad (3.1.12)$$

The variation of η_{cg} with time for each experiment is shown in Figure 3.1.6. Its decrease with time is due to reduction in CV of syngas as explained above. The variation of the average η_{cg} with ER for each experiment is studied in Figure 3.1.7. The dependency of average η_{cg} on average CV causes an increase in η_{cg} with increase in ER, reaches maximum (68.45%) at ER = 0.296 and decreases with further increase in ER. Figure 3.1.8 shows the variation of gas production rate with ER. The gas production rate increases with increase in ER due to increase in the quantity of both biomass and air flow rate. More biomass produces more gas but rate of producing gas per unit biomass (SGP) depends upon the air flow rate and rate of biomass gasification. The maximum value of SGP is found as 2.150 m³/kg at ER = 0.296.

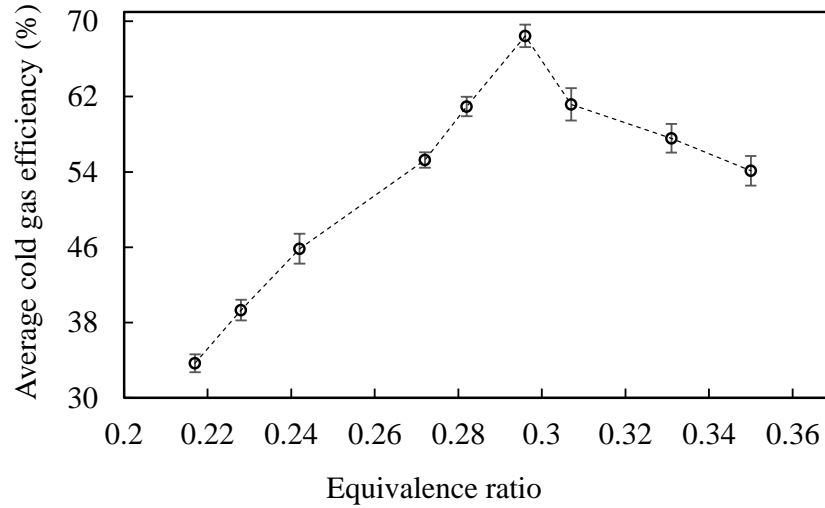


Figure 3.1.7: Variation of average cold gas efficiency with equivalence ratio for each experiment

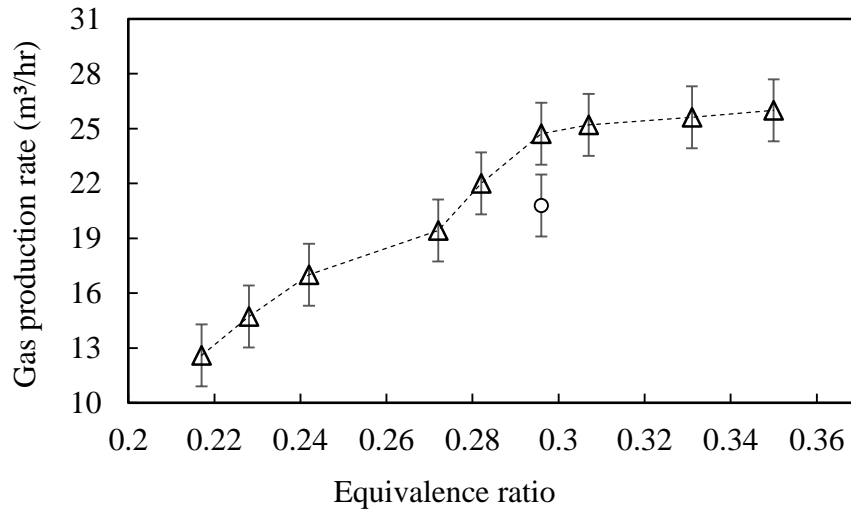


Figure 3.1.8: Variation of gas production rate with equivalence ratio for each experiment

3.1.4.4 Flame quality

The condition of flame is determined by the quality of syngas. The best conceivable quality gas is created at an optimum ER (= 0.296). [Figure 3.1.9](#) indicates three flames at low, optimum and high values of ER. Below the optimum value, the flame shows more red and relatively lesser blue and white zones due to poor quality of syngas. The presence of red zone indicates the presence of soot particles due to incomplete gasification. The red zone progressively decreases with increase in ER and almost blue flame is produced at the

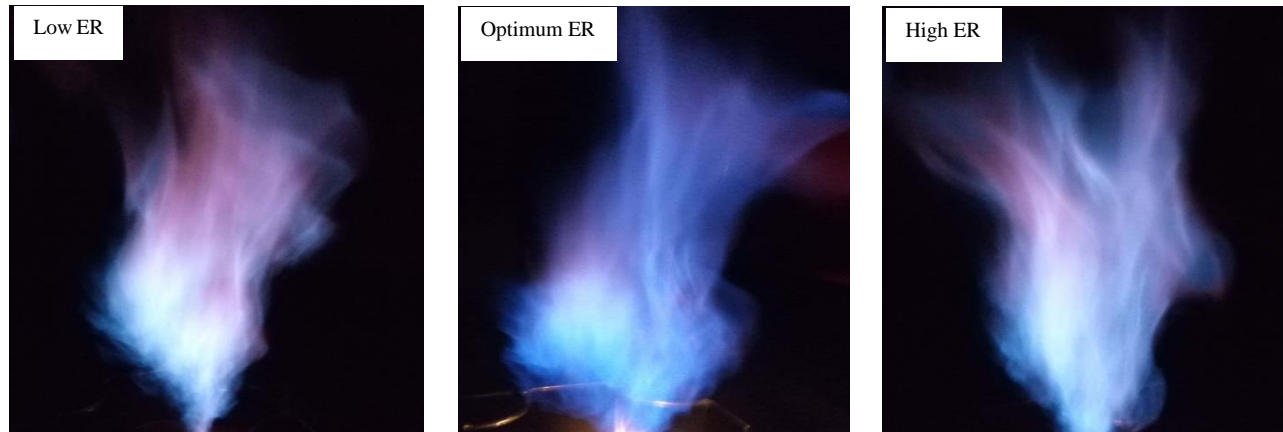


Figure 3.1.9: Flame of syngas at various ERs

optimal ER as indicated in Figure 3.1.9. If ER is more than the optimum point, the condition of flame again reduces and the flame comprises of additional white zones. This may be because of more burning of N_2 inside the gas [Kirshenbaum and Grosse 1956] since at greater ER, additional N_2 is found [Hernandez et al. 2012].

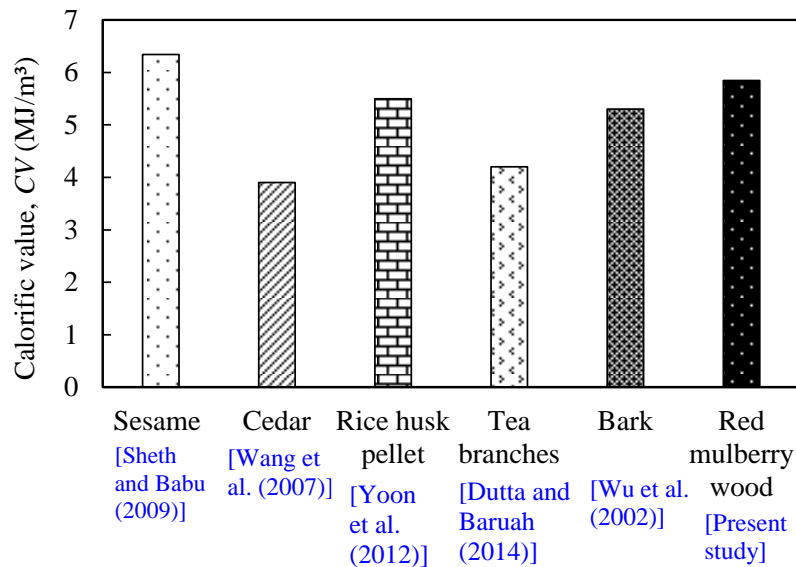


Figure 3.1.10: Comparisons of CV with various biomass available in the published literature

3.1.4.5 Comparison of performance

In

Figure 3.1.10 and Figure 3.1.11 average CV of syngas and η_{cg} of the current biomass gasifier at optimal ER were compared with the behavior of other biomass resources exposed to downdraft gasification. The highest value of CV for the *Morus Rubra* was found as 5.846 MJ/m³ that is lesser

than the CV of sesame (6.34 MJ/m³) discussed by [Sheth and Babu 2009], but more than the CV of cedar (3.9 MJ/m³) and tea twigs (4.2 MJ/m³) as stated by [Wang et al. 2007] and [Dutta and Baruah 2014], respectively. The CV of the rice husks (5.497 MJ/m³) and bark (5.3 MJ/m³) as conveyed by [Yoon et al. 2012] and [Wu et al. 2002], respectively were comparatively reduced with to the *Morus Rubra*.

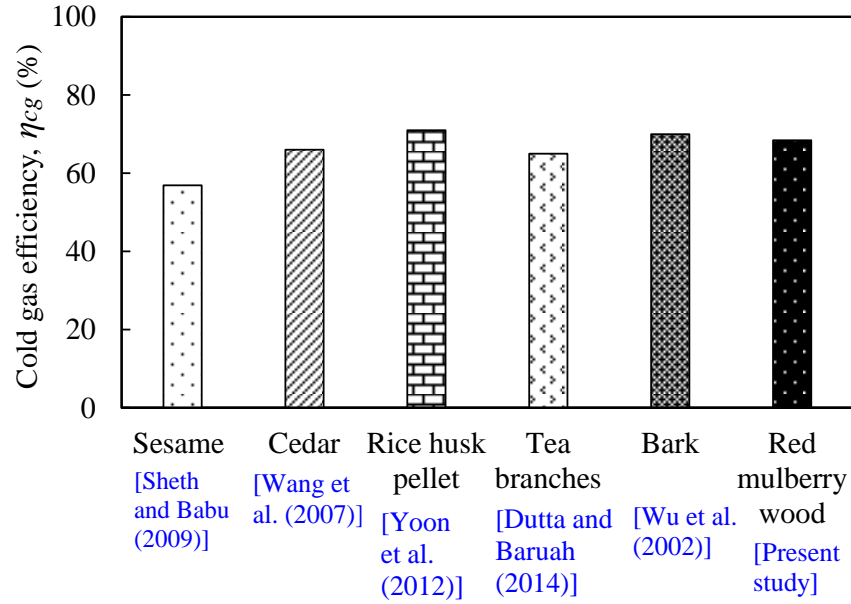
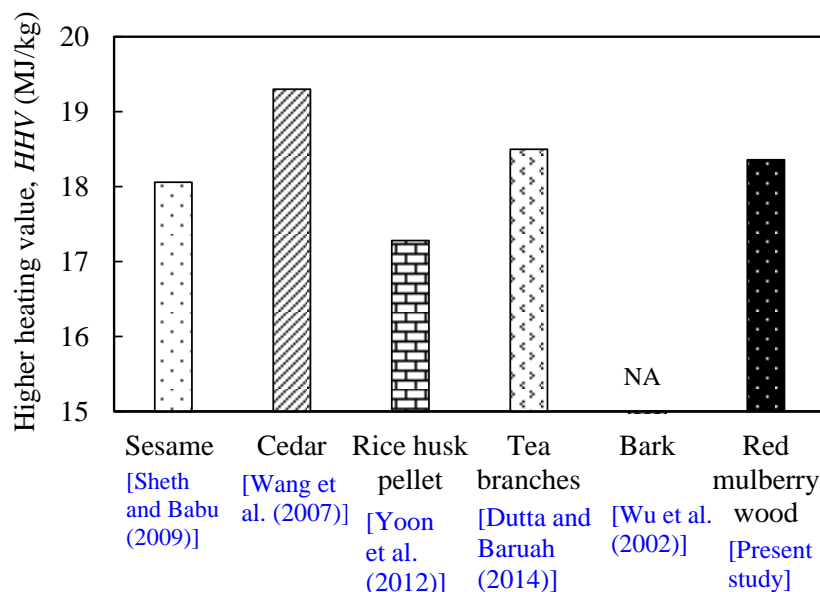


Figure 3.1.11: Comparisons of η_{cg} with different biomass available in the published literature

The average η_{cg} of the present biomass gasifier at optimal ER for the current analysis was computed as 68.45% that was marginally lesser than that of the gasifier functioned with rice husks (71%), and bark (70%) as described by [Yoon et al. 2012] and [Wu et al. 2002] respectively. Nevertheless, the current η_{cg} was established more with respect to sesame (56.87%), cedar (66%) and tea twigs (65%) as discussed by [Sheth and Babu 2009], [Wang et al. 2007], and [Dutta and Baruah 2014], respectively.

The appraisal of HHV of present biomass (*Morus rubra* with the HHV of biomass presented in numerous published studies has been portrayed in Figure 3.1.12. It was seen that the HHV of present biomass (18.36 MJ/kg) was marginally more than the HHV of sesame (18.06 MJ/kg), and rice husks (17.28 MJ/kg) as suggested by [Sheth and Babu 2009] and [Yoon et al. 2012], respectively, and the same was somewhat lesser than the HHV of cedar (19.30 MJ/kg) and tea twigs (18.50 MJ/kg) as stated by [Wang et al. 2007] and [Dutta and Baruah 2014], respectively.



*NA indicates Not Applicable (valid for all figures)

Figure 3.1.12: Comparisons of HHV with other biomass available in the published literature

The evaluation of ultimate analysis of the present biomass (*Morus rubra*) with the ultimate analysis of the biomass undertaken in different published studies is performed in Figure 3.1.13. It was perceived that the amount of C in present biomass (45.03%) was slightly higher than the amount of C in tea twigs (44.43%) as stated by [Dutta and Baruah 2014] (Figure 3.1.13a). But, the same is lesser than the quantity of C in other samples as informed in published work. The quantity of H is nearly identical for all samples (Figure 3.1.13b). Remarkably, present biomass consisted the least quantity of N and S_u when associated with other samples [Figure 3.1.13 (c, d)]. The quantity of O in present biomass was seen as 40.75% that is more than quantity of O found in rice husks (37.40%) as found in the work of [Yoon et al. 2012] (Figure 3.1.13e). Nonetheless, the quantity of O in present biomass was somewhat lesser than that of the sesame (44.87%), cedar (41.70%) and tea twigs (41.90%) as stated by [Sheth and Babu 2009], [Wang et al. 2007], and [Dutta and Baruah 2014] respectively.

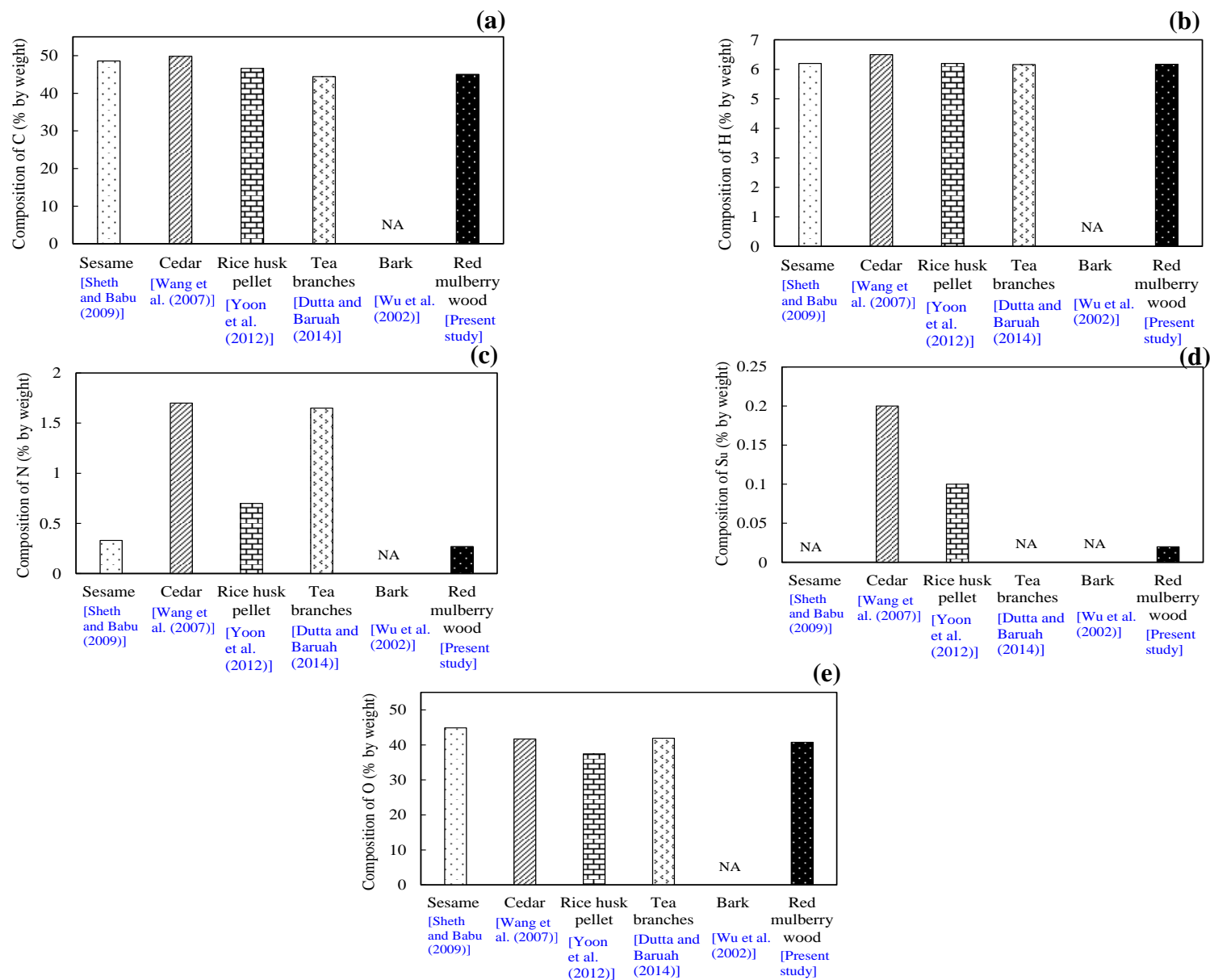


Figure 3.1.13: Comparison of ultimate analysis of red mulberry wood biomass with the biomass available in literature

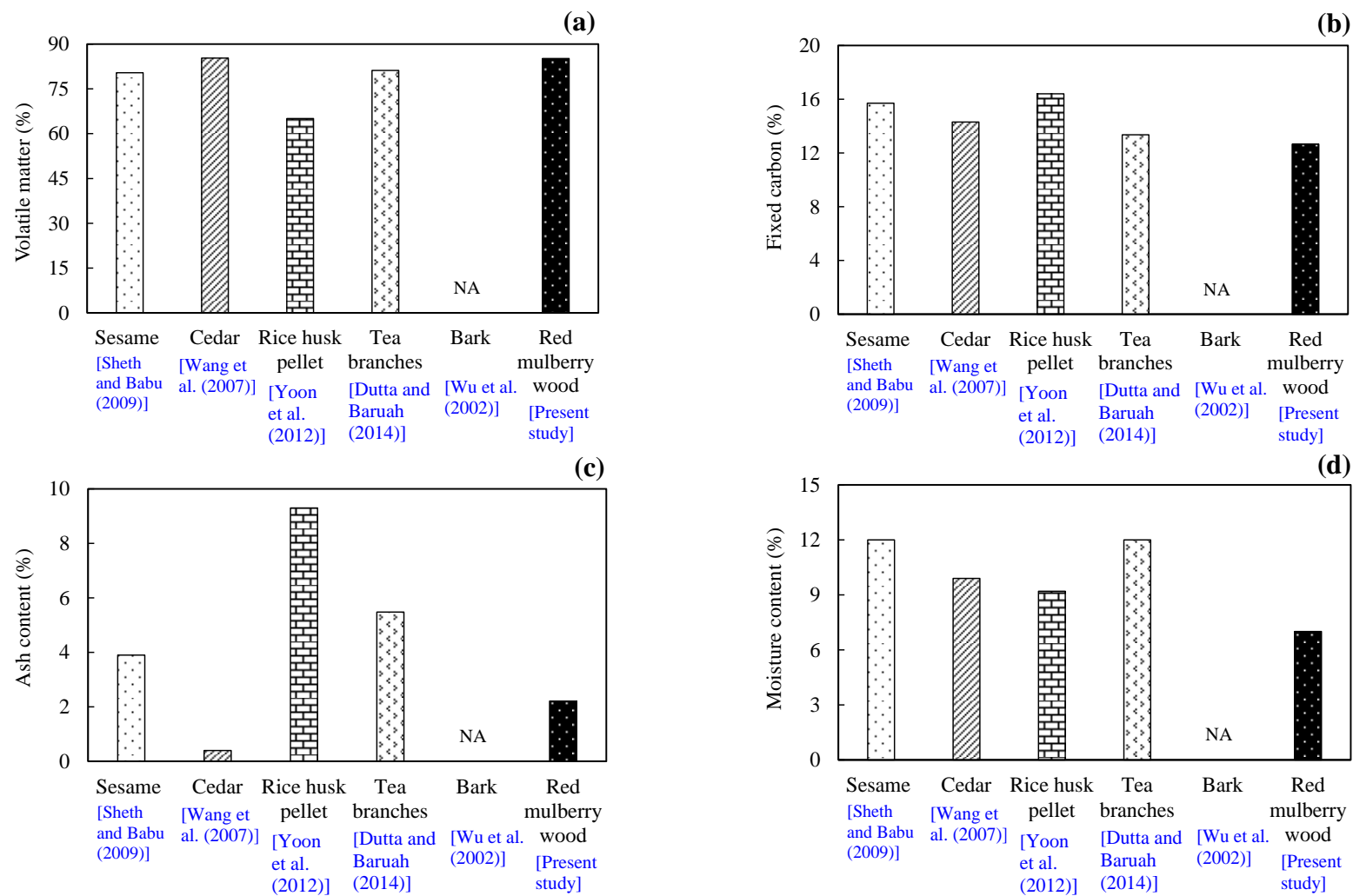


Figure 3.1.14: Comparison of proximate analysis of red mulberry wood biomass with biomass available in literature

An assessment of proximate analysis of red mulberry (*Morus rubra*) biomass against other biomass studied in different published papers is exhibited in Figure 3.1.14. The VM for red mulberry was computed as 78.13% which was lesser with respect to the cedar [Wang et al. 2007] (Figure 3.1.14a). However, its value was seen to be more than sesame (80.40%), rice husks (65.10%) and tea twigs (81.16%) as stated by [Sheth and Babu 2009], [Yoon et al. 2012], and [Dutta and Baruah 2014], respectively. The FC of present biomass (12.65%) was observed lowest when compared with other biomasses described by several papers (Figure 3.1.14b). The AC for the present biomass was computed to be 2.21% that was more than cedar (0.40%) as informed by [Wang et al. 2007], but lesser than sesame (3.90%), rice husks (9.30%) and tea twigs (5.48%) as reported by [Sheth and Babu 2009], [Yoon et al. 2012], and [Dutta and Baruah 2014], respectively (Figure 3.1.14c). Also, the present biomass contained the least MC when paralleled with other candidates as revealed in Figure 3.1.14d, however, the same was established within the norms as declared by [Sheth and Babu 2009].

3.1.4.6 Characteristics of bio-oil and biochar

The chemical composition of bio-oil is identified by Gas Chromatography-Mass Spectrometry or GC-MS (Agilent Technologies 7890B GC System). The column containing helium (carrier gas) flowing at a rate of 0.8 mL/minute is injected with a liquid sample (bio-oil) of volume 1 μ L. The liquid sample compounds get ionized at 70 eV, 200 °C and are analyzed over a mass electron (m/z) range of 25-280. The results obtained corresponding to different retention time and respective mass spectra are plotted as shown in Figure 3.1.15. The bio-oil contains many valuable compounds (identified through spectrum) along with chemical formula, number of scans, retention time, and peak area as presented in Table 3.1.2. The bio-oil contains 7 chemical compounds such as Aminocynoacetic acid (2.43%), Acetic acid (84.93%), O-Methylisourea (4.76%), Nickel tetracarbonyl (2.44%), 1-Methyl-2-propenylhydrazine (4.02%), Allophanic acid and phenyl ester (1.42%). The presence of various functional groups in the biochar are determined by Fourier Transform-Infrared Radiation spectroscopy or FT-IR (PerkinElmer Spectrum IR Version 10.6.1) spectrum observed at wavenumber range of 400-4000 cm^{-1} as presented in Figure 3.1.16.

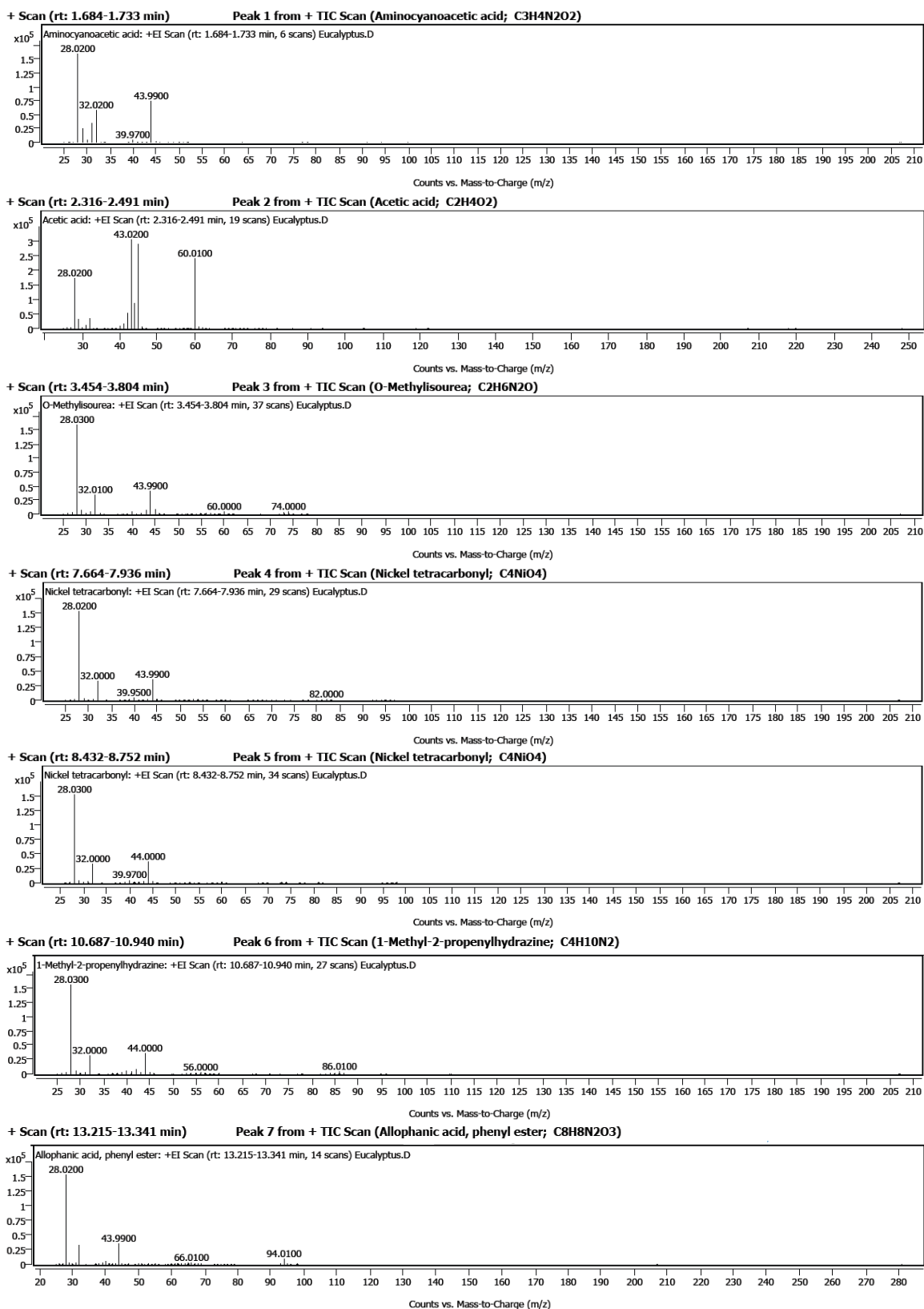


Figure 3.1.15: GC-MS test spectrum results at various peak for bio-oil

The results indicate the presence of alcohol, carboxylic acid, alkyne, isothiocyanate, conjugated acid halide, aromatic compound, sulfoxide, alkene, and halo compound as pronounced in [Table 3.1.3](#).

Table 3.1.2: Identified compounds in the bio-oil with chemical formulas

| Peak No. | Identified compounds | Chemical formula | Retention time (minutes) | Number of scans | Peak area (%) |
|----------|-------------------------------|------------------|--------------------------|-----------------|---------------|
| 1 | Aminocyanoacetic acid | $C_3H_4N_2O_2$ | 1.684-1.733 | 6 | 2.43 |
| 2 | Acetic acid | $C_2H_4O_2$ | 2.316-2.491 | 19 | 84.93 |
| 3 | O-Methylisourea | $C_2H_6N_2O$ | 3.454-3.804 | 37 | 4.76 |
| 4 | Nickel tetracarbonyl | C_4NiO_4 | 7.664-7.936 | 29 | 1.13 |
| 5 | Nickel tetracarbonyl | C_4NiO_4 | 8.432-8.752 | 34 | 1.31 |
| 6 | 1-Methyl-2-propenylhydrazine | $C_4H_{10}N_2$ | 10.687-10.940 | 27 | 4.02 |
| 7 | Allophanic acid, phenyl ester | $C_8H_8N_2O_3$ | 13.215-13.341 | 14 | 1.42 |

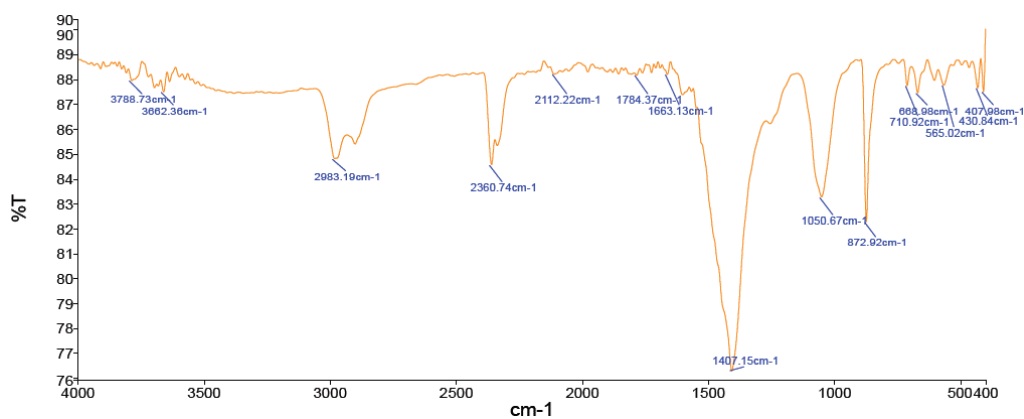


Figure 3.1.16: FT-IR spectroscopy test spectrum results for biochar

Table 3.1.3: Identified functional groups in the biochar corresponding to different wavenumber

| Peak No. | Wave number (cm ⁻¹) | Group | Appearance of vibration | Functional groups |
|----------|---------------------------------|------------------------------------|-------------------------|--|
| 1 | 3788.73 | O-H stretching | medium | alcohol |
| 2 | 2983.19 | N-H stretching O-H stretching | strong, broad | amine salt carboxylic acid |
| 3 | 2360.74 | O=C=O stretching | strong | carbon dioxide |
| 4 | 2112.22 | C≡C stretching | weak | alkyne |
| 5 | 1784.37 | N=C=S stretching C=O stretching | strong | isothiocyanate conjugated acid halide |
| 6 | 1663.13 | C=N stretching | medium | imine /oxime |
| 7 | 1050.67 | C-O stretching S=O stretching | strong | primary alcohol sulfoxide |
| 8 | 710.92 | C=C bending | strong | alkene |
| 9 | 668.98 | C-Br stretching | strong | halo compound |

3.1.4.7 Analysis of zero waste production technology

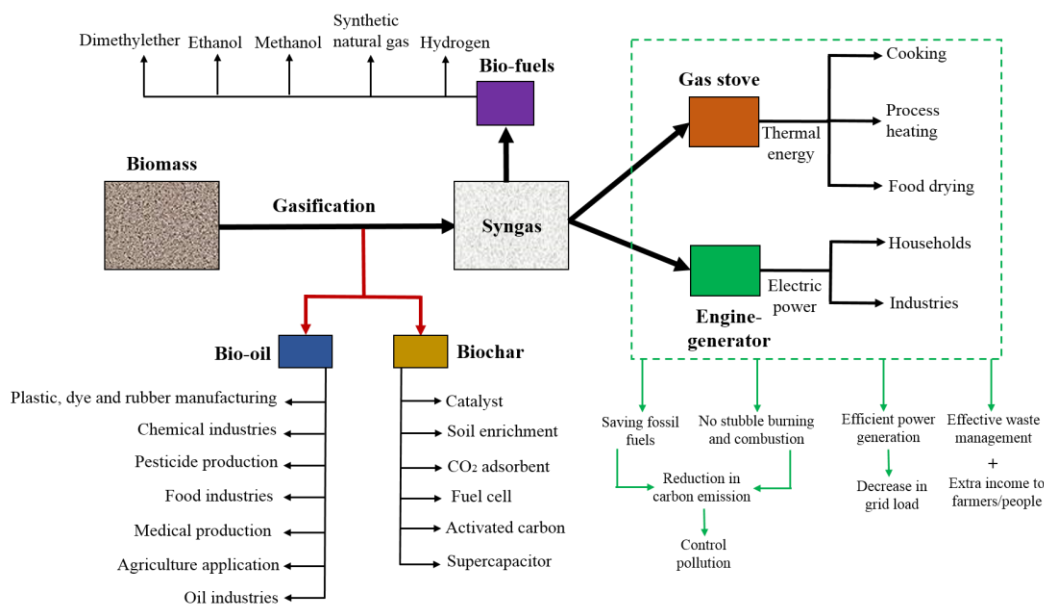


Figure 3.1.17: Analysis of zero waste production technology through different applications of products (syngas, biochar and bio-oil)

The most portion of biomass energy content is mainly converted into syngas through the gasification technology and the remaining part comes out with two byproducts: biochar and bio-oil as described in [Figure 3.1.17](#). The syngas contains the energy content in chemical form and can burn directly using a stove to have thermal energy which could be utilized for various applications like cooking, chemical activity and food drying. In addition to that, this syngas can be used as a fuel for the engine-generator to produce electric power for households and industries [\[J1\]](#). An optimistic route is also available for bio-fuels production from the syngas such as methanol, ethanol, dimethylether, synthetic natural gas and hydrogen which could be used as fuels for automobiles, railways, ships and many more [\[Tao et al. 2022\]](#). By executing this technology, many promising results come out with benefits to the society such as saving of fossil fuels, reduction of carbon emission, decrease in grid load, effective waste management and extra income to people/farmers. The biochar has many attractive properties that make it usable in many areas. The use of biochar for tar removal has been appeared recently based on its pore dimension, area, and matter content. Further, it also acts as a catalyst for the conversion of syngas into liquid hydrocarbons and a solid acid catalyst for biodiesel production [\[Dehkhoda and Ellis 2013\]](#). The use of biochar as a soil enrichment through improving fertility and overall soil health leads to the mitigation of greenhouse gas emissions directly by confiscating solid carbon present in the ground for many years. This also helps in plant growth which leads to additional CO₂ ingesting and decreases the need of fertilizer input that reduces carbon emissions discharge during fertilizer production, transferring and application. Carbon emissions can be shortened by 0.9 Gt/year if 67% of global forestry residues and 50% of global crop residues/waste are utilized as feedstock for generating biochar as soil amendments [\[Laird et al. 2009\]](#). The use of biochar as a gas adsorbent has proven the capture of post-combustion CO₂ due to its high adsorption capacity, low cost, long life and ease of regeneration. The biochar-based activated carbon can adsorb upto 4.8 mmol/g at 1 atm, pressure and 0 °C temperature [\[Gonzalez et al. 2009\]](#). The use of biochar has wide applications in fuel cell systems. It has been used as a fuel source in a recently developed direct carbon fuel cell and can also be used as a low-cost anode material as well as a catalyst in microbial fuel cell [\[Yuan et al. 2013\]](#). Furthermore, the biochar is also used as a raw material for making activated carbon and as a supercapacitor for energy storage. The bio-oil has wide range of applications in different industries for the manufacturing of plastic, dye, rubber, pesticide, chemicals, medicals and oil [\[Yuan et al. 2013\]](#).

3.1.4.8 Uncertainty analysis

Uncertainties are perpetually connected with the measurements because of devices and experimental readings. Thus, the uncertainties included within each experimented value needs to be assessed to gauge the confidence in the experimental results. Let, ϕ be the measuring parameter/dependent variable of interest which is a function of r number of independent variable (z) as shown in Eq. (3.1.13),

$$\phi = \text{function}(z_1, z_2, z_3, \dots, z_r) \quad (3.1.13)$$

Assuming, ξ_z is the absolute uncertainty corresponding to an independent variable, z . Then, the absolute uncertainty in ϕ (i.e. ξ_ϕ) is calculated by using Eq. (3.1.14) as reported by [Moffat 1982],

$$\xi_\phi = \sqrt{\left(\frac{\partial \phi}{\partial z_1} \times \xi_{z_1}\right)^2 + \left(\frac{\partial \phi}{\partial z_2} \times \xi_{z_2}\right)^2 + \left(\frac{\partial \phi}{\partial z_3} \times \xi_{z_3}\right)^2 + \dots + \left(\frac{\partial \phi}{\partial z_r} \times \xi_{z_r}\right)^2} \quad (3.1.14)$$

Subsequently, the ratio of absolute uncertainty to measuring value is known as relative uncertainty, i.e. ξ_ϕ / ϕ . The uncertainties involved in proximate analysis, HHV, SAFR and performances parameters at optimum ER are presented in Table 3.1.4.

Table 3.1.4: Uncertainties in proximate analysis, HHV, SAFR and others quantities at optimum ER

| Parameter | Absolute uncertainty | Relative uncertainty |
|-------------|--|----------------------|
| VM | $4 \times 10^{-3} \%$ | 5×10^{-5} |
| FC | $4 \times 10^{-3} \%$ | 3×10^{-4} |
| AC | $3 \times 10^{-3} \%$ | 1×10^{-3} |
| MC | $2 \times 10^{-3} \%$ | 3×10^{-4} |
| HHV | $4 \times 10^{-4} \text{ MJ/kg}$ | 2×10^{-5} |
| SAFR | $1 \times 10^{-2} \text{ kg/kg of fuel}$ | 2×10^{-3} |
| CV | $4 \times 10^{-3} \text{ MJ/m}^3$ | 7×10^{-4} |
| η_{cg} | $4 \times 10^{-2} \%$ | 6×10^{-4} |
| SGP | $1 \times 10^{-3} \text{ m}^3/\text{kg}$ | 5×10^{-4} |

3.1.5 Summary

In this chapter, gasification features of dead wood biomass acquired from red mulberry (*Morus rubra*) is presented using a downdraft gasifier driving a 10 kW generator. Arrangements were also made to produce flame. Experimentations were done at diverse biomass consumptions as well as flow rates to optimize its operation. From this study, the following key findings are observed,

- The ER is found to vary in the range 0.217 to 0.350 and the optimal point was observed at ER of 0.296. The average CV, η_{cg} , and flame quality deteriorates at both ends of the optimized point of the ER.
- The SAFR and HHV for the current biomass for the present set of settings were computed to be 5.459 kg/kg of fuel and 18.36 MJ/kg, respectively.
- CO₂ increases while CO reduces with time whereas H₂ and CH₄ contents marginally decrease with time. At optimized ER, the maximum values of CO, CH₄ and H₂ are found as 19.02%, 9.2% and 5.25%, respectively.
- At optimum operating condition, the maximum CV and η_{cg} are obtained as, 5.846 MJ/m³ and 68.45%, respectively.
- The calculated parameters show the consistency in their results. The minimum and the maximum standard error in the average CV is found as 0.049 MJ/m³ and 0.115 MJ/m³, respectively. In gas compositions, minimum error is observed for CH₄ (0.04%) and maximum error is observed for H₂ (0.59%), whereas, 0.57% and 1.34% are the respective minimum and maximum standard errors for average η_{cg} .
- A blue colour flame is observed at the optimum ER. Below this, the quality of syngas is low which shows relatively more red zones due to the presence of soot particles. Above the optimal value of ER, the flame shows relatively more white zones due to the presence of N₂ compound.
- The HHV of red mulberry is found relatively higher than the HHV of sesame and rice husk pellet and very close to the HHV of tea branches.

The present study is proposed to be suitable for efficiently using the present dead red mulberry (*Morus rubra*) wood-based biomass for domestic cooking, power generation, and other heating applications in areas where it is available, but not efficiently utilized. The comparison of red mulberry biomass with the other biomass presented by published literature shows that the red mulberry biomass has encouraging potential towards energy conversion.

3.2 Energy production from the sustainable waste biomass (dried grass, leaves and dead branches)

The use of waste biomass for energy production has many advantages such as easy waste management and low-cost power generation. Also, the utilization of waste biomass for energy production can fulfill the energy demand not only in rural areas but also in the industrial sector and this in turn can increase the economic strength of the developing countries. The disposal of waste biomass not only requires large dumping grounds but also proves to be inconvenient to the humankind. The processing of waste biomass for the creation of energy enhances the economics of power generation and encourages the use of renewable energy. The waste biomass (dried grass, leaves and dead branches) produced by Indian Institute of Technology Ropar has been converted into syngas to run an I.C. engine for power generation. However, dead branches need to be preprocessed (reduced in size up to 5-8 cm in length) before they can be used in the biomass gasifier while dried grass and leaves can be directly used as it is. A 10 kW Enersol downdraft biomass gasifier (Model No.: ESB-R10) as shown in [Figure 3.1.1 \(b, c\)](#) is used for the gasification of leaves, dried grass and dead branches for power generation. The details about the experimental setup and its procedure are described in [section 3.1.1 and 3.1.2](#) respectively.

3.2.1 Characterization of biomass

In Indian Institute of Technology Ropar, Punjab, significant amount of waste biomass gets collected daily in the form of leaves (collected from the bottom of trees), grass (harvested from cricket and football grounds) and dead branches (branches cut off from the trees) and is dumped at the landfill area. This generated waste biomass has been used as a source of energy production through the gasification technology. The waste biomass (leaves and dead branches) are air dried for two weeks while harvested grass is air dried for one month before use in the biomass gasifier. Three samples (of leaves, dried grass and dead branches of trees) are converted into powder form of approximate size 2-5 mm as shown in [Figure 3.2.1](#) and used for the proximate analysis (MC, AC, VM and FC) as per ASTM D121 standards described in [section 3.1.3](#). The composition of biomass (C, H, O) has been found by the relation between FC and VM using [Eq. \[3.2.1\(a-c\)\]](#) as reported by [\[Parikh et al. 2007\]](#). The HHV of the biomass was estimated by two correlations, [Eq. \(3.2.2a\)](#) based on proximate analysis and [Eq. \(3.2.2b\)](#) based on ultimate analysis as suggested by [\[Yin 2011\]](#).

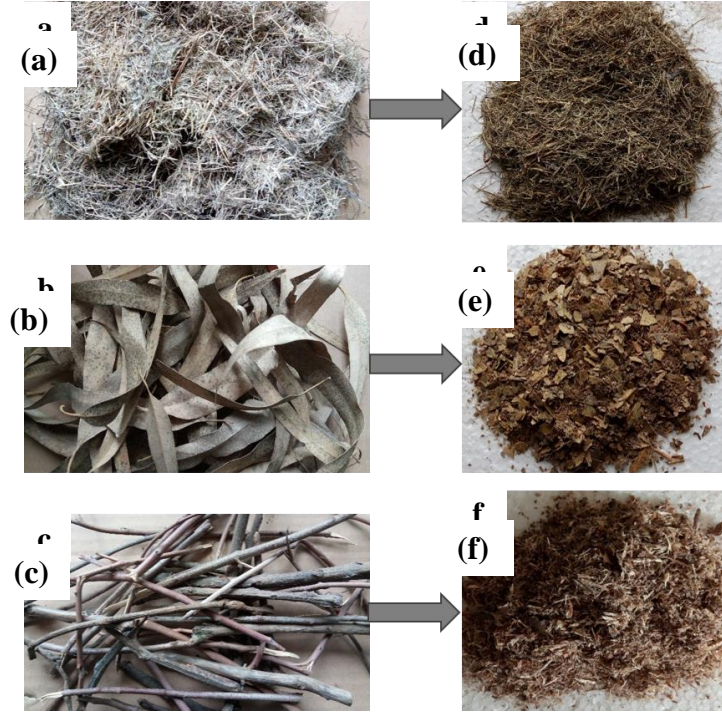


Figure 3.2.1: Specimens of dried grass, leaves and dead branches used for gasification (a, b, c) as raw biomass and their powdered form for characterization (d, e, f) respectively

$$C(\%) = 0.637 \times FC(\%) + 0.455 \times VM(\%) \quad (3.2.1a)$$

$$H(\%) = 0.052 \times FC(\%) + 0.062 \times VM(\%) \quad (3.2.1b)$$

$$O(\%) = 0.304 \times FC(\%) + 0.476 \times VM(\%) \quad (3.2.1c)$$

$$HHV_{\text{Proximate}} (\text{MJ/kg}) = 0.252 \times FC(\%) + 0.190 \times VM(\%) \quad (3.2.2a)$$

$$HHV_{\text{Ultimate}} (\text{MJ/kg}) = 0.2949 \times C(\%) + 0.8250 \times H(\%) \quad (3.2.2b)$$

The proximate analysis of the biomass as summarized in [Table 3.2.1](#) shows that leaves and dead branches contain higher VM as compared to dried grass. Gasification temperature and gas quality are affected by MC and AC present in the biomass [[Dogru et al. 2002](#)]. Amongst the studied biomass, leaves have the lowest MC (7.07%) and AC (5.61%) as compared to the other two. [Table 3.2.2](#) shows the composition of biomass and HHV of biomass. The calculated average HHV (arithmetic mean of $HHV_{\text{Proximate}}$ and HHV_{Ultimate}) of dried grass (15.58 MJ/kg) and dead branches (15.785 MJ/kg) are approximately the same, but leaves possess a relatively higher amount of average HHV (17.075 MJ/kg).

Table 3.2.1: Proximate analysis of dried grass, leaves and dead branches

| Parameters (%) | Dried grass | Leaves | Dead branches |
|----------------|-------------|--------|---------------|
| FC | 11.50 | 12.52 | 10.54 |
| VM | 68.16 | 74.80 | 70.23 |
| MC | 8.46 | 7.07 | 11.16 |
| AC | 11.88 | 5.61 | 8.07 |

Table 3.2.2: Ultimate analysis and HHV estimated by correlations

| Parameters | Dried grass | Leaves | Dead branches |
|----------------------------------|-------------|--------|---------------|
| C (%) | 38.33 | 42.01 | 38.67 |
| H (%) | 4.82 | 5.29 | 5.01 |
| O (%) | 35.94 | 39.41 | 36.63 |
| HHV _{Proximate} (MJ/kg) | 15.88 | 17.40 | 16.03 |
| HHV _{Ultimate} (MJ/kg) | 15.28 | 16.75 | 15.54 |

3.2.2 Results and discussion

3.2.2.1 Gas composition

Gas composition involved the evaluation of four gas parameters, namely the CO, CO₂, CH₄ and H₂ contents. For dried grass, the suitable gasification was observed to occur in the temperature range of 300-600°C and the maximum concentration of CO (19.48%) and H₂ (7.11%) in this temperature range is shown in [Figure 3.2.2a](#). It can be observed from figure 3.2.2a that lower gasification temperatures during starting phase of the experiment leads to incomplete gasification of biomass and produces lower value for gas composition. Further, once it reached to the point of the required gasification temperature, it rapidly starts complete gasification that leads to produce high value for gas composition. The same principle is also applicable for other figures (3.2.2 b and c). [Figure 3.2.2b](#) shows the composition of syngas produced from gasification of leaves biomass. The suitable range of gasification temperature was found to be 250-550°C where the maximum concentration of CO (18.73%) and H₂ (7.42%) was observed. The gasification of dead branches provides the highest value of CO (18.43%) and H₂ (9.83%) as shown in [Figure 3.2.2c](#) within the

temperature range of 300-500°C. However, the concentration of CH₄ is relatively lower than other species and it decreases with increase in gasification temperature.

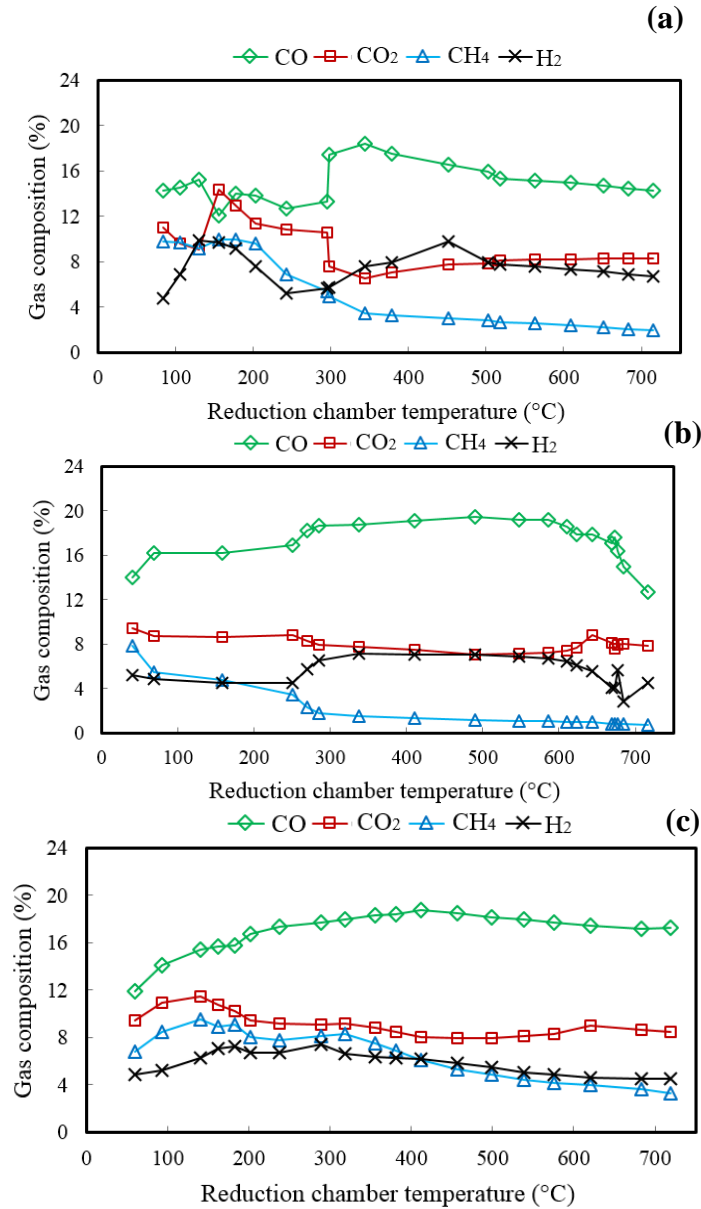


Figure 3.2.2: Gas composition at various reduction chamber temperatures (°C) for gasification of (a) dried grass, (b) leaves and (c) dead branches

3.2.2.2 Calorific value and cold gas efficiency

The CV of syngas describes the quality of gas produced through the gasification process and is affected by the characteristics of biomass, the design of gasifier and gasification temperature. The

variation of CV relative to the temperature of reduction chamber for three waste biomass (dried grass, leaves and dead branches) is shown in Figure 3.2.3. The gasification of leaves and dead branches produces high CV relative to dried grass due to low AC. The average CV generated from dried grass, leaves and dead branches were calculated as 3.52 MJ/m^3 , 5.14 MJ/m^3 and 4.15 MJ/m^3 , respectively. Average η_{cg} derived from dried grass, leaves and dead branches' gasification is found as 50.83%, 64.72%, and 59.15%, respectively.

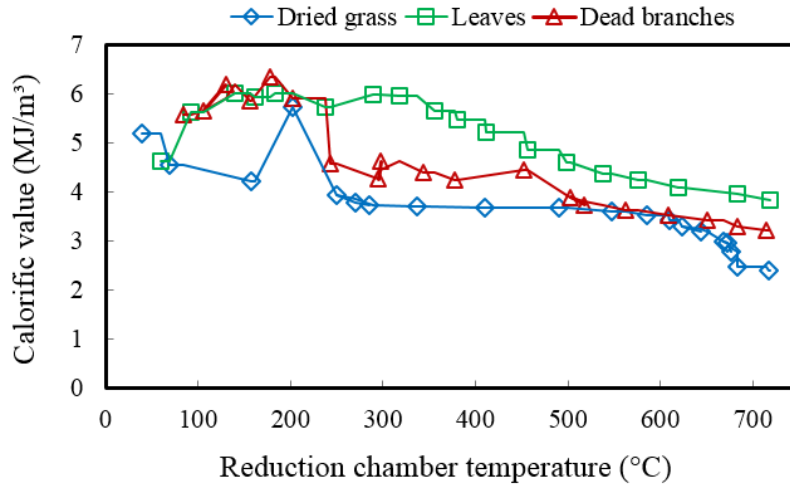


Figure 3.2.3: Calorific value of gas at various temperatures of reduction chamber (°C) for dried grass, leaves, and dead branches

3.2.3 Summary

The characterization of waste biomass shows that dried grass, leaves and dead branches possess considerable potential towards energy production. The appropriate gasification temperature is found to be in the 300-500°C for all waste biomass. The average CV for dried grass, leaves and dead branches are obtained as 3.52 MJ/m^3 , 5.14 MJ/m^3 and 4.15 MJ/m^3 respectively. For all waste biomass, gasifier provides appreciable η_{cg} of 50.83% for dried grass, 64.72% for leaves and 59.15% for dead branches. It has been observed that these waste biomasses can play an important role in strengthening the economy of developing countries where such type of waste biomass is regularly generated and disposed off.

3.3 Economic and feasibility study of biomass-based electric power generation

3.3.1 Energy scenario in India

In India, the electricity demand is fulfilled by thermal power plant (52%), hydro power plant (25%), natural gas power plant (10%), renewable energy power plant (9%), nuclear power plant

(3%) and diesel engine power plant (1%) [Kumar et al. 2010]. Most of the electricity demand is met by thermal power plant which is one of the major reasons of environment pollution. Also, the incessant usage of fossil fuels may create energy crisis in India due to limited availability of these resources. In villages, people are still using traditional cook stove having low conversion efficiency and stubble burning (Figure 3.3.1) which create indoor air pollution that causes many hazardous diseases. Therefore, sincere efforts are being required toward the cost-effective power production from the renewable resources. In this context, biomass is found to be most promising source in Indian perspective, but people are still using it inefficiently and the most efficient way of energy production from the biomass is through gasification process [Situmorang et al. 2020].



Figure 3.3.1: Inefficient use of biomass for (a) cooking and (b) agriculture purposes

3.3.1.1 Energy potential status of biomass

India has abundant availability of biomass resources which are either used inefficiently or wasted on the landfill areas. In India, every year approximately 450 MT (million tons) of biomass is generated from crop waste, coconut shells and sugarcane waste [Kumar et al. 2010]. The capacity of various biomass resources and their energy potential to generate power (GW) are shown in Figure 3.3.2. The maximum quantity of biomass (240 MT/year) is generated from the cotton stalk and coconut shells having a power generation capacity of 28 GW. The generation capacities of sugarcane waste and solid wood biomass are approximately 163.5 MT/year (energy potential of 8.9 GW) and 84 MT/year (energy potential of 9.7 GW), respectively. Interestingly, it is found that solid wood biomass has a higher energy potential at lower capacity than the sugarcane waste. This is ascribed to high energy content (HHV) and low AC of solid biomass. Rice husk and straw also has considerable generation capacity (41 MT/year) with an energy potential of 4.7 GW. Stalk and cobs from maize biomass has the lowest capacity (6.2 MT/year) contributing 0.7 GW.

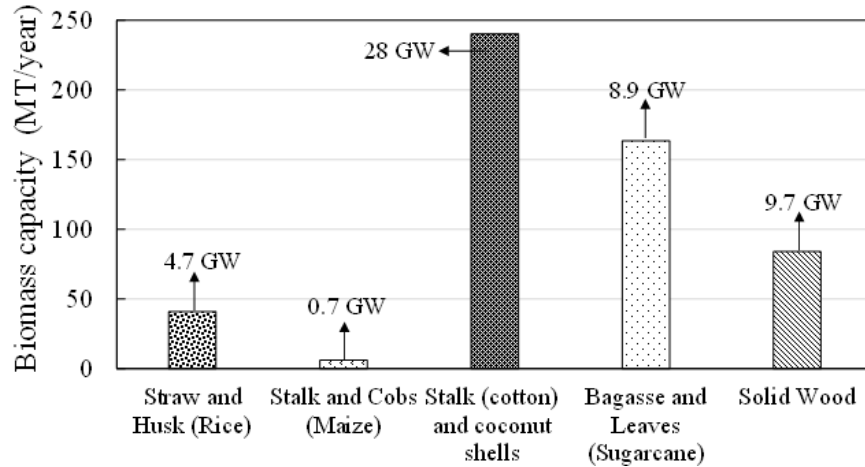


Figure 3.3.2: Energy potential of different biomass in India [Kumar et al. 2010]

3.3.1.2 Trend of electricity demand

The annual growth rate of population (1.58%) in India [Kumar et al. 2010] has significantly increased the energy demand over the last few decades. Figure 3.3.3 shows the trend of electricity demand in India over the past few decades. In 1991-92, the electricity demand in India was only 231 TWh which has escalated up to 725 TWh in 2009-10 with a growing rate of 27.44 TWh/year. The growing rate found to be increased with time and expected to reach 91.40 TWh/year when demand is projected as 2531 TWh [Laha et al. 2020]. This concern needs an alternative to fossil fuels to meet the energy demand in a sustainable manner.

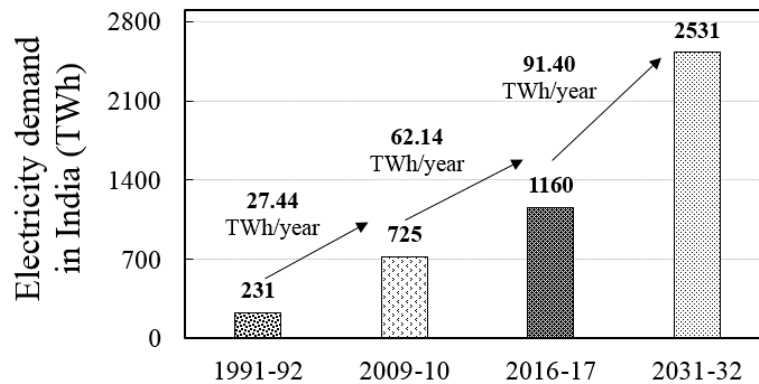


Figure 3.3.3: Trend of electricity demand in India [Kumar et al. 2010] and [Laha et al. 2020]

3.3.2 Economic analysis

An economic analysis of the biomass gasification-based power plant for different capacities is performed through the electricity generation cost and payback period. Two type of costs are involved in generating the power from any system: (i) capital cost and (ii) operating cost.

3.3.2.1 Capital cost

The capital cost of a biomass gasification-based power plant is primarily contributed by four sets: (a) Gasifier combined with cooling tower, filtration and auxiliary items, (b) Genset (engine-generator system), (c) Construction work of the setup and (d) installation [Wu et al. 2002]. The biomass gasification-based power plant having 10 kW capacity has been installed in the campus at IIT Ropar, Punjab. The capital costs of a biomass gasification-based power plant for different capacities (10 kW, 500 kW, and 1000 kW) are presented in Table 3.3.1. The capital cost of a 10 kW capacity as revealed in Table 3.3.1 is the original cost of the plant installed at IIT Ropar. The original capital costs for other two capacities power plant are verified from the manufacturer,

Table 3.3.1: Capital costs of different capacities power plant (gasification-based) in present scenario of India

| <i>x</i> | Component | Capacity of power plant | | |
|----------|---|--|---|--|
| | | 10 kW, Rs. $\times 10^3$ (USD $\times 10^3$) | 500 kW, Rs. $\times 10^3$ (USD $\times 10^3$) | 1000 kW, Rs. $\times 10^3$ (USD $\times 10^3$) |
| 1 | Gasifier | 360 (4.519) | 12,600 (158.172) | 23,400 (293.748) |
| 2 | Cooling tower | 35 (0.439) | 1,225 (15.378) | 2,275 (28.559) |
| 3 | Filtration | 85 (1.067) | 2,975 (37.346) | 5,525 (69.357) |
| 4 | Auxiliary items (pump, motor, fan etc.) | 15 (0.188) | 525 (6.591) | 9,75 (12.240) |
| 5 | Genset | 310 (3.892) | 10,850 (136.204) | 20,150 (252.950) |
| 6 | Setup construction works | 50 (0.628) | 1,750 (21.968) | 3,250 (40.798) |
| 7 | Installation | 20 (0.251) | 700 (8.787) | 1,300 (16.319) |
| Total | | 875 (10.984) | 30,625 (384.446) | 56,875 (713.971) |

*Exchange rate, 1 USD = Rs. 79.66 during September, 2022 [Currency Exchange Rates 2022].

Enersol Biopower Pvt. Ltd., Jaipur, India [ESB-R49/500kW 2022] and [ESB-R50/1000kW 2022] and capital costs of various components are calculated in a similar proportion as of 10 kW plant which is given by the following equation,

$$\text{Cost of } x \text{ component}|_{500/1000\text{kW}} (\text{Rs.}) = \frac{\text{Cost of } x \text{ component}|_{10\text{kW}} (\text{Rs.}) \times \text{Total capital cost}|_{500/1000\text{kW}} (\text{Rs.})}{\text{Total capital cost}|_{10\text{kW}} (\text{Rs.})} \quad (3.3.1)$$

The capital cost per kW decreases with an increase in the capacity of plant as shown in Figure 3.3.4. Therefore, a higher capacity power plant is found to be more attractive as compared to a small capacity plant.

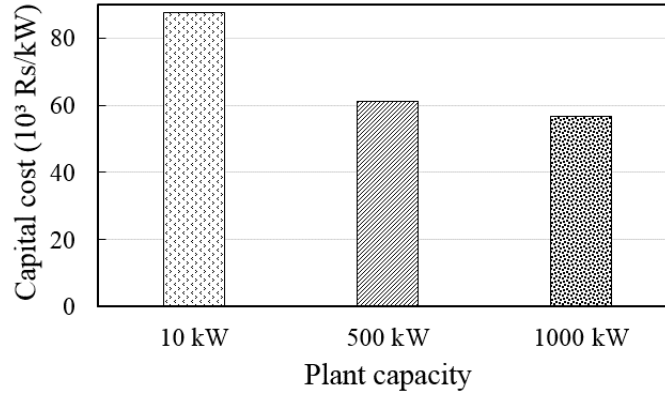


Figure 3.3.4: Capital cost per kW for different capacities power plant

3.3.2.2 Electricity generation cost

The running cost of plant drives the electricity generation cost which includes cost of different factors such as labour, biomass, maintenance and depreciation [Wu et al. 2002]. Operating life of biomass gasifier-based power unit was considered around 15 years while working for 24 hours with a total of over 300 days per year [C2]. Some portion of the generated power is consumed by the various auxiliary components such as water pump, motor and cooling fan. For the present 10 kW power plant, the power consumed by water pump, motor and cooling fan is noted as 0.09 kW, 0.37 kW and 0.18 kW, respectively. By considering other power losses, the total power consumed by running equipments is supposed to be 10% of the rated capacity [Panwar and Rathore 2009]. The net output capacity (kW) from the plant is gauged by the following equation [Wu et al. 2002],

$$\text{Net output capacity (kW)} = \text{Plant capacity (kW)} - \frac{\text{Power consumption (\%)} \times \text{Plant capacity (kW)}}{100} \quad (3.3.2)$$

The net electricity production (kWh/year) from the plant is the multiplication of operating time (h/year) and the net output capacity (kW). Wages/person is found as per the existing labour cost in India when working for 8 hours in 3 shifts. The labour cost paid for running the power plant is determined by the expressed mentioned hereunder [Panwar and Rathore 2009],

$$\text{Labour cost (Rs./year)} = \text{Operating time of plant (day/year)} \times \text{Wages (Rs./day)} \quad (3.3.3)$$

The electricity generation cost mainly depends upon the cost of biomass which varies with the geographical location. In present scenario of India, the biomass cost is considered as Rs.2000/ton (25.107 USD/ton). [C2] and [Bisht and Thakur 2022]. The total cost of biomass can be found by the equation given below [Wu et al. 2002],

$$\begin{aligned} \text{Total cost of biomass (Rs./year)} = & \text{Specific consumption of biomass (kg/kWh)} \times \text{Biomass cost (Rs./ton)} \\ & \times \text{Operating time of plant (h/year)} \times \text{Plant capacity (MW)} \end{aligned} \quad (3.3.4)$$

The maintenance cost is necessary in order to repair/maintain the plant for smooth operation and it is assumed as 10 % of the plant's capital cost [Fracaro et al. 2011]. It is considered that the cost of power plant remains 10% after operating the plant over a life period of 15 years and based on that the depreciation cost is computed by the following equation [Wu et al. 2002],

$$\text{Depreciation cost (Rs./year)} = \frac{\text{Capital cost (Rs.)} - \text{Remaning cost (Rs.)}}{\text{Operating life of power plant (year)}} \quad (3.3.5)$$

The electricity generation cost provided by the biomass power plant is the ratio of total operating/running cost of power plant and the net electricity production and it is mentioned in the following equation [Wu et al. 2002],

$$\text{Electricity generation cost (Rs./kWh)} = \frac{\text{Total operating cost (Rs./year)}}{\text{Net electricity production (kWh/year)}} \quad (3.3.6)$$

The electricity generation cost for 1000 kW, 500 kW and 10 kW capacities plant are obtained as Rs.4.34/kWh (0.055 USD/kWh), Rs.4.65/kWh (0.058 USD/kWh) and Rs.9.57/kWh (0.120 USD/kWh), respectively and relevant details are presented in Table 3.3.2. Presently, the available cost of electricity from the grid in Punjab, India is Rs.7.15/kWh (0.090 USD/kWh) [Punjab Electricity Tariff, ChandigarhMetro.Com, 2017] for 301-500 units of the average consumption range which is high as compared to electricity generation cost from 500 kW and 1000 kW capacities plant.

Table 3.3.2: Various parameters involved in electricity generation costs (Rs./kWh) from various capacities power plant

| Parameter, unit | 10 kW | 500 kW | 1000 kW |
|--|---|---|---|
| Operating time of plant, h/year | 7,200 | 7,200 | 7,200 [Panwar and Rathore 2009] |
| Power consumption, % of rated capacity | 10 | 10 | 10 |
| Net output capacity, kW | 9 | 0.45×10^3 | 0.90×10^3 |
| Net electricity production, kWh/year | 64.8×10^3 | $3,240 \times 10^3$ | $6,480 \times 10^3$ |
| Number of labour required | 1 | 6 | 8 [Panwar and Rathore 2009] |
| Wages, Rs./day (USD/day) | 1,050 (13.181) | 6,300 (79.086) | 8,400 (105.448) |
| Labour cost, Rs./year (USD/year) | 315×10^3 (3.954×10^3) | $1,890 \times 10^3$ (23.726 $\times 10^3$) | $2,520 \times 10^3$ (31.634 $\times 10^3$) |
| Specific consumption of biomass, kg/kWh | 1.15 [J1] | 1.15 | 1.15 |
| Cost of biomass, Rs./ton (USD/ton) | 2,000 (25.107) | 2,000 (25.107) | 2,000 (25.107) |
| Total cost of biomass, Rs./year (USD/year) | 165.60×10^3 (2.079×10^3) | $8,280 \times 10^3$ (103.942 $\times 10^3$) | $16,560 \times 10^3$ (207.884 $\times 10^3$) |
| Depreciation cost, Rs./year (USD/year) | 52.50×10^3 (0.659×10^3) | $1,837.50 \times 10^3$ (23.066×10^3) | $3,412.50 \times 10^3$ (42.838×10^3) |
| Maintenance cost, Rs./year (USD/year) | 87.50×10^3 (1.098×10^3) | $3,062.5 \times 10^3$ (38.445 $\times 10^3$) [Fracaro et al. 2011] | $5,687.5 \times 10^3$ (71.397 $\times 10^3$) [Fracaro et al. 2011] |
| Total operating cost, Rs./year (USD/year) | 620.60×10^3 (7.790×10^3) | $15,070 \times 10^3$ (189.179×10^3) | $28,180 \times 10^3$ (353.753 $\times 10^3$) |
| Electricity generation cost, Rs./kWh (USD/kWh) | 9.57 (0.120) | 4.65 (0.058) | 4.34 (0.055) |

3.3.2.3 Payback Period and Feasibility

Based on the electrical energy consumption of a household, payback period and feasibility of various plant capacities have been evaluated. The electricity generation cost for a 10 kW plant capacity is found to be greater than the current electricity cost in Punjab, so such a low capacity plant will not be profitable. However, small capacities (10-50 kW) gasification-based power plant is feasible in remote areas, where the cost of biomass is very less, labor cost is low, and biomass availability is more. Moreover, the electricity production cost from the diesel power plant is Rs. 14.44/kWh (0.181 USD/kWh) [Ravindranath and Balachandra 2009] in India which can be replaced by this small capacity power plant driven by the renewable source i.e., biomass. The average consumption of electricity for a household per day was nearly 1 kWh in 1999 [Ghost et al. 2004]. During the period 1999-2017, the increase in electricity demand is found to be approximately 5 times. Therefore, the average electricity consumption for a household per day is approximated to be around 5 kWh. A power plant that can supply the electricity to a number of households is calculated by using equation given below,

$$\text{Number of households electrified} = \frac{\text{Net electricity production (kWh/year)}}{\text{Electricity consumption rate (kWh/day/household)} \times \text{time (day/year)}} \quad (3.3.7)$$

When the electricity is supplied by the grid system, then it has been assumed that the investment or capital cost is zero but paying cost of electricity is Rs.7.15/kWh (0.090 USD/kWh) [Punjab Electricity Tariff 2017]. After investment in the biomass-based gasification power plant, the paying cost of electricity from 500 kW and 1000 kW capacity power plant is found to be Rs.4.65/kWh (0.058 USD/kWh) and Rs.4.34/kWh (0.055 USD/kWh), respectively. Total cost paid per annum is found by using Eq. (3.3.8),

$$\text{Total cost paid (Rs./year)} = \text{Electricity cost (Rs./kWh)} \times \text{Total electricity consumption (kWh/year)} \quad (3.3.8)$$

The profit in the electricity cost is evaluated by following rule,

$$\text{Profit (Rs./year)} = \text{Total cost paid}_{\text{Grid}} \text{ (Rs./year)} - \text{Total cost paid}_{\text{Biomass power plant}} \text{ (Rs./year)} \quad (3.3.9)$$

Table 3.3.3 shows the profit in the electricity cost when biomass power plant is used under various plant capacities. The profit gained is found Rs.8,098×10³/year (101.657×10³ USD/year) and Rs.18,206×10³/year (228.546×10³ USD/year) for a plant capacity of 500 kW and 1000 kW,

respectively under prescribed conditions. For a biomass-based power plant, the acceptable economic feasibility is designed as per following condition [Leung et al. 2004],

$$\frac{\text{Capital cost (Rs.)}}{\text{Profit (Rs./year)}} \leq 5 \quad (3.3.10)$$

Table 3.3.3: Profit in electricity costs from various capacities of biomass-based power plant

| Parameter (unit) | 10 kW | 500 kW | 1000 kW |
|---|--|--|--|
| Total electricity consumption (kWh/year) | 1825 | 1825 | 1825 |
| Number of household electrified | 35 | 1775 | 3550 |
| Total cost paid to grid system, Rs./year (USD/year) | 456×10^3 (5.724×10^3) | $23,161 \times 10^3$ (290.748×10^3) | $46,323 \times 10^3$ (581.509×10^3) |
| Total cost paid to biomass power plant, Rs./year (USD/year) | 611×10^3 (7.670×10^3) | $15,063 \times 10^3$ (189.091×10^3) | $28,117 \times 10^3$ (352.963×10^3) |
| Profit, Rs./year (USD/year) | -155×10^3 (-1.946×10^3) [loss] | $8,098 \times 10^3$ (101.657×10^3) | $18,206 \times 10^3$ (228.546×10^3) |

The payback period to recover the capital cost of biomass gasification-based power plant for various capacities is reported in Figure 3.3.5. For a plant capacity of 500 kW and 1000 kW, the payback period is found to be 3.78 years and 3.12 years, respectively which is less than 5 years. It has been observed that plant capacity over 500 kW is economically feasible under the prescribed conditions and it becomes more beneficial with higher capacity power plant. Here, it has been realized that a 10 kW capacity power plant is not feasible compared to grid system (as represented by not applicable/NA in figure 3.3.5).

Many industries such as timber and sugar mills generate surplus waste biomass which can be effectively converted into useful energy through gasification technology. There are many other available waste biomass every year such as leaves, grass, crop residue, forest waste and dead branches [B1] which can be collected from gardens, institutes, organizations, fields, road and canal sides. Therefore these waste biomasses have the capability to produce electricity and can significantly substitute the fossil fuels for power generation.

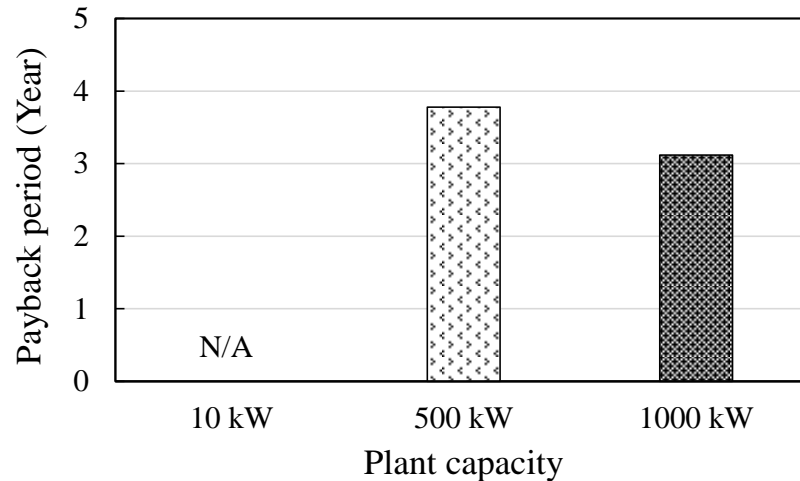


Figure 3.3.5: Payback period of various capacities power plant

3.3.3 Summary

This study demonstrated the economic analysis of various capacities gasification-based power plant and following key points are made:

- The economic investigation of various capacities plant shows that plant with higher capacity is more favorable/economical as compared to small capacity plant.
- The electricity production cost (Rs.4.34/kWh or 0.055 USD/kWh) and payback period (3.12 years) are found minimum for the largest capacity plant i.e., 1000 kW.

In view of above, biomass gasification-based power plants can produce efficient energy from the waste biomass and meeting the energy demand gap.

CHAPTER 4

*USE OF BIOMASS GASIFICATION FOR EFFECTIVE POWER GENERATION

This chapter completed into three stages. In the first stage, the electrical power is generated from the WH of biomass energy driven engine-generator using two TEGs-thermosyphon-based HRSs and output power is used to charge a 12 V UPS battery for end use. In the second stage, these two TEGs-thermosyphon-based HRSs are installed in a SGSP which is run by the solar energy to produce power. In the last stage, a new TEGs-array-based HRS is developed for the effective power generation from SGSP that is driven by solar energy as well as waste heat of a biomass engine-generator.

This chapter addresses the problem of waste heat energy loss in order to fulfill the electricity demand and used it in an effective manner for thermoelectric power generation through advanced design systems of HRS that are based on thermosyphon, array, TEGs and SGSP. Firstly, the WH has been recovered using TEGs integrated with two thermosyphons for electric power generation and performance has been analyzed at varying conditions of input parameters. A thermal resistance model is also developed to analyze the thermal barrier in the flow of heat transfer and the output power is used for charging 12 V, 7 Ah and 80 Ah batteries. Next, these two thermosyphon-based systems have installed in a SGSP to harvest the stored energy for power generation. The performance of the system has been investigated under actual weather conditions and it was found that this system is not able to generate the minimum required output to charge a battery due to the involvement of various thermal resistances. Therefore, a new array-based system is developed for the effective power generation operated first by the solar energy and then externally heated by the WH of gasifier.

* Content presented in this chapter can be found in the publication J2, J3, J4, C1, C3, C4

4.1 Waste heat recovery from the biomass engine using the TEGs-thermosyphon-based HRS

4.1.1 Experimental setup details

Two TEGs-thermosyphon-based HRSs ([Figure 4.1.1](#)) are operated using WH from a biomass engine. The setup consists of (1) an air blower, (2) a resistance heater, (3) a hopper, (4) a cyclone filter (5) a charcoal filter, (6) a cooling tower, (7) two sawdust filters, (8) a gas burner, (9) a cotton filter, (10) a gas analyzer, (11) a gas flow meter, (12) an engine-generator (genset), (13) a control panel, (14) an inverter-battery system, (15) an engine exhaust pipe, (16) a sealed plate, (17) an evaporator section, (18) two-phase flow thermosyphon (2 nos.), (19) a thermal insulation, (20) a condenser section, (21) a pipe for creating vacuum, (22) a water inserting port, (23) 48 TEGs connected in series, (24) the output wires of TEG, (25) two submersible pumps, (26) a water circulation pipe, (27) a vacuum pressure gauge, (28) a vacuum pump, (29) a multimeter, (30) a rheostat, (31) an uninterruptible power source (UPS) battery, (32) a temperature indicator, and (33) a biomass dryer. For convenience in understanding, a block diagram of the experimental facility is also shown in [Figure 4.1.1](#).

WH generated from the biomass engine possess sufficient temperature to heat a plate that in turn transfers the heat to two stainless steel containers (acting as heat sources for the evaporator sections of thermosyphon) attached to it. TEGs could not be directly attached to the hot plate, because the plate vibrates during the operation of the engine. Not only this, difficulty also arises to cool the other end of TEG due to very small thickness (3.9 mm) between the hot and cold ends. Therefore, source container/evaporator is necessary. To minimize heat loss to environment, the sides of both source containers are insulated by thermal insulation of cross linked polyethylene foam (XLPE). The water present in source containers get heated by the hot plate and well-calibrated K-type thermocouple is used to measure the water temperature. Two octagonal thermosyphons are fabricated using the copper sheets of 1.0 mm thickness and the evaporation sections of two thermosyphons are immersed in source containers separately. Thermosyphon acts as a HRS for the WH to transfer the heat energy from one location to another. Each thermosyphon is filled with a pre-measured quantity of distilled water. Two ports are provided on the top of each thermosyphon, the first one is for conveying the distilled water, whereas, the second one is connected to the vacuum pump. 48 series connected TEGs are fixed to the upper end (i.e.,



Figure 4.1.1: Details of the experimental setup with block diagram

condenser section) of the two thermosyphons (24 TEGs on each thermosyphon) to form TEGs-thermosyphon-based HRS. Two sink containers holding cold water are fixed to the upper end of the thermosyphon. For each thermosyphon, one submersible water pump (20 W having discharge of $1.81 \times 10^{-4} \text{ m}^3/\text{s}$) is dipped inside each sink container (condenser) to transfer warm water to a water tank attached to the cooling tower. Further, another water pump of the same capacity is inserted at the cooling tower water tank to circulate cold water to the condenser section i.e. sink containers. This water circulation maintains nearly cold temperature inside the sink container (i.e. at the condenser section). Before operating the thermosyphon, adequate vacuum is created inside it to ensure water boiling at evaporator temperatures in the range (75-90 °C). Vacuum inside the thermosyphon is measured using a vacuum pressure gauge. A multimeter is used to measure voltage and current generated from the TEG, whereas, a rheostat is used to create variable external load resistance. A UPS battery is used to store the power generated from the TEG system.

The calibration of multimeter is accomplished by taking a known power supply (12 V for voltage, 2 A for current) as reference [Sosso and Cerri 2000]. Firstly, multimeter is properly connected with the power supply and the readings (voltage as well as current) from multimeter are measured. These values are compared with the known values (voltage and current) of power supply.

4.1.2 Experimental procedure

The clean syngas runs the biomass engine of the genset to produce electricity by following the procedure as described in [section 3.1.2](#). A pre-measured quantity of distilled water is then fed into the each thermosyphon and the water inserting port is tightly closed. Thereafter, vacuum is created (-700 mm of *Hg* gauge) inside each thermosyphon with the aid of vacuum pump (ultimate vacuum capacity: -734 mm of *Hg* gauge, with maximum air displacement: $6.33 \times 10^{-4} \text{ m}^3/\text{s}$) and the valve provided in the pipe is closed. WH from the engine at high temperature heats a sealed flat plate and the heat is then subsequently transferred from the plate to water inside the source tank. Since the evaporation section of thermosyphon is direct in contact with the heated source water, where heat from the source water is transferred to the distilled water inside the thermosyphon. Meanwhile thermosyphon is under vacuum pressure, distilled water inside the thermosyphon boils at a temperature lower than 100 °C. The generated steam flows upwards to lose its latent heat of vaporization to the upper zone (condenser section) of the thermosyphon. Thus the inner surface of

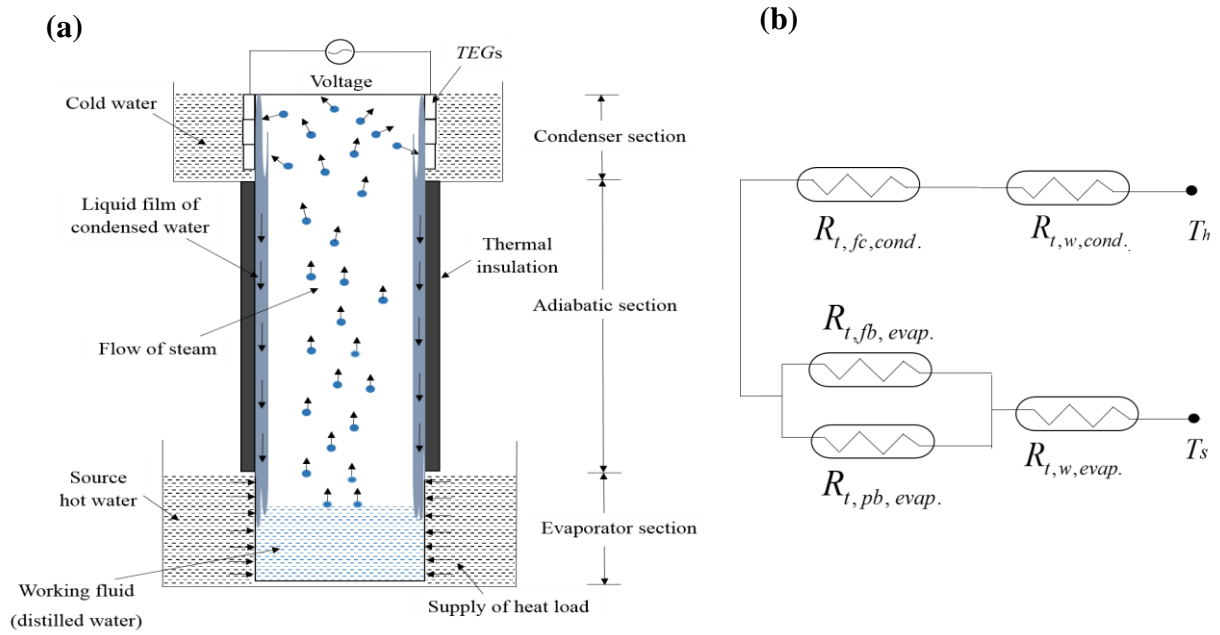
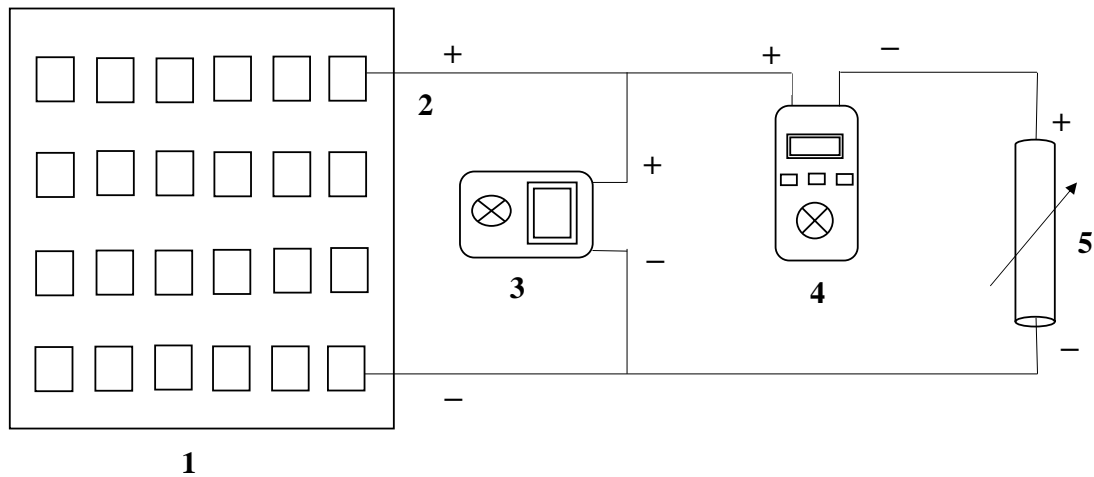


Figure 4.1.2: Schematic diagram of (a) a two-phase closed thermosyphon and (b) the network of resistances offered in the heat flow



1 24 TEG connected in series 3 Voltmeter 5 Rheostat
2 Output wires of TEG 4 Ammeter

Figure 4.1.3: Circuit diagram for measuring the output current and voltage at variable external load resistance

the condenser section is always maintained nearly at a uniform temperature to keep one end of the TEG under hot condition because the one surface of TEG is directly in contact with the outer surface condenser section. The other surface of the TEG is cooled by water circulation from the tank of the cooling tower. This phenomenon results in a potential difference by Seebeck effect.

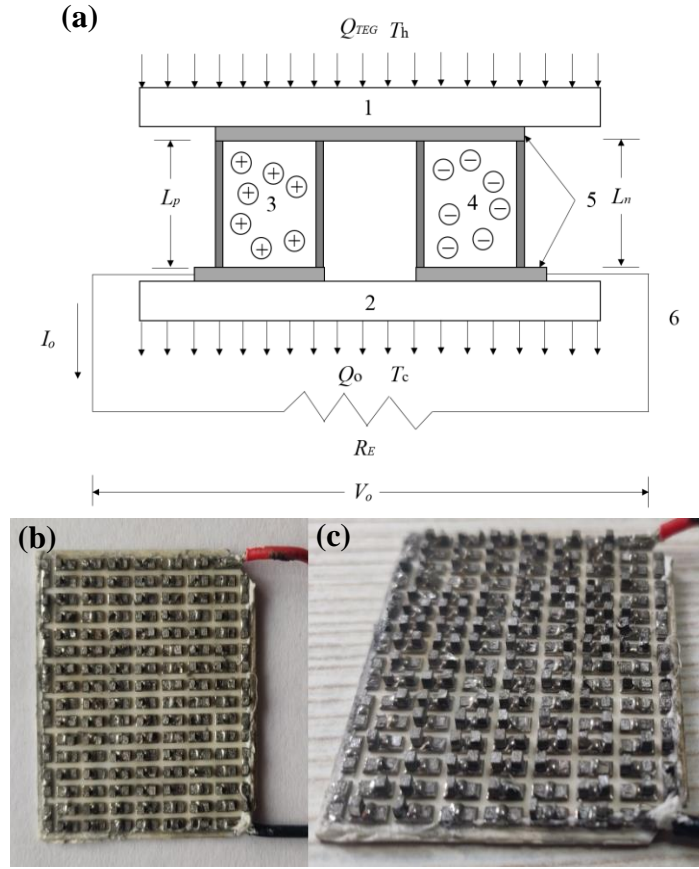
The condensed water at the internal surface of condenser section falls down and collected again inside the lower evaporator section of the thermosyphon as shown in [Figure 4.1.2](#). The loaded/output voltage as well as current are measured by applying a variable external load resistance (rheostat) in the circuit ([Figure 4.1.3](#)). The power generated from the *TEG* is used for charging a 12 V, 7 Ah *UPS* battery that stores the energy and can be used for further different applications.

4.1.3 Principle, specifications and performance parameters of thermoelectric generator

TEG are accomplished devices to directly transform heat energy into electrical energy through Seebeck effect and made up of two semiconductor materials. Therefore, the thermo-physical properties of semiconductor materials play a significant role in TEG-based electric power generation. Although, the maximum conversion efficiency is low (<10%) but the conversion efficiency and cost of TEG varies with type of materials used. Although a wide range of TEGs are available in the market, but Bi_2Te_3 made TEGs are preferred to use due to high performance, operating temperatures limit and low cost as suggested by many researchers [[Mamur et al. 2018](#)] and [[Pourkiaei et al. 2019](#)]. The working principle of a TEG is described in [section 1.6](#). Various parameters like Seebeck coefficients of p-type (α_p) and n-type (α_n) semiconductor materials, electrical resistivities of p-type (ρ_p) and n-type (ρ_n) semiconductor materials, thermal conductivities of p-type (k_p) and n-type (k_n) semiconductor materials and the number of series-connected couples in a TEG (n_{couples}) directly influence the power of a TEG module. [Figure 4.1.4](#) shows a schematic illustration of a TEG made up of “p” and “n”-types of semiconductor materials. In this study, TEGs used (Model No.: SP1848-27145, Size: 40 mm × 40 mm × 3.9 mm) are made of Bi_2Te_3 materials and their properties are provided in [Table 4.1.1](#).

Table 4.1.1: Properties of Bi_2Te_3 semiconductor materials used for TEGs

| α_p ($\mu\text{V/K}$) | α_n ($\mu\text{V/K}$) | ρ_p ($\mu\Omega\text{m}$) | ρ_n ($\mu\Omega\text{m}$) | k_p W/(m · K) | k_n W/(m · K) | R_T (Ω) | K_e (W/K) |
|-------------------------------------|-------------------------------------|---|-------------------------------------|-------------------------------------|-------------------------------------|---|----------------|
| [Kim et al. 2010] | [Yoo et al. 2005] | $\alpha_e \times 10^3$ ($\mu\text{V/K}$) | [Kim et al. 2010] | [Yoo et al. 2005] | [Kim et al. 2010] | [Takashiri et al. 2007] | |
| 140.0 | -188.5 | 41.1 | 6.0 | 29.5 | 6.0 | 1.3 | 0.8 |
| | | | | | | | 0.2 |



1 Hot side of TEG
2 Cold side of TEG
3 p-type semiconductor material
4 n-type semiconductor material
5 Electric conductive material
6 Output wire of TEG

Figure 4.1.4: (a) Schematic diagram of a TEG (b) top internal view and (c) side view of TEG used

The output power (P_o) generated from the TEG module is a function of the output voltage (V_o), output current (I_o) and the external load resistance in the circuit (R_E) and is calculated by Eq. (4.1.1), whereas, I_o in the circuit is computed by Eq. (4.1.2) [Karri 2011]. I_o depends upon the equivalent Seebeck coefficient (α_e), temperature gradient across TEG (ΔT_{TEG}), total internal electrical resistance for the TEG (R_T) and R_E .

$$P_o = V_o \times I_o = I_o^2 \times R_E = (\alpha_e \times \Delta T_{TEG} - I_o \times R_T) \times I_o \quad (4.1.1)$$

$$I_o = \frac{\alpha_e \times \Delta T_{TEG}}{R_T + R_E} \quad (4.1.2)$$

The equivalent Seebeck coefficient i.e. α_e is dependent upon α_p , α_n and $n_{couples}$ as given by Eq. (4.1.3) below [Karri 2011],

$$\alpha_e = n_{couples} \times (\alpha_p - \alpha_n) \quad (4.1.3)$$

The internal electric resistance i.e R_T is again a function of $n_{couples}$, ρ_p , ρ_n and aspect ratio (γ) as shown in Eq. (4.1.4) [Karri 2011 [188]],

$$R_T = n_{couples} \times \gamma \times (\rho_p + \rho_n) \quad (4.1.4)$$

where, γ is the ratio of vertical length (L_p or L_n) of semiconductor materials and its crosssectional area (A) i.e. $\gamma = \frac{L_p}{A} = \frac{L_n}{A}$. Next, the dimensionless figure of merit (ZT) is the one of the comprehensively accepted performance criteria of thermoelectric materials. It is described by α_e , R_T , equivalent thermal conductance (K_e) and the average temperature of cold and hot sides of TEG ($T_{Ch, avg.}$), i.e., [Karri 2011],

$$ZT = \frac{\alpha_e^2}{R_T + K_e} \times T_{Ch, avg.} \quad (4.1.5)$$

In Eq. (4.1.5), K_e is calculated as [Karri 2011],

$$K_e = \frac{n_{couples}}{\gamma} \times (k_p + k_n) \quad (4.1.6)$$

4.1.4 Results and discussion

In this study, electrical power is generated using TEGs-thermosyphon-based HRS by recovering the WH generated from the biomass engine that is run by purely syngas. The average (of 13 readings taken over 2 hours of each experiment) temperature of waste heat ($T_{WH, avg.}$) is first studied at various ERs to obtain its maximum value at an optimal ER. At an optimum ER, the transient variations of source water temperature (T_s) and sink water temperature (T_c) are analyzed to see the maximum T_s . Further, the highest value of maximum open circuit voltage ($V_{max.}$) is found at an optimum TFR by performing nine experiments at an optimum ER, maximum T_s and different TFR. At optimum ER and TFR, the variations of open circuit voltage (V), short circuit current (I_s) and ZT corresponding to ΔT_{TEG} (obtained at various time period) are then studied. Corresponding to a maximum value of ΔT_{TEG} (got at the highest T_s), P_o is analyzed and at the end the conversion efficiency of TEG (η_{TEG}) is examined at various hot side temperature of TEG (T_h). The attempt is

made to store the generated P_o in a 12 V, 7 Ah UPS battery for real life applications. Finally, the experimental results are compared with a theoretical thermal resistance network model. The average value (of a parameter) taken over three replicates of each experiment are presented in all plots.

4.1.4.1 Variations of average waste heat temperature

An engine-generator driven by purely syngas (generated from biomass gasification) is used to produce primary electrical power. From thermodynamics point of view, even under ideal conditions, an engine can't convert the total thermal energy of syngas into useful work. As pointed out earlier, that in practice, approximately 60-70% of the available thermal energy at reasonably high temperatures (550 K-950 K) is lost in the form of WH and coolant [Skogtjarn 2002] and [Jadhao and Thombare 2013]. Recovering this WH into useful power generation using TEGs-based HRS serves as the motivation for this work. Figure 4.1.5 shows the variation of $T_{WH, avg.}$ at various ER ranging from 0.239 to 0.352. The maximum value of $T_{WH, avg.}$ is found as 283 °C at optimum ER of 0.305. This high temperature WH possesses sufficient energy for TEG-based power generation. The energy content (i.e., CV) of syngas directly affects the combustion temperature of engine as more CV creates high temperature in the engine. The syngas produced during the initial stages of ER has low CV and gradually increases to a maximum at the optimum ER. Beyond this, the CV of syngas again decreases. For a particular designed gasifier, the syngas produced is always of the highest CV at an optimal ER that favours the optimum combustion of air-fuel mixture which consequently results in the highest possible temperature of WH.

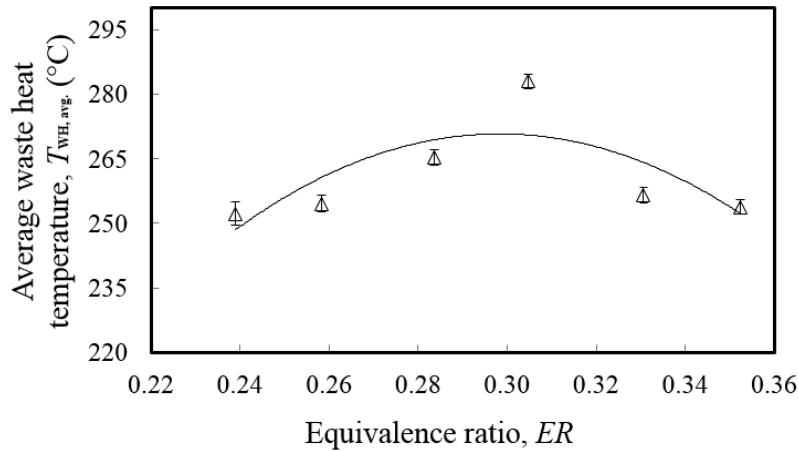


Figure 4.1.5: Profile of average waste heat temperature at various ER

4.1.4.2 Variation of source and sink temperatures

WH exiting the engine heats a metallic plate, and ideally to utilize the maximum available energy, the evaporator of thermosyphon should be affixed to it. However, there are practical limitations due to vibration suffered by the plate. Additionally, to maintain the other end of TEGs under cold condition, water cooling is necessary. Therefore, source and sink containers are respectively used to minimize the vibration and provide better cooling with respect to air. However, due to irreversibility, less temperature will be available for boiling the working fluid inside the thermosyphon. T_s is the temperature of hot water contained inside the source container (i.e., lower container), whereas T_c is the cold water temperature contained within the sink container (i.e., the upper container). The distilled water contained within the thermosyphon is heated by hot (source) water whereas the heat rejected by the water vapor is released to the cold (sink) water. Figure 4.1.6 shows the variation of T_s and T_c with time (t) for both thermosyphons. As highlighted, at an optimum ER, the maximum $T_{s,1}$ and $T_{s,2}$ (here subscripts 1 and 2 are correspond to source container 1 and 2, respectively) are found as 87 °C and 77 °C, respectively. Since, the source container 1 is located closer to the engine exhaust port than the source container 2, therefore more heat is transferred to source container 1 compared container 2. Initially $T_{s,1}$ and $T_{s,2}$ are low and they increase with t upto a certain period and thereafter almost remain constant at the end. This is because after a definite period of time, the rate of heat addition to the source water becomes almost equal to the heat lost from the surface of source hot water to the working fluid. However, both $T_{c,1}$ and $T_{c,2}$ remain almost constant with t because cooling tower yields a fixed temperature at its outlet.

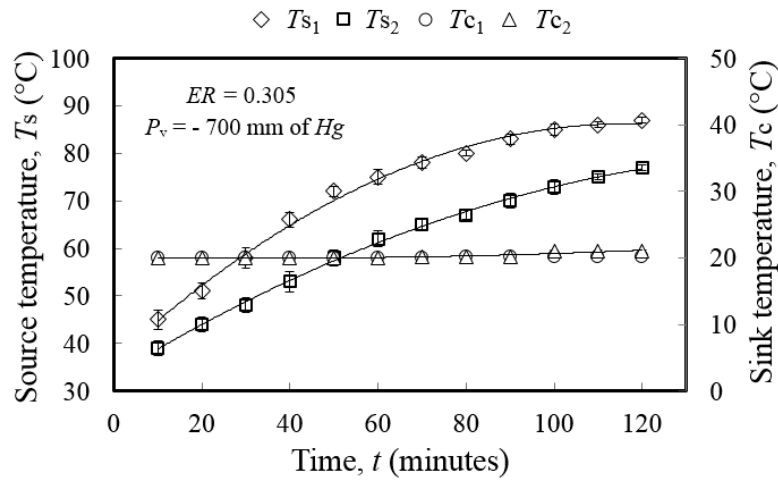


Figure 4.1.6: Transient variation of source and sink temperatures

4.1.4.3 Maximum open circuit voltage

The $V_{\max,1}$ and $V_{\max,2}$ (here subscripts 1 and 2 are correspond to thermosyphons 1 and 2, respectively) obtained at various TFR and an optimum ER are studied in Figure 4.1.7. It has been envisioned that with increase in TFR, $V_{\max,1}$ and $V_{\max,2}$ also increase which reach maximum at optimum TFR (0.496 for both thermosyphons). Beyond the optimum level, further increase in TFR decreases the $V_{\max,1}$ and $V_{\max,2}$. This is due to the reason that when TFR is gradually increased, more heat transfer occurs between the source tank and the working fluid at evaporator section. Consequently, there is more heat transfer at the condensing section and more wall temperature attached at the hot side of TEGs. However, beyond a particular limit, thick liquid film is formed that offers thermal resistance to the heat transport, thereby reducing the temperature difference between the two ends of TEG. The largest values of $V_{\max,1}$ and $V_{\max,2}$ are obtained as 17.12 V and 14.40 V respectively, which yields a total of 31.52 V. Under the same vacuum pressure (P_v) and an optimum TFR, thermosyphon 1 produces more V_{\max} that of thermosyphon 2. This is because, the source container of thermosyphon 1 contains water at a higher temperature (87 °C) because it is attached close to the exit port of engine whereas the same for thermosyphon 2 is at a low temperature (77° C). Therefore, more heat is transferred to the hot side of TEG when using thermosyphon 1 that leads to a higher value of maximum ΔT_{TEG} ($\Delta T_{\text{TEG, max.}} = 39$ °C) than thermosyphon 2 ($\Delta T_{\text{TEG, max.}} = 31$ °C).

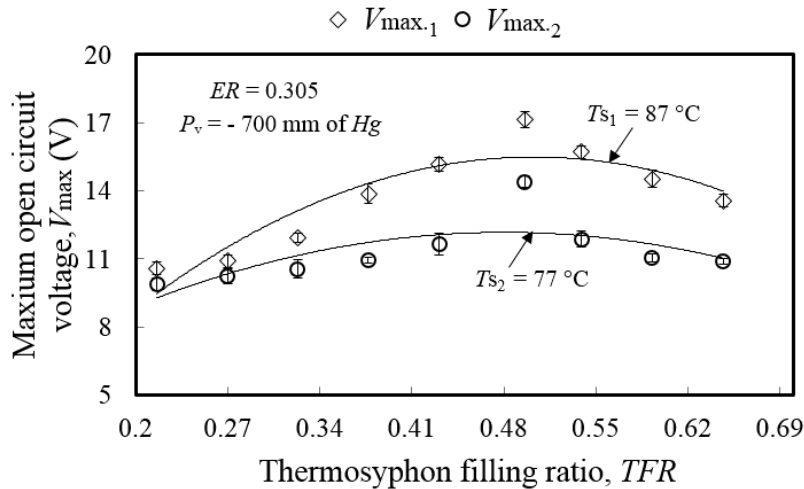


Figure 4.1.7: Variation of maximum open circuit voltage obtained at various TFR for thermosyphon 1 and 2

4.1.4.4 Variation of open circuit voltage and short circuit current

V is the maximum voltage obtained at zero current flow condition, whereas, I_s is the maximum current flow inside the circuit when voltage across the resistance is zero. The variation of V and I_s with ΔT_{TEG} is studied in Figure 4.1.8. The analysis has been done for the optimum TFR ($= 0.496$). It is revealed from the figure that V always increases with increase in ΔT_{TEG} . Since, the cold surface of TEGs is in direct contact with the sink water, therefore the temperature of cold water is considered equivalent to T_c whereas T_h nearly equals to the outer surface temperature at condenser section. As discussed above, T_c remains almost constant, therefore ΔT_{TEG} is invariably proportional to T_h . From this study, V_{max} , observed from thermosyphons 1 and 2 are 17.12 V (at maximum $\Delta T_{\text{TEG},1} = 39^\circ\text{C}$) and 14.40 V (at maximum $\Delta T_{\text{TEG},2} = 31^\circ\text{C}$) respectively. The maximum values of I_s (or $I_{s, \text{max}}$) obtained corresponding to 17.12 V and 14.40 V are 0.152 A and 0.127 A respectively.

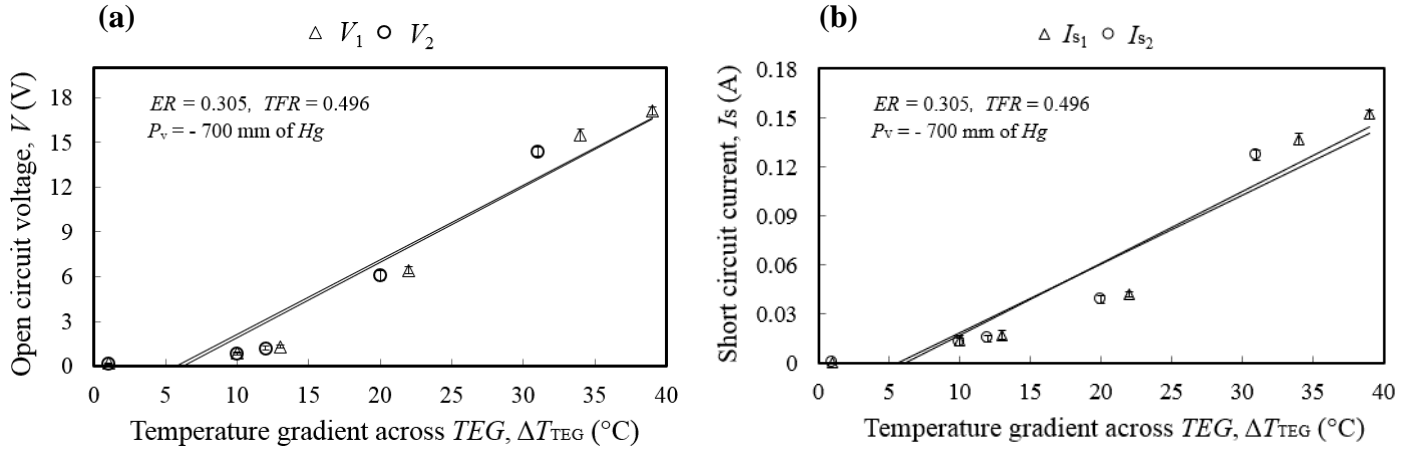


Figure 4.1.8: Variation of V and I_s for thermosyphons (a) 1 and (b) 2

4.1.4.5 Variation of power output and conversion efficiency of TEG

Figure 4.1.9 shows the variation of $P_o (= V_o \times I_o)$ and I_o for thermosyphon 1 and 2 at the optimum ER (0.305) and TFR (0.496). As discussed above, the highest values of $V_{\text{max},1}$ and $V_{\text{max},2}$ are found at the optimum value of TFR. Therefore, under similar conditions of T_c and P_v in both thermosyphons, the power generated from the TEG is governed only by ΔT_{TEG} . The profiles of P_o as shown in Figure 4.1.9 are obtained by varying the external load resistance (used rheostat) and meanwhile V_o as well as I_o being noted by voltmeter and ammeter respectively. For thermosyphon

1, maximum P_o (or $P_{o, \max.}$) is obtained as 0.615 W at 7.98 V of V_o and 0.077 A of I_o when $\Delta T_{\text{TEG},1}$ was maintained at 39 °C as shown in Figure 4.1.9a. Similarly for thermosyphon 2, maximum P_o is found as 0.418 W at 6.33 V of V_o and 0.066 A of I_o when $\Delta T_{\text{TEG},2} = 31$ °C as revealed in Figure 4.1.9b. For both thermosyphons, I_o linearly decreases with increase in the external load resistance. η_{TEG} is the ratio of P_o and the rate of heat energy supplied to TEG (\dot{Q}_{TEG}). Figure 4.1.10 shows the variation of η_{TEG} with T_h . Since T_c remains almost invariant with t , therefore η_{TEG} is mainly governed by T_s and T_h . As expected, η_{TEG} proportionally increases with increase in T_h for both thermosyphons. The maximum values of η_{TEG} (or $\eta_{\text{TEG}, \max.}$) corresponding to thermosyphon 1 and 2 are found as 2.218 % at $T_{h,1} = 59$ °C and 1.472 % at $T_{h,2} = 52$ °C respectively. Although η_{TEG} is low but generating continuous power from TEGs by recovering the WH can be an environment friendly and cost-effective alternative.

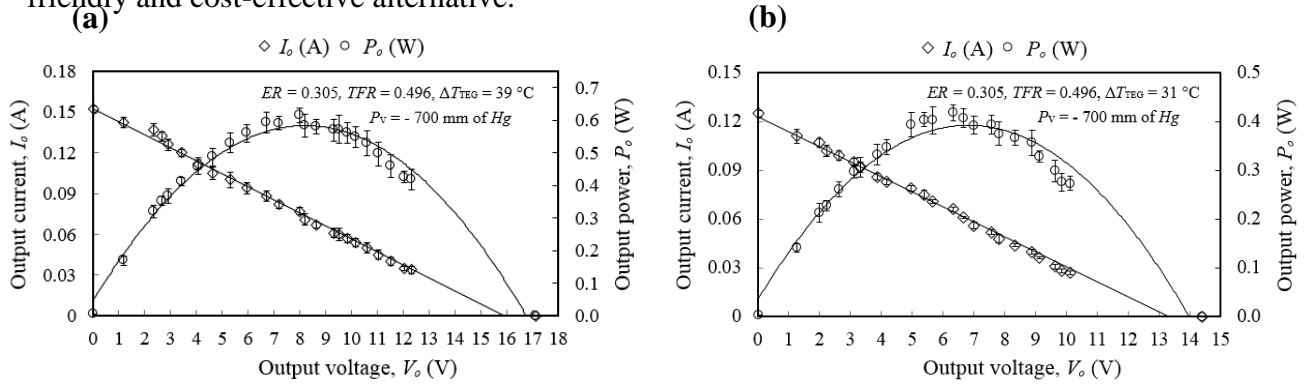


Figure 4.1.9: Variation of output current and power for thermosyphons (a) 1 and (b) 2

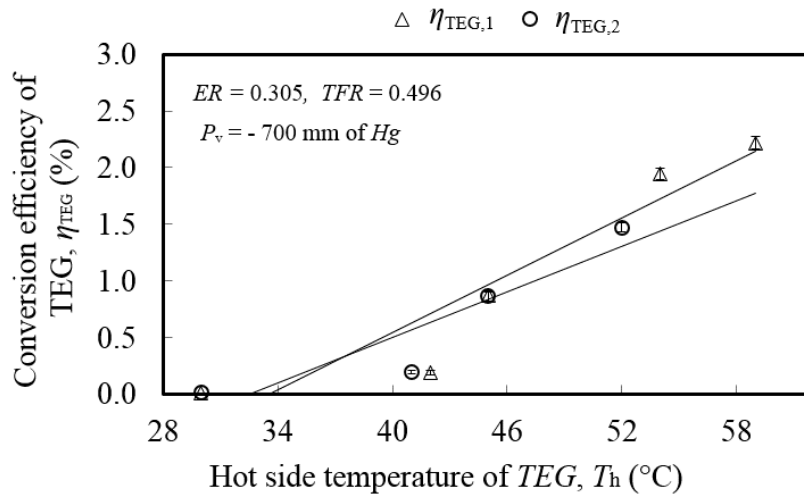


Figure 4.1.10: Variation of heat conversion efficiency with T_h

4.1.4.6 Variations of dimensionless figure of merit

ZT is the design criteria for thermoelectric materials and the variations of ZT with ΔT_{TEG} is shown in Figure 4.1.11. It has been found that ZT increases linearly with ΔT_{TEG} and the maximum values of ZT for thermosyphons 1 and 2 are calculated as 0.456 and 0.451 corresponding to ΔT_{TEG} of 39 °C and 31 °C respectively. To obtain a high η_{TEG} , the high value of ZT is required. For the temperature range studied here, material properties are considered independent of temperature therefore the value of Z also remains constant over the studied values of ΔT_{TEG} . However, to attain high η_{TEG} , the thermoelectric material should have high value of α_e with low values of R_T and K_e . Due to this reason, to derive maximum η_{TEG} , the TEG should be operated at the maximum available ΔT_{TEG} . It is highlighted from the this study that when T_h increases from 45 °C ($\Delta T_{\text{TEG},1} = 25$ °C) to 59 °C (maximum $\Delta T_{\text{TEG},1} = 39$ °C) with T_c remaining nearly at a constant value (20-21 °C), η_{TEG} increases from 0.867% to 2.218% (Figure 4.1.10). The increase in ZT with ΔT in Figure 4.1.11 is mainly attributed to increase in T_h at the condenser section.

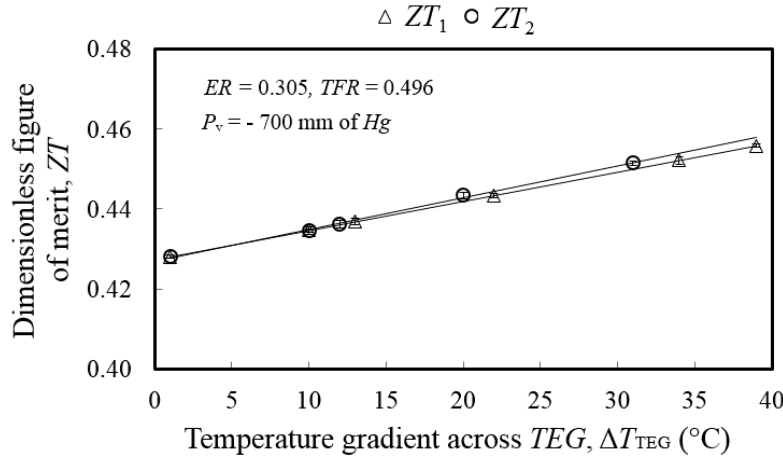


Figure 4.1.11: Variation of dimensionless figure of merit with ΔT_{TEG}

4.1.4.7 Charging of a 12 V, 7 Ah UPS battery

The power generated from TEG has been utilized for charging a 12 V, 7 Ah UPS battery. The circuit as shown in Figure 4.1.3 is used for charging the battery where rheostat was replaced by a UPS battery. Before charging the battery, V from the UPS battery was measured through voltmeter and found 10.21 V. While charging the UPS battery, the flow of current in the circuit starts when

I_s reaches upto a certain value of 0.118 A and V of 13.54 V (at this point $V_o = 12.00$ V and $I_o = 0.001$ A). After charging the battery for 20 minutes under I_s of 0.152 A and V of 17.12 V (at this point $V_o = 12.65$ V and $I_o = 0.035$ A), V is again measured and obtained 12.31 V that shows the fully charged condition of battery. The suitable value of V and minimum I_s required for charging a 12 V, 7 Ah UPS battery are found to be 14-17 V and 0.118 A respectively. As the current increases above the given value, the rate of charging is found to increase. Therefore P_o from the TEG can be stored in a battery which can be used for further various applications such as providing the backup power to computer system, lighting in remote areas as shown in [Figure 4.1.12](#).



Figure 4.1.12: Real life use of fully charged UPS battery for various applications

4.1.4.8 Comparison of theoretical and experimental parameters

During the transfer of heat from source water to hot side of TEGs, various thermal resistances are involved which offer restriction to the heat flow. It is assumed that source water is well-mixed and holds constant temperature throughout. Since source water is stationary, thus convective resistance offered by source water layer on thermosyphon surface at the evaporator section can be neglected. Thus, at the evaporator section, the thermal resistances consist of thermosyphon wall conduction resistance ($R_{t, w, \text{evap.}}$), pool ($R_{t, pb, \text{evap.}}$) and film boiling ($R_{t, fb, \text{evap.}}$) resistances as presented in Eq. [4.1.7(a-c)] whereas in the condenser section, resistance is offered by film condensation ($R_{t, fc, \text{cond.}}$) along with thermosyphon wall conduction ($R_{t, w, \text{cond.}}$) as revealed in Eq. [4.1.7(d, e)] [Kumar et al. 2018] and [Tundee et al. 2014],

$$R_{t, w, \text{evap.}} = \frac{\delta_{\text{cop.}}}{k_{\text{cop.}} \times A_{s, \text{evap.}}} \quad (4.1.7a)$$

where $A_{s, \text{evap.}} = 8 \times a \times L_{\text{evap.}}$

$$R_{t, pb, \text{evap.}} = \frac{1}{Z_{pb} \times g^{(1/5)} \times \dot{Q}_{\text{evap.}}^{(2/5)} \times (A_{s, \text{evap.}})^{(3/5)}} \quad (4.1.7b)$$

$$\text{where, } Z_{pb} = 0.325 \times \left| \frac{\rho_{wf, l}^{(1/2)} \times k_{wf, l}^{(3/10)} \times c_{wf, l}^{(7/10)}}{\rho_{wf, v}^{(1/4)} \times h_{fg, wf}^{(2/5)} \times \mu_{wf, l}^{(1/10)}} \right| \times \left| \frac{p_{\text{vap.}}}{p_{\text{atm.}}} \right|^{(23/100)},$$

$$\dot{Q}_{\text{evap.}} = A_{s, \text{evap.}} \times \left| \frac{\dot{Q}_{\text{cont.}}}{A_{\text{cont.}}} \right|, \quad A_{\text{cont.}} = \frac{\pi}{4} \times |D_{\text{cont.}}|^2, \quad \dot{Q}_{\text{cont.}} = m_s \times c_{\text{water}} \times \left. \frac{dT}{dt} \right|_{\text{Source water}}$$

$$R_{t, fb, \text{evap.}} = \frac{0.235 \times \dot{Q}_{\text{evap.}}^{(1/3)}}{Z_{fb}^{(4/3)} \times g^{(1/3)} \times D_e^{(4/3)} \times L_{\text{evap.}}} \quad (4.1.7c)$$

$$\text{where, } Z_{fb} = \left| \frac{L_{\text{cond.}} \times \rho_{wf, l}^{(2)} \times k_{wf, l}^{(3)}}{\mu_{wf, l}} \right|^{1/4}, \quad D_e = \left| \frac{8 \times a}{\pi} \right|$$

if, $R_{t, pb, \text{evap.}} > R_{t, fb, \text{evap.}}$, then $R_{t, \text{max}} = R_{t, pb, \text{evap.}}$

else, $R_{t, \text{max}} = TFR \times R_{t, pb, \text{evap.}} + |1 - TFR| \times R_{t, fb, \text{evap.}}$

$$R_{t, fc, \text{cond.}} = \frac{0.235 \times \dot{Q}_{\text{evap.}}^{(1/3)}}{Z_{fb}^{(4/3)} \times g^{(1/3)} \times D_e^{(4/3)} \times L_{\text{cond.}}} \quad (4.1.7d)$$

$$R_{t,w,cond.} = \frac{\delta_{cop.}}{k_{cop.} \times (A_{s,cond.})} \quad (4.1.7e)$$

where $A_{s,cond.} = 8 \times a \times L_{cond.}$

The equivalent thermal resistance ($R_{t,e}$) between heat source and hot side of TEGs is then calculated by the following expression,

$$R_{t,e} = R_{t,w,evap.} + R_{t,max.} + R_{t,fc,cond.} + R_{t,w,cond.} \quad (4.1.8)$$

Various properties of working fluid can be obtained from the literature [Fadhil 2015]. While computing the thermal resistance, interfacial resistances between vapour-liquid at evaporator and condenser sections are considered negligible [Kumar et al. 2018] and [Tundee et al. 2014]. In the mathematical model, the maximum ΔT_{TEG} is obtained using Eq. (4.1.9) [Kumar et al. 2018] and [Tundee et al. 2014],

$$\text{Maximum } \Delta T_{TEG} = |\text{maximum of } T_s - T_c| - \dot{Q}_{evap.} \times R_{t,e} \quad (4.1.9)$$

For both thermosyphons (1 and 2), a study is made in Figure 4.1.13 to compare the model and experimental values of maximum ΔT_{TEG} at different values of TFR. It has been envisaged that at the optimum TFR, maximum ΔT_{TEG} for thermosyphon 1 and 2 are found as 40.12 °C and 32.38 °C respectively by the resistance model whereas the same are obtained as 39 °C and 31 °C from the experiments. The relative error is also studied in the same figure and it is defined as the ratio of absolute error (the difference between model and experiment values) to the model value as reported by [Chen et al. 2010], i.e.

$$\text{Absolute error} = |\text{Model value} - \text{Experiment value}| \quad (4.1.10a)$$

$$\text{Relative error} = \frac{\text{Absolute error}}{\text{Model value}} \quad (4.1.10b)$$

The maximum and minimum relative errors in maximum ΔT_{TEG} are found as 14.91% and 2.79 % respectively. In Table 4.1.2, a comparative assessment of the present V obtained with a single TEG per unit ΔT_{TEG} is done against other published literatures. The reported studies [Nuwayhid et al. 2005], [Singh et al. 2011], [Tundee et al. 2014], [Singh et al. 2012], [Deng et al. 2013] and [Singh et al. 2012] considered different quantities of TEGs powered through different heat sources, thereby leading to different voltages. For instance, woodstove and electrical heater simulating a

SGSP were employed in [Nuwayhid et al. 2005] and [Singh et al. 2011] respectively. Electrical heating was also considered in [Singh et al. 2012] and [Singh et al. 2012] whereas a solar thermal collector was used in [Deng et al. 2013]. It is apparent from the comparison that this TEGs-thermosyphon-based HRS utilizing WH of a biomass engine performs in accordance with the other systems.

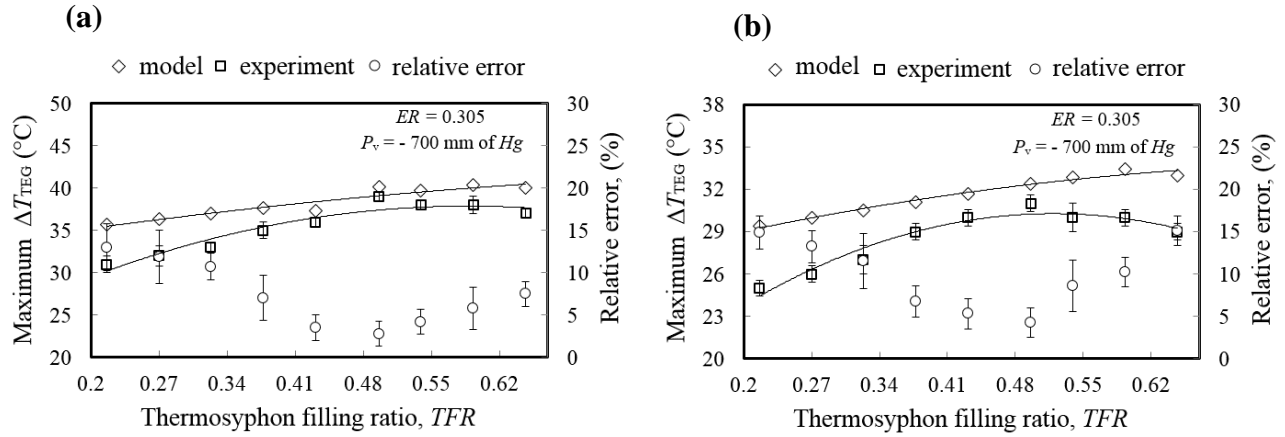


Figure 4.1.13: Comparison of model and experiment results for thermosyphons (a) 1 and (b) 2

Table 4.1.2: Comparison of V per ΔT_{TEG} for one TEG with the previous published literature

| Parameter | Present work | Nuwayhid et al. 2005 | Singh et al. 2011 | Tundee et al. 2014 | Singh et al. 2012 | Deng et al. 2013 | Singh et al. 2012 |
|-------------------------------|--------------------|----------------------|--------------------|--------------------|--------------------|--------------------|--------------------|
| $V/\Delta T_{TEG}/TEG$ (V/°C) | 2×10^{-2} | 4×10^{-2} | 6×10^{-2} | 2×10^{-2} | 2×10^{-2} | 3×10^{-2} | 2×10^{-2} |

4.1.4.9 Uncertainty analysis

The sensitivities associated with the multimeter for measuring the voltage and current are 0.001 V and 0.001 A respectively. Temperatures are measured by K-type thermocouples with sensitivity of 1 °C. The uncertainties associated with various parameters are calculated as described in section 3.1.4.6 and are shown in Table 4.1.3.

Table 4.1.3: Uncertainty analysis of various parameters

| ER = 0.305, TFR = 0.496, $P_v = -700$ mm of Hg | | | | | | | | | |
|--|---|---|---|---|---|---|---|------------------------------|------------------------------|
| | T_{WH} | $T_{S,1}$ | $T_{S,2}$ | $T_{C,1}$ | $T_{C,2}$ | $T_{h,1}$ | $T_{h,2}$ | V_1 | V_2 |
| Absolute | $6 \times 10^{-2} \text{ }^\circ\text{C}$ | $8 \times 10^{-2} \text{ }^\circ\text{C}$ | $8 \times 10^{-2} \text{ }^\circ\text{C}$ | $8 \times 10^{-2} \text{ }^\circ\text{C}$ | $8 \times 10^{-2} \text{ }^\circ\text{C}$ | $1 \times 10^{-1} \text{ }^\circ\text{C}$ | $1 \times 10^{-1} \text{ }^\circ\text{C}$ | $1 \times 10^{-4} \text{ V}$ | $1 \times 10^{-4} \text{ V}$ |
| Relative | 2×10^{-4} | 1×10^{-3} | 1×10^{-3} | 4×10^{-3} | 4×10^{-3} | 3×10^{-3} | 4×10^{-3} | 2×10^{-5} | 3×10^{-5} |
| ER = 0.305, TFR = 0.496, $T_{h,max,1} = 59.0 \pm 0.3 \text{ }^\circ\text{C}$, $T_{C,1} = 20.0 \pm 0.3 \text{ }^\circ\text{C}$, $T_{h,max,2} = 52 \pm 0.3 \text{ }^\circ\text{C}$, $T_{C,2} = 21.0 \pm 0.3 \text{ }^\circ\text{C}$, $P_v = -700$ mm of Hg | | | | | | | | | |
| | $V_{max,1}$ | $V_{max,2}$ | $I_{o,max,1}$ | $I_{o,max,2}$ | $P_{o,max,1}$ | $P_{o,max,2}$ | $\eta_{TEG, max,1}$ | $\eta_{TEG, max,2}$ | |
| Absolute | $3 \times 10^{-4} \text{ V}$ | $3 \times 10^{-4} \text{ V}$ | $3 \times 10^{-4} \text{ A}$ | $3 \times 10^{-4} \text{ A}$ | $2 \times 10^{-3} \text{ W}$ | $2 \times 10^{-3} \text{ W}$ | $2 \times 10^{-2} \%$ | $2 \times 10^{-2} \%$ | |
| Relative | 2×10^{-5} | 2×10^{-5} | 2×10^{-3} | 2×10^{-3} | 4×10^{-3} | 4×10^{-3} | 9×10^{-3} | 1×10^{-2} | |
| ER = 0.305, TFR = 0.496, $T_{h,max,1} = 59.0 \pm 0.3 \text{ }^\circ\text{C}$, $T_{C,1} = 20.0 \pm 0.3 \text{ }^\circ\text{C}$, $T_{h,max,2} = 52 \pm 0.3 \text{ }^\circ\text{C}$, $T_{C,2} = 21.0 \pm 0.3 \text{ }^\circ\text{C}$, $P_v = -700$ mm of Hg | | | | | | | | | |
| | $V_{o,1}$ | $V_{o,2}$ | $I_{o,1}$ | $I_{o,2}$ | $P_{o,1}$ | | $P_{o,2}$ | | |
| Absolute | $6 \times 10^{-5} \text{ V}$ | $6 \times 10^{-5} \text{ V}$ | $6 \times 10^{-5} \text{ A}$ | $6 \times 10^{-5} \text{ A}$ | $2 \times 10^{-7} \text{ W}$ | | $1 \times 10^{-7} \text{ W}$ | | |
| Relative | 8×10^{-6} | 1×10^{-5} | 7×10^{-4} | 9×10^{-4} | 5×10^{-7} | | 5×10^{-7} | | |

*max.: specifies the maximum value of a parameter

4.1.5 Summary

The WH of biomass driven engine-generator has been recovered by using the TEGs-thermosyphon-based HRS for power generation and the following key findings are highlighted,

- An optimum ER of gasifier resulting in highest possible T_s is found to be 0.305 whereas the optimum TFR of thermosyphon is obtained as 0.496. At low TFR, the formation of vapour is less whereas at high TFR, liquid film formation is more. Both these phenomena affect the power generation from the TEG system. The performance of TEGs-thermosyphon-based HRS is found maximum at the optimum values of ER and TFR.
- $T_{WH, avg.}$ varies in the range 252-283 °C. However the maximum T_s is found as 87 °C for thermosyphons 1 and 77 °C for thermosyphons 2. The corresponding maximum ΔT_{TEG} in thermosyphon 1 and 2 are found as 39 °C and 31 °C respectively.
- With respect to maximum ΔT_{TEG} , thermosyphon 1 and 2 have produced a maximum $V (I_s)$ of 17.12 V (0.152 A) and 14.40 V (0.127 A) respectively. The corresponding maximum $P_o (\eta_{TEG})$ are measured as 0.615 W (2.218%) and 0.418 W (1.472%) respectively. ZT always increases nearly in a direct proportion to ΔT_{TEG} and found its maximum values of 0.456 and 0.451 for thermosyphon 1 and 2 respectively.
- The minimum I_s required for charging a 12 V, 7 Ah UPS battery is found as 0.118 A. Under the optimized condition, the time taken by battery to charge it is found as 20 minutes.
- The values of maximum ΔT_{TEG} obtained from thermal resistance network model are found as 40.12 °C (thermosyphon 1) and 32.38 °C (thermosyphon 2). However the same as obtained from experiments are 39 °C (thermosyphon 1) and 31 °C (thermosyphon 2). The maximum relative error between model and experimental values is found as 14.91 %.

It is observed that TEGs-thermosyphon-based HRS uses only a small portion of WH zone and major portion of it gets bypassed. Therefore, a heat storage device (with several turns) is suitable for efficiently storing WH and it was found that a SGSP can play the same role with many favorable characteristics. Since, it can store the solar energy also along with the WH, therefore, performance of HRS has been analyzed using both energy source (solar energy and WH).

4.2 TEGs-thermosyphon-based HRS operated by the stored energy of SGSP

It is well-known that SGSP can be eminently used as a heat source for the generation of electric power [Singh et al. 2011] and [Tchanche et al. 2011]. To utilize the stored heat of SGSP, two same

structure TEGs-thermosyphon-based HRSs have been actually installed. The evaluation of thermal and electrical performance parameters such as temperature, thermal conductivity, specific heat, density, electrical conductivity (EC) and total dissolved solids (TDS) can provide useful insights related to such systems. Additionally, the determination of salinity and TDS is useful for desalination applications using the SGSP [Lu et al. 2001]. Furthermore the assessment of EC is important in manufacturing processes based on brine-based electrolyte [Bhattacharyya et al. 2002]. Based on the aforesaid reasons, a study is carried out for the analysis of physics associated with the various parameters in a SGSP before installing the HRSs.

4.2.1 Investigation of thermal and electrical performance in a SGSP

4.2.1.1 Experimental setup

For this analysis, an SGSP of trapezoidal shape (Figure 4.2.1) has been fabricated with dimensions $1 \times 1 \text{ m}^2$ at its bottom surface and $2 \times 2 \text{ m}^2$ at the top with 1 m of total height. The internal surface area of SGSP is covered with black colored Ethylene Propylene Diene Monomer (EPDM) that acts as a absorber of solar thermal radiation and provides insulation to heat loss [Fathurrohman et al. 2015]. As the thermal conductivity of glass wool is very low, the outer surface area is covered with glass wool to make it perfectly insulated and reduces further the heat loss from SGSP. Solar thermal energy is stored inside bottom LCZ as a sensible heat, whereas NCZ acts as a heat insulator and UCZ remains cool. Therefore, a perfect salinity gradient or halocline within the NCZ plays a key role to increase the heat storage capacity of LCZ. These layers are made by using a water diffuser. Salt concentration (SC) in LCZ under saturated condition is measured as 20.04% by weight. In this SGSP, NCZ contains eight layers with continuously reducing SC from bottom to top layer. UCZ contains normal water having very low SC (0.38%). Since the heat loss by convection largely affects the heat storage capacity of LCZ, thus the present SGSP has been covered with glass (fixed with the steel structure) at the top in order to prevent heat loss during night. Additionally, the glass cover permits smooth operation of SGSP without disturbing NCZ during rainy season. A high-quality reflector is used to increase the temperature of LCZ. National Instruments based data acquisition system (DAQ) and well calibrated K-type thermocouples are used to measure the temperatures across three zones of SGSP. A total of fourteen thermocouples (out of which, eight were inserted into NCZ and three each were located inside UCZ and LCZ) were placed into the SGSP. SC, EC and TDS are measured by a Salinometer (Horiba made Model

No.: LAQUAAactEC120) whereas the intensity of solar radiation is measured by a solar radiation pyranometer (Sivara Systems and Solutions made Model No.: PYRA300). Based on these data, thermal conductivity, density and specific heat are implicitly determined from the appropriate expressions. The experiments are conducted during the period of August-September 2018 for 28 days at Indian Institute of Technology, Rupnagar (30.97°N, 76.53°E), Punjab.

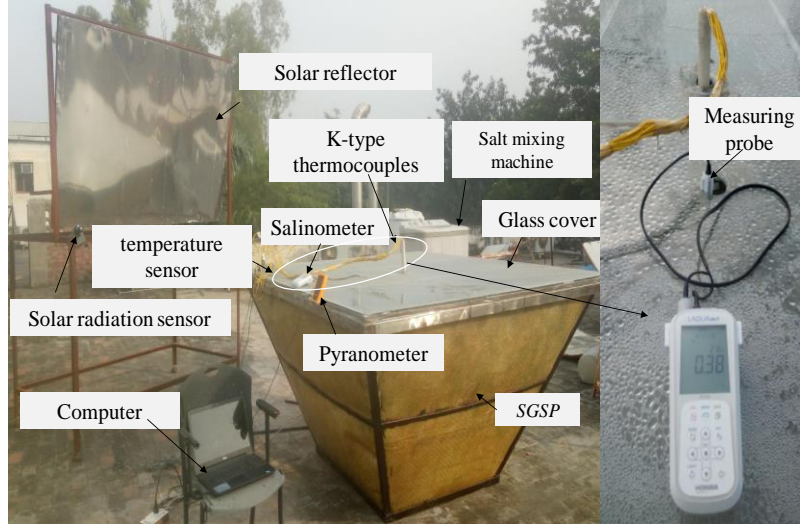


Figure 4.2.1: Experimental setup details of a SGSP

The thermocouples are calibrated by using a reference thermometer (used mercury thermometer) through following procedure [Sarbu and Beniuga 2018]. Initially, the reference thermometer and thermocouples to be calibrated are placed at ice point as well as boiling point of water and allowed to stabilize at the desired temperature (i.e., 0 ± 1 °C for ice point and 100 ± 1 °C for boiling point) for a sufficient period of time of approximately 15-20 minutes. This process is repeated for 3 times and the final recorded readings of thermocouple are found to be 1 °C for ice point and 99 °C for boiling point. The pyranometer is calibrated at the factory by using a reference instrument (pyrheliometer) for the measurement [Forgan 1996]. For this, the surface of sensor is cleaned using a soft cloth and a cleaning solution to remove any dirt or debris. Then, it is placed in a location that receives direct sunlight with no obstructions and the output (637 W/m^2) of pyranometer is recorded. Further, the solar radiation at same location is measured using the reference instrument, i.e., pyrheliometer. The output of pyranometer is found to be almost same as that of reference instrument.

4.2.1.2 Calculation of thermal efficiency and various parameters of SGSP

At first, the thermal efficiency of SGSP (η_{SGSP}) is computed as expressed below,

$$\eta_{SGSP} = \frac{Q_{LCZ} \text{ (J)}}{S_{T,avg.} A_{t,SGSP} \text{ (W)} \times \text{time of exposure (s)}} \quad (4.2.1)$$

where, $S_{T, avg.}$ (W/m^2) is the average of total solar radiation incident on the surface of SGSP over the exposure time period, $A_{t, SGSP}$ (m^2) is the top area of SGSP and Q_{LCZ} is the stored heat in LCZ which is calculated in the following manner,

$$Q_{LCZ} = (A_{s, LCZ} \times H_{LCZ} \times \rho_{LCZ}) \times c_{LCZ} \times \Delta T_{LCZ} \quad (4.2.2)$$

where, c_{LCZ} ($\text{J/(kg}\cdot\text{K)}$) and ρ_{LCZ} (kg/m^3) represent the specific heat and density of LCZ water respectively, H_{LCZ} ($= 0.25 \text{ m}$) indicates the height of LCZ, ΔT_{LCZ} is the temperature gain within LCZ (or the difference between final and initial temperatures of LCZ) and $A_{s, LCZ}$ (m^2) denotes the total surface area of LCZ evaluated as given below,

$$A_{s, LCZ} = 4 \times \left[2 \times \left(\frac{1}{2} \times H_{LCZ} \right) + A_{b, LCZ} \times H_{LCZ} \right] \quad (4.2.3)$$

where, $A_{b, LCZ}$ (m^2) is the bottom area of LCZ. Based on the data collected under the present set of experimental conditions, η_{SGSP} is calculated 6.06%. For the same $A_{t, SGSP}$ of 4 m^2 , this value is somewhat lesser than 10% as determined in the literature [Jaefarzadeh 2006]. The reason may be due to the solar radiation available along with some rainy days occurring during the month of September. Next, the density of salt water (ρ_{sw}) at various points in the SGSP is computed in the following manner [Perry 2016],

$$\rho_{sw} = \frac{SC \times \rho_{salt} + (100 - SC) \times \rho_{water}}{100} \quad (4.2.4)$$

where, ρ_{salt} (2170 kg/m^3) and ρ_{water} (1000 kg/m^3) [Perry 2016] represent the density of salt and pure water respectively. As mentioned above, SC is determined using a Salinometer but it measures the salinity upto a maximum of 10%. So, for measuring the higher values of SC beyond its limit, a dilution method is used as elaborated further. First a 5 ml sample is taken out from any point of measurement in SGSP and diluted with 95 ml of distilled water. Thereafter, the obtained salinity value (shown by salinometer) of diluted solution is multiplied by a factor of 20 to determine the corresponding SC of sample taken from SGSP. Finally, the thermal conductivity of salt water (k_{sw}) is related to the density according to the following relationship [Ozbek and Phillips 1979],

$$k_{SW} = k_{water} \times \frac{c_{SW}}{c_{water}} \times \left(\frac{\rho_{SW}}{\rho_{water}} \right)^{4/3} \times \left(\frac{M_{water}}{M_{SW}} \right)^{1/3} \quad (4.2.5)$$

where, k_{water} (0.617 W/m·K), c_{water} (4186 J/kg·K) and M_{water} (0.018 kg/mol) denote the thermal conductivity, specific heat and molecular mass/weight of pure water respectively whereas c_{SW} and M_{SW} (0.0584 kg/mol) [Myerson 2002] indicate the specific heat and molecular mass/weight of salt water respectively. In Eq. (4.2.5), c_{SW} at various measurement points in the SGSP is calculated based on its linear relationship with salinity as indicated below,

$$\frac{c_{water} - 4186}{3160 - 4186} = \frac{c_{SW}}{20.04} \quad (4.2.6)$$

M_{SW} is computed in a similar manner as ρ_{SW} and an analogous expression indicated in Eq. (4.2.6) has been used for the same.

4.2.1.3 Results and discussion

In Figure 4.2.2a, the variation of average (over a day) solar radiation incident ($S_{avg.}$), maximum temperature acquired (in a day) inside LCZ ($T_{LCZ, max.}$) and ambient temperature (T_a) are studied. Solar radiation intensity (S) during a day invariably depends upon the climate conditions and season. During the entire period of experiments, the minimum and maximum $S_{avg.}$ are found to be 257.4 W/m² (on cloudy day) and 728.4 W/m² (on sunny day). T_a is observed almost constant during the experiment days and it varies between 30 °C and 32 °C as indicated in Figure 4.2.2a. The variation of $T_{LCZ, max.}$ corresponding to $S_{avg.}$ with different ambient conditions are also shown in the same figure. Experiments are started at LCZ temperature of 36.02 °C that reached up to a maximum ($T_{LCZ, max.}$) of 52.08 °C after 28 days with a total gain 16.06 °C. During the initial phase, the rate of temperature gain is higher as compared to later phases of experiments. This is attributed to the fact that the specific heat capacity of water decreases with SC [Harbeck 1955]. During the initial phases of operation, the diffusion of salt is very slow, whereas during the later phases the same is relatively faster. Consequently, for a given level of solar insolation, the specific heat capacity would be lesser during the initial phases that enable LCZ to attain higher temperatures than the later phases. The maximum temperature in UCZ ($T_{UCZ, max.}$) suddenly falls in the middle due to very low $S_{avg.}$ during that period of time as shown in Figure 4.2.2b.

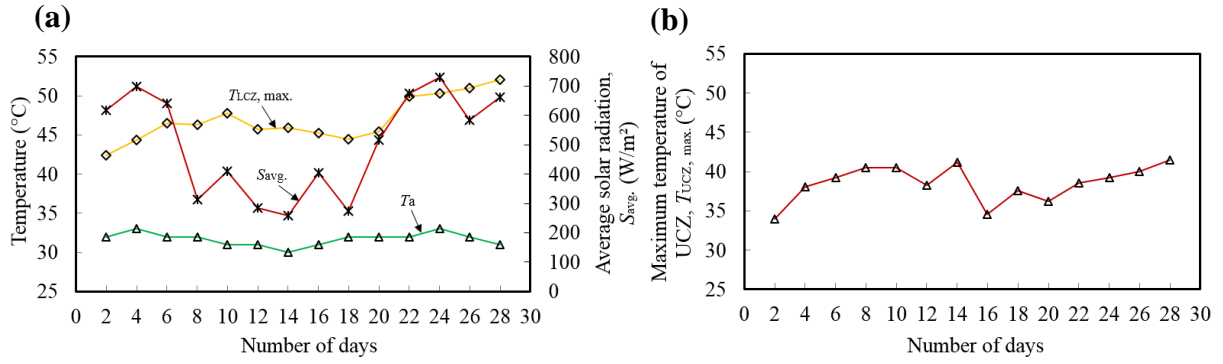


Figure 4.2.2: (a) Transient variations of temperatures and average solar radiation and (b) maximum UCZ temperature

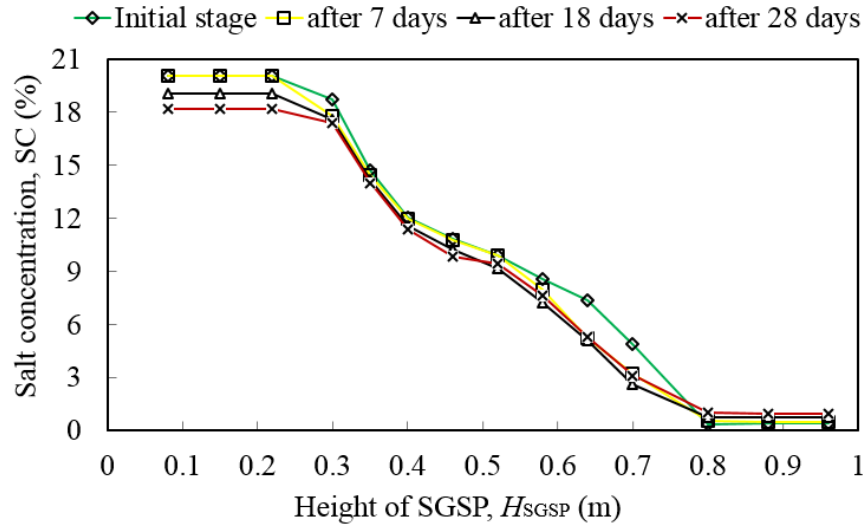


Figure 4.2.3: Transient variation of salt concentration across H_{SGSP}

Figure 4.2.3 presents the variation of SC across three zones of SGSP during different days. During the initial stage, saturated SC in LCZ is 20.04% and the same within UCZ is 0.38%. The initial SCs in the eight layers of NCZ are varied as 18.75%, 14.69%, 12.07%, 10.87%, 9.89%, 8.57%, 7.39%, and 4.92% from bottom to top layer. It is inferred that salinity (SC) within LCZ gradually decreases whereas the same within UCZ increases with time (days). However for a given time, SC across these zones remains constant but the same with NCZ yields a mixed trend.

The variation of EC within SGSP is shown in Figure 4.2.4. It is envisaged that the profile of EC with the height of SGSP (H_{SGSP}) is similar to SC. Furthermore EC remains almost constant with time within LCZ and UCZ. This behaviour may be caused due to an increase in EC with increase in temperature [Hayashi 2004] and nearly equal decrease in EC with decrease in SC [Lewandowski et al. 2017]. This ultimately cancels the effect of each other. However for a particular height inside NCZ, the change of EC from initial state is described by the change in SC (diffusion to the upper

layers and infusion from the lower layers) along with the temperature variation. The minimum and maximum EC are observed as 5.13×10^{-1} S/m in UCZ and 153.4×10^{-1} S/m in the LCZ.

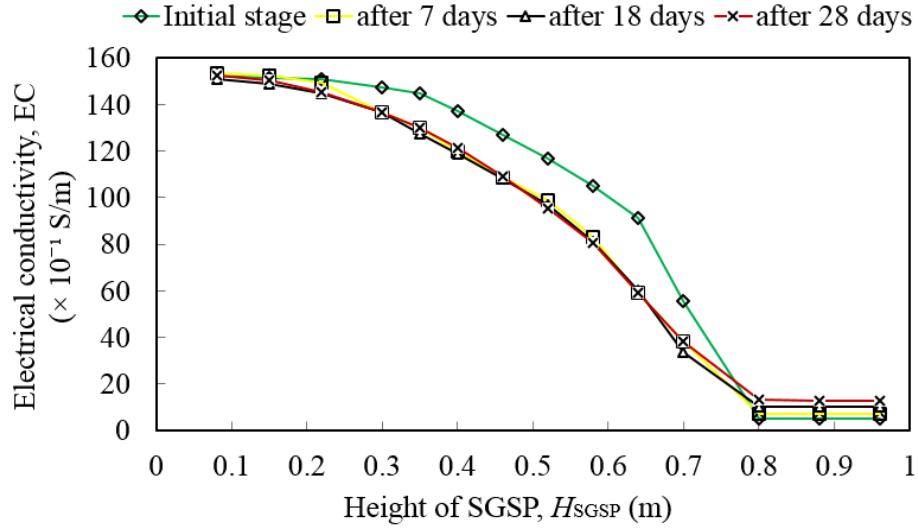


Figure 4.2.4: Transient variation of electrical conductivity across H_{SGSP}

The variation of TDS across H_{SGSP} is studied in Figure 4.2.5. It is highlighted that in case too, the trend of TDS with H_{SGSP} is analogous to SC and EC because it is directly proportional to EC [Rusydi 2018]. Therefore, the same argument relating to Figure 4.2.4 holds good in this case also.

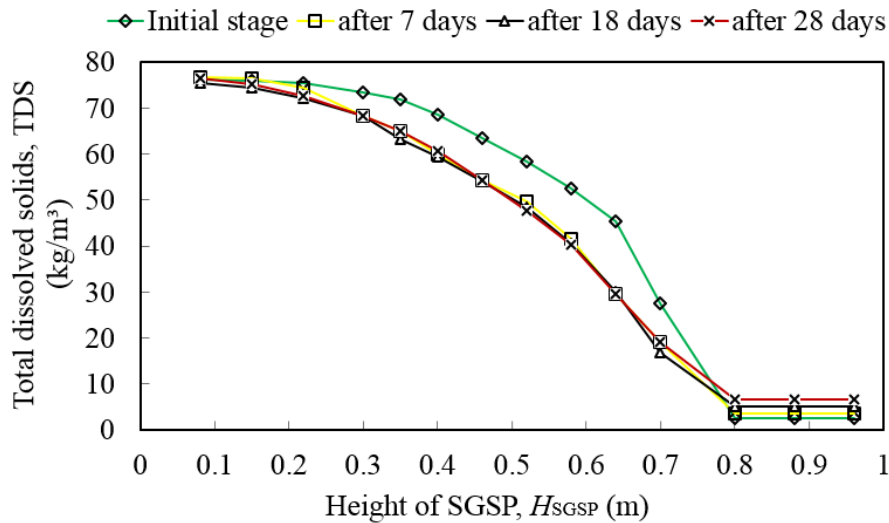


Figure 4.2.5: Transient variation of TDS across H_{SGSP}

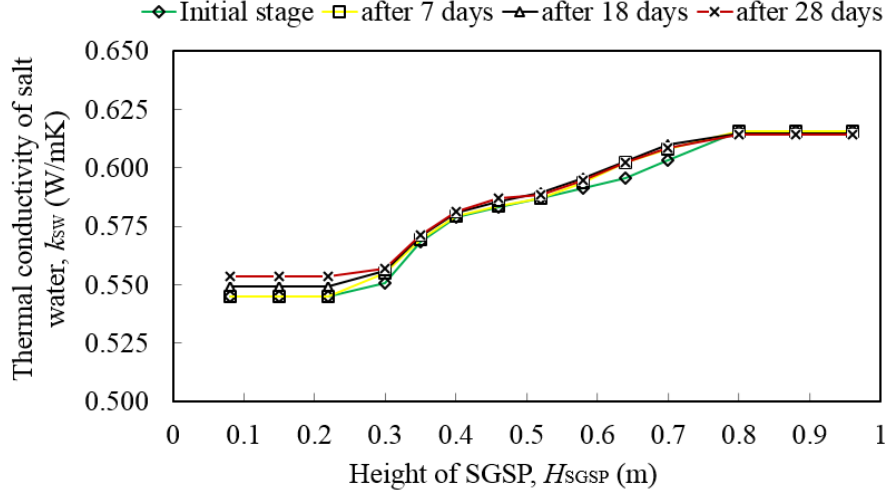


Figure 4.2.6: Transient variation of thermal conductivity of salt water across H_{SGSP}

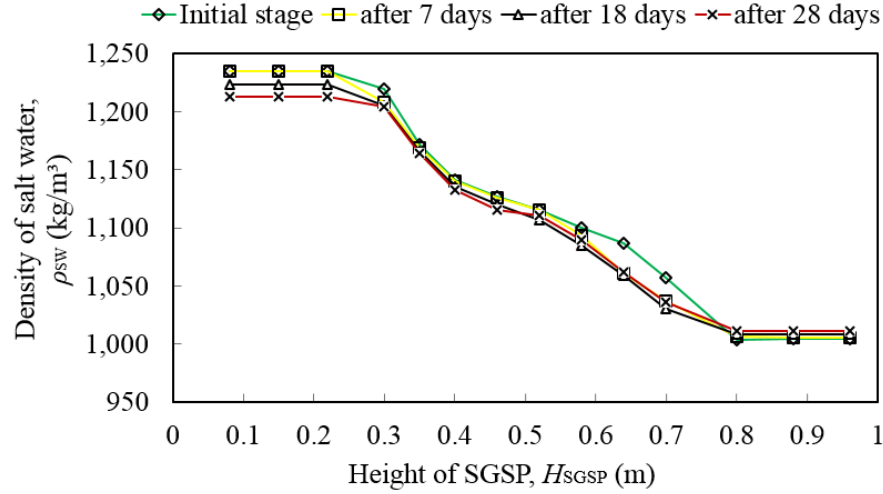


Figure 4.2.7: Transient variation of density of salt water across H_{SGSP}

Figure 4.2.6 presents the variation of k_{SW} across H_{SGSP} . It is noticed that in this case, k_{SW} decreases with the depth of SGSP (i.e. as H_{SGSP} attains smaller values) for all days of the month. This is an interesting observation because at the given temperature range, salt possesses considerably high value of k (i.e. k_{salt}) than water (i.e. k_{water}), so the effective k (i.e. k_{SW}) should intuitively increase. The decrease of k_{SW} is expected due to the temperature decrement within the solution caused through endothermic reaction. However at a given height, this variation is small. This leads to infer that k_{SW} is strongly related to SC and its dependence on temperature is relatively weak. A similar effect for ρ_{SW} and c_{SW} is envisaged from Figure 4.2.7 and Figure 4.2.8 respectively. The variation of ρ_{SW} is obvious. With increase in SC, more heat is absorbed from the solution due to endothermic reaction. This decreases the temperature and internal degrees of freedom [Reif 1965].

Consequently, less heat is needed to raise its temperature through a finite value and c_{sw} decreases with SC. Although the effect of temperature on k_{sw} , ρ_{sw} and c_{sw} is observed lesser than the corresponding effect of SC, but its influence is subjective. On one hand, the values of k_{sw} and c_{sw} marginally increases with increase in temperature whereas on the other hand the value of ρ_{sw} reduces with rise in temperature. The finding is in line with the previous observations [Sharqawy et al. 2010]. Due to this reason, almost constant values of k_{sw} , ρ_{sw} and c_{sw} are observed at all time levels within UCZ. With increase in temperature, the internal degrees of freedom of molecules present in solution increases, therefore the heat storage capacity of molecules increases [Reif 1965].

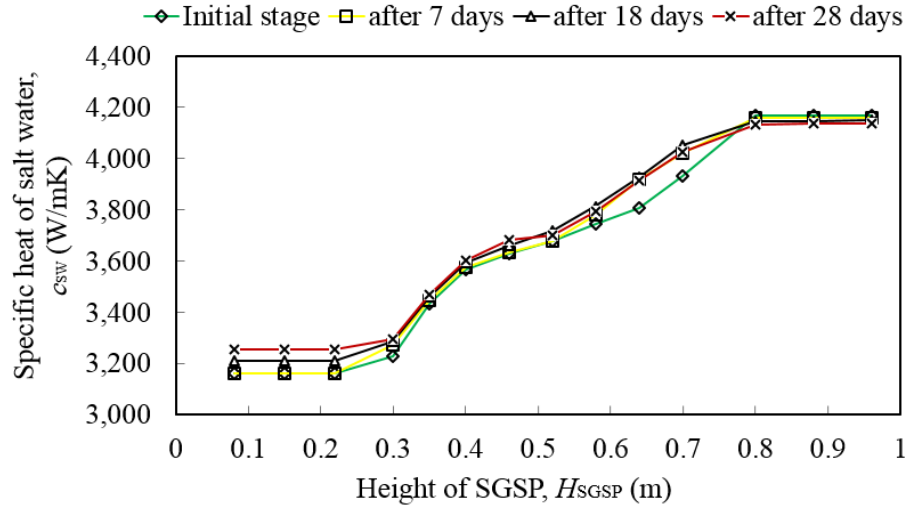


Figure 4.2.8: Transient variation of specific heat of salt water across H_{SGSP}

4.2.1.4 Summary

- SC inside LCZ always decreases whereas the same within UCZ increases with time. However, inside zone NCZ a mixed behavior is observed.
- Under similar incident solar insolation, a higher rate of temperature increase (within LCZ) during the initial stages of operation is directly related to the slower rate of salt diffusion.
- The variations of EC and TDS across H_{SGSP} are found similar to SC. However these two parameters are also found be affected by temperature which makes these two parameters to attain nearly constant values in LCZ and UCZ.

- Inside LCZ, k_{sw} , ρ_{sw} and c_{sw} are observed to vary more with SC and insignificantly with temperature. However the effect of temperature on these parameters is realized only within UCZ.
- With increase in SC, k_{sw} decreases due to reduced effective conductivity caused by possible endothermic reaction that lowers the temperature of salt water.
- The k_{sw} within SGSP is observed to be governed by the internal degrees of freedom offered by salt and temperature variations.

These above results are found to be useful in SGSP based water desalination and power generation applications.

4.2.2 TEGs-thermosyphon-based HRS installed in a SGSP

4.2.2.1 Experimental methodology

The details of the experimental setup are presented in [Figure 4.2.9](#). The maximum SC of 24.01% is achieved in LCZ whereas a lowest of 0.28% is obtained for UCZ. Two same capacity TEGs-thermosyphon-based HRSs (the construction details about it are described in [section 4.1.1](#)) are installed inside SGSP to transport the heat from LCZ to condenser portion which is fully immersed into UCZ. Here, a high vacuum pressure (-720 mm of Hg) inside both thermosyphons is created to enable boiling of working fluid (distilled water) in the temperature range corresponding to the temperature of LCZ. Each thermosyphon is filled with the distilled water with 0.496 of optimum TFR where maximum heat transfer occurs [\[Naresh and Balaji 2017\]](#) and [\[J3\]](#). A total of 48 (24 series-connected TEGs on each thermosyphon) affixed on the periphery of two thermosyphons at condenser section are surrounded (directly in contact) by UCZ contains cold water. This arrangement always keeps one end of TEGs at a higher temperature whereas other end is exposed to a lower temperature because UCZ remains cold. Consequently, an electrical potential is always generated through Seebeck effect from thermoelectric cells (TEGs) and produced V as well as I_s are measured by using a multimeter. The experiments are performed for 40 days of operation.

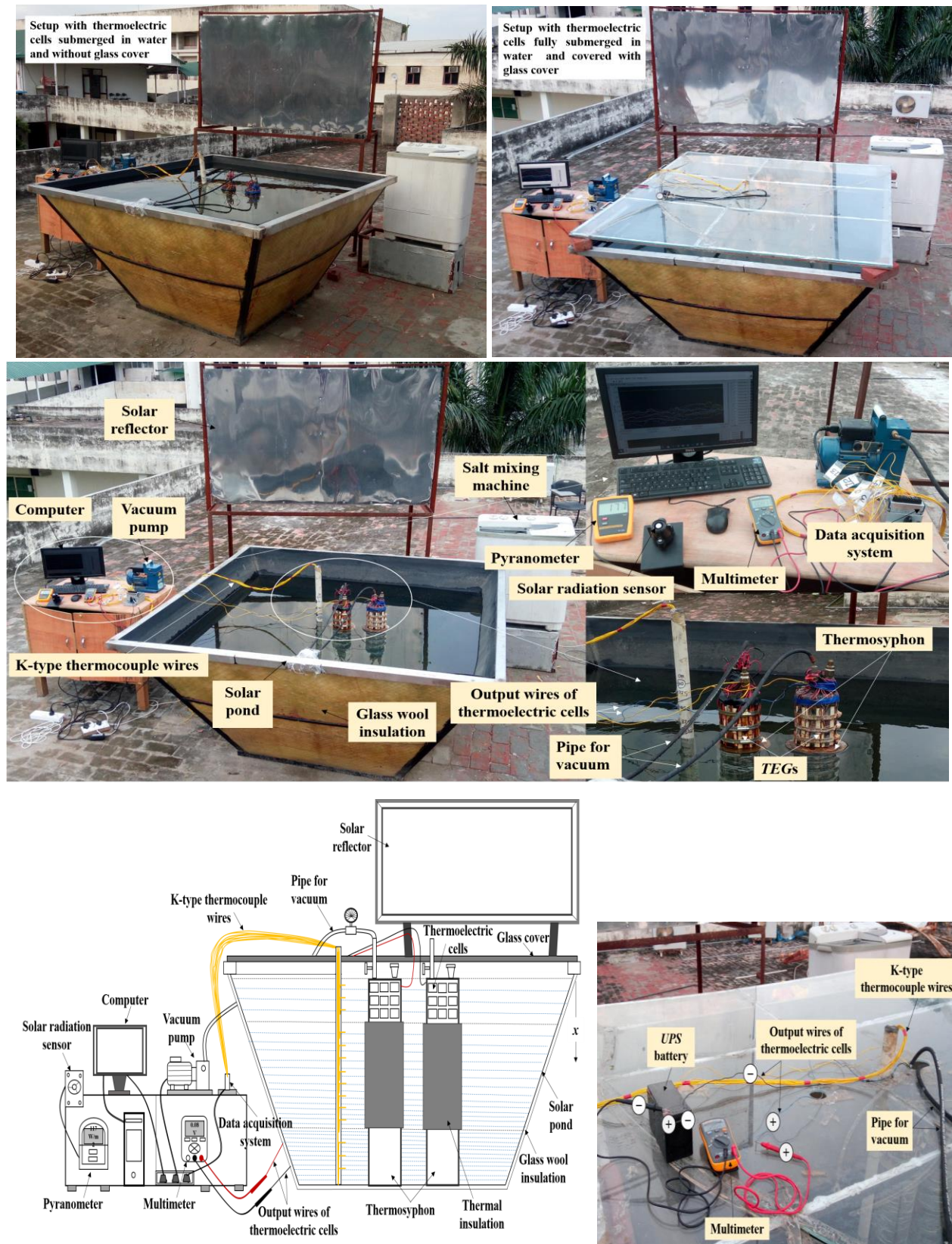


Figure 4.2.9: Details of the experimental setup and its block diagram

4.2.2.2 Results and discussion

Experimentations on the SGSP were performed during the months of May and June 2019 [Taggar et al. 2012]. Quantities including temperatures and solar radiative intensity are noted from 9:00 am (morning) to 6:00 pm (evening) at each one hour gap. Since, UCZ is always subjected to ambient air, the water level in that zone continuously decreases due to evaporation. So, in order to maintain the same water level, SGSP is charged with approximately 240 liters of fresh water after each 10 days of operation. Also, LCZ is charged after 30 operational days with 25 liters of fully saturated salt water in order to compensate the loss of salt due to upward diffusion.

Since, the evaporator and condenser sections of thermosyphons are exposed to LCZ and UCZ respectively, the amount of heat transferred to working fluid is mainly depends upon LCZ temperature. At higher temperature of LCZ, the boiling rate of working fluid increases which leads to high transfer of heat energy to the condenser section passing through various thermal resistances. This enhances T_h for TEGs that are imposed on the surface of thermosyphon at condenser section. NCZ temperature has no effects on the thermosyphon because the part of thermosyphon that comes in contact with NCZ is thermally insulated known as adiabatic section while cooled UCZ directly comes in contact with other side of TEGs. Therefore the temperatures of LCZ and UCZ play a significant role in generating V as well as I_s from TEGs. But at low temperature of UCZ, the boiling of working fluid is not so effective which results in low T_h . The difference between the temperatures of LCZ (T_{LCZ}) and UCZ (T_{UCZ}) at particular instant of time is known as temperature gradient (ΔT_{LU}) i.e. $\Delta T_{LU} = T_{LCZ} - T_{UCZ}$. Figure 4.2.10 shows the variations of maximum (in a day) and average (over a day) values of ΔT_{LU} and V . It may be highlighted that the maximum value can be more than or can even nearly close to average value. For instance, at the last day of operation (i.e., 40th day), both the maximum and average values are closely approximate each other. During the experiments, maximum ΔT_{LU} (or $\Delta T_{LU, \max.}$) is found to be 23.57 °C and corresponding $V_{\max.}$ of 1.435 V is obtained. For charging a 12 V, 7 Ah UPS battery, the minimum V and I_s of 14-17 V and 0.118 A respectively are required as recognized by [J2]. It has been found the actual obtained $T_{LCZ, \max.}$ in summer season is although not possible to generate minimum threshold V and I_s required for charging. Therefore, it has been externally electrically heated to generate the required V and I_s and found that at minimum ΔT_{LU} of 45.62 °C or above, the system is able to charge a 12 V, 7 Ah UPS battery.

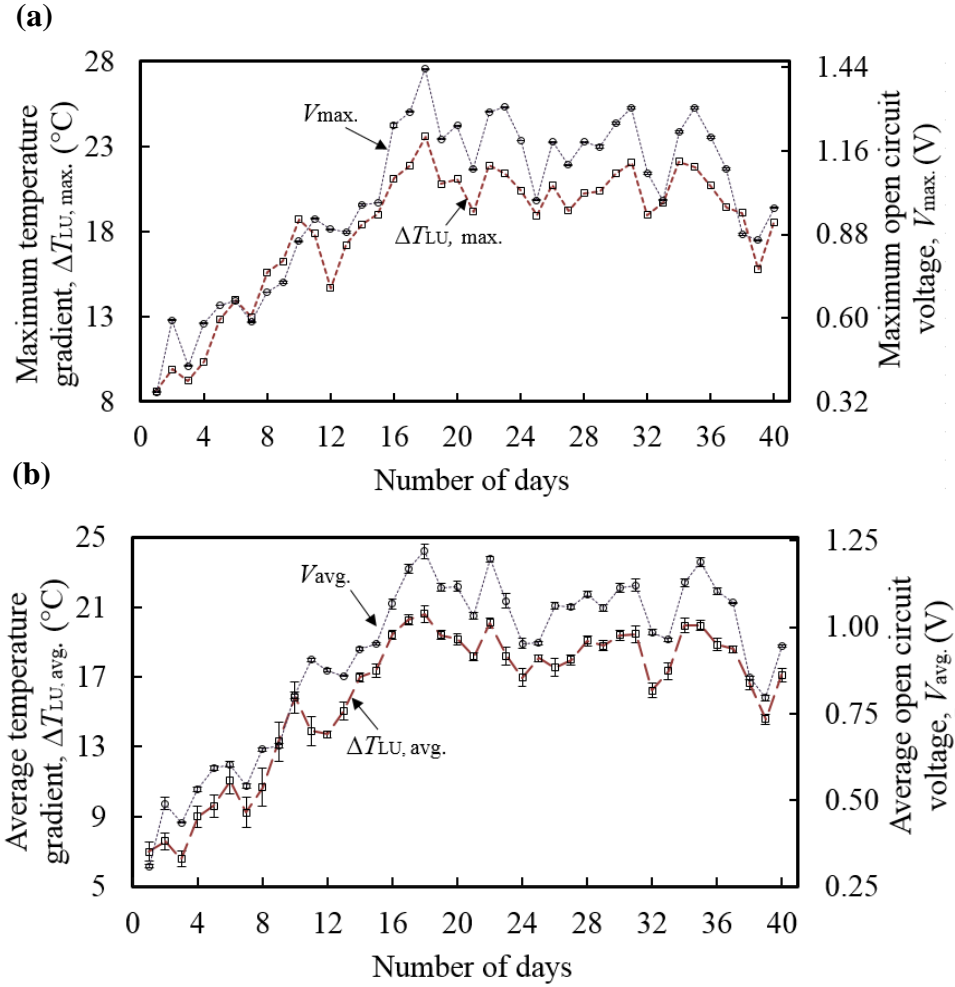


Figure 4.2.10: Variations of (a) maximum and (b) average values of ΔT_{LU} and V

Weather conditions and season affect S as well as T_a and the observed values of these parameters are studied in Figure 4.2.11. Many interesting observations can be made from Figure 4.2.10 and Figure 4.2.11. First of all, the attainment of $\Delta T_{LU, \max.}$ (day 18) does not correspond to either the day of attaining maximum solar radiation intensity or the day of maximum temperature attainment in LCZ. This is because, as S increases, T_{LCZ} and T_{UCZ} both are raised. Another finding from Figure 4.2.11 is that T_{UCZ} undergoes change to a limited extent whereas T_{LCZ} increases at a faster rate during the initial stages of operation and experiences lesser perturbations after some days. This enables to conclude that the heat gain inside UCZ during day time is almost lost in night but LCZ does not act in the same manner during night time and continuously raises its temperature due to the storage of thermal energy. However, when LCZ approaches steady state condition, it experiences a lesser change. Further, it is also highlighted that although ΔT_{LU} in any day is equal to average ΔT_{LU} ($\Delta T_{LU, \text{avg.}}$) but $\Delta T_{LU, \max.}$ need not equal to the difference of maximum T_{LCZ} ($T_{LCZ, \max.}$) and minimum T_{UCZ} ($T_{UCZ, \min.}$). This is because the time of attaining $T_{LCZ, \max.}$ may not be the

same as that of acquiring $T_{UCZ, \min.}$. The minimum ($S_{\min.}$) and maximum ($S_{\max.}$) solar radiation in a day observed during the entire duration of experiments are 26 W/m² and 976 W/m² respectively. Under this range of S , T_{LCZ} is found to be in the range 28.92-55.50 °C. Additionally, T_{UCZ} changes within the range of 23.68-35.92 °C whereas T_a varies from 27.95 °C to 43.05 °C.

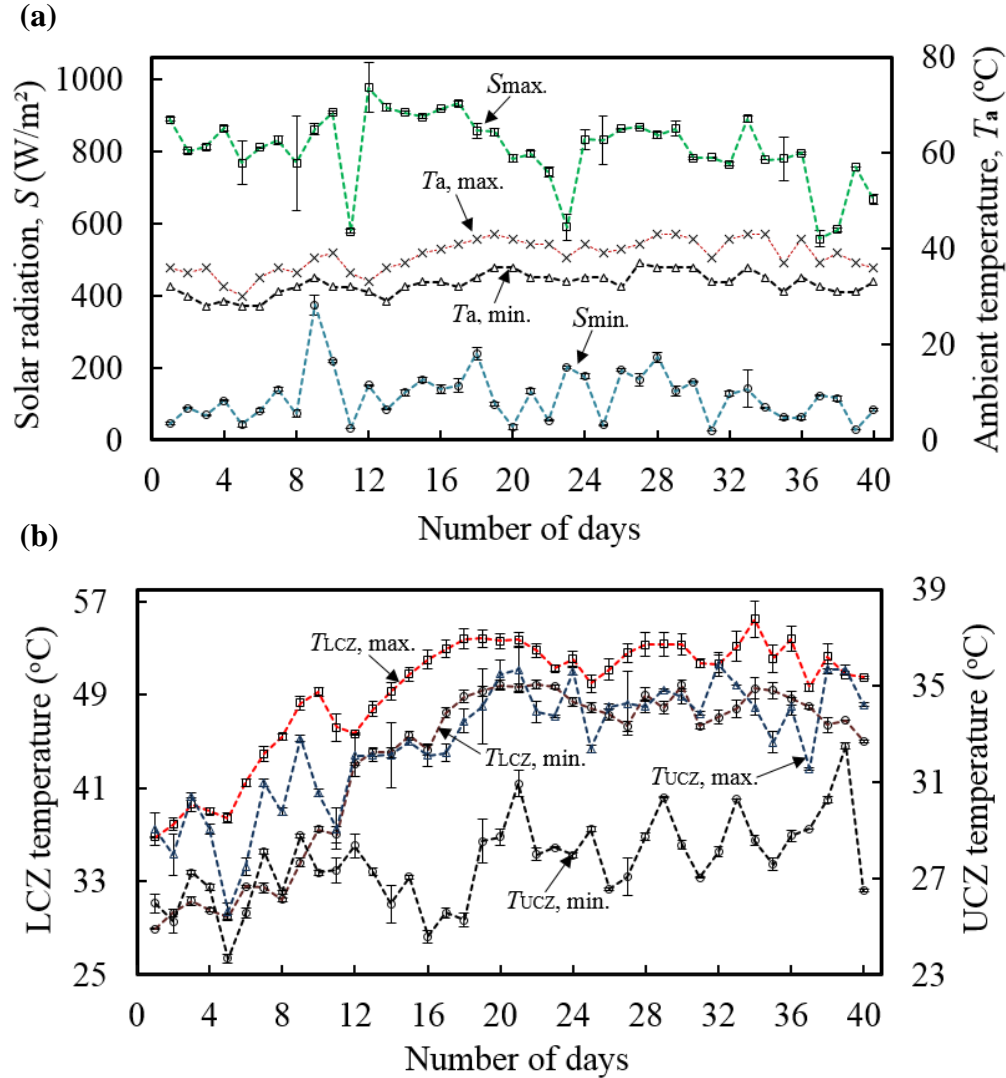


Figure 4.2.11: Variations of maximum and minimum values (a) S and T_a , (b) T_{LCZ} and T_{UCZ}

The convection free NCZ plays a key role in the storage capacity of SGSP. This layer shields the convection heat loss from LCZ to UCZ and increases T_{LCZ} . However, a small amount of heat is lost from between these two zones due to finite heat conduction. Figure 4.2.12 shows the variation of maximum temperature of NCZ ($T_{NCZ, \max.}$) obtained at four points (0.25 m, 0.41 m, 0.57 m, and 0.73 m) from the water surface. The first point ($x = 0.25$ m) is very close to UCZ with low SC, whereas the last point ($x = 0.73$ m) is in close proximity to LCZ with a higher SC. The other two

points ($x = 0.41$ m and 0.57 m) are located between first and last points of NCZ. It is observed that NCZ temperature is largely dependent upon T_{LCZ} and the profile obtained is approximately the same order as $T_{LCZ, \max.}$. During the entire experiments, $T_{NCZ, \max.}$ is observed in the range of 33.08 - 47.82 °C.

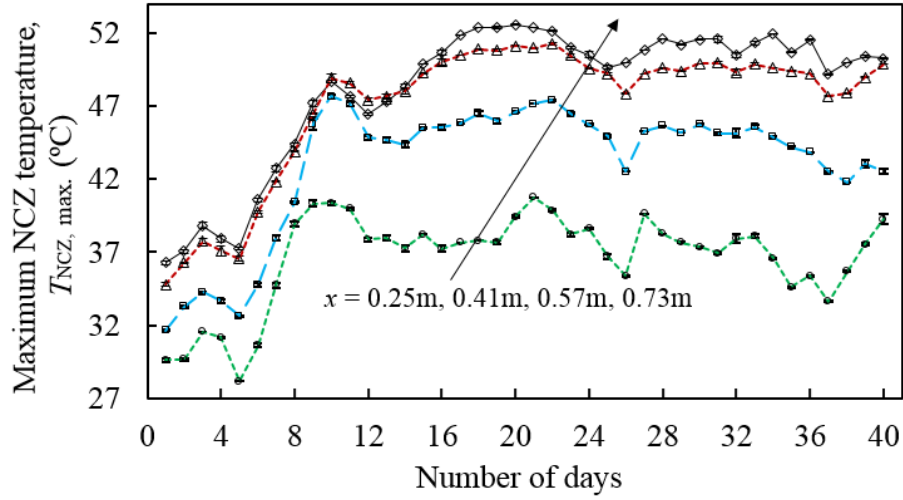


Figure 4.2.12: Variation of maximum temperature in NCZ

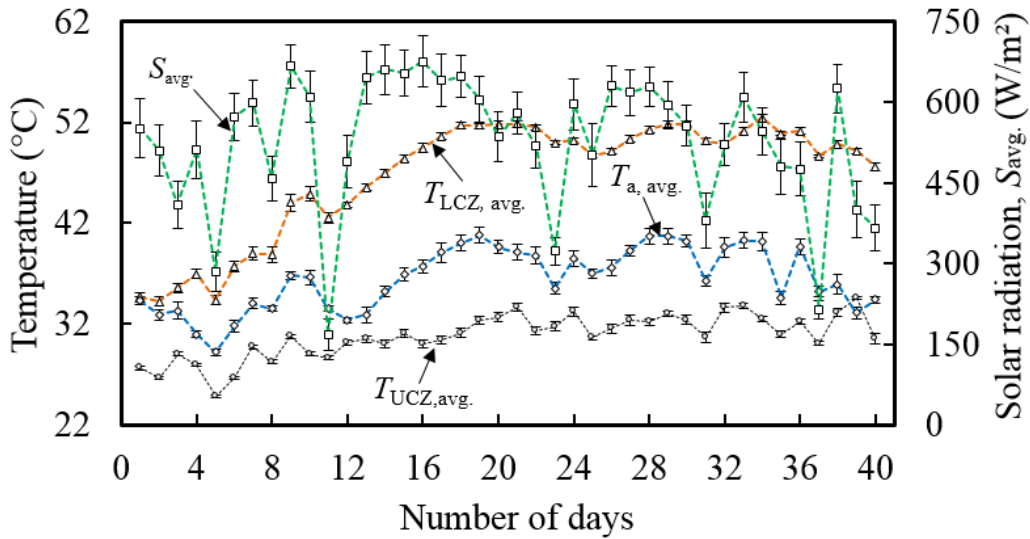


Figure 4.2.13: Variations of average values of S , T_a , T_{LCZ} and T_{UCZ}

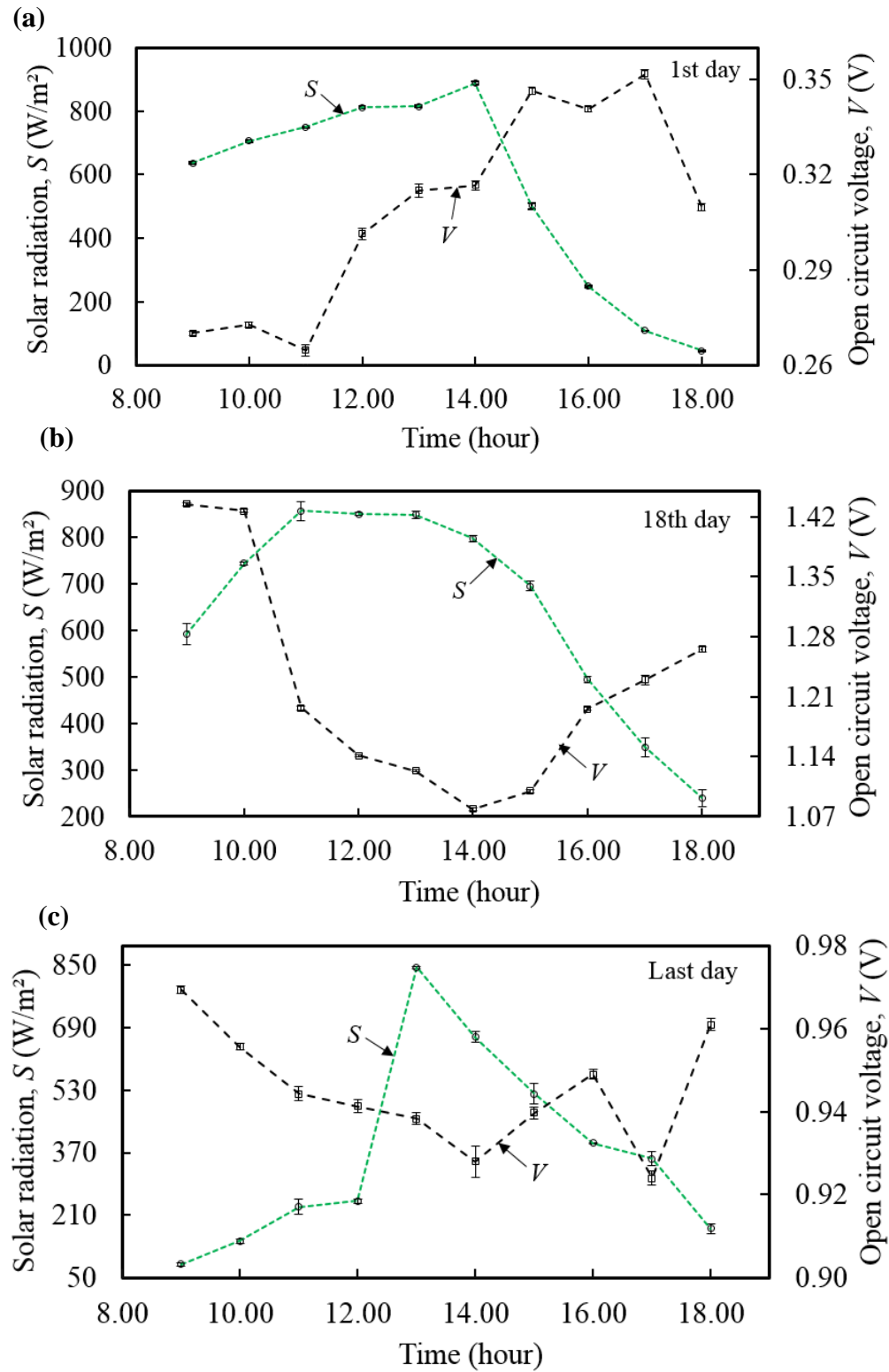


Figure 4.2.14: Variation of V corresponding to S with time (a) first day (b) 18th day (c) last day

The evolutions of $S_{\text{avg.}}$, average (over a day) temperatures of ambient ($T_{\text{a, avg.}}$), LCZ ($T_{\text{LCZ, avg.}}$) and UCZ ($T_{\text{UCZ, avg.}}$) are presented in Figure 4.2.13. The profile acquired by $T_{\text{LCZ, avg.}}$ mainly depends upon $S_{\text{avg.}}$ incident on the top surface of pond and ambient conditions. It is found that $T_{\text{LCZ, avg.}}$ does not exceed 52.44 °C (maximum value) whereas $T_{\text{UCZ, avg.}}$ remains below 33.81 °C. The maximum values of $S_{\text{avg.}}$ and $T_{\text{a, avg.}}$ during the entire experiments are recorded as 676 W/m² and 40.80 °C respectively. It has been recognized from the figure that the variations in $T_{\text{UCZ, avg.}}$ during the 40 days of experiments is quite small. This is attributed to the fact that during day time whatever heat is gained in UCZ is almost lost during the night time.

In order to evaluate the temporal variation of V corresponding to S during a given day, a study has been carried out in Figure 4.2.14. It is noticed that sheer attainment of $S_{\text{max.}}$ does not result in $V_{\text{max.}}$. Interestingly, the probability of getting $V_{\text{max.}}$ is more when S approaches its minimum values (for example during morning and evening times). This is mainly because; when S is more, both T_{LCZ} and T_{UCZ} are raised approximately in a similar manner but heat dissipation from LCZ is suppressed by prevailing salinity gradient whereas UCZ cools faster. During the experiments the maximum and minimum values of V are found as 1.44 V (obtained on the 18th day of experiments) and 0.27 V (observed on the 1st day of experiments) respectively.

The some portion of incident solar radiation get reflected from the water surface and most of the incident solar radiation is transmitted to NCZ after absorbing a small magnitude by UCZ. After capturing a certain part of incident solar radiation in NCZ, a significant amount of solar radiation is transmitted to LCZ. However, a little part is reflected back to UCZ from NCZ and bottom of SGSP. The transmitted solar intensity is absorbed by saline/salt water present in LCZ which rises its temperature. The amount of heat energy stored in LCZ is known as heat storage capacity of SGSP (Q_{SGSP}) and it depends upon mass of LCZ water (m_{LCZ}), c_{LCZ} and T_{LCZ} as calculated by following equation,

$$Q_{\text{SGSP}} = \frac{m_{\text{LCZ}} \times c_{\text{LCZ}} \times \Delta T_{\text{LCZ}}}{10^6} \quad (4.2.7)$$

where, ΔT_{LCZ} indicate the temperature gain in LCZ and it is defined as the difference between final and initial values of T_{LCZ} . Figure 4.2.15 shows the variation of Q_{SGSP} with increasing number of operational days. In the initial phase of experiments, the line of Q_{SGSP} has high slope upto 11 days of operation due to large rate of increase in T_{LCZ} . However a lot of variation is observed in-between that because of change in weather conditions during these operating days. Thereafter the slope of

Q_{SGSP} line reduces in further operational days and reaches approximately near to steady state condition at the later phase. The maximum value of Q_{SGSP} is found to be 23.88 MJ during the 34th day of experiments.

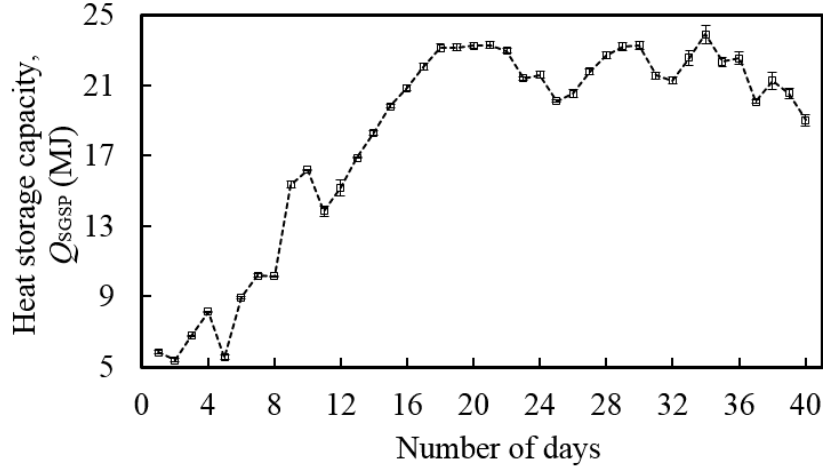


Figure 4.2.15: Variation of heat storage capacity of SGSP during the operational days

4.2.2.3 External energy required in SGSP for charging a UPS battery

It is observed that the achieved $\Delta T_{LU, \max.}$ ($= 23.57\text{ }^{\circ}\text{C}$) is not sufficient to generate the required power to charge a 12 V, 7 Ah UPS battery from TEGs and the required minimum critical/threshold temperature gradient ($\Delta T_{LU, \text{req.}}$) is found as $45.62\text{ }^{\circ}\text{C}$. Consequently, the external heat energy must be supplied to it. To fulfill that requirement, this external heat can be supplied from WH of a biomass driven engine-generator system as indicated in [Figure 4.2.16](#). The supplied heat energy is transferred to SGSP via gasifier, engine-generator and exhaust pipe. Initially, biomass is converted into syngas (through gasification process) to run the engine-generator which produces power and left out WH in the form of flue gases can be utilized as an external heat source for SGSP. This enables to acquire the minimum power necessary for charging the battery through TEGs.

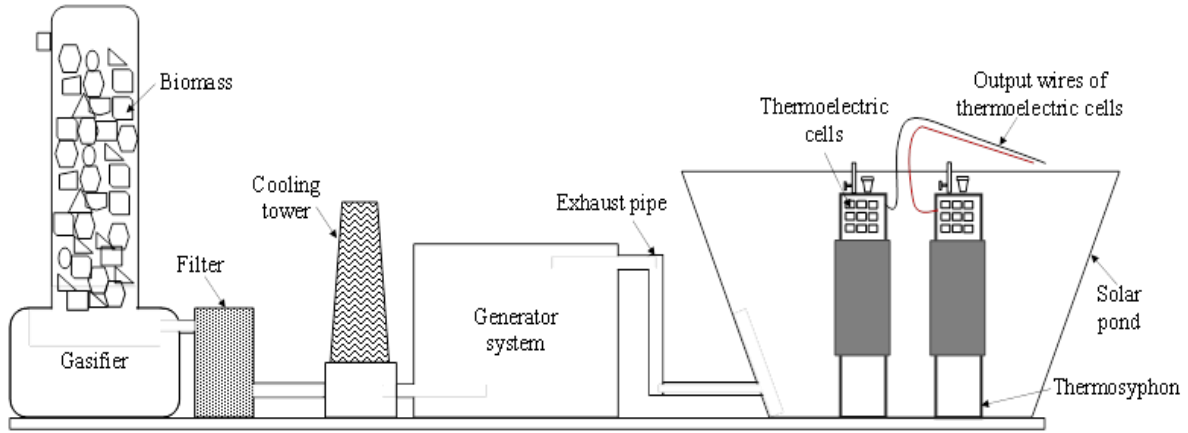


Figure 4.2.16: Proposed system of SGSP for power generation from TEGs

The required external heat energy supplied to SGSP mainly depends on the actual temperature gradient obtained in SGSP (i.e. ΔT_{LU}). The required biomass energy (Q_b) to be supplied to SGSP in order to meet the essential heat energy is estimated as given below,

$$Q_b = \frac{m_{LCZ} \times c_{LCZ} \times (\Delta T_{LU, req.} - \Delta T_{LU})}{\eta_{cg} \times (1 - 0.25 - \eta_e) \times \eta_p} / 10^6 \quad (4.2.7)$$

The engine-generator translates the chemical energy of syngas in electrical energy through a limited translation efficiency (η_e) of 35% and losses the remaining energy as a WH. Some portion (25%) of WH produced from engine-generator is consumed to cool the engine and the left over heat (40%) is transferred to the ambient [Jadhao and Thombare 2013]. WH delivers from the exit port of engine to the SGSP through an exhaust pipe and during this phenomenon, some portion (0.5 based on the temperature differential) gets lost to ambient through pipe efficiency (η_p) of 50%. The mass of biomass required (m_b) to deliver the extra thermal energy is calculated from Eq. (4.2.8) as specified below,

$$m_b = \frac{Q_b}{HHV} \quad (4.2.8)$$

where HHV (18.36 MJ/kg) [J1] is the higher heating value of biomass.

Figure 4.2.17 depicts the variation of m_b corresponding to actual obtained $\Delta T_{LU, avg.}$. It is evaluated that 10.11 kg of m_b is required for the gasifier corresponding to maximum $\Delta T_{LU, avg.}$ of 20.61 °C in order to supply the essential WH whereas the same is found as 15.60 kg with respect to minimum $\Delta T_{LU, avg.}$ of 7.0 °C.

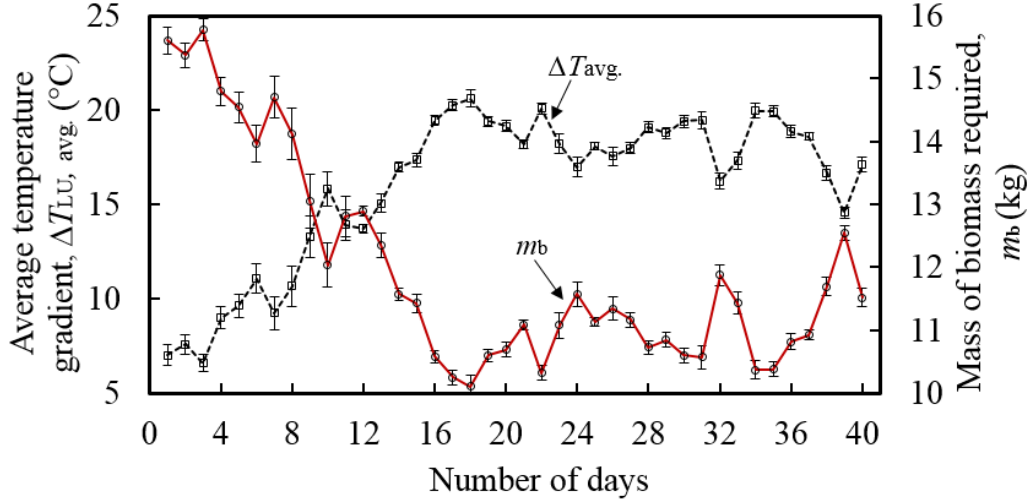


Figure 4.2.17: Biomass requirement corresponding to the average temperature gradients

4.2.2.4 Economic analysis

4.2.2.4.1 Capital cost

The proposed system consists of two parts (a) a gasifier combined with filters, a cooling tower and an engine-generator and (b) an insulated SGSP combined with thermosyphons and TEGs. The cost of gasifier unit depends upon manufacturing company, location, capacity and many other variable factors. In general, for a 10 kW gasifier system, the cost based on current market scenario is observed as 8,25,000 INR (10,835.30 USD) [J3]. The cost of SGSP unit varies with volume capacity, materials of construction, type of insulated material and manufacturer labor cost. The volume of used SGSP is 2.33 m³ in which internal/outer surface area is occupied by 7 m². The SGSP is made of stainless steel (density = 8000 kg/m³) having 3 mm thickness and concluded to a total weight of 168 kg [J3]. The cost of material used for SGSP has the present market price of 255 INR/kg (3.34 USD/kg) [J3] and total material cost of SGSP is calculated as given below,

$$\text{Cost of stainless steel} = 255 \times 168 = 42,840 \text{ INR (562.64 USD)} \quad (4.2.9)$$

The internal surface of SGSP (with considering 1 m² scrub) is covered with 2 mm thickness EPDM rubber sheet and total mass required is around 23 kg when considering the density of 1430 kg/m³ for EPDM [J3]. As per availability in market, the cost of EPDM sheet is witnessed as 230 INR/kg (3.02 USD/kg) [J3]. Therefore the total cost in utilization of EPDM to cover 7 m² of internal surface area is evaluated by following equation,

$$\text{Cost of EPDM} = 230 \times 23 = 5,290 \text{ INR (69.47 USD)} \quad (4.2.10)$$

The outer surface of SGSP is insulated by glass wool with thickness 50 mm and required weight is around 25 kg. The cost of glass wool as per availability in the market is recognized as around 600 INR (7.88 USD) [J3]. To bind up the glass wool around the pond's outer surface, commercially available fiber sheet of thickness 1.5 mm is used and required a quantity of approximately 10 kg. The cost associated with the fiber sheet as per available in commercially market is found to be 120 INR/kg (1.57 USD/kg) [J3]. Therefore, the total cost of fiber sheet for 10 kg weight is computed by equation given below,

$$\text{Cost of fiber} = 120 \times 10 = 1,200 \text{ INR (15.76 USD)} \quad (4.2.11)$$

Two octagonal-shaped thermosyphons are made from copper sheet (density = 8960 kg/m³) of 1 mm thickness [J3] and resulted a total surface area of 0.671 m² for both. The total weight of both thermosyphons is found as 6 kg. The cost of copper sheet available in the market is realized as 500 INR/kg (6.56 USD/kg) [J3]. Thus, the total cost of copper sheet to make the two thermosyphons is calculated by following equation,

$$\text{Cost of copper sheet} = 500 \times 6 = 3,000 \text{ INR (39.40 USD)} \quad (4.2.12)$$

Manufacturer labor cost is also considered in construction of thermosyphon, SGSP and adhesive the thermal insulation materials (EPDM and glass wool). The cost related to manufacturing of both thermosyphon and SGSP through local manufacturer are considered to be 8500 INR (111.63 USD) based on actual constructed cost (around 50 INR/kg or 0.65 USD). A total of 48 commercially available TEGs are used to generate power and each having a cost of 380 INR (4.99 USD) [J3]. The total cost of 48 TEGs is found as

$$\text{Cost of TEGs} = 380 \times 48 = 18,240 \text{ INR (239.55USD)} \quad (4.2.13)$$

The cost of SGSP unit is computed by following equation

$$\begin{aligned} \text{Cost of SGSP unit} = & \text{Cost of (a) stainless steel} + \text{(b) EPDM} + \text{(c) glass wool} + \text{(d) fiber sheet} \\ & + \text{(e) copper sheet} + \text{(f) manufacturing} + \text{(g) TEGs} \end{aligned} \quad (4.2.14a)$$

$$\text{Cost of SGSP unit} = 79,670 \text{ INR (1,046.36USD)} \quad (4.2.14b)$$

These are the original costs of materials and it is customized after adding tax on all materials. In the present scenario of India, generally 18 % GST is applied for most of the constructed materials [J3]. Therefore, the total cost of tax paying for all materials is calculated as,

$$\text{Cost of tax} = 0.18 \times (\text{Gasifier unit} + \text{SGSP unit}) = 1,62,840 \text{ INR (2,138.69 USD)} \quad (4.2.15)$$

The capital cost of proposed system for generating power is given below,

$$\begin{aligned}\text{Capital cost} &= \text{Cost of (a) gasifier unit} + \text{(b) SGSP unit} + \text{and (c) tax} \\ &= 10,67,510 \text{ INR (14,020.35 USD)}\end{aligned}\quad (4.2.16)$$

*Exchange rate, 1 USD = 76.14 INR @ April, 2020

4.2.2.4.2 *Operating cost*

The operational cost is connected to expense of consumables resources (salt and biomass), labor, depreciation and maintainance to run the unit [Wu et al. 2002]. The salt is used to make the saturated (LCZ) and gradient (NCZ) layers in SGSP. Initially, for the existing capacity of SGSP, total requirement of salt is around 165 kg. Thereafter, during the process time, salt is also obligatory in order to maintain the salt concentration at regularly interval of time. For the existing SGSP, around 6 kg of salt per month is required to preserve the salinity and a total of 72 kg salt is desirable over an operation period of one year. Thus, the total amount of salt required is 237 kg to operate the SGSP. From the market point of view, the cost of salt is 17 INR/kg (0.22 USD) [J3]. So, the total cost of salt for 237 kg is found by equation given below,

$$\text{Cost of salt} = 17 \times 237 = 4,029 \text{ INR/year (52.91 USD/year)} \quad (4.2.17)$$

It was presumed that system is functioning 24 hours for 300 days per year (7,200 h/year) and lifespan of the Gasifier as well as TEGs is considered as 25 years [Panwar and Rathore 2009]. The costs of biomass as well as labor are found same as described in section 3.3.2.2 and given below

$$\text{Cost of biomass} = 1,65,600 \text{ INR/year (2,174.94 USD/year)} \quad (4.2.18)$$

$$\text{Cost of labor} = 3,15,000 \text{ INR/year (4,137.12 USD/year)} \quad (4.2.19)$$

After functioning the unit for 25 years, it was presumed that cost of system remains 10% of its principal cost. Then, the deprecation cost per year is evaluated by following manner [Wu et al. 2002],

$$\text{Deprecation cost} = \frac{10,67,510 - 1,06,751}{25} = 38,430 \text{ INR/year (504.73 USD/year)} \quad (4.2.20)$$

The upkeeping cost is necessary for repair and unceasing working of the system and the same is taken as 10% of its principal cost. Therefore, cost related to maintainance is observed as,

$$\text{Maintenance cost} = 0.1 \times 10,67,510 = 1,06,751 \text{ INR/year (1,402.03 USD/year)} \quad (4.2.21)$$

The operating cost for running of proposed system is found as,

$$\begin{aligned} \text{Operating cost} = & \text{Cost of (a) salt + (b) biomass + (c) labor} \\ & + \text{(d) deprecation + (e) maintenance} \end{aligned} \quad (4.2.22a)$$

$$\text{Operating cost} = 6,29,810 \text{ INR/year (8,271.73 USD/year)} \quad (4.2.22b)$$

4.2.2.4.3 *Electricity generation cost*

The net electricity output from the engine-generator is calculated as 64,800 kWh/year as described in [section 3.3.2.2](#). By the continuous storing of WH produced from the engine-generator, LCZ temperature can be reached up to 80-90 °C whereas UCZ remains cool nearly to ambient temperatures. Under these conditions, 48 TEGs can produce the electricity of 1.033 W [\[J2\]](#) and the net electricity output from these TEGs by operating the system for 7,200 h/year is found as 7.44 kWh/year. This electricity generation is very low compared to engine-generator but it can be increased by adding more number of TEGs because this system is not limited to 48 TEGs. The overall net electricity output from the proposed system is observed as 64807.44 kWh/year. The electricity generation cost from the proposed system depends upon the operating cost and the net electricity output as given below [\[Wu et al. 2002\]](#),

$$\text{Electricity generation cost} = \frac{6,29,810}{64807.44} = 9.71 \text{ INR/kWh (0.127 USD/kWh)} \quad (4.2.23)$$

The electricity generation cost is found as 9.71 INR/kWh (0.127 USD/kWh).

4.2.2.4.4 *Payback period and feasibility*

Payback period is that time period in which capital cost of the system is recovered through profit. It depends upon the number of household electrified by the system, electricity generation cost and capital cost. The number of household electrified through the system over a period of year (365 days) is found to be 35 as elaborated in [section 3.3.2.3](#). The electricity generation cost from the conventional diesel is estimated as 14.44 INR/kWh during the period of 2007 in India which is rising continuously over the period of time because of incessantly rise in diesel price [\[Ravindranath](#)

and Balachandra 2009]. By considering 14.44 INR/kWh (0.189 USD/kWh), the saving potential in power generation from proposed system can be 4.73 INR/kWh (0.062 USD/kWh) over the conventional power generation from diesel. The profit in electricity generation cost during a year is computed by following manner,

$$\text{Profit} = 5 \times 365 \times 35 \times (14.44 - 9.71) = 3,02,128 \text{ INR/year (3,968.05 USD)} \quad (4.2.24)$$

Then, payback for the proposed system in order to recover the capital cost is evaluated as given below

$$\text{Payback period} = \frac{10,67,510}{3,02,128} = 3.53 \text{ years} \quad (4.2.25)$$

Therefore, the proposed system is feasible because payback period is observed under 5 years. It has been realized that the proposed system can be replaced the conventional diesel power generation with considerable amount of profit. Also, the complete system is totally operated by renewable source of energy (biomass and solar energy) which are environment friendly, abundant and easily availability in nature. Further, it is more attractive in remote areas for the power generation where supply of electricity is not possible or required a high input/capital cost.

4.2.2.5 Uncertainty analysis

For a direct measurement of parameters such as solar radiation and voltage, the absolute uncertainties will be the half of the resolution of equipment used. The uncertainties associated in average values are calculated as per procedure discussed in [section 3.1.4.6](#). Uncertainties associated with various measuring parameters are presented in [Table 4.2.1](#).

Table 4.2.1: Uncertainty analysis of various measuring parameters

| | $S_{\min.}$ (31 th day, 6:00 PM) | $S_{\max.}$ (12 th day, 1:00 PM) | $S_{\text{avg, min.}}$ (11 th day) | $S_{\text{avg, max.}}$ (16 th day) |
|----------|---|---|--|---|
| Absolute | 0.3 W/m ² | 0.3 W/m ² | 0.09 W/m ² | 0.09 W/m ² |
| Relative | 1×10^{-2} | 3×10^{-4} | 5×10^{-4} | 1×10^{-4} |
| | $T_{\text{LCZ, min.}}$ (1 st day, 9:00 AM) | $T_{\text{LCZ, max.}}$ (34 th day, 5:00 PM) | $T_{\text{LCZ, avg, min.}}$ (2 nd day) | $T_{\text{LCZ, avg, max.}}$ (34 th day) |
| Absolute | 0.4 °C | 0.9 °C | 0.06 °C | 0.2 °C |
| Relative | 1×10^{-2} | 2×10^{-2} | 2×10^{-3} | 4×10^{-3} |
| | $T_{\text{UCZ, min.}}$ (5 th day, 9:00 AM) | $T_{\text{UCZ, max.}}$ (32 th day, 3:00 PM) | $T_{\text{UCZ, avg, min.}}$ (5 th day) | $T_{\text{UCZ, avg, max.}}$ (39 th day) |
| Absolute | 0.1 °C | 0.2 °C | 0.04 °C | 0.09 °C |
| Relative | 4×10^{-3} | 6×10^{-3} | 2×10^{-3} | 3×10^{-3} |
| | $T_{\text{a, min.}}$ (5 th day, 6:00 PM) | $T_{\text{a, max.}}$ (29 th day, 2:00 PM) | $T_{\text{a, avg, min.}}$ (5 th day) | $T_{\text{a, avg, max.}}$ (34 th day) |
| Absolute | 0.5 °C | 0.5 °C | 0.2 °C | 0.2 °C |
| Relative | 2×10^{-2} | 1×10^{-2} | 7×10^{-3} | 5×10^{-3} |
| | $\Delta T_{\text{LU, max.}}$ (18 th day, 9:00 AM) | $\Delta T_{\text{LU, avg, max.}}$ (18 th day) | $V_{\max.}$ (18 th day, 9:00 AM) | $V_{\text{avg, max.}}$ (18 th day) |
| Absolute | 0.4 °C | 0.1 °C | 3×10^{-4} V | 9×10^{-5} V |
| Relative | 2×10^{-2} | 5×10^{-3} | 2×10^{-4} | 7×10^{-5} |

4.2.2.6 Summary

The outcomes of this study revealed that when S varies within a range of 26-976 W/m², T_{LCZ} varies in the range 28.92-55.50 °C with a gain of 26.58 °C. Additionally, UCZ also heats up from 23.68 °C to 35.92 °C when T_{a} varies between 27.95-43.05 °C. The value of obtained $\Delta T_{\text{LU, max.}}$ is found to be 23.57 °C and corresponding V is obtained as 1.435 V. However, this obtained V is not found useful for charging a 12 V, 7 Ah UPS battery, thereby necessitating the supply of additional thermal energy from an external heat source. $\Delta T_{\text{LU, req.}}$ for charging the UPS battery is experimentally determined as 45.62 °C. It has been realized that during the peak time of summer

season, the obtained $\Delta T_{LU, \max}$ under actual conditions is even not sufficient to generate the required power. Further, in winter season where the weather conditions are not favorable to SGSP, practical applications of it has no more use in generating power for remote areas. Thus, to overcome this issue, a high temperature in SGSP must be needed. It is therefore concluded that under an actual experimental conditions an external heat source is always mandatory for harnessing useful power from SGSP. It is found that the demand of additional heat can be fulfilled by WH of biomass driven engine-generator system through gasification of minimum 10.11 kg of biomass. In order to study the feasibility of system, the economic analysis is also performed for SGSP externally heated by WH of 10 kW gasifier system. The electricity generation cost is obtained as 9.71 INR/kWh (0.127 USD/kWh). It has been observed that a 10 kW capacity system is not feasible over the electricity utilization from grid system but must be feasible with large capacity plants. However, the proposed system of 10 kW capacity is feasible in replacing the power generation from diesel (used in remote areas and industries) by returning the capital cost of system within 3.53 years. The cost of electricity generation can be improved by enlarging the capacity of system and by increasing the appropriate number of TEGs. This renewable energy based system is eco-friendly and small capacity plant is more suitable for household applications in remote areas.

4.3 Experimental study on the developed TEGs-array-based HRS operated by a SGSP driven by waste heat

As proven above, the TEGs-thermosyphon-based HRS for harvesting the heat from the high temperature sources is a well-known technology for power generation. However, various thermal resistances are involved in the thermosyphon-based HRS between heat sources and TEGs which generate irreversibility that ultimately reduces its performance. Therefore, the thermosyphon-based HRS is not able to generate the enough output to charge a 12 V, 7 Ah UPS battery when driven by a SGSP that is operated from the solar energy only and referred for an external heat source to meet the requirement. Therefore, to generate the effective power from the low temperatures of SGSP, a new design of HRS i.e. TEGs-array-based is developed and integrated with a SGSP (having a small capacity). This SGSP is first operated by the solar energy and then externally heated by the waste heat of biomass energy-driven engine-generator. Before this, the capability of a new fabricated SGSP is analyzed for recovering the storing the WH of biomass energy-driven engine-generator.

4.3.1 Performance analysis of a SGSP

It is evident from the literature that an effective storage system is required to recover WH which can store it high temperatures for long term [Ganguly et al. 2017]. In view of that, a small capacity trapezoidal-shaped SGSP is developed for efficiently recovering and storing WH generated from the renewable energy (biomass) driven engine. Before integration TEGs-array-based HRS with SGSP, the capability of developed SGSP is first experimentally investigated in terms of temperature profile, effectiveness, temperature gain, heat storage capacity and thermal efficiency.

4.3.1.1 Experimental setup details

The photograph and schematic diagram of the experimental setup describing various parts are shown in Figure 4.3.1. The setup consists of (a) a gasifier combined with filters and a cooling tower, (b) an engine generator (genset) and (c) a SGSP. WH of the biomass energy driven engine-generator is used as a heat source for the SGSP. The details about the process of producing syngas and power are discussed in section 3.1.1 and 3.1.2. To capture WH, the exhaust pipe of engine-generator system is passed through LCZ of SGSP in order to store it as a thermal energy. The exhaust pipe is made of iron but the portion of it which installed within SGSP is made of stainless steel to avoid rusting/corrosion and escalate the heat transport rate. The lateral area over which WH is transferred to SGSP is enlarged by increasing the number of turns (= 4) in the exhaust pipe. SGSP is made of steel in which the internal surface is insulated by EPDM and the outer surface is insulated by glass wool. It has a total capacity of 150 litres with dimensions of $0.6 \times 0.6 \text{ m}^2$ at the top and $0.5 \times 0.5 \text{ m}^2$ at its bottom along with 0.5 m of height. The size of SGSP is estimated based on the capacity of engine-generator system (10 kW) and WH generated by it. WH delivered to ambient is about 40% of the fuel energy consumed by engine-generator [J2] Only this heat is supposed to be stored in SGSP after accounting some losses through surface of exhaust pipe based on the location. Therefore, SGSP's size is predicted based on principle of equivalent heat i.e. the net generated WH is equal to the maximum possible capacity of SGSP. LCZ (thickness = 0.15 m) has the maximum SC at saturated state whereas UCZ (thickness = 0.10 m) has the lowest SC. SC in NCZ (thickness = 0.20 m) increases in downward direction. The thickness of different zones is selected (in the same proportion) as per the optimization study of SGSP to obtain a maximum temperature in LCZ as reported in [Sayer et al. 2016]. SC along with various fluid properties such as ρ_{sw} , c_{sw} and k_{sw} across the three zones of SGSP are presented in Table 4.3.1. SC is measured

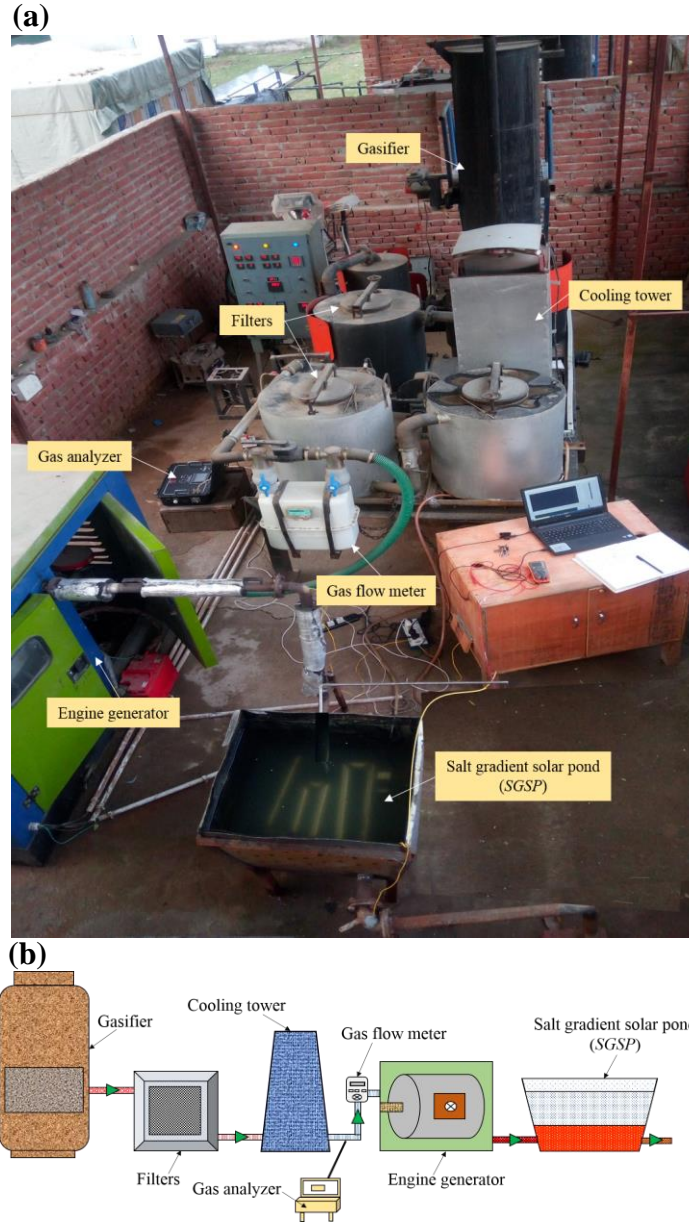


Figure 4.3.1: (a) Photograph and (b) block diagram of the experimental setup

by a Horiba made salinometer while the other properties are calculated via different correlations as mentioned in [section 4.2.1.2](#). The temperature at different locations (LCZ, NCZ, UCZ, waste heat, inlet and outlet of SGSP) is measured by using K-type thermocouples connected with DAQ. A total of 4 experiments (Exp. 1, 2, 3 and 4) with three replicates of each have been performed during 1 hour under variable conditions of engine load (W_L), frequency (f) and ambient temperature i.e. T_a as presented in

[Table 4.3.2](#) and recorded the values of various measured parameters at 10 minutes of interval. Since the biomass engine combined with gasifier is placed inside a closed room due to space

constraints, therefore, SGSP connected to engine is purely operated by WH but it is limited and can place in open in order to access to solar radiation.

Table 4.3.1: Properties of salt/saline water (fluid) stored in SGSP

| Zone | | Thickness (m) | Salt concentration (%) | Density (kg/m ³) | Specific heat kJ/(kg·K) | Thermal conductivity W/(m·K) |
|------|-------------|------------------|------------------------------|---------------------------------|-------------------------------|------------------------------------|
| UCZ | | 0.10 | 0.49 | 1005.73 | 4.16 | 0.616 |
| NCZ | Sub-layer 1 | 0.05 | 3.14 | 1036.74 | 4.03 | 0.608 |
| | Sub-layer 2 | 0.05 | 8.28 | 1096.99 | 3.76 | 0.592 |
| | Sub-layer 3 | 0.05 | 13.82 | 1161.69 | 3.48 | 0.572 |
| | Sub-layer 4 | 0.05 | 19.57 | 1228.97 | 3.18 | 0.547 |
| LCZ | | 0.15 | 22.65 | 1265.01 | 3.03 | 0.532 |

Table 4.3.2: Experiments run under different conditions

| Parameter | Exp. 1 | Exp. 2 | Exp. 3 | Exp. 4 |
|---------------------------------|--------|--------|--------|--------|
| Engine load, W_L (kW) | 1 | 1 | 3 | 3 |
| Frequency, f (Hz) | 45 | 45 | 48 | 48 |
| Ambient temperature, T_a (°C) | 16 | 21 | 13 | 16 |

4.3.1.2 Materials and methods

The schematic of SGSP with three regions (LCZ, NCZ and UCZ) is characterized in [Figure 4.3.2](#). The temperatures at different locations are symbolized by blue colored crossed circles as shown in the same figure where waste heat, inlet and outlet of SGSP, LCZ, NCZ, UCZ and ambient temperatures are represented by T_{WH} , $T_{WH, in}$, $T_{WH, out}$, T_{LCZ} , T_{NCZ} , T_{UCZ} and T_a respectively. Additionally, m_{WH} , m_{LCZ} and m_{NCZ} respectively represent the mass (kg) of flue gases (waste heat/WH) over period of 1 hour, LCZ and NCZ water whereas c_{WH} , c_{LCZ} and c_{NCZ} respectively indicate the specific heat (kJ/kg·K) of the same.

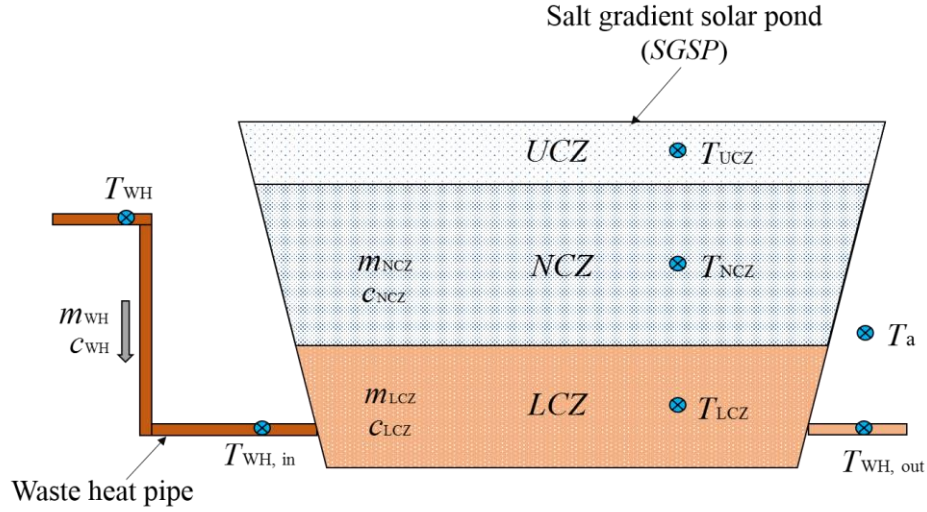


Figure 4.3.2: Schematic of a SGSP with various notations

4.3.1.2.1 Effectiveness of exhaust pipe

The effectiveness of exhaust pipe installed in the SGSP is a function of actual heat transfer to saline water of SGSP ($Q_{act.}$) and maximum possible heat transfer to SGSP ($Q_{max.}$) as given below [Wakeland, and Keolian 2004],

$$\text{Effectiveness} = \frac{Q_{act.}}{Q_{max.}} \quad (4.3.1)$$

Since, mainly transferred heat is occupied in LCZ and NCZ while UCZ do not store the thermal energy or it absorbs a very minor value that can be ignored. Therefore, the actual heat gained by saline water i.e. $Q_{act.}$ is calculated as given below,

$$Q_{act.} = m_{LCZ} \times c_{LCZ} \times \Delta T_{LCZ} + m_{NCZ} \times c_{NCZ} \times \Delta T_{NCZ} \quad (4.3.2)$$

$Q_{max.}$ occurs when the fluid of the smallest heat capacity undergoes the maximum temperature difference available and it is given by the following equation,

$$Q_{max.} = C_{min.} \times (T_{WH, in} - T_{LCZ, i}) \quad (4.3.3)$$

where, subscript i indicates the initial temperature, $C_{\min.}$ represents the minimum heat capacity between WH (C_{WH}) and salt water (C_{SW}). Here, the minimum value is found for WH i.e., $C_{WH} < C_{SW}$.

4.3.1.2.2 Thermal efficiency of SGSP

The capability of a SGSP is evaluated through thermal efficiency i.e. η_{SGSP} which shows the amount of heat stored in LCZ over the total heat transferred by WH as described below,

$$\eta_{SGSP} = \frac{m_{LCZ} \times c_{LCZ} \times \Delta T_{LCZ}}{m_{WH} \times c_{WH} \times \Delta T_{WH}} \quad (4.3.4)$$

where, ΔT_{WH} represents the temperature gradient of WH across SGSP i.e. $T_{WH, in} - T_{WH, out}$.

4.3.1.3 Results and discussion

4.3.1.3.1 Calorific value of syngas

CV measures the quality of syngas produced in the gasifier and optimum gasification process results in maximum CV. Therefore, higher value of CV is always desirable for better combustion in engine-generator to produce efficient power. Thus, it is initially directly measured to analyze the gasification process from a gas analyzer as presented in [Figure 4.3.3a](#) and the same has been found in the range of 5.31-5.43 MJ/m³ as shown in [Figure 4.3.3b](#). The variation in CV for all experiments is found to be very less and analyzed that it is very close to the optimum level (5.486 MJ/m³) as reported in [section 3.1.4.2](#).

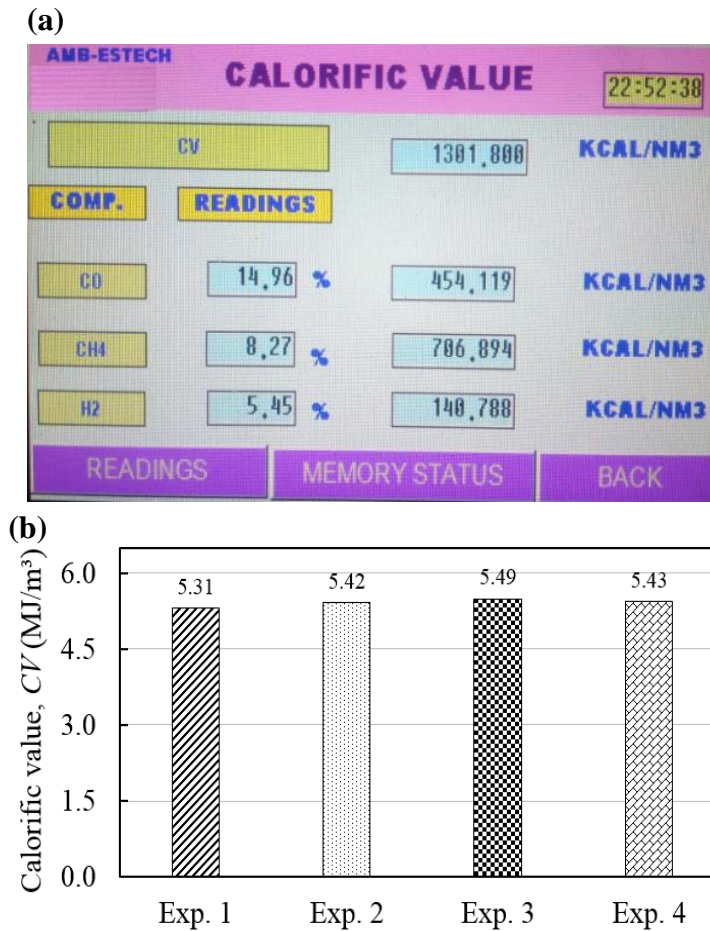


Figure 4.3.3: (a) Photograph of measured CV from analyzer and (b) CV of syngas measured for all run

4.3.1.3.2 Waste heat temperature at inlet and outlet of a SGSP

WH generated from the engine-generator system is directly recovered by combining a SGSP. Therefore, the performance of SGSP mainly depends upon T_{WH} which is measured at three locations: (a) waste heat in the exhaust pipe (2 m from the exit port of engine), (b) at inlet and (c) outlet of SGSP as presented in Table 4.3.3. The maximum value of T_{WH} is found as 396.16 °C at $W_L = 3$ kW and $f = 48$ Hz. SGSP is connected to exhaust pipe at a location 3.5 m from the exit port of engine and the stainless steel made exhaust pipe has given 4 turns in LCZ to obtain a large temperature difference between inlet and outlet of SGSP. The maximum temperature differentials of 166.65 °C, 181.54 °C, 215.02 °C and 237.8 °C are obtained at the end points (60 minutes) corresponding to Exp. 1, 2, 3, and 4 respectively. This may be further increased by connecting the SGSP close to the engine's exit port, but for safety purpose the same has been kept at a certain distant.

Table 4.3.3: Waste heat temperatures at inlet and outlet of a SGSP for all run

| Parameter | Times (minutes) | Exp. 1 | Exp. 2 | Exp. 3 | Exp. 4 |
|--|--------------------|--------|--------|--------|--------|
| Waste heat at inlet, $T_{WH, in}$ (°C) | 10 | 262.45 | 281.86 | 335.56 | 372.76 |
| | 20 | 246.82 | 281.04 | 331.48 | 365.73 |
| | 30 | 241.20 | 267.98 | 316.61 | 354.47 |
| | 40 | 235.79 | 264.08 | 310.18 | 351.80 |
| | 50 | 221.96 | 262.87 | 316.19 | 350.14 |
| | 60 | 237.86 | 263.07 | 315.68 | 350.12 |
| Waste heat at outlet, $T_{WH, out}$ (°C) | 10 | 64.22 | 71.09 | 83.01 | 103.21 |
| | 20 | 69.62 | 79.71 | 90.95 | 108.26 |
| | 30 | 69.37 | 80.66 | 94.76 | 109.48 |
| | 40 | 70.88 | 82.35 | 100.32 | 110.50 |
| | 50 | 72.33 | 81.79 | 99.01 | 112.22 |
| | 60 | 71.21 | 81.53 | 100.66 | 112.32 |

4.3.1.3.3 Effectiveness of exhaust/waste heat pipe

The system is known to be effective when $Q_{act.}$ reaches as close as possible to $Q_{max.}$ under the given conditions. Figure 4.3.4 displays the effectiveness of exhaust pipe and found in the range of 0.75-0.77 which is much higher than 0.55 obtained experimentally for the heat exchanger applied to the exhaust of diesel engine [Bari and Hossain 2013]. This shows that the heat is transferred effectively in SGSP through the structure of exhaust pipe. Also, the effectiveness could be further improved if a copper made pipe was used instead of steel which has high thermal conductivity (k) of about 400 W/(m²K).

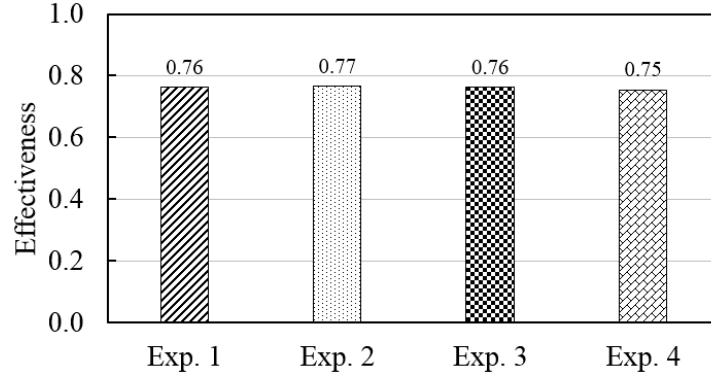


Figure 4.3.4: Effectiveness of exhaust pipe for all experiments

4.3.1.3.4 Maximum temperature achieved in LCZ, NCZ and UCZ of SGSP

Figure 4.3.5 shows the maximum temperature achieved in LCZ ($T_{LCZ, \max.}$), NCZ ($T_{NCZ, \max.}$), and UCZ ($T_{UCZ, \max.}$) of SGSP for all experiments. It can be clearly seen that $T_{LCZ, \max}$ is measured as 65.42 °C at $W_L = 3$ kW and $f = 48$ Hz. Corresponding to that, the values of $T_{NCZ, \max.}$ and $T_{UCZ, \max.}$ are observed 49.89 °C and 20.88 °C respectively at T_a of 16 °C. Therefore, the thermal energy can be stored at high temperatures in LCZ for long duration which can be further processed for various applications.

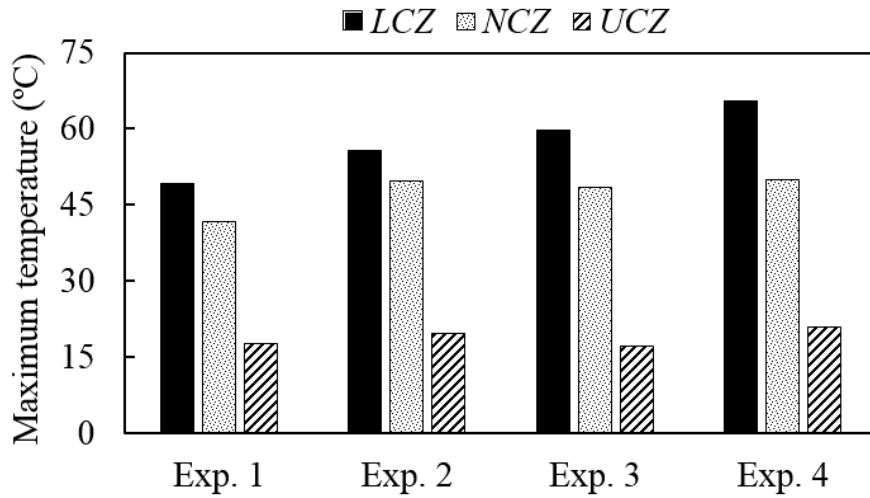


Figure 4.3.5: Maximum temperature attained in LCZ, NCZ and UCZ of SGSP

4.3.1.3.5 Transient change of temperature profile corresponding to elevation from bottom

Figure 4.3.6 represents the transient change of temperature profile within SGSP corresponding to elevation from bottom at $W_L = 3 \text{ kW}$ and $f = 48 \text{ Hz}$. It is observed that during the starting phase of experiment, T_{LCZ} (elevation range within 0-0.15 m) increases at a higher rate as compared to later phase. This is attributed to the fact that initially the temperature difference between the exhaust/waste heat pipe and LCZ is high, whereas the same is decreasing with time. Therefore, at a certain T_{WH} , the maximum heat is transferred at the starting phase compared to end phase. This leads to attaining a higher T_{LCZ} at early stages of experiment. Another factor also involves that initially c_{LCZ} is low but it marginally increases with time due to slightly diffusion of salt. Therefore, at a given heat input, the lesser $(mc)_{LCZ}$ at initial stages enable LCZ to obtain a higher temperature rise compared to end stage of experiment. From the experimental results, it is observed that at initial phase (0-20 minutes), T_{LCZ} rises at an increasing rate of $1.11 \text{ }^\circ\text{C/min}$. (0-10 minutes) and $0.82 \text{ }^\circ\text{C/min}$. (11-20 minutes). But at later phase, the same is found as $0.42 \text{ }^\circ\text{C/min}$. (41-50 minutes) and $0.31 \text{ }^\circ\text{C/min}$. (51-60 minutes).

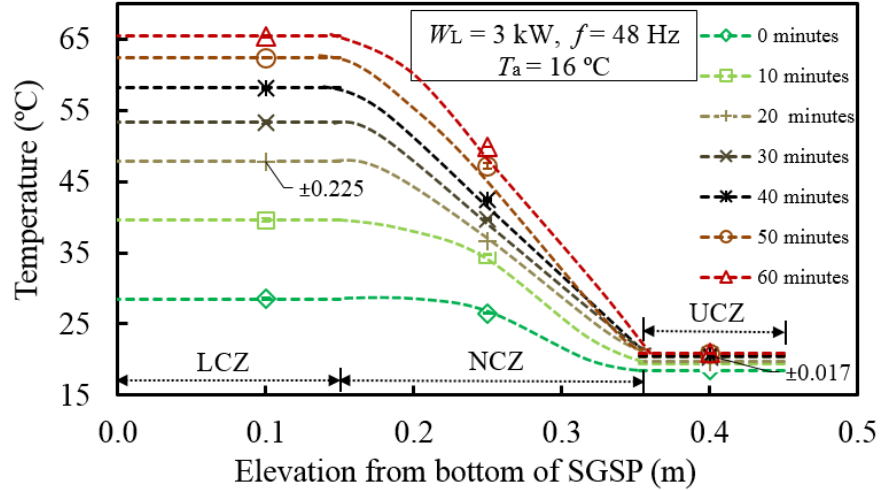


Figure 4.3.6: Transient change of temperature profile within SGSP corresponding to elevation from bottom

4.3.1.3.6 Temperature gain in LCZ

Figure 4.3.7 represents the temperature gain in LCZ i.e. ΔT_{LCZ} of SGSP at various ambient conditions. It has been observed that the maximum ΔT_{LCZ} is found as $36.91 \text{ }^\circ\text{C}$ at $W_L = 3 \text{ kW}$ and

$f = 48$ Hz. It can also be clearly seen that ΔT_{LCZ} is independent of T_a , therefore SGSP can store the thermal energy at high temperatures even at low T_a . This is due to the fact that five surfaces (front, back, left side, right side and bottom) of LCZ are thermally insulated that restricting the conduction heat loss, while the sixth surface (upper one) is in direct contact with NCZ which also acts as an insulation to convective heat loss. However, some heat is still lost from LCZ to UCZ through NCZ via conduction.

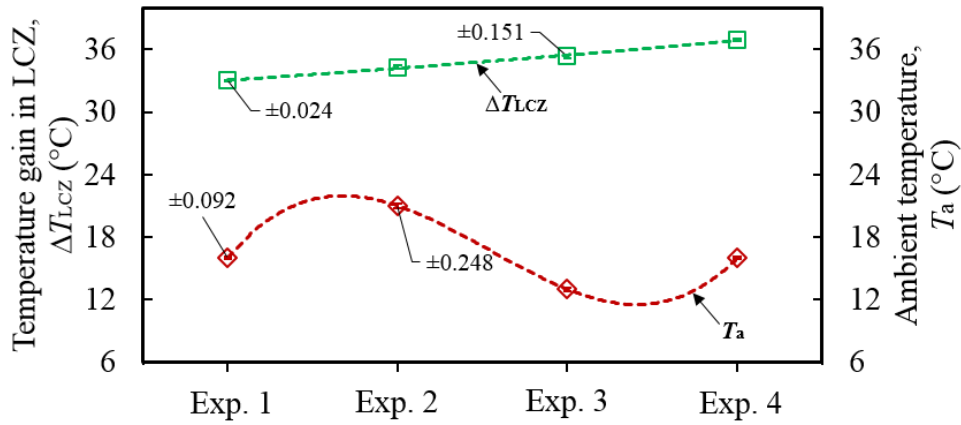


Figure 4.3.7: Temperature gain in LCZ for all experiments

4.3.1.3.7 Thermal storage capacity and efficiency of SGSP

Thermal storage capacity of SGSP i.e. Q_{SGSP} mainly depends upon its size, design, insulation structure and the properties of fluid. So, a large SGSP obviously has large thermal capacity but its maximum accessible capacity depends upon the properties of fluid as well as the development of various zones in SGSP. This is because NCZ plays a key role in storing the heat in LCZ because it acts as an insulation to convective heat loss, therefore the sub-layers in NCZ need to be carefully developed. Figure 4.3.8 shows Q_{SGSP} and η_{SGSP} obtained for all experiments and the same are found in the range of 5.18-5.79 MJ and 42.31-47.73% respectively. Since, Q_{SGSP} depends upon ΔT_{LCZ} and further η_{SGSP} depends upon Q_{SGSP} , therefore both vary in accordance with ΔT_{LCZ} .

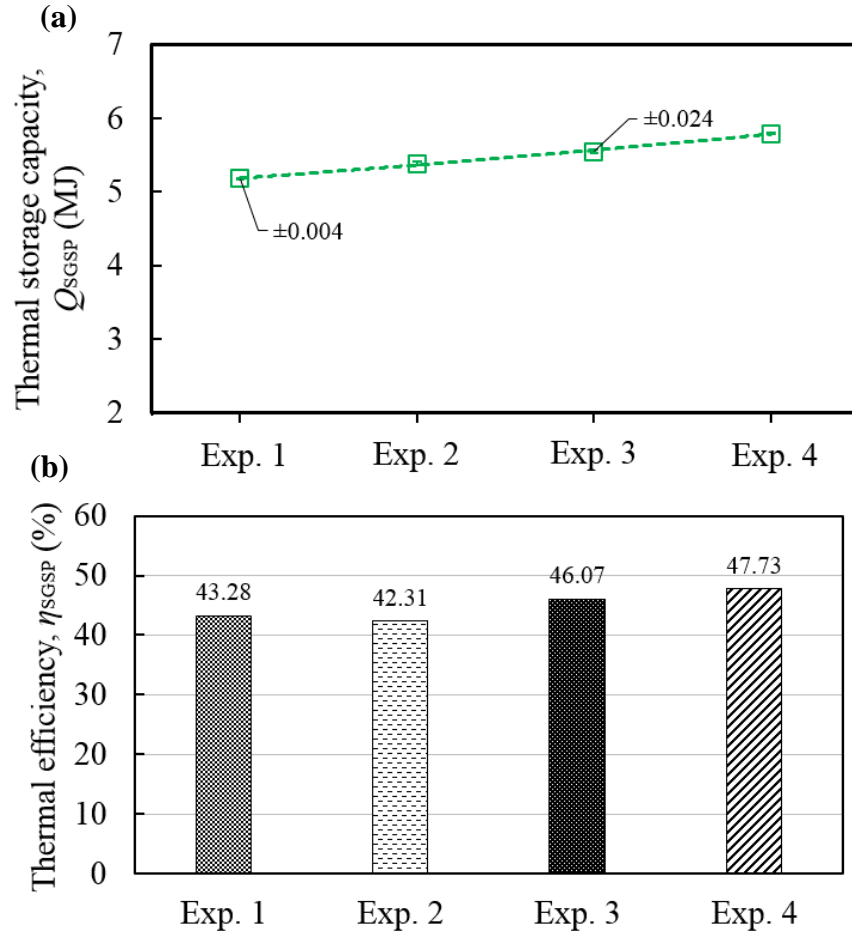


Figure 4.3.8: (a) Thermal storage capacity and (b) thermal efficiency of SGSP for all experiments

4.3.1.4 Summary

The summary of key points is given below,

- CV of syngas is measured in the range of 5.31-5.43 MJ/m³ and found the optimum gasification process.
- WH generated from the biomass engine has the maximum value of 396.16 °C at $W_L = 3$ kW and $f = 48$ Hz and corresponding $T_{LCZ, \max}$ is measured as 65.42 °C. The structure of waste heat/exhaust pipe installed in SGSP is able to efficiently transfer the energy with the effectiveness of 0.75-0.77.

- Lastly, the maximum ΔT_{LCZ} and Q_{SGSP} during 1 hour of experiment are noted as 36.91 °C and 5.79 MJ respectively with 47.73% of η_{SGSP} .

From the above outcomes, it is realized that SGSP could be an efficient thermal storage device for the available WH which can be further used for various applications such as power generation, desalination, drying and process heating.

4.3.2 Performance analysis of the developed TEGs-array-based HRS integrated with SGSP

4.3.2.1 Experimental setup details

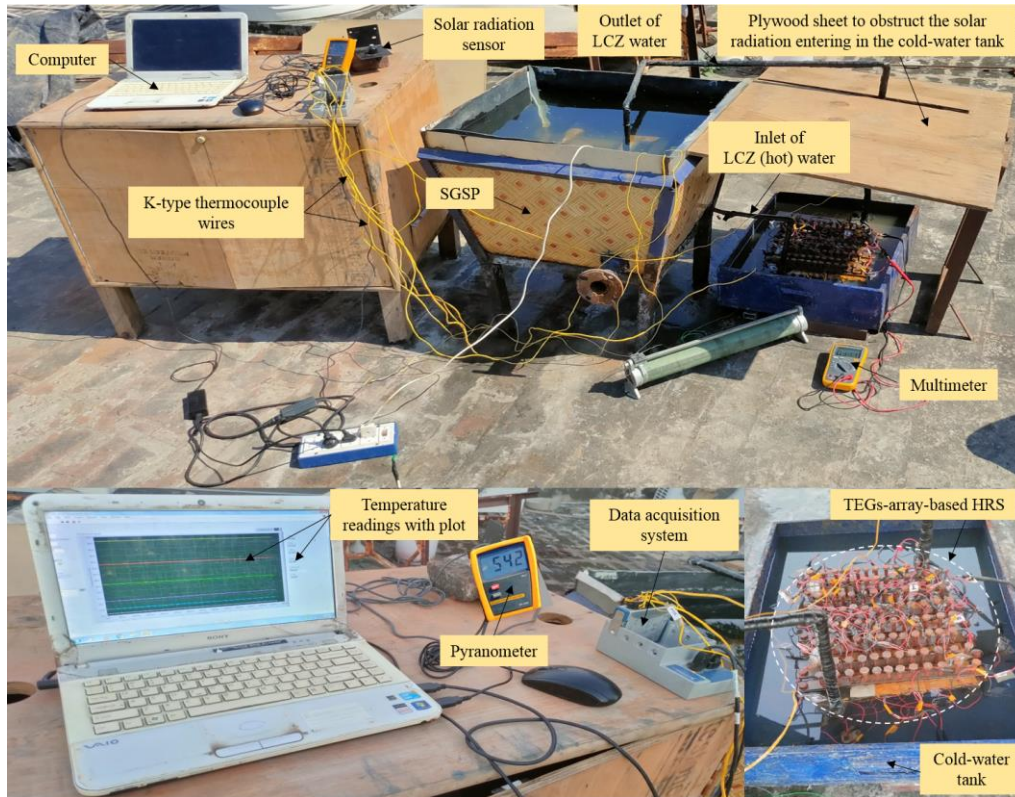
A TEGs-array-based HRS is developed for effective power generation at low temperature of SGSP as shown in

[Figure 4.3.9](#). The stored energy of LCZ acts as a heat source for the TEGs-array-based HRS. After operating the system for 27 days, it has been realized that the output produced from the developed HRS is not enough to charge a 12 V, 80 Ah battery, so it is further driven by another available heat source i.e., WH of biomass driven engine-generator. Therefore, the experimental work on the developed TEGs-array-based HRS is completed into two phases (a) the developed HRS integrated with SGSP (proposed system) is first run by the solar energy under real ambient conditions and (b) then the same proposed system is operated by WH biomass driven engine-generator. The second-phase of the experimental work is needed to address the deficiencies involved in the first portion (a) of work. The details about the first part (a) of the setup is shown in

[Figure 4.3.9](#). Since, the same proposed system is an integral part of the second phase of setup, so all the details about this setup are collectively described in next phase (b) of the setup. The experimental arrangement and schematic of the second phase (b) of the setup describing various components are shown in [Figure 4.3.10](#). The setup consists of (1) a gasifier, (2) filters, (3) a cooling tower, (4) a gas analyzer (5) a gas flow meter, (6) a biomass engine-generator, (7) a WH (flue gas) exhaust pipe, (8) a control panel, (9) a SGSP, (10) a TEGs-array-based HRS, (11) a water tank, (12) submersible pumps, (13) a water circulation pipe, (14) thermocouple wires with a DAQ, (15) a computer and (16) a multimeter. The numbers here refer to the different denotations as shown in [Figure 4.3.10 \(a, e\)](#). The developed HRS is first run by the solar energy (where solar radiation i.e. S is measured using a pyranometer equipped with a sensor) and thereafter operated by the WH of a 10 kW capacity biomass engine. The biomass engine is fuelled by syngas produced from the gasification process carried out in a downdraft biomass gasifier and the more details about it are

explained in [section 3.1.1 and 3.1.2](#). Most of the chemical energy of syngas supplied to the engine-generator however is lost in the form of WH through exhaust pipe and this WH is further stored in LCZ of SGSP which drives the developed TEGs-array-based HRS for producing power. The construction details of SGSP is described in [section 4.3.1.1](#). A leak-proof rectangular-shaped array HRS with size $0.33 \text{ m} \times 0.25 \text{ m} \times 0.01 \text{ m}$ is fabricated from a high thermal conductive material sheet (i.e. copper) of 0.001 m thickness via drilling, taping and welding (gas) process. The size of HRS is chosen based on the surface area (top and bottom) of HRS equivalent to the surface area of available TEGs. The thickness of array HRS is kept equal to water circulation pipe for smooth flow of hot LCZ water through it. On the both sides (top and bottom) of array HRS, a total of 92 TEGs are connected in series (46 series-connected TEGs on either side) to form the TEGs-array based HRS. On two parallel sides of HRS a water circulation pipe made of stainless steel (diameter = 0.01 m) is welded for the inflow and outflow of hot LCZ water. The TEGs-array-based HRS is dipped inside a separate water tank made of galvanized iron (GI) sheet containing cold water. The cold water temperature (T_{cw}) is maintained by recirculation of water between GI water tank and water tank of cooling tower by using two same capacity submersible pumps in order to maintain a constant water level in GI tank. This TEGs-array-based HRS can be directly immersed in the water tank of a cooling tower in order to eliminate the use of submersible pumps but it is immersed in a separate tank for ease of operation and the space constraint between the cooling tower and array system. Further it is being suggested that a small modifications is desirable in the location of components to remove the space limitations. A total of nine K-type thermocouples are provided at various points, represented by + sign surrounded with circle in [Figure 4.3.10e](#) to monitor the temperature variations. Other sides of the thermocouple wires are connected to a DAQ system and temperature values are displayed on the computer screen. Various measurement points are located at LCZ, NCZ and UCZ, cold water in GI tank, WH at engine exhaust, inlet and outlet of SGSP, ambient and outlet of TEGs-array-based HRS. Voltage and current generated from the TEGs-array-based HRS are measured by a multimeter.

(a)



(b)

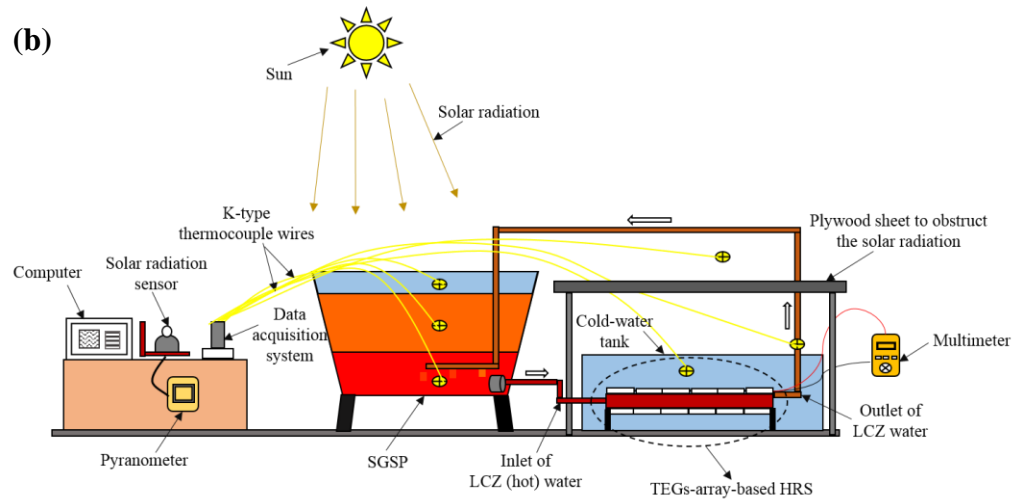
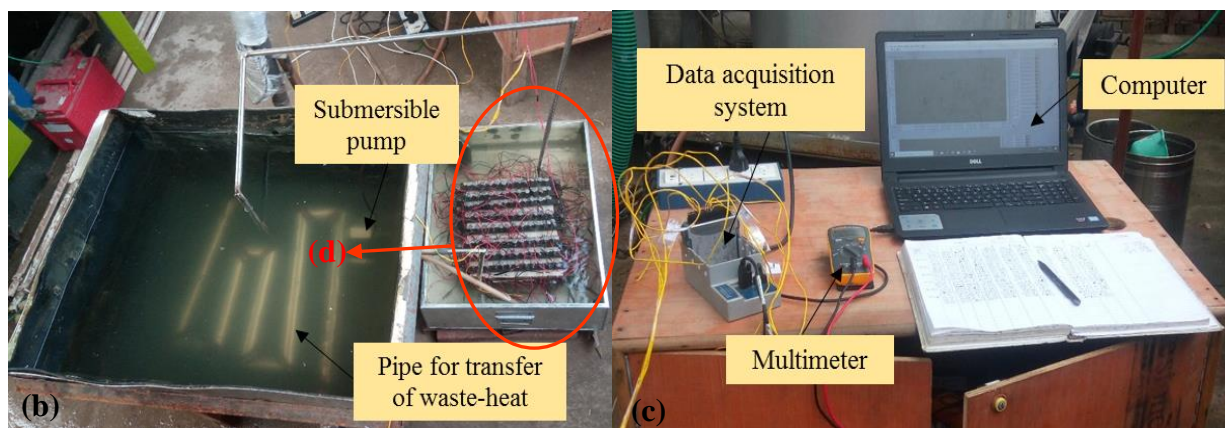
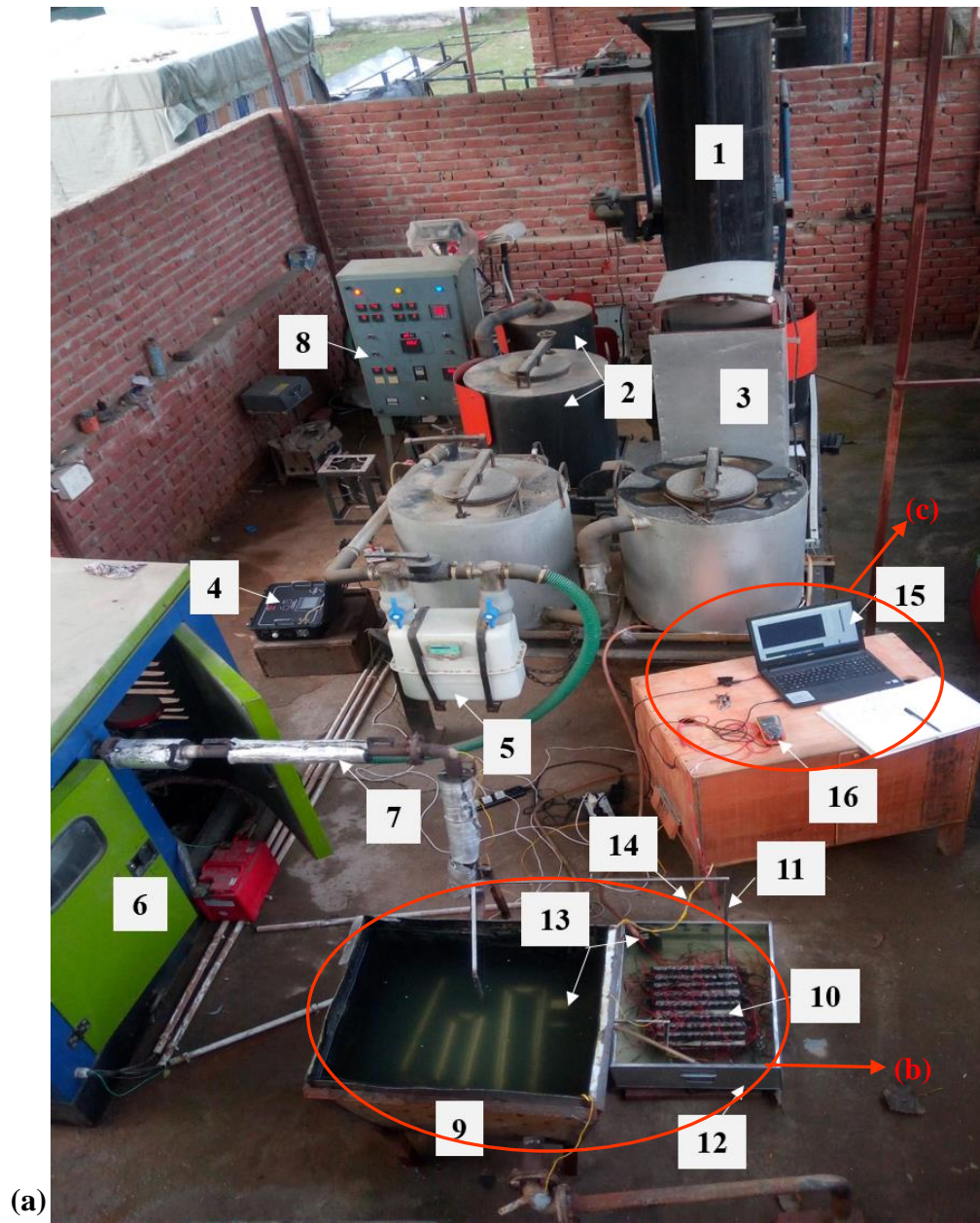


Figure 4.3.9: (a) Photograph and (b) block diagram describing about the first part of the experimental setup



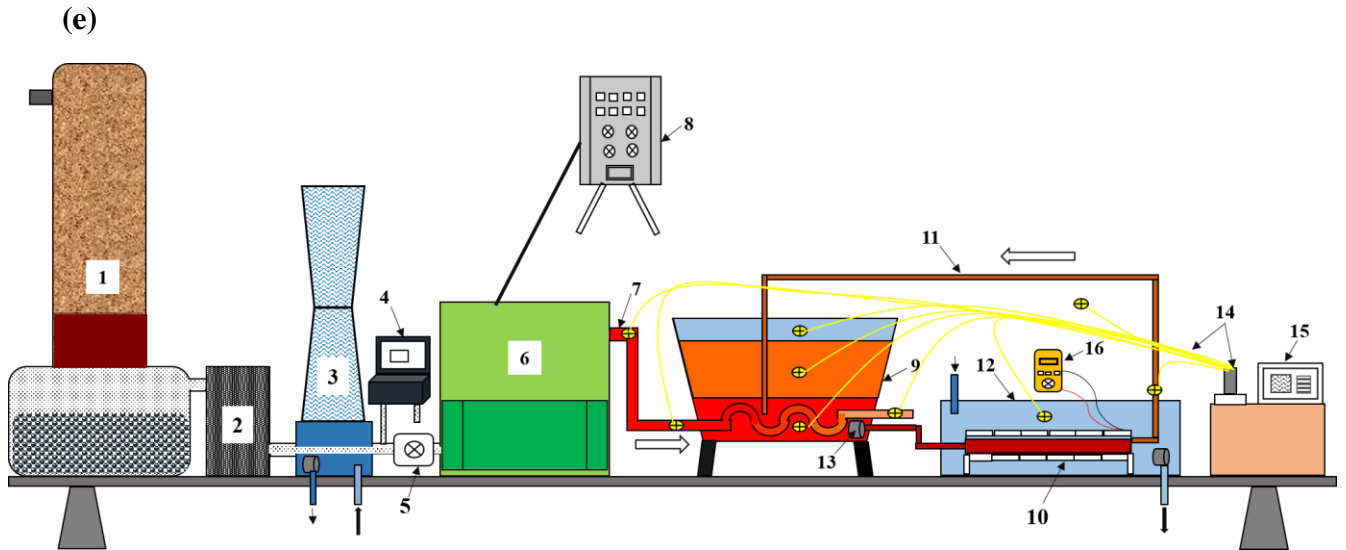
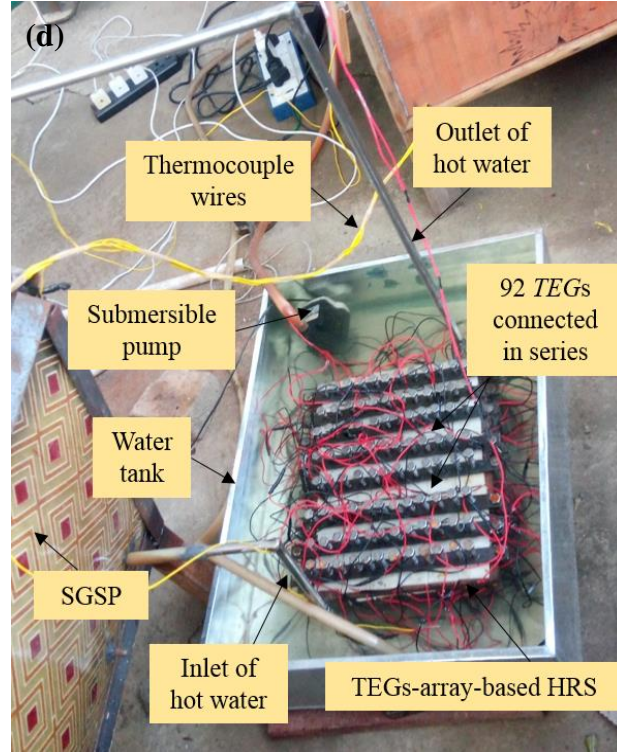


Figure 4.3.10: (a-d) Experimental setup and (e) schematic of the proposed HRS

4.3.2.2 Experimental procedure

In the first phase of work, S is entered in SGSP from top and reaches at bottom LCZ of pond where it stores them as a thermal energy by halocline effect. This process continuously increases temperature of LCZ water i.e. T_{LCZ} but in second phase, WH of biomass driven engine-generator is stored in SGSP which rises its T_{LCZ} . Thereafter this hot LCZ water is passed through TEGs-

array-based HRS using a submersible pump where it transfers heat to the hot side of TEG by conduction and convection that keeps one side of TEGs hot. During this process, the other side of TEGs is in direct contact with cold water to keep a low temperature at this side since TEGs-array-based HRS is dipped inside GI water tank containing cold water. The direct contact of cold water with TEGs allows the maximum transfer of heat from TEG's surface. This creates a temperature gradient across TEGs i.e. ΔT_{TEG} and produces voltage as well as current which are measured by a multimeter. The output power is measured when the external load resistance is provided by a rheostat as shown in Figure 4.3.11a.

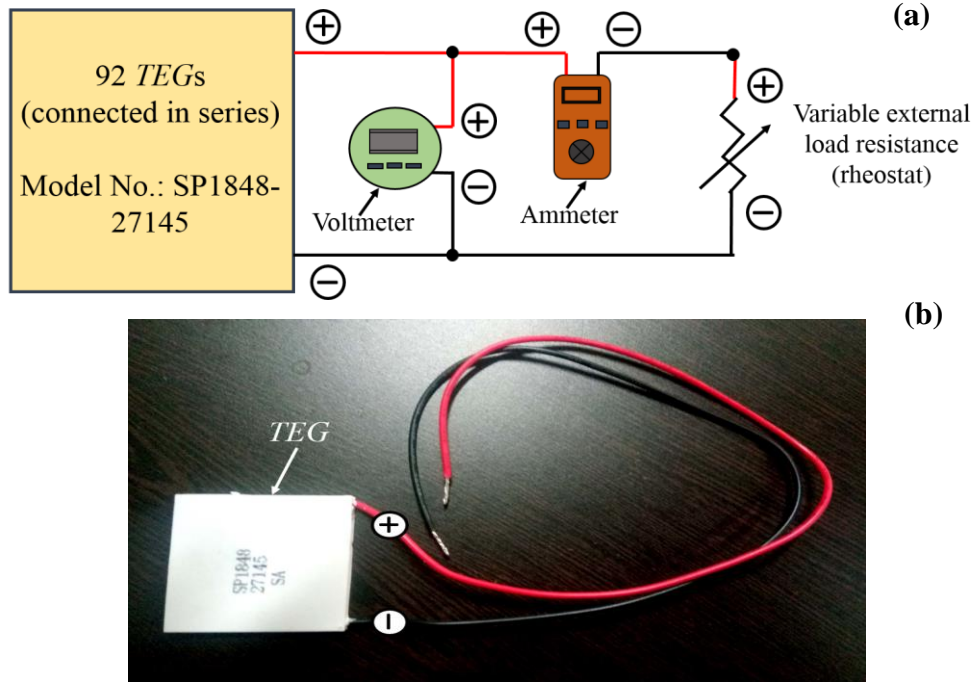


Figure 4.3.11: (a) Wiring connection for measuring the output power of TEGs and (b) photo of TEG module used

4.3.2.3 Thermal resistances between heat source (LCZ) and hot side of TEGs

Here, hot water from LCZ of a SGSP is passed through the TEGs-array-based HRS for effectively transferring the heat to hot surface of TEGs (Figure 4.3.12). The heat is transferred from flowing hot LCZ water to inner surface of copper-made array via convection and further to its outer surface (where hot side of mounted TEGs is equilibrium with this outer surface) through conduction. Convection ($R_{t, \text{conv.}}$) and array wall conduction ($R_{t, \text{cond.}}$) resistances are offered at both top and bottom surfaces.

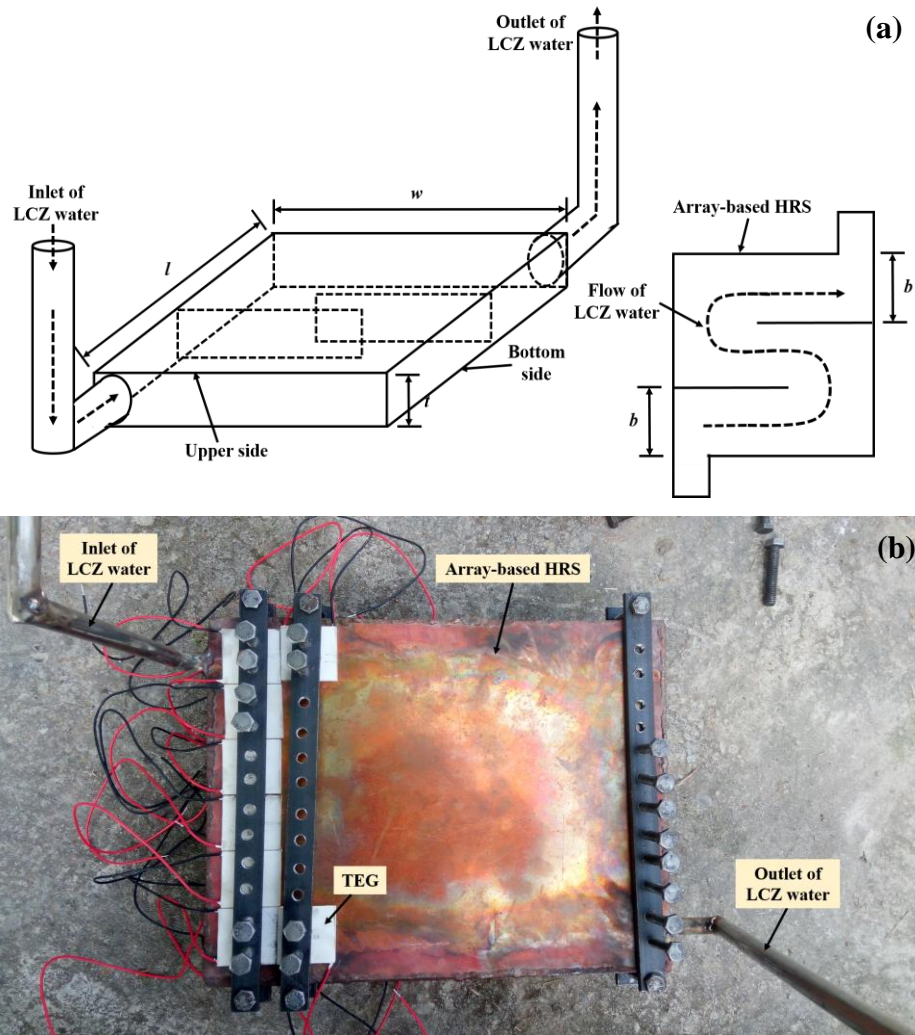


Figure 4.3.12: (a) Schematic and (b) actual photograph of the array-based HRS

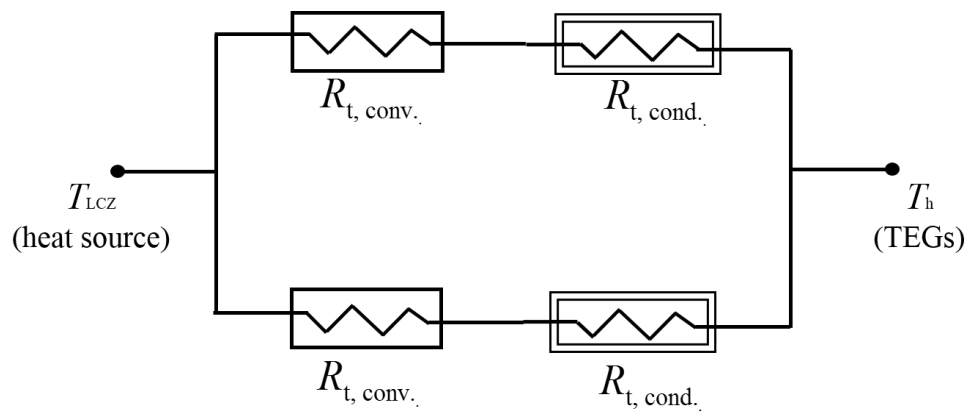


Figure 4.3.13: Thermal resistances between LCZ and hot side of TEGs

of array-based HRS as represented by the resistance network in [Figure 4.3.13](#). At both surfaces, $R_{t, \text{conv.}}$ is connected in series with $R_{t, \text{cond.}}$ and the equivalent thermal resistance ($R_{t, \text{eq.}}$) of array-based HRS is calculated by using [Eq. \(4.3.5\)](#) as:

$$\frac{1}{R_{t, \text{eq.}}} = \frac{1}{R_{t, \text{cond.}} + R_{t, \text{conv.}}} + \frac{1}{R_{t, \text{cond.}} + R_{t, \text{conv.}}} \Rightarrow R_{t, \text{eq.}} = \frac{R_{t, \text{cond.}} + R_{t, \text{conv.}}}{2} \quad (4.3.5)$$

$R_{t, \text{cond.}}$ ($= 1 / h \times A_{\text{wall}}$) is regulated by convective heat transfer coefficient (h) and array wall surface area (A_{wall}) in which $A_{\text{wall}} = l \times w = 0.0825 \text{ m}^2$, where l and w represent the length and width of array HRS, respectively. The value of h is calculated from the Nusselt number (Nu) as given below:

$$Nu = \frac{h \times d_{\text{eq.}}}{k_{\text{LCZ}}} \Rightarrow h = \frac{Nu \times k_{\text{LCZ}}}{d_{\text{eq.}}} \quad (4.3.6)$$

where, k_{LCZ} ($0.532 \text{ W/m} \cdot \text{K}$) is the thermal conductivity of LCZ water while $d_{\text{eq.}}$ [$= (2 \times b \times t) / (b + t) = 0.0183 \text{ m}$] represents the equivalent diameter of flow passage through HRS where, $b = 0.11 \text{ m}$ and $t = 0.01 \text{ m}$, respectively indicate the width and thickness of cross-sectional area through which LCZ water is flowing in HRS. Reynolds number (Re) of flow is estimated by using [Eq. \(4.3.7\)](#) as:

$$Re = \frac{\rho_{\text{LCZ}} \times u \times d_{\text{eq.}}}{\mu_{\text{LCZ}}} \quad (4.3.7)$$

where, ρ_{LCZ} ($= 1265.01 \text{ kg/m}^3$) and μ_{LCZ} ($= 1.7 \times 10^{-3} \text{ N} \cdot \text{s/m}^2$) [[Palliser and McKibbin 1998](#)] denote the density and viscosity of LCZ water respectively whereas u ($= 0.1645 \text{ m/s}$) indicates the velocity of flowing LCZ water and it is equivalent to the ratio of discharge of pump ($1.8 \times 10^{-4} \text{ m}^3/\text{s}$) and area ($b \times t$) of flow passage. Here, Re is found to be 2240 (< 2300) and therefore the flow will be of laminar nature. Nu for laminar flow under forced convection is estimated by using [Eq. \(4.3.8\)](#) as reported by Nagy [[Nagi 2018](#)]:

$$Nu = \frac{h \times d_{\text{eq.}}}{k_{\text{LCZ}}} = 1.86 (Re \times Pr)^{1/3} \left(\frac{d_{\text{eq.}}}{L} \right)^{1/3} \left(\frac{\mu_{\text{LCZ}}}{\mu_{\text{water}}} \right)^{0.14} \quad (4.3.8)$$

where, L represents the length of flow passage in array and μ_{water} ($= 0.596 \times 10^{-3} \text{ N} \cdot \text{s/m}^2$) indicates the dynamic viscosity of pure water. Here, Prandtl number (Pr) is calculated by using [Eq. \(4.3.9\)](#) as:

$$Pr = \frac{c_{\text{LCZ}} \times \mu_{\text{LCZ}}}{k_{\text{LCZ}}} \quad (4.3.9)$$

The values of h and $R_{t, \text{conv.}}$ are obtained as $506.42 \text{ W/m}^2 \cdot \text{K}$ and $0.02393 \text{ }^\circ\text{C/W}$ respectively. The thickness of copper sheet ($\delta_{\text{cop.}}$) is very less (0.001 m) and it has a high thermal conductivity ($k_{\text{cop.}}$) of $400 \text{ W/m} \cdot \text{K}$ [Khaleghi et al. 2012]. $R_{t, \text{cond.}}$ offered by a array wall surface area is calculated by equation given below [J2]:

$$R_{t, \text{cond.}} = \frac{\delta_{\text{cop.}}}{k_{\text{cop.}} \times A_{\text{wall}}} \quad (4.3.10)$$

The value of $R_{t, \text{eq.}}$ for array-based HRS is found as $0.01198 \text{ }^\circ\text{C/W}$, which is very low and can be neglected. Therefore, the hot side temperature of TEGs i.e. T_h may be considered equal to T_{LCZ} . This array-based design enhances the thermal efficiency of heat transfer provided at hot side of TEGs and hence increases its performance. The cold side of TEGs is directly in contact with cold water maintained at a constant low temperature by a cooling tower. Therefore, the cold side temperature of TEGs i.e. T_c is presumed equal to T_{CW} .

4.3.2.4 Results and discussion

The first phase of work covers the measurement of $T_{\text{LCZ, max.}}$, $T_{\text{LCZ, avg.}}$, $S_{\text{avg.}}$ and $T_{\text{a, avg.}}$ during the entire experiments. The values of these parameters are noted from 10 a.m. to 5 p.m. at on hour of interval over 27 days (26 September – 22 October 2021). After reaching T_{LCZ} to the steady-state point, the performance of TEGs-array-based HRS is analysed in the form of V and I_s . The second phase involves the study of T_{WH} , T_{LCZ} , V , I_s , P_o and η_{TEG} at different operating conditions of W_L (1 kW and 3 kW) and f (45 Hz, 48 Hz and 51 Hz). The values (average taken over three replicates) of several performance parameters are measured at a time interval of 10 minutes over 60 minutes of an experiment and presented in plots with standard error.

4.3.2.4.1 Average solar radiation, LCZ and ambient temperatures

$T_{\text{LCZ, avg.}}$, $S_{\text{avg.}}$ and $T_{\text{a, avg.}}$ over a day (daily average) during the entire experiments are presented in Figure 4.3.14. The high $S_{\text{avg.}}$ ($607.83 - 732.75 \text{ W/m}^2$) during the early days raises $T_{\text{LCZ, avg.}}$ upto $39.55 \text{ }^\circ\text{C}$ (4th day) with an average gain (over a day) of $1.17 \text{ }^\circ\text{C}$ per day. Since $S_{\text{avg.}}$ and $T_{\text{a, avg.}}$ directly affect $T_{\text{LCZ, avg.}}$, therefore further variation in $T_{\text{LCZ, avg.}}$ due to change in weather conditions can be seen in the same figure. $S_{\text{avg.}}$ gets fall down to 205.79 W/m^2 (7th day) with $T_{\text{a, avg.}}$ of $31.75 \text{ }^\circ\text{C}$. The change in ambient condition further lowers $T_{\text{LCZ, avg.}}$ to $33.23 \text{ }^\circ\text{C}$. Afterward, the continuous $S_{\text{avg.}}$ increases $T_{\text{LCZ, avg.}}$ to a maximum value of $39.74 \text{ }^\circ\text{C}$, (16th day) at $T_{\text{a, avg.}}$ of $34.06 \text{ }^\circ\text{C}$. Later, it remains in steady-state condition during which $T_{\text{LCZ, avg.}}$ remains close to $38.50 \text{ }^\circ\text{C}$ until the further

change in ambient conditions. The slightly lower of steady-state temperature (of LCZ) than the maximum value is due to decrease in $T_{a, \text{avg.}}$. In the last period of experiment, a large deviation in $S_{\text{avg.}}$ is also observed which again drops $T_{\text{LCZ, avg.}}$ but it rises up with time due to incessant availability of $S_{\text{avg.}}$. During the entire experiments, the maximum $S_{\text{avg.}}$ is found as 732.75 W/m^2 on the 4th day of experiment where $T_{a, \text{avg.}}$ has the value of 33.89°C . The maximum value of $T_{\text{LCZ, avg.}}$ is recorded as 39.74°C (16th day).

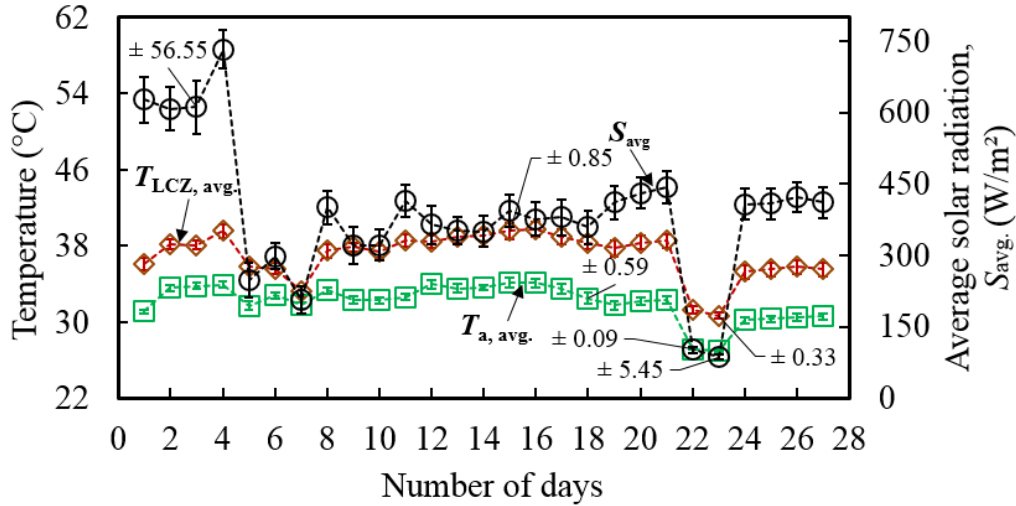


Figure 4.3.14: Deviation in average (over a day) solar radiation, LCZ and ambient temperatures during the entire experiments

4.3.2.4.2 Maximum LCZ temperature in SGSP

$T_{\text{LCZ, max.}}$ attained in a day during the entire experiments is shown in Figure 4.3.15a. The initial T_{LCZ} at the start of experiment is recorded as 30.38°C . During the initial period of experiment, a high rate of temperature gain is observed for T_{LCZ} . Just on the 4th day of experiments, T_{LCZ} reaches to a maximum value of 42.78°C from 30.38°C . This could be continuously increased to a new maximum T_{LCZ} but the change in ambient conditions do not allow to increase it further and reduced to 36.55°C due to a low T_a . This reveals the importance of ambient conditions and dependency of T_{LCZ} on it. Further to reach T_{LCZ} to 41.99°C , it takes 7 days with the continuous availability of S and reached to a highest value of 43.84°C on the 15th day. During the period of steady-state, $T_{\text{LCZ, max.}}$ remains around 43.50°C and thereafter again variable weather conditions play a significant role in the change of $T_{\text{LCZ, max.}}$. The profile of T_{LCZ} with time on the day (15th) of maximum achieved temperature is presented in Figure 4.3.15b. During morning (10:00-12:00), the rate of temperature rise is observed as 1.90°C per hour while the same is found as 2.84°C per hour in afternoon (12:00-14:00) due to the high S falls normal to the surface of water which leads to reaching of all

radiation at LCZ. This normal penetration of S increases the rate of rise in T_{LCZ} . Reaching to evening (14:00-16:00), a low rate of temperature rise ($0.70\text{ }^{\circ}\text{C}$ per hour) is noticed but T_{LCZ} achieves its maximum value at evening (16:00) because of continuous gain in T_{LCZ} upto the maximum capacity under certain value of S .

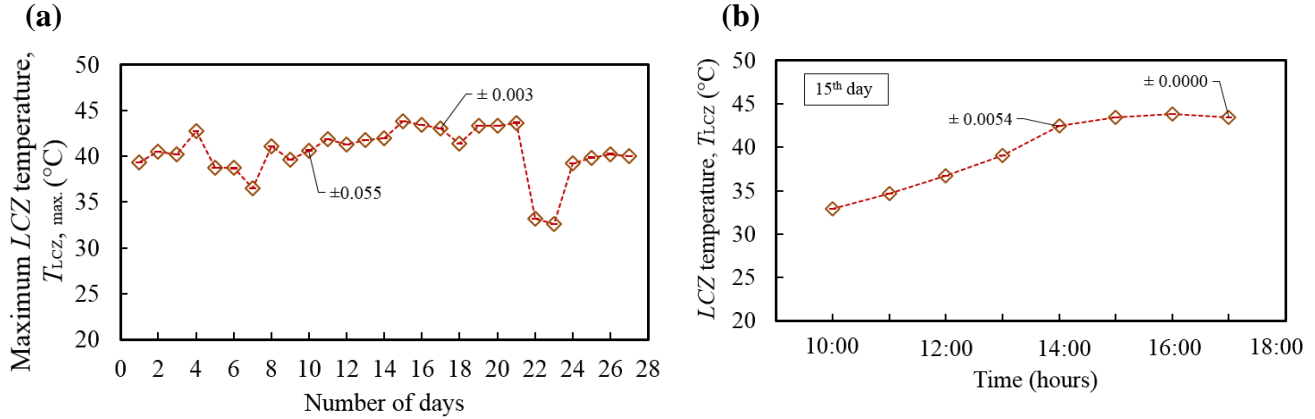


Figure 4.3.15: (a) Variation of maximum LCZ temperature in a day during the entire experiments and (b) the profile of LCZ temperature on the day (15th) of maximum attained temperature

4.3.2.4.3 Open circuit voltage and short circuit current

The obtained V and I_s under the steady-state conditions are shown in Figure 4.3.16. The profile of V and I_s is found almost similar to T_{LCZ} i.e. ambient conditions play a key role in the performance of TEGs-array-based HRS. Therefore, V and I_s are not constant during the steady-state condition and varied from 5.15 V (23th day) to 7.97 V (20th day) and 0.019 A (23th day) to 0.031 A (20th day) respectively. The maximum V i.e. V_{max} is obtained as 7.97 V at 43.36 $^{\circ}\text{C}$ of T_{LCZ} but at a higher T_{LCZ} (43.67 $^{\circ}\text{C}$), a lower V of 7.89 V is obtained. This means the output of TEGs-array-based HRS is not only depend upon T_{LCZ} but also on T_{CW} as well. It has been observed that at the initial stage of LCZ water flow, T_{LCZ} rapidly losses 1-2 $^{\circ}\text{C}$ of temperature in heating up the internal surface area of water circulation pipe and array-based HRS. Thereafter, it remains constant for short period of time and then starts to decline even with continuous influx of S in SGSP because continuously lossing of heat from LCZ water to TEGs is high compared to absorption of S (as a thermal energy) in LCZ. Furthler, the same also declines in the night too due to unavailability of S at that time. The continuous flow of LCZ water transfers the heat energy at hot side of TEGs and heats up. The direct contact of cold water at other side of TEGs takes most of the heat energy. Since, the cold water is still in the GI tank, the water adjacent to cold surface of TEGs has more temperature than the water far away from the surface. With time, the temperature of water close to the surface of

TEGs continues to increase due to the high rate of energy transfers from TEGs to cold water as compared to cold water to ambient, thereby leading in declination of output performance. So, there are lots of inflation in the output when operated from the SGSP driven by solar energy. Therefore, the required constant output from this proposed HRS working under the actual weather conditions is not possible in certain conditions due to some of the above-mentioned issues. To obtain a constant output from the system, it is further operated purely from WH of biomass engine for continuous power generation and efficient recovering of WH. The WH from the biomass engine ensures nearly constant heat input into SGSP.

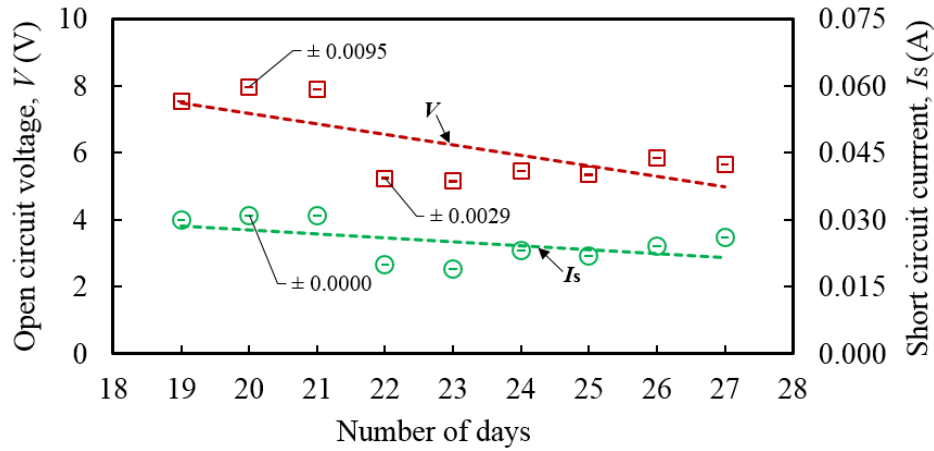


Figure 4.3.16: Open circuit voltage and short circuit current during the steady-state condition

4.3.2.4.4 Transient variation of waste heat temperature

Figure 4.3.17 illustrates the transient variation of T_{WH} under different loading conditions (W_L) and operating frequencies (f) of engine. In the initial phase of experiments, T_{WH} increases drastically up to a maximum point and then decreases slightly with time due to a decrease in CV of syngas [J1]. The decrease in CV lowers the temperature of combustion chamber and subsequently decreases T_{WH} [J3]. It is observed that with an increase in operating f , T_{WH} also increases because more fuel energy enters in the combustion chamber of engine at higher f . The rate of increment of T_{WH} is almost same as that of f . A large amount of energy entering the engine, having a constant thermal efficiency of 30-40%, releases WH at relatively higher temperatures. The maximum values of T_{WH} are obtained as 360.72 °C and 437.55 °C at 1 kW and 3 kW of W_L respectively when engine was run at f of 51 Hz.

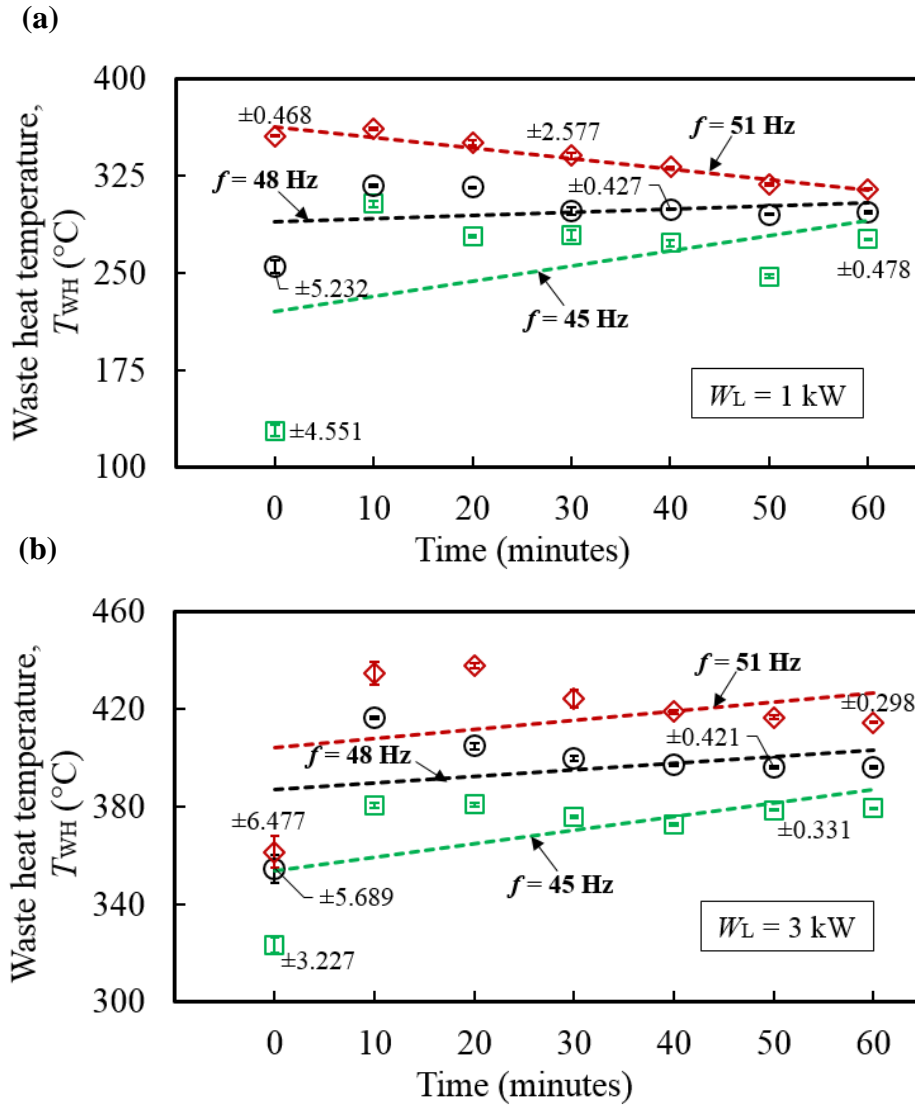


Figure 4.3.17: Transient variation of waste heat temperature at engine loads of (a) 1 kW and (b) 3 kW under different operating frequencies

4.3.2.4.5 Transient variation of LCZ temperature

Since WH of biomass engine is conveyed to LCZ of SGSP via steel made exhaust pipe, therefore T_{WH} directly affects T_{LCZ} . The transient variation of T_{LCZ} at 1 kW and 3 kW of W_L under different operating f and T_a are presented in Figure 4.3.18. It is observed that T_{LCZ} increases with the passage of time as more and more WH gets transferred to water present in LCZ through conduction and convection. Furthermore, the dependence of T_{LCZ} on T_{WH} leads to an increase in T_{LCZ} with the operating time. The increase of T_{LCZ} due to increase of f from 45 Hz to 48 Hz is larger than the same when f increases from 48 Hz to 51 Hz. Therefore, it should also be noted that T_{LCZ} does not increase at a constant rate with respect to increase in f . The reason being is the decrease in T_a which causes more surface heat losses from the exhaust pipe to ambient and declines the efficiency as

well as effectiveness of exhaust pipe. Under the operating conditions of 1 kW load at $T_a = 11.77$ °C and 3 kW load at $T_a = 12.46$ °C, the maximum T_{LCZ} is measured as 57.36 °C and 68.04 °C respectively at engine f of 51 Hz.

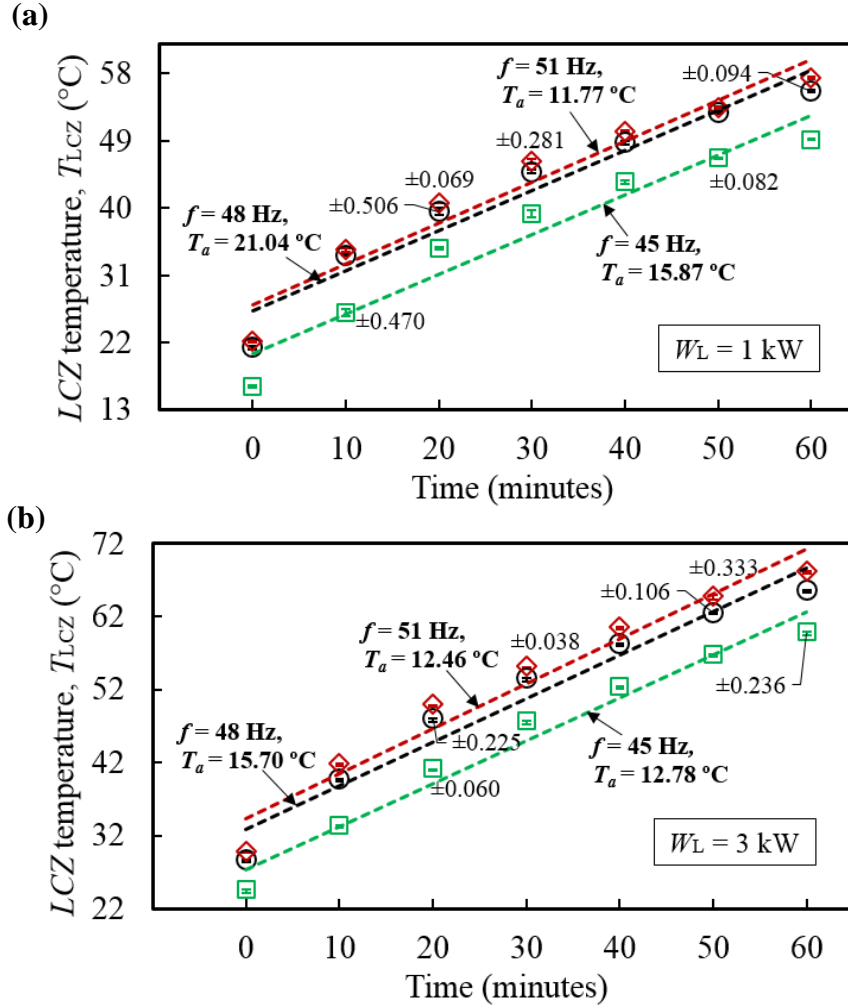


Figure 4.3.18: Transient variation of LCZ temperature at engine loads of (a) 1 kW and (b) 3 kW under different operating frequencies and ambient conditions

4.3.2.4.6 Variation of temperature gradient across TEG

Figure 4.3.19 shows the transient variation of ΔT_{TEG} corresponding to T_{LCZ} at different W_L and T_a at fixed operating f of 51 Hz. It can be seen that with an increase in T_{LCZ} , ΔT_{TEG} increases almost linearly in the initial phase because T_{CW} remains nearly constant. However, in the last phase of experiment, its slope slightly decreases due to rise of T_{CW} . At high T_{LCZ} , more heat transfer occurs to cold water through TEGs and a constant heat loss from cold water to ambient leads to rise T_{CW} that lowers ΔT_{TEG} . At the highest f level, ΔT_{TEG} reaches up to a maximum point of 37.63 °C (Figure

4.3.19a) at W_L of 1 kW and 46.37 °C (Figure 4.3.19b) at W_L of 3 kW. It has been observed that corresponding to a T_{LCZ} of 68.04, ΔT_{TEG} is found to be 46.37 °C through the minor $R_{l,eq.}$ of 0.01198 °C/W. This is quite appreciable in comparison to TEGs-thermosyphon-based conventional HRS where ΔT_{TEG} of 27 °C is obtained corresponding to a high heat source temperature i.e. T_S of 90 °C [Singh et al. 2011] and ΔT_{TEG} of 39 °C is achieved corresponding to a T_S of 87 °C with almost same temperatures at cold side for both cases [J2].

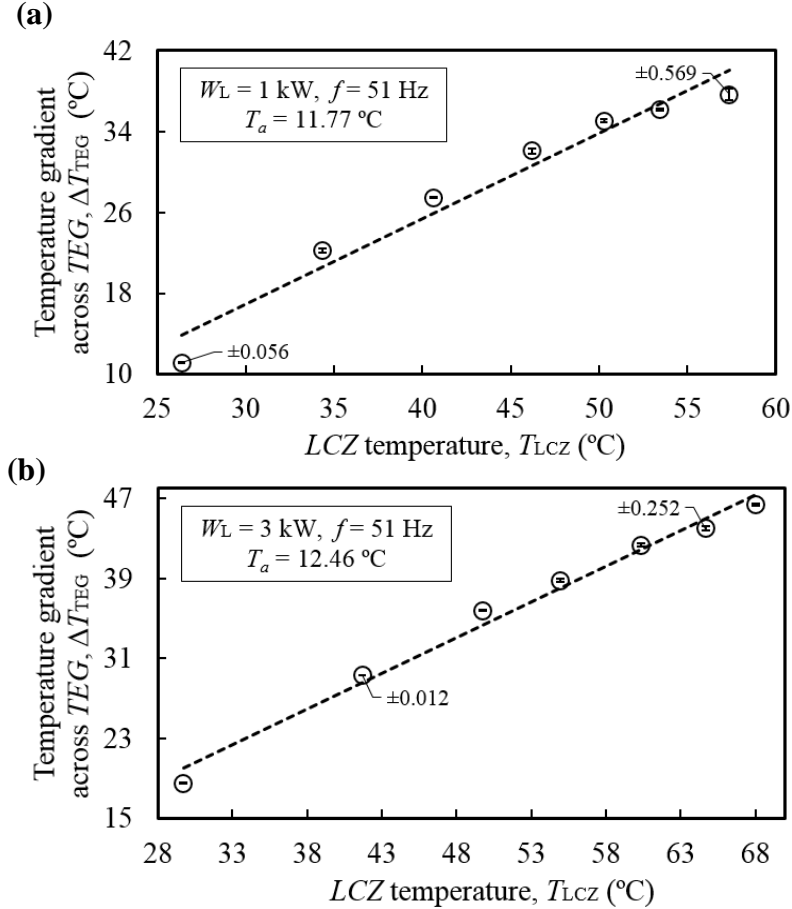


Figure 4.3.19: Variation of temperature gradient across TEG at engine loads of (a) 1 kW and (b) 3 kW under the ambient temperatures of 11.77 °C and 12.46 °C respectively

4.3.2.4.7 Variation of open circuit voltage and short circuit current

At highest operating f of 51 Hz, the variation of V and I_S with ΔT_{TEG} under diverse loading conditions is shown in Figure 4.3.20. V produced from TEGs is directly proportional to ΔT_{TEG} [J2] and therefore V increases linearly with an increase in ΔT_{TEG} and consequently I_S also increases. Initially at very low ΔT_{TEG} of 11.10 °C, the minimum V of 30.813 V is obtained at W_L of 1 kW and operating f of 51 Hz and it increases up to 69.86 V when $\Delta T_{TEG} = 37.63 \text{ °C}$. Similarly, V of

32.55 V is measured initially at ΔT_{TEG} of 18.52 °C for W_L of 3 kW and operating f of 51 Hz and a maximum V of 81.62 V is obtained when $\Delta T_{\text{TEG}} = 46.37$ °C. I_s obtained corresponding to maximum V of 69.86 V and 81.62 V are 0.240 A and 0.272 A respectively. It has been observed that V and I_s of each TEG are obtained as 0.89 V and 0.272 A respectively at T_s (here T_{LCZ} acts as a T_s) of 68.04 °C. These values are larger than the corresponding V and I_s values of 0.71 V and 0.152 A

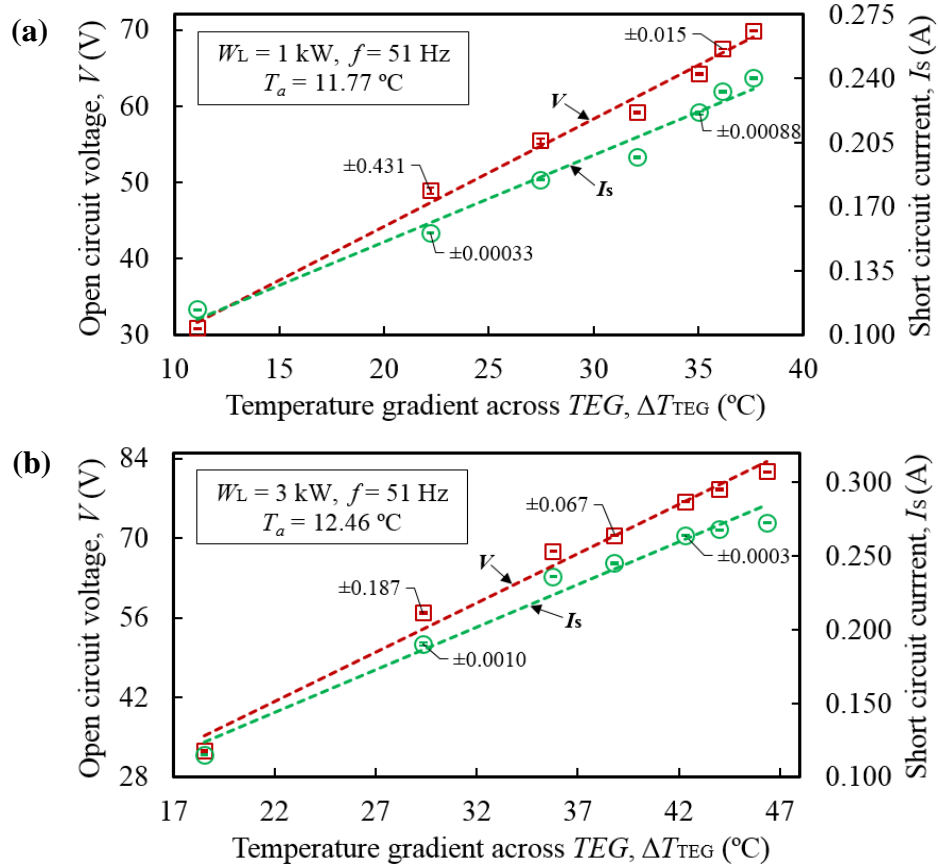


Figure 4.3.20: Variation of open circuit voltage, and short circuit current with ΔT_{TEG} at engine loads of (a) 1 kW and (b) 3 kW under different ambient conditions and fixed operating f of 51 Hz

respectively for the conventional TEGs-thermosyphon-based HRS obtained at T_s of 87 °C under the same characteristics of TEGs and keeping almost same temperature at cold side of TEGs [J2]. In conventional system, a high T_s is required to generate sufficient V and I_s for charging a battery however, the proposed design of TEGs-array-based HRS combined with SGSP is able to generate considerable amount of V and I_s even at lower T_s with certain cooling conditions. For instance, in another study, a maximum V of 1.435 V was generated from 48 TEGs (connected in series) at T_s of 53.76 °C obtained under actual weather conditions [J3], however with T_s of 54.96 °C, the

proposed system has produced V of 36.756 V from the same number of TEGs This achieved because of upgrading in HRS and cooling system.

4.3.2.4.8 Variation of output power and conversion efficiency

Figure 4.3.21 indicates the variation of I_o and P_o against the generated V_o at variable operating conditions. Under 1 kW of W_L , the maximum P_o is measured as 4.804 W at $V_o = 40.02$ V and $I_o = 0.120$ A. Similarly, the maximum P_o of 7.483 W is obtained at V_o and I_o of 48.28 V and 0.155 A respectively under W_L of 3 kW. The rate of heat energy supplied to TEGs i.e. \dot{Q}_{TEG} by LCZ water

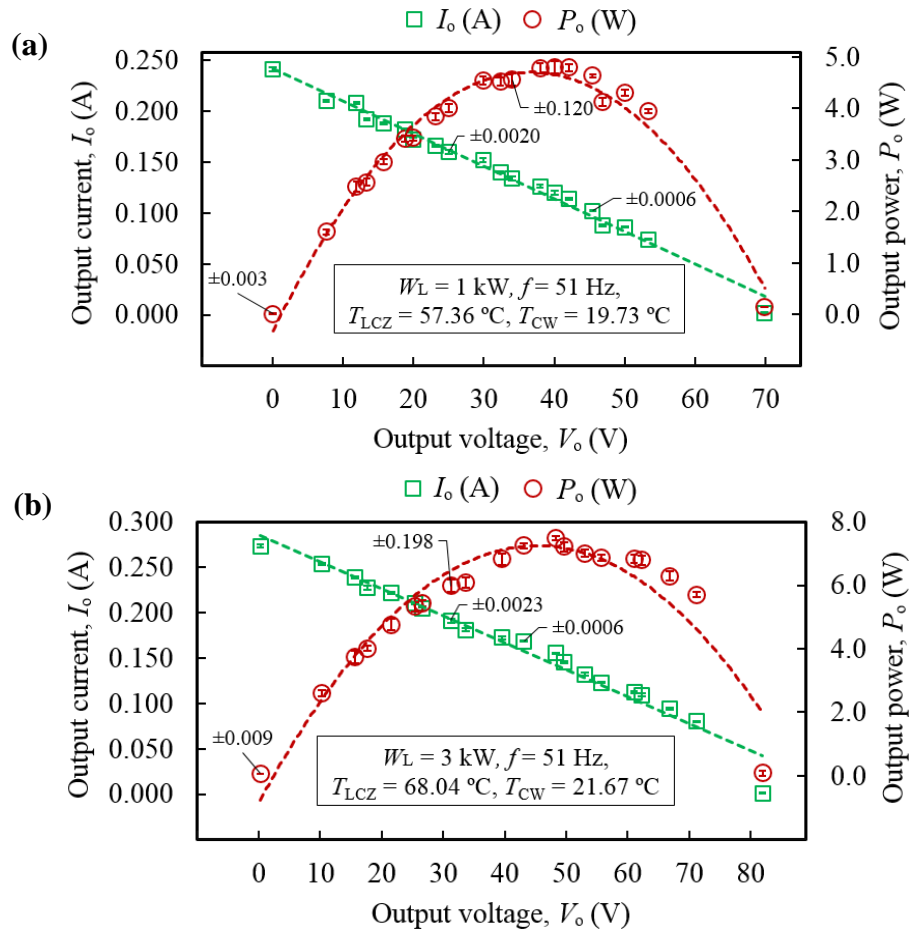


Figure 4.3.21: Output current and power profiles of TEG varying with output voltage for engine load of (a) 1 kW and (b) 3 kW at different LCZ and cold water temperatures

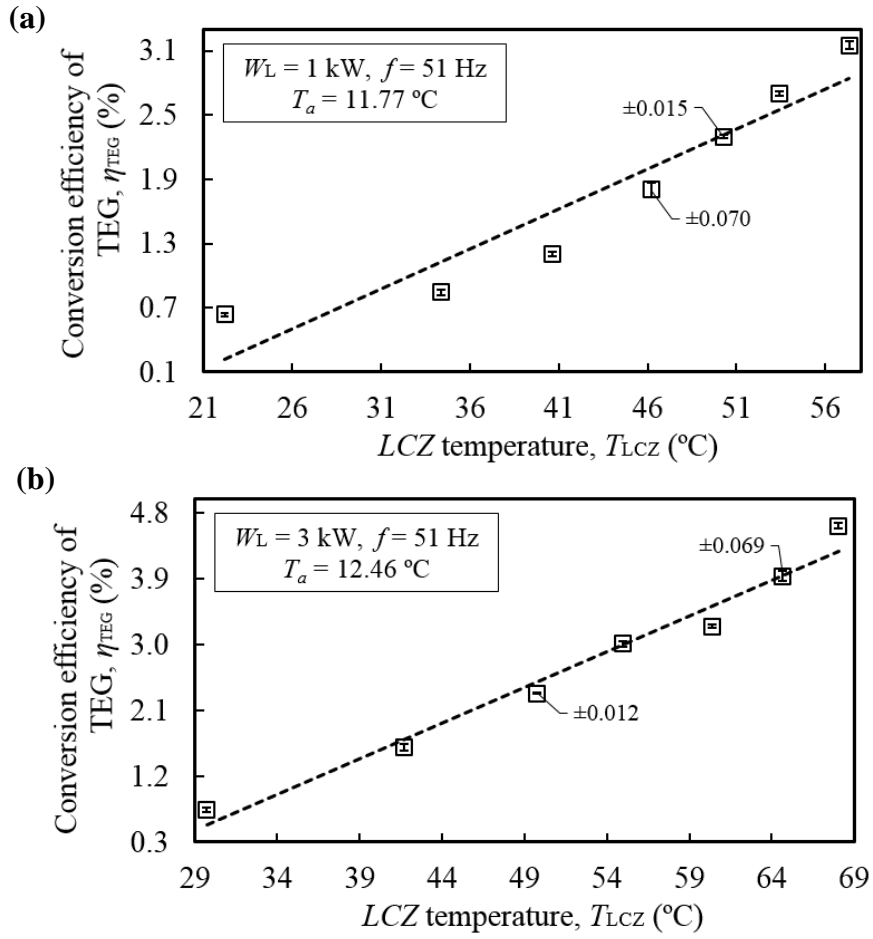


Figure 4.3.22: Variation of conversion efficiency of TEG with LCZ temperature at (a) 1 kW and (b) 3 kW loads

is converted into electricity (P_o) using TEGs and the ratio of P_o to \dot{Q}_{TEG} is known as conversion efficiency of TEG i.e. η_{TEG} as given below,

$$\eta_{\text{TEG}} = \frac{P_o}{\dot{Q}_{\text{TEG}}} \times 100 = \frac{P_o}{\dot{m}_{f,\text{LCZ}} \times c_{\text{LCZ}} \times (T_{\text{LCZ}} - T_{\text{LCZ,out}})} \times 100 \quad (4.3.11)$$

where, $\dot{m}_{f,\text{LCZ}}$ indicates the mass flow rate of LCZ water passes through array-based HRS and $T_{\text{LCZ,out}}$ is the temperature of LCZ water at the outlet of array-based HRS. Figure 4.3.22 shows the variation of η_{TEG} with T_{LCZ} . It has been observed that with increase in T_{LCZ} , η_{TEG} increases in

a similar manner. This is due to the fact that with rise in T_{LCZ} , both P_o and \dot{Q}_{TEG} increase but the rate of increment of P_o is higher than \dot{Q}_{TEG} . The maximum value of η_{TEG} is found to be 4.63% corresponding to T_{LCZ} of 68.04 °C at 3 kW of W_L and 51 Hz of f . As compared with thermosyphon-based conventional system [J2], this array-based design involves 1.52 times more energy input to TEGs system, however here P_o increases by 3.17 times that leads to upgrading η_{TEG} by nearly two times with array-based design.

4.3.2.4.9 *Comparison of thermal resistances*

In conventional system, a SGSP is used as a heat source for producing power from TEGs-thermosyphon-based HRS as reported in various literature [Singh et al. 2011], [Ding et al. 2016], [Kumar et al. 2018] and [Singh et al. 2012], where the energy of LCZ is transferred to hot side of TEGs via various (a total of nine) thermal resistances [Kumar et al. 2018] as presented in Figure 4.3.23a. For instance, the heat source temperatures i.e. T_s of 77 °C and 87 °C for TEGs-thermosyphon-based HRS were reduced to 52 °C and 59 °C respectively at the hot side of TEGs due to heat losses in various thermal resistances [J2]. This is a huge drawback of conventional thermosyphon-based HRS which offered almost 25-28 °C of thermal resistance barrier. However, the value of resistance barrier varies with operating conditions of thermosyphon and T_s . Here, the proposed design of TEGs-array-based HRS combined with SGSP enhances the heat transfer efficiency delivered to the hot side of TEGs by reducing thermal resistances (via eliminating seven thermal resistances out of total nine) through direct contact of LCZ water with TEGs (via copper sheet) as shown in Figure 4.3.23b. The thermal resistances offered between LCZ and hot side of TEGs for the proposed TEGs-array-based HRS are compared with previously studied conventional HRS in Table 4.3.4. The resistance potential of convection, vapour flow and interfaces (between liquid and vapour) is low while others (pool boiling, conduction, film boiling, and film condensation) have high potential of resistance as described by [J2]. The low as well as high potential resistances are mostly eliminated with TEGs-array-based HRS and offers a very low resistance (via conduction and convection) in the heat transfer. Further, the existing conduction resistance is lowered by using a low thickness (0.001 m) and high conductive material (copper). A comparison of obtained $R_{t, eq}$ of the proposed TEGs-array-based HRS with the conventional HRS available in the literature is presented in

Table 4.3.5. As compared to the available literature studies, a lowest $R_{t,eq}$ of $0.01198\text{ }^{\circ}\text{C/W}$ is observed for the proposed design of HRS and almost negligible resistance is realized in the flow of heat transfer.

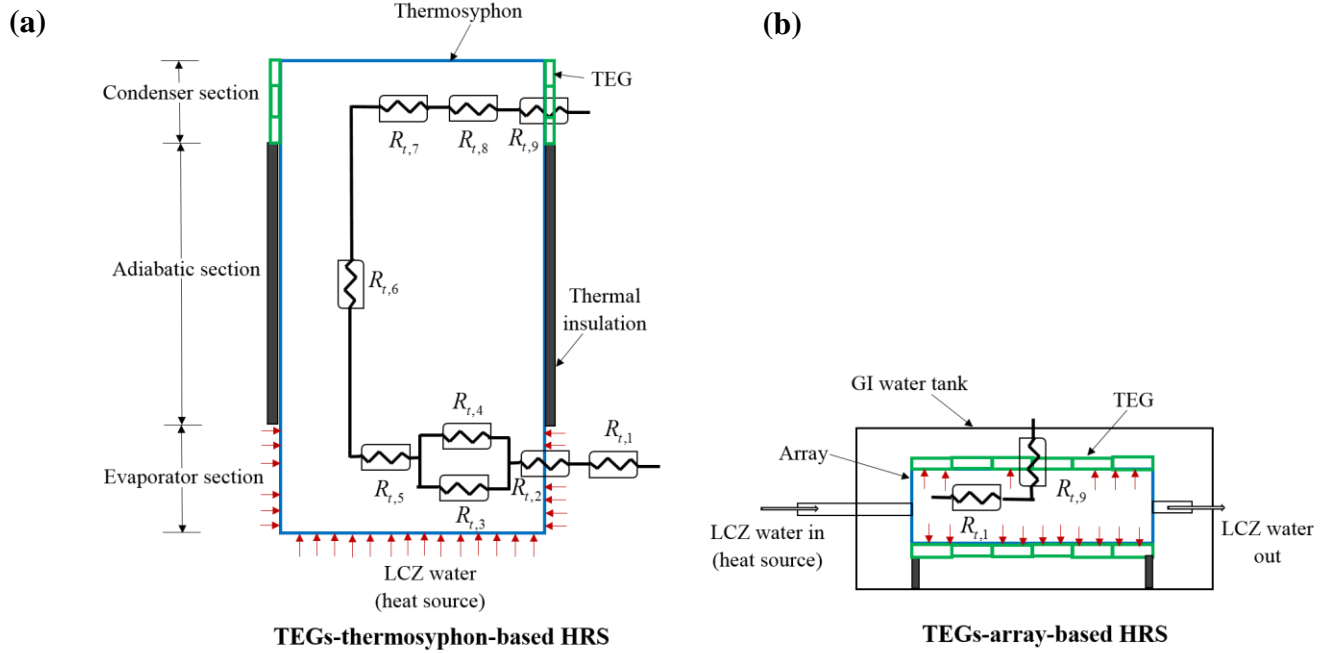


Figure 4.3.23: Schematic representation of thermal resistances for (a) TEGs-thermosyphon-based HRS (conventional system) and (b) TEGs-array based HRS (proposed)

Table 4.3.4: Thermal resistances offered between heat source and TEG's hot side for conventional and proposed systems

| S. No. | Thermal resistance, R_t | Location | Conventional system [Kumar et al. 2018] | Proposed system |
|--------|---------------------------|------------|---|-----------------|
| 1 | Convective | Evaporator | Present | Present |
| 2 | Wall conduction | Evaporator | Present | Absent |
| 3 | Pool boiling | Evaporator | Present | Absent |
| 4 | Film boiling | Evaporator | Present | Absent |
| 5 | Liquid-vapour interface | Evaporator | Present | Absent |
| 6 | Vapour flow | Adiabatic | Present | Absent |
| 7 | Vapour-liquid interface | Condenser | Present | Absent |
| 8 | Film condensation | Condenser | Present | Absent |

| | | | | |
|---|-----------------|-----------|---------|---------|
| 9 | Wall conduction | Condenser | Present | Present |
|---|-----------------|-----------|---------|---------|

Table 4.3.5: Comparison of equivalent thermal resistance, $R_{t,eq}$, with the published literature

| Source | T_{LCZ} (°C) | T_{CW} (°C) | ΔT_{TEG} (°C) | $R_{t,eq}$ (°C/W) |
|------------------------|----------------|---------------|-----------------------|-------------------|
| Ding et al. 2016 | 84 | 21.1 | 59 | 0.75 |
| J2 | 77 | 21.0 | 31 | 0.88 |
| Naresh and Balaji 2017 | 49 | - | - | 0.40 |
| Chehade et al. 2014 | 55 | - | - | 0.80 |
| Present study | 68 | 21.7 | 46.3 | 0.012 |

4.3.2.4.10 Charging a 12 V, 80 Ah heavy-duty battery

P_o produced from TEGs is used to charge a heavy-duty battery (EXIDE: 12 V, 80 Ah, Model No. : FXP8-XP800) to demonstrate the real life applications of the proposed system. A total of 46 TEGs (series-connected at the top surface) are connected parallelly with another 46 series-connected TEGs (at the bottom surface) to enhance the flow current. V delivered from the battery is measured before and after charging along with the time taken for charging. At the beginning of charging process, $V = 10.94$ V is recorded from the discharged battery. When V from TEGs reaches a certain value of 13.46 V, I_o (0.001 A) starts to flow in the circuit. At that time V and I_s are measured as 12.00 V and 0.155 A respectively. Therefore, the minimum I_s required to charge a 12 V, 80 Ah battery is found to be 0.155 A under the given conditions. After a small interval of time, the observed V and I_s reaches up to 14.72 V and 0.175 A respectively when T_{LCZ} attains a temperature of 35.45 °C. Thereafter, the battery is connected with TEGs by arranging the wire connections of Figure 4.3.11 where the variable external load resistance is now replaced by a battery to be charged. At the same time, T_{CW} is maintained at 19.17 °C which leads to ΔT_{TEG} of 16.28 °C. By maintaining this ΔT_{TEG} , the battery is charged with V_o and I_o of 12.42 V and 0.021 A respectively. After charging the battery with $P_o = 0.26$ W for nearly 2 hours 45 minutes, V delivered from the battery is measured as 12.01 V. This shows the charged condition of the heavy-duty battery. Figure 4.3.24 displays the charging of 12 V, 80 Ah heavy-duty battery from P_o of TEGs.

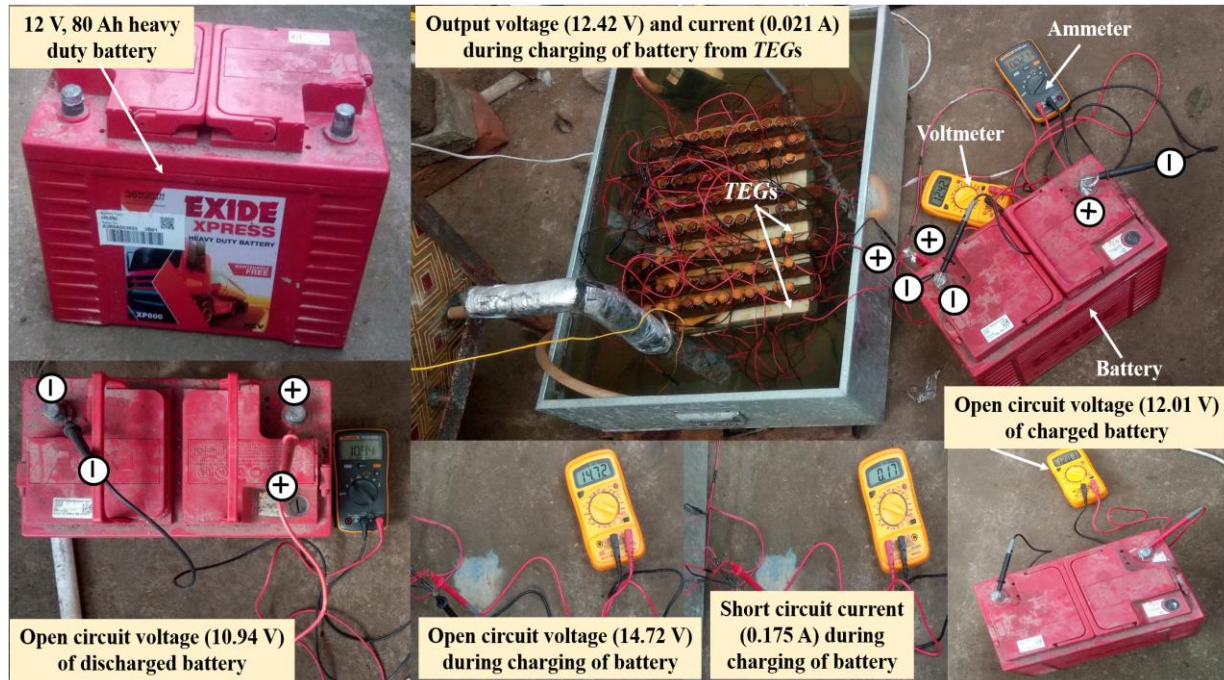


Figure 4.3.24: Charging a 12 V, 80 Ah heavy-duty battery from the output power of TEGs

4.3.2.4.11 Uncertainty analysis

Table 4.3.6 shows the uncertainties analysis of different measuring parameters that are calculated by the method as described in section 3.1.4.6.

Table 4.3.6: Uncertainties assessment of different measuring quantities

| Uncertainty | $S_{\text{avg.}}$ (4 th day) | $T_{\text{a, avg.}}$ (15 th day) | $T_{\text{LCZ, max.}}$ (15 th day) | V (20 th day) |
|---|---|---|---|---|
| Absolute | $1 \times 10^{-1} \text{ W/m}^2$ | $7 \times 10^{-2} \text{ }^\circ\text{C}$ | $6 \times 10^{-3} \text{ }^\circ\text{C}$ | $3 \times 10^{-4} \text{ V}$ |
| Relative | 1×10^{-4} | 2×10^{-3} | 3×10^{-3} | 4×10^{-5} |
| $f = 51 \text{ Hz}$, $W_L = 1 \text{ kW}$, Time = 60 minutes | | | | |
| Uncertainty | T_{WH} | T_{LCZ} | T_{CW} | T_{a} |
| Absolute ($^\circ\text{C}$) | 6×10^{-1} | 1×10^{-1} | 6×10^{-1} | 2×10^{-1} |
| Relative | 2×10^{-3} | 2×10^{-3} | 3×10^{-2} | 2×10^{-2} |
| $f = 51 \text{ Hz}$, $W_L = 3 \text{ kW}$, Time = 60 minutes | | | | |
| Absolute ($^\circ\text{C}$) | 3×10^{-1} | 1×10^{-1} | 9×10^{-2} | 7×10^{-2} |
| Relative | 7×10^{-4} | 2×10^{-3} | 3×10^{-3} | 5×10^{-3} |
| $f = 51 \text{ Hz}$, $W_L = 3 \text{ kW}$, $T_{\text{LCZ}} = 57.36 \pm 0.1 \text{ }^\circ\text{C}$, $T_{\text{CW}} = 19.73 \pm 0.6 \text{ }^\circ\text{C}$, $T_{\text{a}} = 11.77 \pm 0.2 \text{ }^\circ\text{C}$ | | | | |
| | V | I_{S} | P_{o} | ΔT_{TEG} |
| Absolute | $3 \times 10^{-4} \text{ V}$ | $3 \times 10^{-4} \text{ A}$ | $1 \times 10^{-2} \text{ W}$ | $6 \times 10^{-1} \text{ }^\circ\text{C}$ |
| Relative | 6×10^{-6} | 1×10^{-3} | 2×10^{-3} | 2×10^{-2} |
| $f = 51 \text{ Hz}$, $W_L = 3 \text{ kW}$, $T_{\text{LCZ}} = 68.04 \pm 0.1 \text{ }^\circ\text{C}$, $T_{\text{CW}} = 21.67 \pm 0.09 \text{ }^\circ\text{C}$, $T_{\text{a}} = 12.46 \pm 0.07 \text{ }^\circ\text{C}$ | | | | |
| Absolute | $3 \times 10^{-4} \text{ V}$ | $3 \times 10^{-4} \text{ A}$ | $1 \times 10^{-2} \text{ W}$ | $2 \times 10^{-1} \text{ }^\circ\text{C}$ |
| Relative | 4×10^{-6} | 1×10^{-3} | 2×10^{-3} | 3×10^{-3} |

4.3.2.5 Expansion of present system

Since, WH heat has a mostly temperature range of 350-450 $^\circ\text{C}$, the direct utilization of it as a heat source for the TEGs-array-based HRS may lead to failure of the system because TEGs are restricted to maximum temperature (T_{h}) of 150 $^\circ\text{C}$. Additionally, the TEGs uses a small portion of

WH and mostly it would be bypassed to the atmosphere if the TEGs-array-based HRS was directly applied to WH. Therefore, purpose in the use of SGSP is to effectively recovering as well as storing

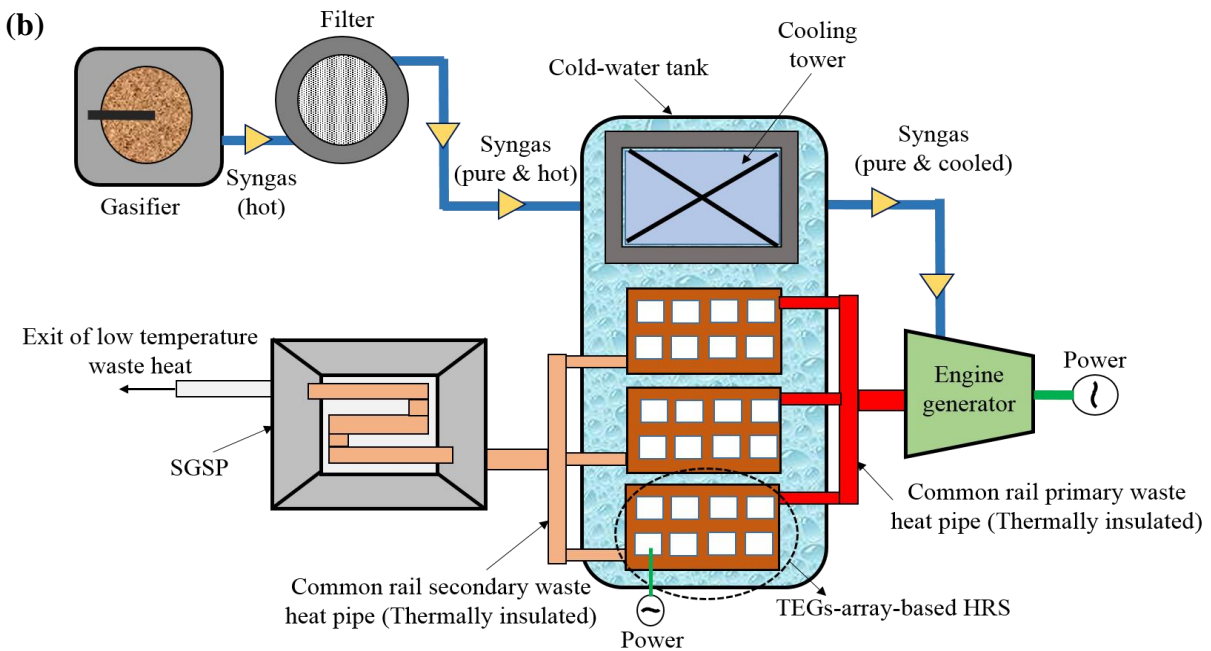
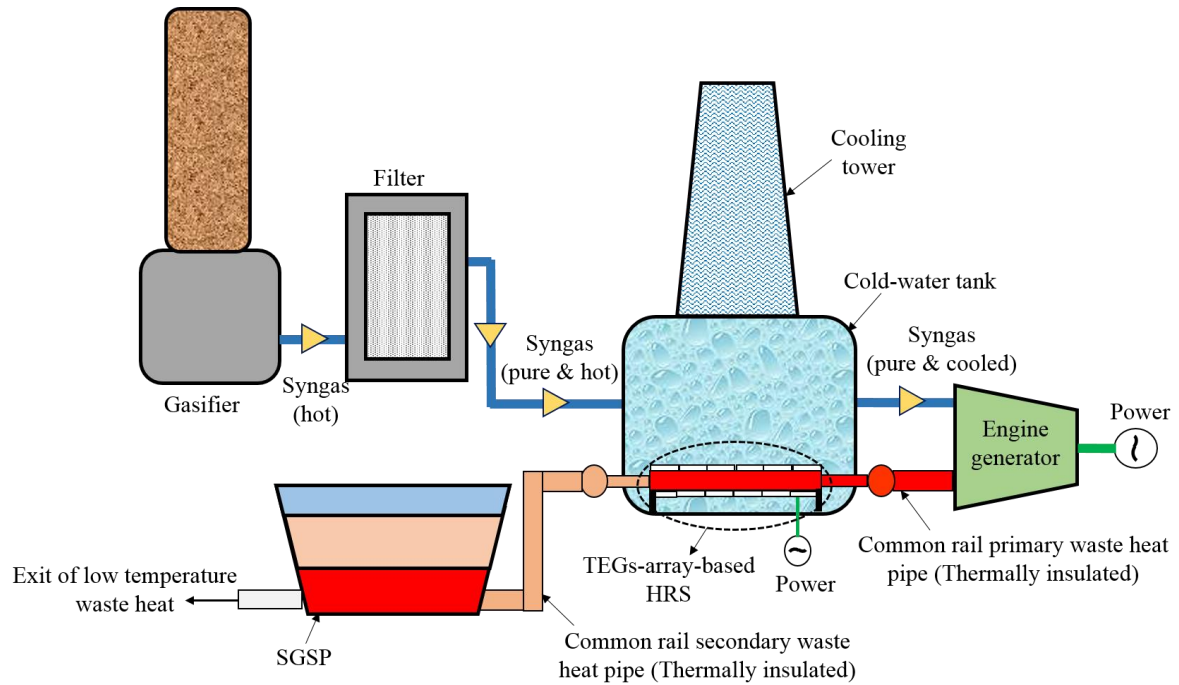


Figure 4.3.25: Expansion of proposed system (a) front view and (b) top view of WH and to provide constant heat input to the TEGs-array-based HRS. However, it has been realized that pumps are required when the TEGs-array-based HRS was connected with the SGSP, although power consumed by pumps are low and they are driven by the electricity produced from an engine-generator. Therefore, to make it more effective for power generation without using pumps, the TEGs-array-based HRS can be applied by the manner as shown in Figure 4.3.25. Here, it can be connected directly via common rail primary waste heat pipe where the distributions of high temperatures heat can be supplied according to temperature bounds of TEGs and the remaining left out low temperatures WH can be stored in the SGSP via common rail secondary waste heat pipe for further numerous applications. Furthermore, the higher temperatures of WH would be more favourable, because higher its value, more numbers of HRSs to be installed, leading to larger power production. Also, there is no requirement of pumps because WH flows by itself.

4.3.2.6 Summary

From this experimental study, the following findings have been drawn,

- The maximum values of $S_{avg.}$ and $T_{LCZ, avg.}$ are found as 732.75 W/m^2 (4th day) and $39.74 \text{ }^\circ\text{C}$ (16th day) respectively when operated from solar energy under actual weather conditions.
- The highest value of T_{LCZ} obtained during the entire experiments is recorded as $43.84 \text{ }^\circ\text{C}$ on the 15th day and found that T_{LCZ} is not constant under the steady-state condition.
- During the steady-state condition, the obtained C are varied in the range of $5.15\text{-}7.97 \text{ V}$ and $0.019\text{-}0.031 \text{ A}$ respectively and observed many constraints with the cooling system of TEGs and ambient conditions.
- The maximum values of T_{LCZ} and ΔT_{TEG} are found to be $68.04 \text{ }^\circ\text{C}$ and $46.37 \text{ }^\circ\text{C}$ respectively when the system is operated using WH of biomass engine running at 3 kW load ($f = 51 \text{ Hz}$). Corresponding to these conditions, the maximum value of V and I_s are obtained as 81.62 V and 0.272 A respectively.
- The maximum P_o from the proposed system is noted as 7.483 W ($W_L = 3 \text{ kW}$ and $f = 51 \text{ Hz}$) at 48.28 V and 0.155 A of V_o and I_o respectively. The maximum η_{TEG} is calculated as 4.63% using the proposed system.

- A 12 V, 80 Ah heavy-duty battery is successfully charged from P_o of the proposed system and found that the minimum I_s required to charge a battery is recognized as 0.155 A under the given conditions.
- With the proposed system, a total of seven thermal resistances (out of nine) have been directly eliminated and the remaining two are minimized by using a low thickness (0.001 m) and high conductive construction material (copper). This leads to high heat transfer from the heat source (LCZ) to the hot side of TEGs via minimum $R_{t,eq}$ (0.01198 °C/W) as compared to those available in the existing literature while almost negligible thermal resistance at cold side is achieved.

4.3.3 Performance analysis of the developed TEGs-array-based HRS directly operated from the waste heat

It is evident from the previous study that the direct utilization of WH for the developed TEGs-array-based HRS is more favourable. In view of this, a demonstration study has been carried out experimentally for power generation under the variable operating conditions of heat source, cooling system and the series structure.

4.3.3.1 Experimental setup and procedure

The experimental setup consists of (a) gasifier combined with filters and cooling tower, (b) engine-generator and (c) TEGs-array-based HRS as shown in [Figure 4.3.26](#). Gasifier converts the available biomass into combustible gas known as syngas which gets cleaned and cooled by various filters and a cooling tower respectively. More details about it can be seen in [section 3.1.1 and 3.1.2](#). This clean and cooled syngas purely run the engine-generator (a limited efficiency of about 30-40%) to produce power and WH generated at high temperatures is directly passed through the developed TEGs-array-based HRS. This system is connected with a WH exhaust pipe via a control valve that is located at a distance of 3.5 m from the exit port of the engine. So, the amount of WH passing through the proposed system is regulated by a control valve that governs the operating temperature of heat source and heats up hot side of TEGs. Also, TEGs-array-based HRS is immersed in a GI tank (linked with cold water tank of a cooling tower) in order to maintain at a low temperature of cold side of TEGs through direct contact with cold water. This creates ΔT_{TEG} and produces power which is measured by a multimeter. A total of 13 experiments (with three

replicates of each) are conducted to analyze the performance of proposed system under variable operating conditions.

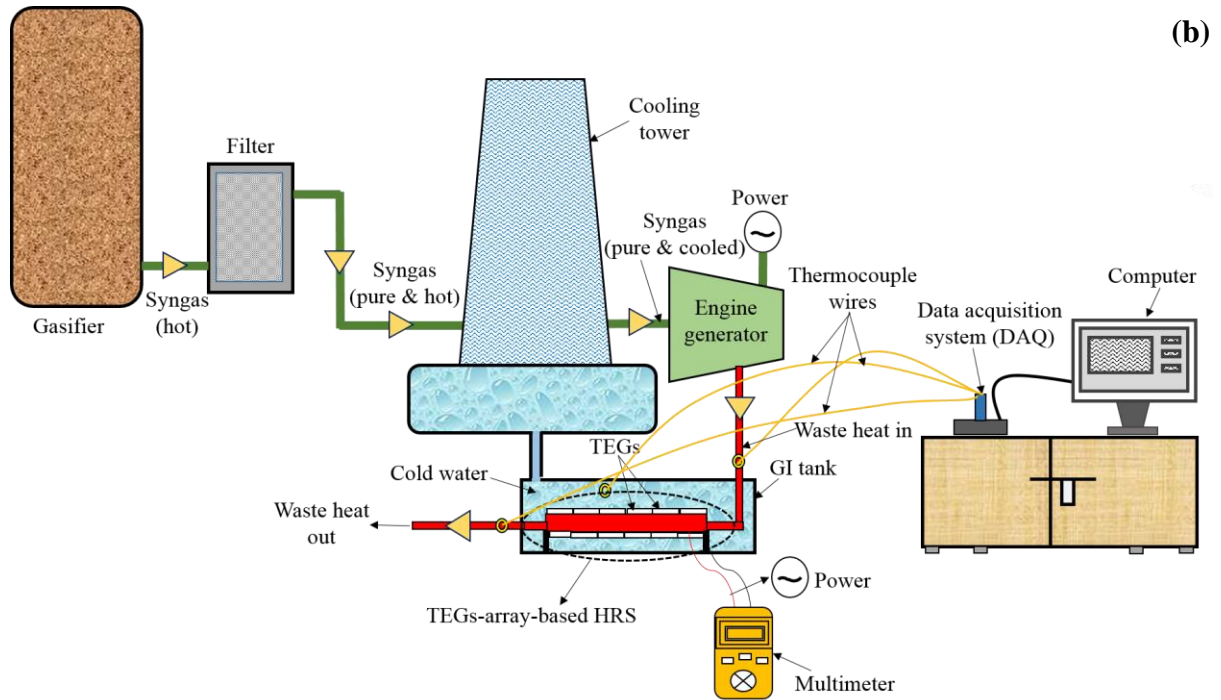
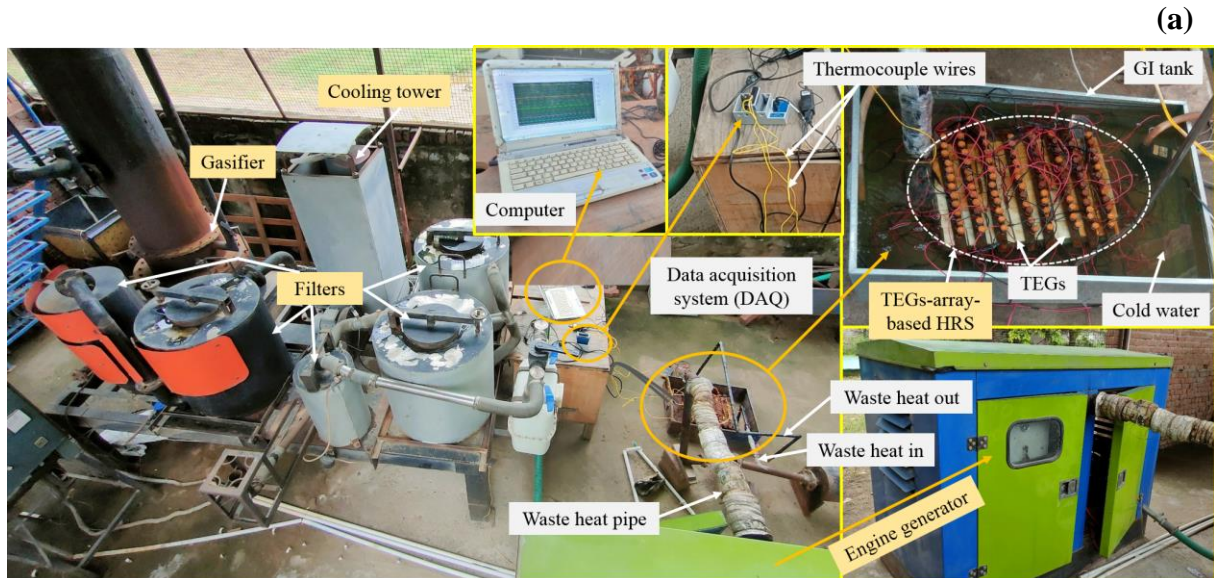


Figure 4.3.26: (a) Photograph and (b) block diagram of the experimental setup

4.3.3.2 Results and discussion

The performance of the TEGs-array-based HRS has been experimentally studied in the form of V , I_s and P_o when directly operated by WH. Initially, the experiments have been conducted for power generation and results are compared with the conventional HRS (thermosyphon-based) when both systems are operated at the same temperature limit. The effect of T_{CW} (sink/cold water temperature i.e. $T_{CW} = T_C$) on the performance has been recognized under pool water and flow water cooling system. Thereafter, various combinations of the series structure are made and the performance is analyzed when operated at heat source temperatures i.e. T_s (here WH acts as a direct heat source and $T_s = T_h$) of 40 °C, 60 °C and 80 °C. The average values over three replicates of all measuring parameters are presented in plots along with the standard error.

4.3.3.2.1 Performance comparison between conventional and proposed system

Figure 4.3.27 shows the trends of V and I_s produced from the TEGs-array-based HRS and their comparisons with the thermosyphon-based HRS (i.e., the conventional design), when both systems are operated under the same temperature limit of T_s and T_{CW} . Initially, the TEGs-array-based HRS is operated at three different temperatures (36 °C, 47 °C and 55 °C) of T_s at which the conventional HRS was run and correspondingly T_C is kept 28 °C, 32 °C and 34 °C respectively. At 36 °C, 47 °C and 55 °C of T_s , the conventional system had generated V values of 0.67 V, 1.36 V and 2.35 V respectively (from 92 series-connected TEGs) [J3] while the proposed system (TEGs-array-based HRS) has produced V values of 8.50 V, 19.17 V and 29.27 V respectively when other operating conditions are kept same. It has been observed that the proposed system has produced 12-14 times more performance than the conventional system because of upgrading in the design of HRS that leads to very low resistance (presence of convection and wall conduction resistances only) in the flow of heat transfer as described in section 4.3.2.4.9. Due to low V , the conventional system was unable to generate the current (i.e., power) even at the maximum temperature (55 °C) of T_s [J3], but the proposed design system has produced 0.120 A of I_s corresponding to that operating condition. So, the maximum P_o gained from the proposed system is found to be 1.176 W at 16.56 V of V_o and 0.071 A of I_o as shown in Figure 4.3.28.

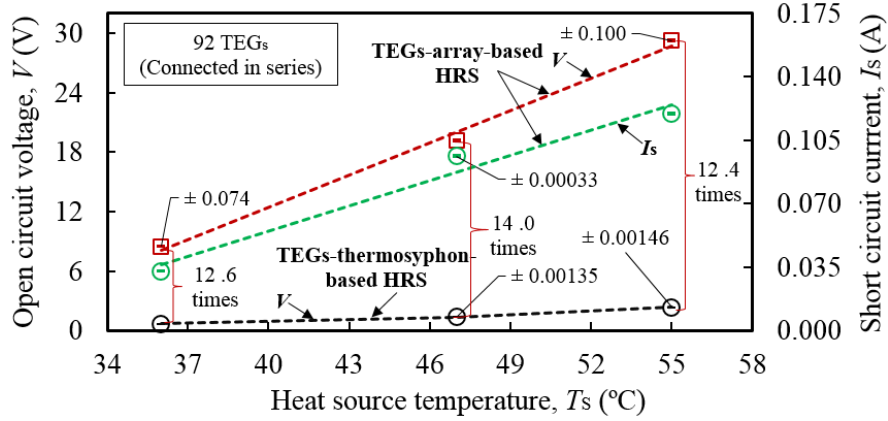


Figure 4.3.27: Comparisons of open circuit voltage and short circuit current

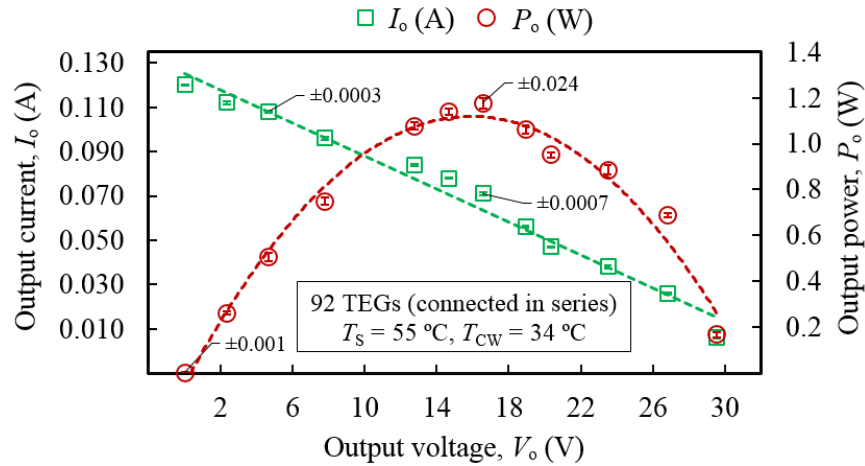


Figure 4.3.28: Profile of output current and power at a heat source temperature of 55 °C

4.3.3.2.2 Effect of sink/cold water temperature

Figure 4.3.29 represents the deviation of V corresponding to variation in T_{CW} under pool water and flow water cooling arrangements when T_S was maintained at 55 °C. It can be observed from Figure 4.3.29a that T_{CW} increases with time and accordingly V decreases, because the performance of a TEG depends upon both temperatures (T_h and T_c), and it requires high T_h i.e., T_S and low T_c i.e. T_{CW} values for maximum performance. The rate of heat transfer from heat source to cold water is more than the heat dissipated by cold water to ambient. Therefore, the heat leftover with time rises up T_{CW} that declines the system's performance. An increase of T_{CW} from 27.52 °C to 34.40 °C leads to a decrease of V from 35.72 V to 24.06 V. As the performance decreases with time, thus to

ensure a constant output from the system, it is necessary to maintain the value of T_{CW} as low as possible. To accomplish the requirement of maintaining low T_{CW} , cold water stored in a tank of cooling tower (assisted with biomass gasifier) can be used for better performance of the proposed system as presented in Figure 4.3.29b. It can be seen that a higher and constant V of 43.59 V is obtained when T_{CW} was maintained at a specific temperature through flow water cooling system.

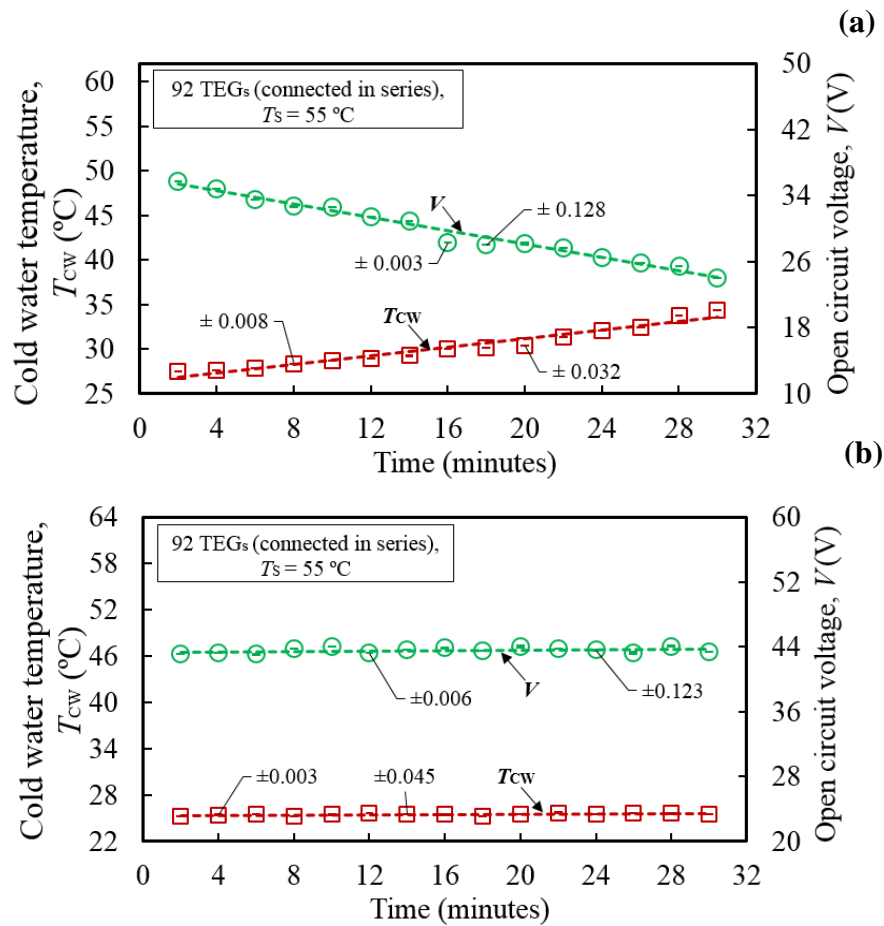
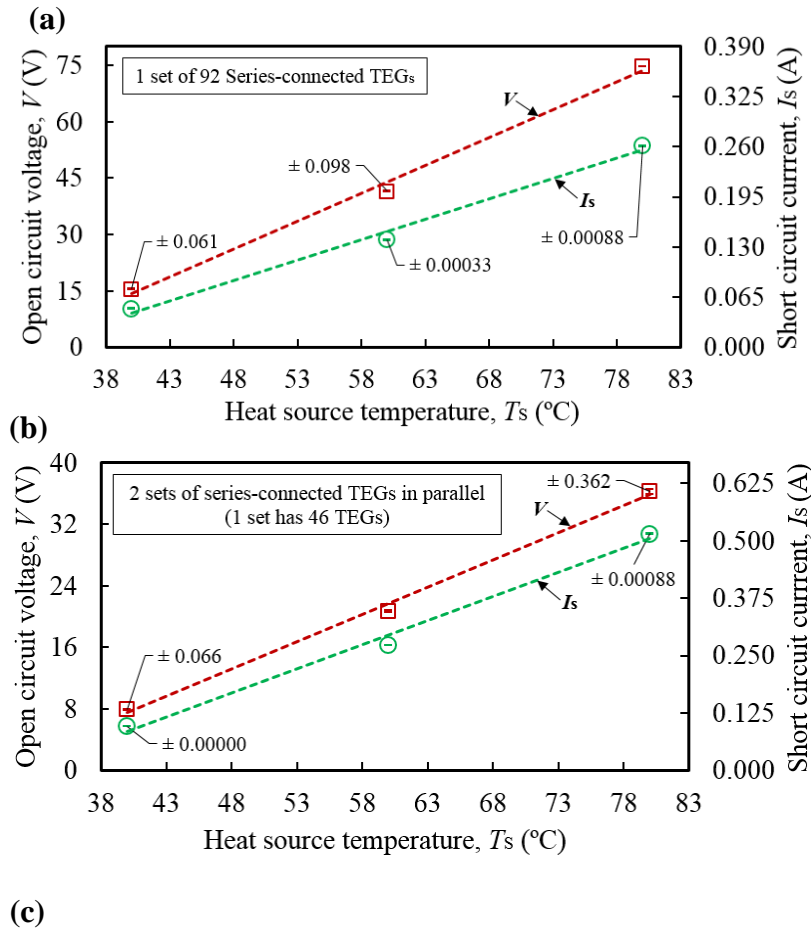


Figure 4.3.29: Effect of cold water temperature on open circuit voltage under (a) pool water and (b) flow water cooling arrangements

4.3.3.2.3 Performance under various combinations of the series structure

Figure 4.3.30 indicates V and I_s obtained at three arrangements of the series structure when the proposed system was operated at three different temperatures of T_s i.e., 40 °C, 60 °C and 80 °C. It is well known that voltage is added in series while current is added in parallel according to Kirchhoff's law. Figure 4.3.30a shows the performance values (V and I_s) obtained from the 1st combination of the series structure where 92 series-connected TEGs are used. The outcomes indicate that a maximum V value of 74.78 V is obtained whereas a maximum I_s of 0.261 A is achieved from the same combination. Further, the 2nd combination is made by parallel connection of two sets of 46 series-connected TEGs and its performance characteristics is presented in Figure 4.3.30b. Here, the maximum V value obtained reduces to nearly half (36.29 V) and I_s value nearly doubles (0.515 A). Finally, the 3rd combination is made by parallel connection of four sets of



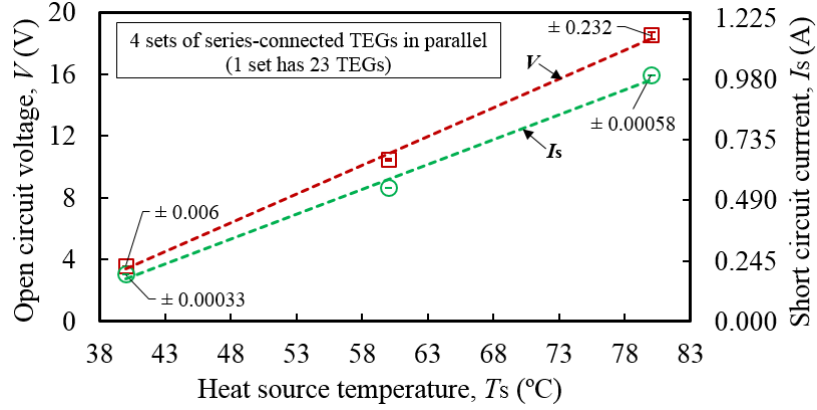


Figure 4.3.30: Performance under various combinations of the series structure; (a) 1 set of 92 series-connected TEGs, (b) 2 sets (each set has 46 TEGs) of series-connected TEGs in parallel, and (c) 4 sets (each set has 23 TEGs) of series-connected TEGs in parallel

series-connected TEGs and each set consists of 23 series-connected TEGs. The outcomes for this arrangement are presented in Figure 4.3.30c and found that the obtained V value reduces by one-fourth (18.51 V) of the 1st combination while I_s gets increased by four times (0.997 A) of the first one. Although, the output power i.e. P_o produced from all combinations of the series structure remains nearly the same (maximum of 4.93 W obtained at a highest T_s of 80 °C as revealed in Figure 4.3.31) at particular temperature limit but these arrangements are useful for specific requirements of voltage and current. As revealed in the literature [J4], the minimum I_s required to charge a 12 V, 80 Ah heavy-duty battery is recognized as 0.155 A with 14-17 V of V . Here, the proposed system is able to produce 29.27 V of V and 0.120 A of I_s when operated at 55 °C and 34 °C of T_s and T_{cw} respectively. At these operating conditions, if the 2nd combination of the series structure is used, then the system will be able to produce nearly 0.240 A of I_s and 14.63 V of V that can charge a 12 V, 80 Ah heavy-duty battery.

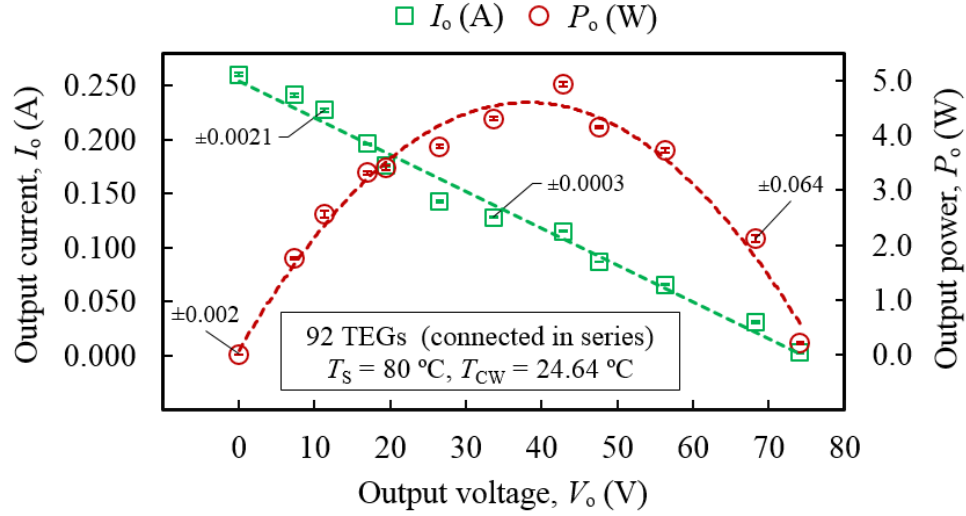


Figure 4.3.31: Variation of output current and power at maximum heat source temperature (80 °C)

4.3.3.2.4 Uncertainty analysis

Table 4.3.7 shows the uncertainties associated with various measuring parameters and calculated by the procedure as discussed in section 3.1.4.6.

Table 4.3.7: Uncertainties associated with various measuring parameters

| | V | I_s | V_o | I_o | P_o |
|--|-----------------------------|-----------------------------|-----------------------------|-----------------------------|-----------------------------|
| 92 TEGs (connected in series), $T_s = 55\text{ °C}$, $T_{CW} = 34\text{ °C}$ | | | | | |
| Absolute | $3 \times 10^{-4}\text{ V}$ | $3 \times 10^{-4}\text{ A}$ | $3 \times 10^{-4}\text{ V}$ | $3 \times 10^{-4}\text{ A}$ | $5 \times 10^{-3}\text{ W}$ |
| Relative | 1×10^{-5} | 2×10^{-3} | 2×10^{-5} | 4×10^{-3} | 4×10^{-3} |
| 92 TEGs (connected in series), $T_s = 80\text{ °C}$, $T_{CW} = 24.64\text{ °C}$ | | | | | |
| Absolute | $3 \times 10^{-4}\text{ V}$ | $3 \times 10^{-4}\text{ A}$ | $3 \times 10^{-4}\text{ V}$ | $3 \times 10^{-4}\text{ A}$ | $1 \times 10^{-2}\text{ W}$ |
| Relative | 4×10^{-6} | 1×10^{-3} | 7×10^{-6} | 3×10^{-3} | 3×10^{-3} |

4.3.3.3 Summary

Here, the following summary has been found from this study,

- The proposed TEGs-array-based HRS is able to produce 12-14 times more performance than the conventional HRS when operated under the same temperature bound.

- The proposed system has produced a maximum V of 74.78 V and corresponding to that I_S and P_o are obtained as 0.261 A and 4.93 W respectively at T_S of 80 °C.
- V and I_S obtained from different series and parallel combinations of TEGs at a specific operating temperature varies according to Kirchhoff law but P_o remains the same.

CHAPTER 5

*USE OF BIOMASS GASIFICATION FOR DESALINATION

This chapter deals with the investigation of use of biomass energy as an external heat source (waste heat of a biomass engine-generator) for water desalination using a new developed wick and copper-finned distillation system (CFDS). Furthermore, the response surface-based correlations (linear and quadratic) are also developed using BBD, ANOVA as well as regression methods. The deviation in the response parameter is analyzed through main effect, interaction, surface and contour plots along with the percentage contribution of each input factor (linear, square and 2-way interaction).

This chapter of thesis addresses the need of pure drinking water by efficiently recovering the WH with the aid of a newly developed distillation system. In this work, a novel design of distillation system has been developed for recovery of WH and the performance (amount of pure water produced) of this system is analyzed at variable operating conditions. Furthermore, the response surface-based correlations (linear and quadratic) are also developed using regression method and contribution/effect of each input factor has been analyzed through surface plots.

5.1 Performance and response surface analysis of a new wick and finned distillation system

Mostly, solar collectors and photovoltaics are extensively used as external heat sources in solar energy-driven distillation system, but WH from biomass energy-driven system is not yet explored. Moreover, there are many factors that affect the output of an active distillation system, like the inclination/angle of glass cover, fabrication/construction materials, insulation materials as well as its thickness, depth/height and temperature of water present in the basin. The temperature difference between basin water and condensing glass cover has a direct effect on the performance of distillation system. In order to maximize the temperature of basin water, limited number of

* Content presented in this chapter can be found in the publications J5

research activities have been performed using fins and wicks. Towards this, hollow square vertical iron fins wrapped with black cotton wick was used in solar energy-based desalination system [Gnanaraj and Velmurugan 2019]. [Yousef et al. 2019] and [Abdelgaied et al. 2021] used cylindrical vertical pin fins, whereas [Mohaisen et al. 2021] used rectangular fins in solar energy-assisted desalination system. [Alatawi et al. 2022] used longitudinal vertical fins wrapped with black cotton wick to increase the basin water temperature and the productivity of distillation system. It has been witnessed from the past literature that fins were vertically placed and wicks were provided over the fins to increase the exposure of basin water to accelerate the evaporation rate. However, this type of provision of increasing the surface area of evaporation is useful in solar energy-based distillation systems, where energy is incident from the top surface and the incoming radiation is along the vertical direction. But, such fin arrangement is not suitable for distillation system operated through WH, where the flow of energy source is along the horizontal direction. Further, condensation rate can be enhanced by cooling of glass cover. With this objective, a new design of biomass WH driven water distillation system has been proposed with horizontal fins and by placing the wick on the glass cover that is kept wet by water circulation from the water tank of a cooling tower combined with a biomass gasifier unit.

5.1.1 Experimental setup details

The setup is essentially a combined system of (a) a biomass gasifier unit and (b) a distillation unit. WH of the gasifier unit acts as a heat source that drives the distillation unit. The gasifier unit consists of (1) a downdraft gasifier, (2) filters (3) a cooling tower, (4) a gas flow meter, (5) an engine-generator with WH pipe and (6) a control panel. The distillation unit comprises of (1) a single basin distillation system integrated with glass (covered with wick), (2) a seawater storage tank connected with a water flow meter, (3) a cold water tank and (4) a temperature indicator as shown in [Figure 5.1.1](#). The gasifier converts the available biomass fuel into syngas which passes through filters (cyclone, charcoal, sawdust and cotton) to remove the impurities and water tank of a cooling tower to get cooled. Thereafter, it is delivered to an engine-generator via a gas flow meter (to measure the amount of syngas supplied) to produce power that is supplied to a control panel and WH is rejected through thermally insulated WH/exhaust pipe. More details about it can be read in [section 3.1.1 and 3.1.2](#). This WH pipe is wrapped with a 30 mm thickness of glass wool and then covered with XPLE thermal insulation of 0.02 m thickness in order to minimize the heat loss. The single basin distillation system is made from GI sheet with a base dimension

(a)



(b)

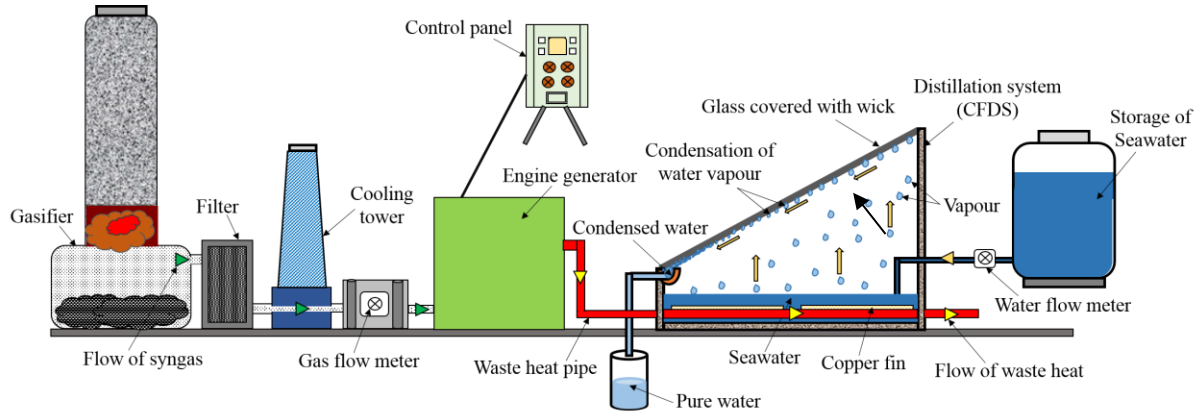


Figure 5.1.1: (a) Photograph and (b) schematic of experimental setup displaying various parts

1.0 m \times 0.6 m (basin section) and the outer surface is covered with XPLE thermal insulation to resist the surface heat losses. WH pipe of 0.05 m diameter is made from iron and the portion of it which installed/fitted in the distillation system is made from stainless steel. A total of six copper fins with dimensions 0.35 m \times 0.07 m \times 0.001 m are fixed just at the top surface of steel-made WH pipe to form copper finned distillation system (CFDS). The surface area of heat transfer is increased by creating two turns in WH pipe and using copper fins. The basin is filled with seawater supplied from a storage tank and the amount of seawater delivered to the basin is recorded by a water flow meter. CFDS is integrated with glass cover with dimensions 0.96 m \times 0.67 m \times 0.004 m. The cold water is supplied from the cooling tower at the top channel of cold water via a flow pipe and flows over the outer surface of glass through various ports. Thereafter, water exits through an outlet via a cold water channel and is sent back to the cooling tower through a cold water tank. The outer surface of glass is covered with a wick for uniform cooling of it because without wick cold water flows over the glass in the layers form that allows partial/incomplete condensation of water vapour at the internal surface. The condensed water falls down in the pure water channel and exits through an outlet to store in the collection tank. A total number of eight k-type thermocouple wires are fixed at different locations (WH inlet and outlet of CFDS, fin_{1st}, fin_{3rd}, fin_{5th}, moist air in CFDS, basin water and cold water in the tank) to measure the temperature and are displayed on the temperature indicator.

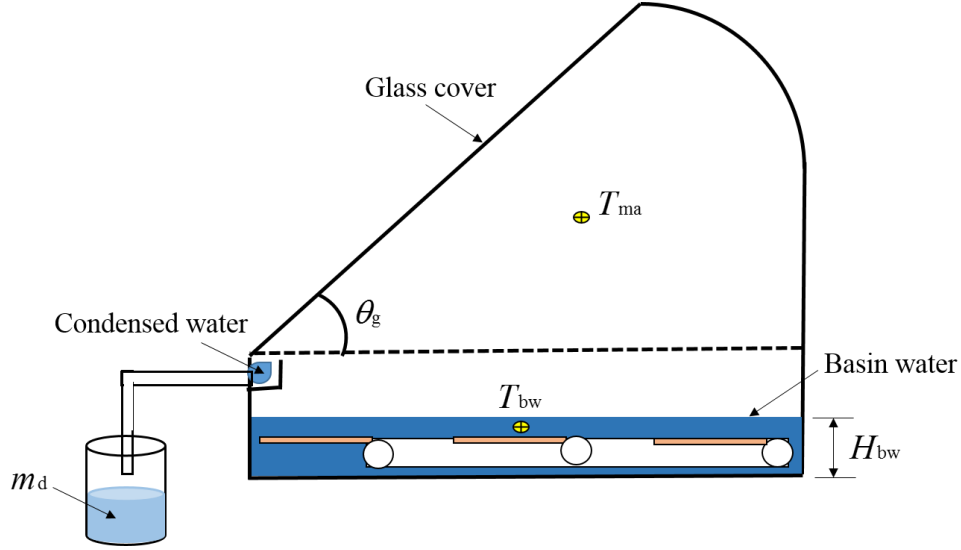
5.1.1.1 Experimental procedure

The experiments are performed at Indian Institute of Technology, Rupnagar, Punjab, India. The process from igniting of biomass to producing power using an engine-generator is explained in [section 3.1.2](#). WH produced from an engine-generator is passed through the basin of CFDS using an exhaust pipe. This leads to transfer of heat energy from the exhaust pipe to the basin water (seawater), which raises its temperature with time and evaporates it. The vapours are condensed at the internal surface of glass cover and get collected in a collection tank. Every experiment is conducted for the period of 100 minutes with three replicates of each and measured the various performance parameters at a certain time interval of 10 minutes. Experimental analysis includes the performance analysis of the CFDS in the form of amount/mass of distilled water (m_d) at various waste heat temperature at the inlet of CFDS ($T_{WH, inl.}$), glass inclination angle (θ_g) and height of the basin water (H_{bw}). $T_{WH, inl.}$ is varied by running the engine at three different frequency levels (45 Hz, 48 Hz and 51 Hz) while θ_g is controlled by using a hanger for the frame of glass and set at three location points. H_{bw} is changed by filling the certain amount of seawater in the basin at three different levels using a water flow meter.

5.1.1.2 Variable input factors and different measuring parameters

The CFDS produces pure/distilled water through evaporation and condensation processes by using the WH of the biomass energy-driven engine. The schematics describing various input and measuring parameters are shown in [Figure 5.1.2](#). The mass of pure/distilled water i.e. m_d of CFDS depends upon the quantity of vapours generated and condensed, which are primarily affected by three input factors: $T_{WH, inl.}$, θ_g and H_{bw} . Among these, $T_{WH, inl.}$ determines the temperatures of basin water (T_{bw}), moist air (T_{ma}), fin (T_f) and outlet of CFDS ($T_{WH, outl.}$). For a given heat input, a large volume of basin water achieves low T_{bw} while a small volume attains high T_{bw} . On the other hand, the amount of vapour condensed is determined by θ_g through the gravity affect of condensing and time to flow the vapours from the water surface leve to glass internal surface. A low θ_g has low gravity affect of condensing, but the time to flow the vapours is less and vice-versa.

(a)



(b)

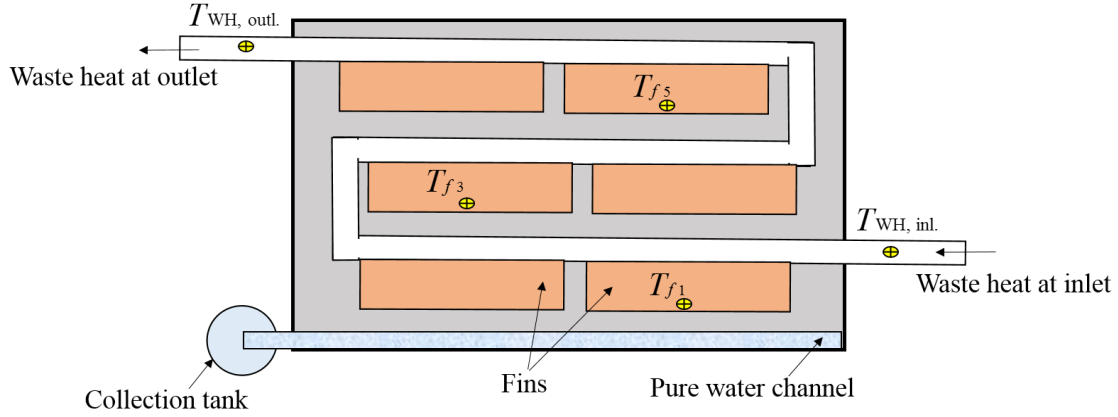


Figure 5.1.2: Schematic of the CFDS displaying various measuring parameters (a) sectional side view and (b) sectional top view

5.1.2 Methodology

5.1.2.1 Box-Behnken design method

Box-Behnken design (BBD) method is a statistical technique that offers an optimum design set of experiments grounded on the existing variable input factors. BBD model needs three levels of each input factor and it is extensively used for the three levels factorial designs, as compared to central composite design (CCD) method [Sarbu and Beniuga 2018]. BBD is a rotatable second-order design and can be represented graphically by a cube with a centre point and middle points of the edges. It works within the safe region because it doesn't contain any axial points outside the cube. BBD uses the lowest and highest values of the factors and doesn't contain combinations which

results in avoiding the experiments of extreme conditions that can have inadequate outcomes. Another advantage of BBD is that it requires less number of experiments for the same number of input factors and has high efficiency. The number of experiments to be performed for the BBD and CCD is calculated as $2^n (n-1) + R_0$ and $2^n + 2^n + R_0$ respectively where n represents the number of input factors and R_0 denotes the number of central points or replicates at the centre. Replicates at the centre are the total number of combinations in the design set of experiments for which the response is recorded at mid-points of all input factors. The comparison of BBD and CCD for the number of experiments and their efficiencies are presented in [Table 5.1.1](#).

Table 5.1.1: Comparison between CCD and BBD

| Number of input factors (n) | Number of coefficients | Number of experiments | | Efficiency | |
|---------------------------------|------------------------|-----------------------|-----|------------|------|
| | | CCD | BBD | CCD | BBD |
| 3 | 10 | 15 | 13 | 0.67 | 0.77 |
| 4 | 15 | 25 | 25 | 0.60 | 0.60 |
| 5 | 21 | 43 | 41 | 0.49 | 0.61 |

Therefore, in this work, BBD is used for the optimal design sets of experiments. In the present system, the performance outcome (m_d) of CFDS depends upon mainly three independent variable input factors ($T_{WH, inl.}$, θ_g and H_{bw}) and their design levels are presented in [Table 5.1.2](#).

Table 5.1.2: Design levels of various operating input factors

| Working parameter | Level-1 (-1) | Level-2 (0) | Level-3 (1) |
|--|--------------|-------------|-------------|
| Waste heat temperature at inlet, $T_{WH, inl.}$ ($^{\circ}C$) | 283 | 302 | 321 |
| Glass angle, θ_g (degree) | 30 | 45 | 60 |
| Height of basin water, H_{bw} (m) | 0.06 | 0.08 | 0.10 |

BBD method has suggested a total of 13 experiments and their design sets of experiments are found using the Minitab software as revealed in [Table 5.1.3](#).

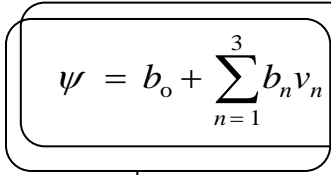
Table 5.1.3: Design sets of experiments based on the three levels BBD

| Experiment run | $T_{WH, \text{inl.}} (^{\circ}\text{C})$ | θ_g (degree) | H_{bw} (m) |
|-------------------|--|---------------------|--------------|
| 1 | 1 | 0 | 1 |
| 2 | 1 | -1 | 0 |
| 3 | 0 | 1 | 1 |
| 4 | -1 | 0 | 1 |
| 5 | 0 | 0 | 0 |
| 6 | 1 | 0 | -1 |
| 7 | -1 | 0 | -1 |
| 8 | 1 | 1 | 0 |
| 9 | 0 | 1 | -1 |
| 10 | 0 | -1 | -1 |
| 11 | -1 | 1 | 0 |
| 12 | -1 | -1 | 0 |
| 13 | 0 | -1 | 1 |

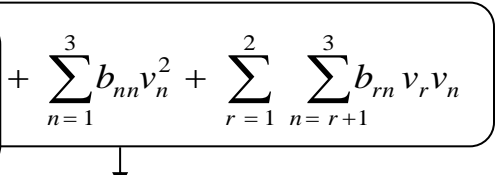
5.1.2.2 Regression analysis and correlations

The regression method analysis the experimental outcomes (as a response parameter) and generates the relationship between the variable input factors and the response parameter. Let, ψ be the dependent or response parameter (m_d) which depends upon the three (n) independent input factors (v) such as $T_{WH, \text{inl.}}$, θ_g and H_{bw} . The polynomial equations (linear and quadratic) for the response parameter (ψ) can be written as given below [Singh and Das 2021],

$$\psi = b_o + \sum_{n=1}^3 b_n v_n + \sum_{n=1}^3 b_{nn} v_n^2 + \sum_{r=1}^2 \sum_{n=r+1}^3 b_{rn} v_r v_n \quad (5.1.1)$$



Linear



Quadratic

where, v_1 , v_2 and v_3 are the governing independent/input factors denoted by $T_{WH, \text{inl.}}$, θ_g and H_{bw} , respectively. The suitable values of coefficient, c in the predicated response parameter, m_d are found using the Minitab software.

5.1.2.3 Analysis of variance and coefficient of determination or R^2

The effect of any particular input factor on the response/outcome is gauged using the analysis of variance (ANOVA) method shown graphically in [Figure 5.1.3](#). Suppose the response/observation (ψ) data points for a specific input/governing factor got at different levels (p) are presented in the matrix form as reported in [Eq. \(5.1.2\)](#).

$$\begin{array}{cc}
 \text{Level} & \text{Response/observation data points} & \text{Mean} \\
 1 & \left[\begin{array}{cccc} \psi_{11} & \psi_{12} & \cdots & \psi_{1q_1} \end{array} \right] & \overline{\psi_1} \\
 2 & \left[\begin{array}{cccc} \psi_{21} & \psi_{22} & \cdots & \psi_{2q_2} \end{array} \right] & \overline{\psi_2} \\
 \vdots & \left[\begin{array}{cccc} \vdots & \vdots & \vdots & \vdots \end{array} \right] & \vdots \\
 p & \left[\begin{array}{cccc} \psi_{p1} & \psi_{p1} & \cdots & \psi_{pq_p} \end{array} \right] & \overline{\psi_p}
 \end{array} \quad (5.1.2)$$

Then, the total sum of squares (TSS) for a specific input factor that shows the total deviation from the mean is given by following expression [\[Kumar et al. 2019\]](#),

$$TSS = \sum_{i=1}^p \sum_{j=1}^{q_i} \psi_{ij}^2 - N_o (\overline{\psi})^2 \quad (5.1.3)$$

In [Eq. \(5.1.3\)](#), the term $\overline{\psi}$ is recognised as the grand mean of all N_o observed data points and it is computed by the equation given below,

$$\overline{\psi} = \frac{1}{N_o} \sum_{i=1}^p \sum_{j=1}^{q_i} \psi_{ij} \quad (5.1.4)$$

where, ψ_{ij} point out the j th observation ($j = 1, 2, \dots, q_i$) taken at the i th level ($i = 1, 2, \dots, p$) and q_i indicates the number of observations completed at the i th level. Likewise, the mean sum of squares (MSS) for a particular input factor is calculated as given below,

$$MSS = \sum_{i=1}^p q_i (\overline{\psi_i})^2 - N_o (\overline{\psi})^2 \quad (5.1.5)$$

where, $\overline{\psi_i} = \frac{1}{q_i} \sum_{j=1}^{q_i} \psi_{ij}$ represents the sample mean of the observed data points at the i th level. The

error sum of squares (ESS) depends upon terms TSS and MSS which is expresses in [Eq. \(5.1.6\)](#),

$$ESS = TSS - MSS \quad (5.1.6)$$

The percentage contribution of each governing factor (C_v) on the response parameter i.e. m_d can be estimated by the following equation,

$$C_v (\%) = \frac{MSS - DFI \times (ESS/DFE)}{TSS} \times 100 \quad (5.1.7)$$

where, DFI and DFE represent the degree of freedom for a input/governing factor and error respectively. The coefficient of determination is also symbolised by R^2 which measures how well the predicted response is simulated by the correlation model created on the amount of total deviation in the outcomes explained by the model. The goodness of fit for a model is measured by R^2 as represented in using Eq. (5.1.8). Lesser the error term (ESS) in the expression, better the model fit i.e. R^2 approaches to the maximum value (1).

$$R^2 = \frac{MSS}{TSS} = 1 - \frac{ESS}{TSS} \quad (5.1.8)$$

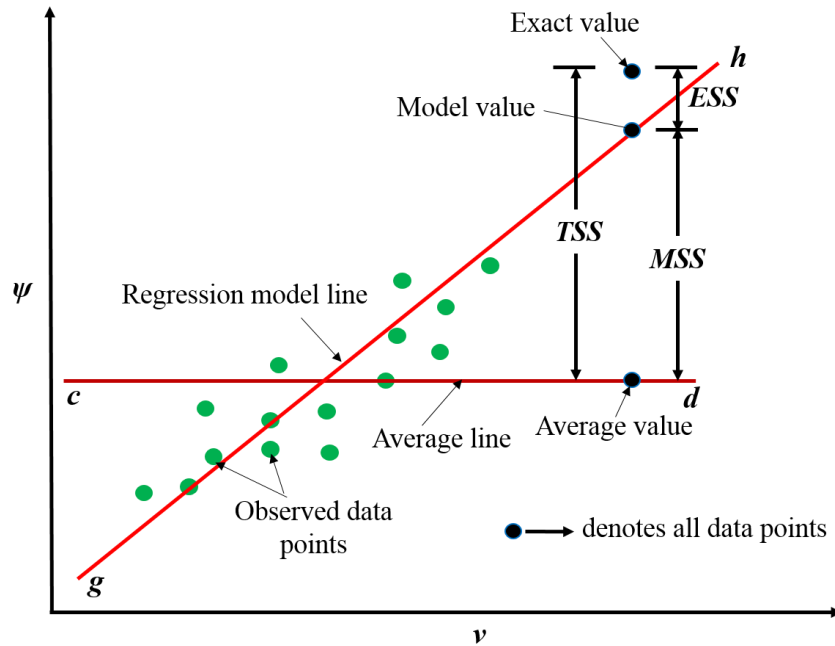


Figure 5.1.3: Graphically representation of ANOVA method for linear

5.1.3 Results and discussion

The first phase of the study covers the performance analysis of the developed CFDS in the form of m_d , variation of T_f , T_{bw} and T_{ma} at variable input conditions of $T_{WH, inL}$, θ_g and H_{bw} . The average values (taken over three replicates) of all performance parameters along with standard error are revealed in all plots. In the second phase, the response surface-based correlations (linear and

quadratic) are developed using BBD, ANOVA and regression methods. A total of 13 optimum design sets of experiments are executed based on the BBD method. The deviation in the response parameter (m_d) is analyzed in terms of input factors ($T_{WH, inl.}$, θ_g and H_{bw}) through main effect and interaction plots using ANOVA method. Then, a regression technique is used for development of correlations and the accuracy or goodness of generated correlations is checked by the coefficient of determination or R^2 . Further, the response surface are plotted and found the percentage contribution of each input factor (linear, square and 2-way interaction) on the response parameter. Lastly, a comparison study is also performed for the response parameter between experimental and correlation values under similar input conditions to analyze the errors.

5.1.3.1 Mass of distilled/pure water

Figure 5.1.4 illustrates the variations of m_d corresponding to θ_g at 0.08 m of H_{bw} and three different $T_{WH, inl.}$. It has been found that at 282.67 °C of $T_{WH, inl.}$, m_d is found slightly greater at 45° (1.857 kg) than at 30° (1.770 kg) of θ_g while a low value of 1.583 kg is obtained at 60° of θ_g . This is due to the fact that at this $T_{WH, inl.}$, a low amount of vapours are formed that can be completely condensed corresponding to a low θ_g . Also, the time required to flow the vapours in the CFDS at low θ_g is less and a fast condensation is possible for a limited amount of vapours while the same is high corresponding to higher a value of θ_g that leads to low production of m_d . A similar behaviour can be seen corresponding to 302.33 °C of $T_{WH, inl.}$ but θ_g of 45° and 60° are found more effective than 30° because the more fast formation of vapours may not be handled by θ_g of 30° due to overflow of vapours at the internal surface of glass and excess condensed vapours fall down to the basin through gravity affect. On the other hand, at θ_g of 45° and 60°, all the vapours can be condensed completely but the time needed in the flow of vapours for 45° of θ_g is less than 60° that leads to a higher value of m_d . At the highest $T_{WH, inl.}$ of 321.53 °C, the overflow of vapours continuously increases at 30° of θ_g which leads to a limited increase in the amount of m_d . In contrast to that the fast movement of vapours declines the time to reach the internal surface glass for 45° and 60° of θ_g which can condense higher vapours. The maximum value of m_d is found to be 2.407 kg at 45° of θ_g and 321.53 °C of $T_{WH, inl.}$. The outcomes revealed that under all set conditions of $T_{WH, inl.}$ and H_{bw} , θ_g of 45° is found the most favourable and higher values of $T_{WH, inl.}$ is always preferred for larger production of m_d . Therefore, corresponding to 321.653 °C of $T_{WH, inl.}$ and 45° of θ_g , the variation of m_d with respect to H_{bw} is observed in Figure 5.1.4b. It has been found that at the highest H_{bw} of 0.10 m, the production of m_d (1.403 kg) is found minimum whereas

the maximum m_d is obtained for H_{bw} of 0.08 m. Corresponding to H_{bw} of 0.06 m, the production of m_d is measured as 2.147 kg. This is due to the fact that for constant temperature heat input, a high volume of basin water for 0.10 m of H_{bw} always attains a low temperature that produces less number of vapours and consequently generates a low amount of m_d .

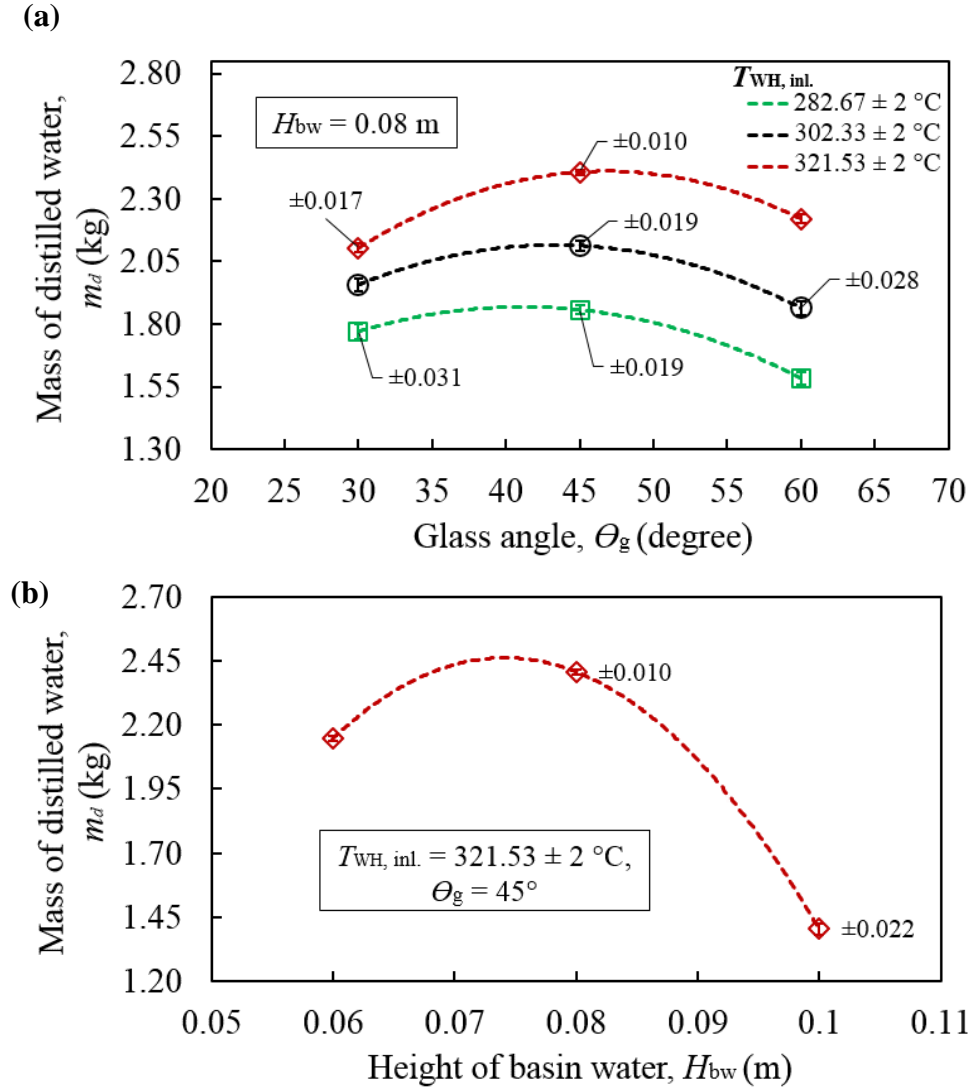


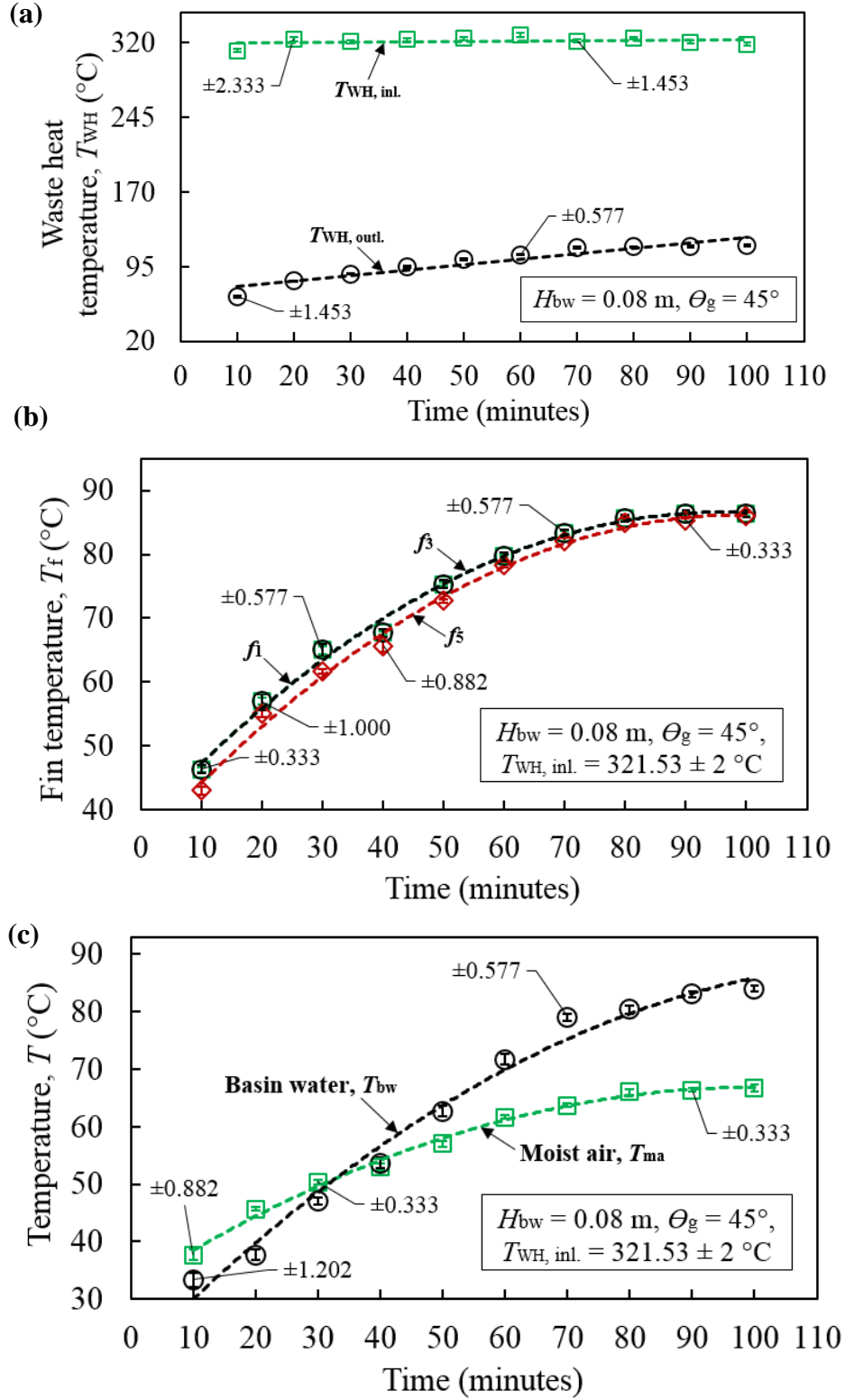
Figure 5.1.4: Variation of m_d with (a) θ_g and (b) H_{bw}

Further, at H_{bw} of 0.08 m, the waste heat pipe is just fully covered with basin water which gets heated at high temperatures through maximum possible heat transfer for fast evaporation of water. At the same time, the level of surface water is just 0.01 m above the copper fins, therefore fins boost the evaporation process by supplying heat to the high energy molecules of surface water. This leads to a fast generation of vapours that completely condense at 45° of θ_g to generate high m_d . During the level of 0.06 m of H_{bw} , the surface of the waste heat pipe is not fully covered and

some surface (0.01 m of height) is open to moist air. This results in a limited transfer of heat to the basin water and generate a certain amount of vapours that produces low m_d .

5.1.3.2 Transient variation of distilled water and temperatures for waste heat, fins, moist air and basin water

Figure 5.1.5a illustrates the transient variation of $T_{WH, inl.}$ at optimum points of θ_g and H_{bw} . It can be seen that $T_{WH, inl.}$ remains nearly constant (321.653 ± 2 °C) throughout the experiment due to the consistent running of the engine-generator at a constant frequency (51 Hz) while the outlet temperature of WH for CFDS i.e. $T_{WH, outl.}$ considerably rises with time. This is attributed to a large temperature difference between the waste heat and basin water at early stage that leads to a high heat transfer and leaving at low $T_{WH, outl.}$. This temperature difference decreases with the passage of time which results in delivering low heat energy from the waste heat and exiting at high $T_{WH, outl.}$. Figure 5.1.5b shows the transient deviation of fins (1st, 3rd, and 5th) temperature (T_{f1} , T_{f3} and T_{f5}) at optimum points of $T_{WH, inl.}$, θ_g and H_{bw} . It has been observed that T_{f1} and T_{f3} remain the same while T_{f5} is found to be slightly lower but this reaches the equilibrium state with T_{f1} and T_{f3} during the last phase of the experiment. This is attributed to the fact that T_f depends upon the surface temperature of waste heat pipe that varies along its length i.e. highest at the inlet side while lowest at the outlet side. Under a constant $T_{WH, inl.}$, T_f reaches to a steady state condition with a maximum value of 86.33 °C during the last phase of the experiment. The transient profiles of T_{bw} and T_{ma} at optimum points of $T_{WH, inl.}$, θ_g and H_{bw} are presented in Figure 5.1.5c and found that T_{bw} varies in accordance with T_f and surface temperature of waste heat pipe due to the direct contact of basin water with them. The maximum T_{bw} is reached as 84.0 °C at the least point of the experiment. The tendency of T_{ma} is found to be high compared to T_{bw} at the primary phase due to the high initial temperature of ambient than basin water but T_{bw} overcomes at a certain point due to the slow rise of T_{ma} with time as the medium of heat is air. The maximum achieved value of T_{ma} is recognised as 66.67 °C. Corresponding to these optimal conditions of $T_{WH, inl.}$, θ_g and H_{bw} , the production of



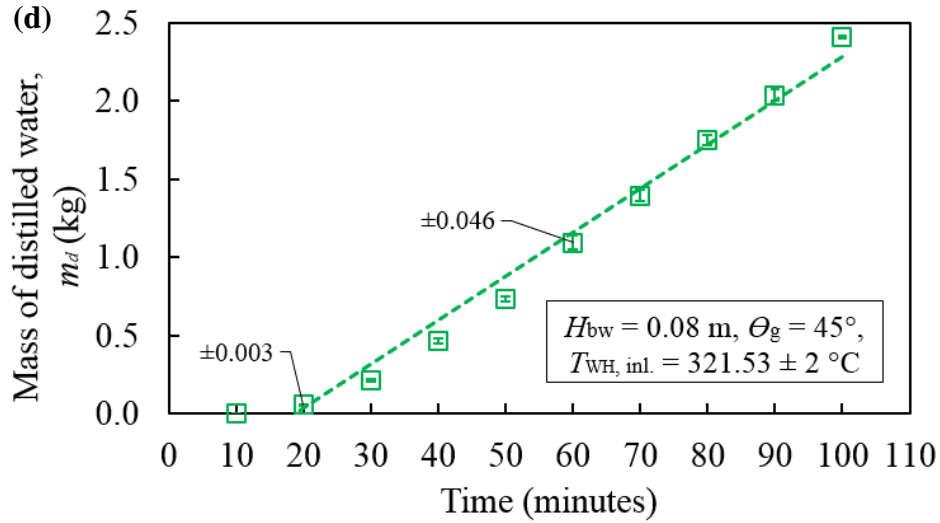


Figure 5.1.5: Transient variation of (a) $T_{WH, inl.}$ and $T_{WH, outl.}$, (b) T_{f1} , T_{f3} and T_{f5} , (c) T_{bw} and T_{ma} , and (d) m_d at optimal working conditions

m_d is analyzed in Figure 5.1.5d. It can be clearly seen that the production of m_d at the exit port of pure water channel starts after 20 minutes of the experiment and it increases almost linearly with time at a higher rate during later period than earlier. This is because of that the initially transferred heat is consumed to reach the certain T_{bw} and vapours formed are very less but as T_{bw} reaches high, consequently the production rate of m_d also rises due to high generation and condensation of vapours. The maximum production of m_d is noted as 2.407 kg.

5.1.3.3 Effect of fins and wick

Figure 5.1.6 shows m_d obtained at different accessibility of fins and wick performed under optimal conditions. In the first case, fins and wick both are not applied and obtained 2.054 kg of m_d . In the second case, fins are accessed but wick is not applied and got 2.245 kg of m_d . With applying the fins, the increased amount for m_d is found to be 0.191 kg with 9.30% improvement in the production yield. The reason is expressed in such a way that fins help to boost the evaporation process by supplying the additional heat to the surface water molecules that require less energy to evaporate than the molecules below the surface level as shown in Figure 5.1.7. The water molecules at surface level have high kinetic energy and needs a very small amount of heat to form vapours because evaporation depends upon the kinetic energy of water molecules and it is a surface phenomenon. In the third case, both fins and wick are accessed and achieved a total production of 2.407 kg with 17.18% of enhancement in the yield of m_d . Without wick, cold water over the outer surface of glass flows in the layers form causing partially covering the glass' surface and remaining

hot surface at some portion [Figure 5.1.8a](#). This leads to the point that the vapours which are come in contact with that portion are not able to condense properly due to this hot surface. Further, the application of a wick on the outer surface of glass ensures the smooth flow of cold water in film form all over the surface which helps in covering/condensation of more vapours [Figure 5.1.8b](#).

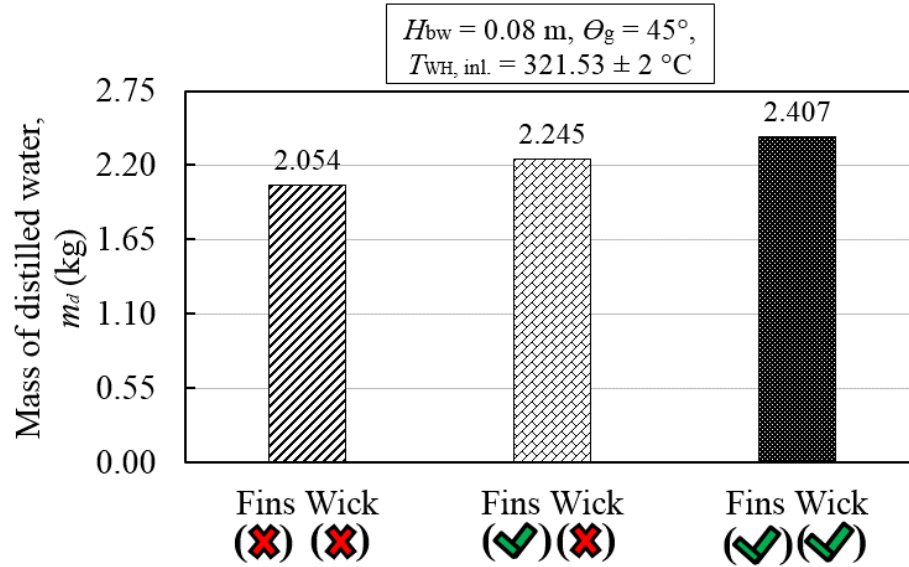


Figure 5.1.6: Mass of distilled water, m_d obtained at different accessibility of fins and wick

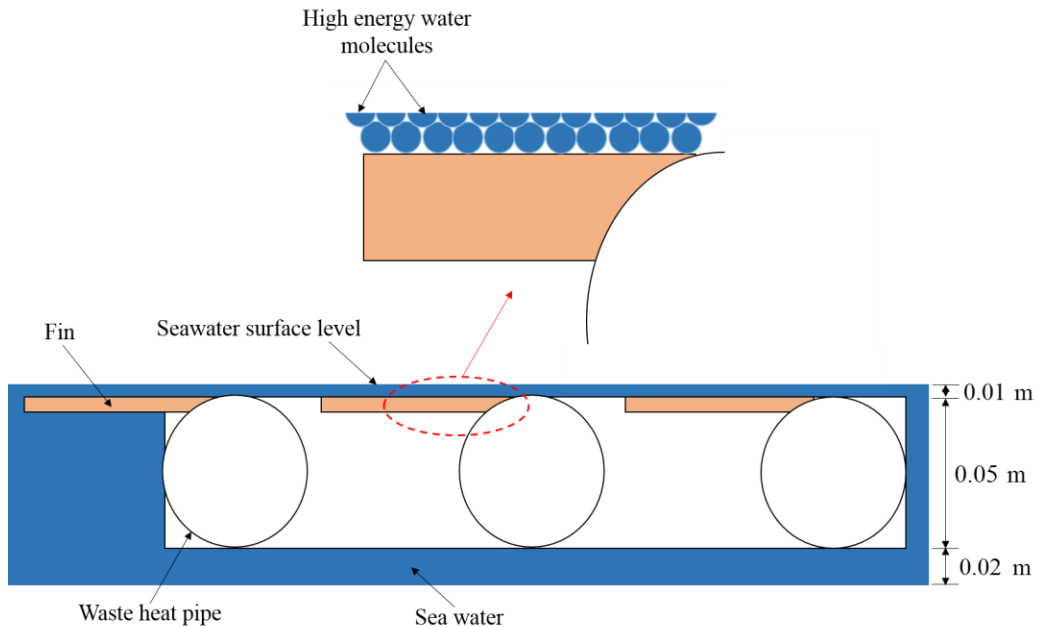


Figure 5.1.7: Effect of fins on m_d through evaporation of high energy water molecules



Figure 5.1.8: (a) Structure of cold water flow over glass' surface without wick and (b) effects of wick on m_d through condensation of water vapours

5.1.3.4 Performance ratio and productivity of distilled water

The efficiency of the distillation system can be gauged by introducing an index known as performance ratio (PR). It is generally defined as the ratio of heat energy accumulated by m_d to the heat energy supplied to CFDS (Q_{CFDS}) as given below [Yeo et al. 2019],

$$PR = \frac{m_d \times (h_{fg} + c_{bw} \times \Delta T_{bw})}{Q_{CFDS}} \quad (5.1.9)$$

where, h_{fg} ($= 2257 \times 10^3$ J/kg) represents the latent heat of evaporation for water, c_{bw} designates as the specific heat of basin water and ΔT_{bw} indicates the temperature rise of basin water before evaporation. Q_{CFDS} can be calculated by the following equation [Yeo et al. 2019],

$$Q_{\text{CFDS}} = \left[\rho_{\text{WH}} \times c_{\text{WH}} \times V_{\text{WH}} \times \frac{1}{r} \sum_{t=t_{10}}^{t_{100}} \{T_{\text{WH,inl.}}(t) - T_{\text{WH,outl.}}(t)\} \right] \times 6000 \quad (5.1.10)$$

where, ρ_{WH} , c_{WH} and V_{WH} denote the density, specific heat and volume flow rate of flue gases (waste heat/WH) respectively [Yeo et al. 2019], t indicates the time at which temperature readings are taken starting from t_{10} to t_{100} (t_{10} , t_{20} , t_{30} ,, t_{100}) with a total of r ($= 10$) readings during 100 minutes (6000 s) of the experiment. The comparisons of PR and productivity of m_d of the CFDS with the published literature are presented in Table 5.1.4 under working conditions of different factors. It can be seen that the distillation system operated by the solar collector as external heat source has found very low productivity as well as PR as reported by [Omara et al. 2013], [Issa and Chang 2017] and [Xiong et al. 2013] compared to the system run by WH [Yeo et al. 2019] and present CFDS. It means that WH is more effective than the solar collector to produce high m_d , however, it is true that collector is driven by the easy accessible solar energy which is also a renewable source of energy. But it is not accessible during the winter, night and rainy seasons that applies limitation on the productivity of distillation system. In contrast to that WH can be accessed at any time and place that make it more flexible to use along with a high productivity. Comparing the performance of distillation system operated from WH, the present CFDS has high productivity (38.51 kg/m²/day) and PR (2.37) than the productivity (31.46 kg/m²/day) and PR (2.32) obtained by [Yeo et al. 2019] in which solar energy was also used in addition to WH. Further, it has been also noticed that the distillation system used by [Yeo et al. 2019] was basin section + multi effect diffusion section (without fins) while the present CFDS has a single basin section (with fins and wick) but still the CFDS produces high performance. [Yeo et al. 2019] also performed the same system using electric heater as well as solar energy as heat sources and found PR of 1.17 as well as 0.71 respectively. If compared to the simple passive distillation run by the solar energy only, the present CFDS is found much superior.

Table 5.1.4: Comparisons of PR and productivity of m_d under working conditions of different parameters

| Parameter | Omara et al. 2013 | Yeo et al. 2019 | Issa and Chang 2017 | Xiong et al. 2013 | Present CFDS |
|---|--|--|---|---|-----------------------------------|
| Type of system | basin section | basin section + multi effect diffusion section | basin section | multi effect diffusion section | basin section |
| Glass area, m ² | 0.58 | 1.00 | 0.83 | 1.28 | 0.64 |
| Basin area, m ² | 0.50 | 0.78 | 0.72 | - | 0.60 |
| θ_g , degree | 30 | 45 | 30 | 20 | 45 |
| Heating source | solar + evacuated tube solar collector | solar + waste heat (gasoline engine) | solar + evacuated tube solar collector | solar + vacuum tube solar collector | waste heat (biomass engine) |
| $T_{WH, inl.}$, °C | - | 280-350 | - | - | 282-321 |
| PR | - | 2.32 | - | 1.86 | 2.37 |
| Productivity of m_d , kg/m ² /day | 16.70 | 31.46 | 3.60 | 9.61 | 38.51 |

5.1.3.5 Properties of distilled/pure water

The seawater contains an average salinity/SC of about 30-35 g/L (3.0-3.5%) with a maximum of 45 g/L (4.4%) [De Villiers 1999]. Therefore, it is made from the typically available normal water by proper mixing of salt in the same proportion as in seawater and used for the experimental work. The properties of synthetic seawater (Figure 5.1.9a) and obtained distilled water (Figure 5.1.9b) are measured by a Horiba made Salinometer and presented in Table 5.1.5 along with BIS maximum limit. It can be seen that a maximum limit of SC (4.45%) is achieved for seawater which has been reduced to an acceptable range (0.00-0.02%) of drinking water through the CFDS.

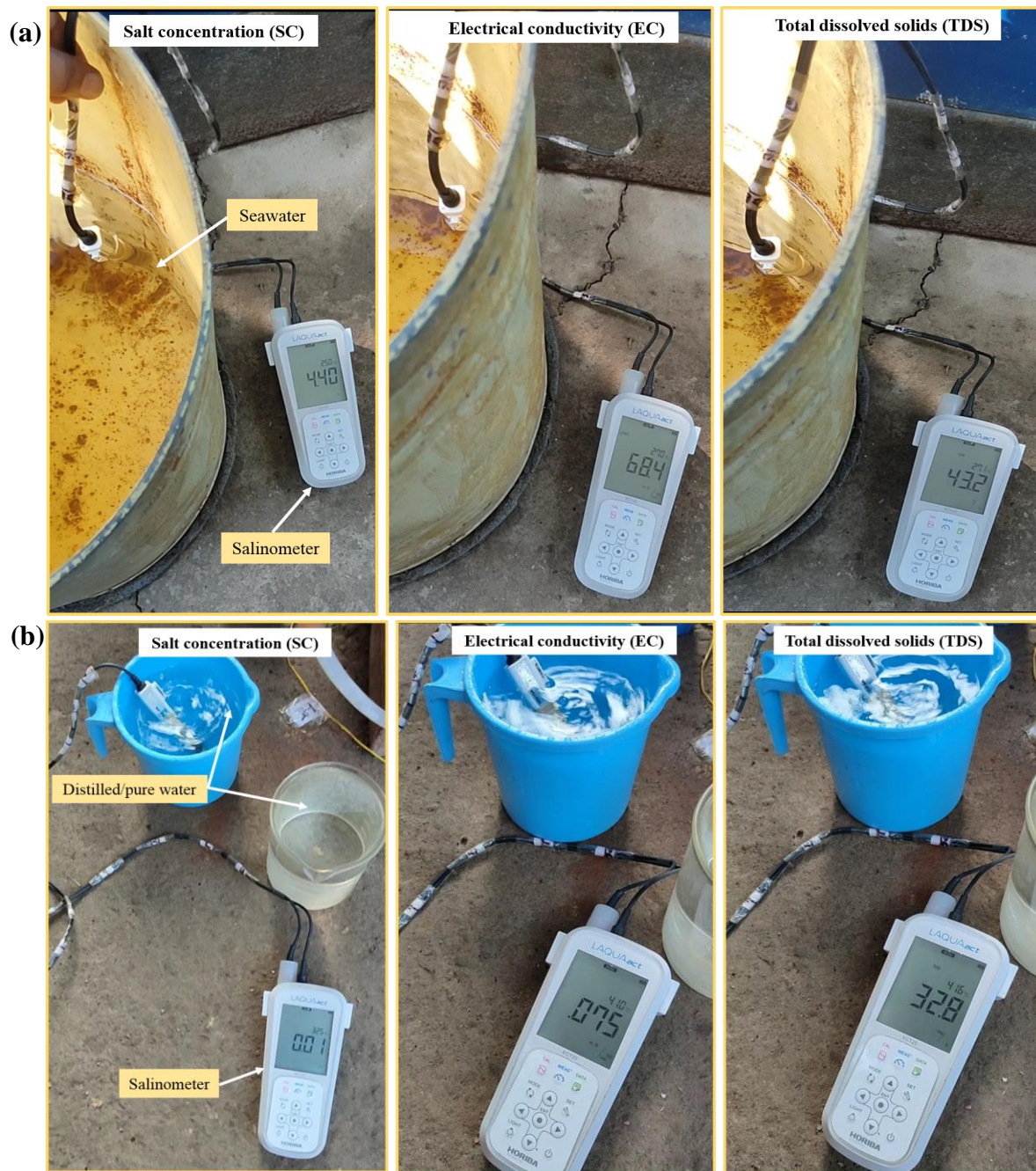


Figure 5.1.9: Measured values of SC, EC and TDS for (a) seawater and (b) distilled/pure water

Table 5.1.5: Properties of seawater, distilled water and BIS maximum limit

| Type of water | SC (%) | EC (mS/cm) | TDS (mg/L) |
|--|------------|-------------|------------|
| Seawater | 4.36-4.45% | 64.1-69.6 | 40.5-44.9 |
| Distilled/pure water | 0.00-0.02% | 0.060-0.085 | 27.1-33.6 |
| BIS maximum limit [Sivakumar et al. 2014] | 0.05% | - | 500 |

5.1.3.6 Response surface analysis

A total of 13 experiments are performed for the response surface analysis at different design set conditions of input parameters and the output in the form of m_d corresponding to these conditions are presented in Table 5.1.6. In order to better performance of the CFDS, the desired output (m_d) needs to be maximum. The three different input factors have their own influence on the production of m_d and it is analysed by plotting the main effects of individual factors using ANOVA method as shown in Figure 5.1.10. It has been observed that each factor has its own certain influence on m_d but $T_{WH, inl.}$ (part I of Figure 5.1.10) and H_{bw} (part III of Figure 5.1.10) are found to be the most dominant factors over θ_g (part II of Figure 5.1.10). With a rise in $T_{WH, inl.}$ from 283 °C to 302 °C, m_d increases at a slower rate but the same increases drastically when $T_{WH, inl.}$ rises from 302 °C to 321 °C. It means that the vapours formation rate at upper $T_{WH, inl.}$ is high compared to lesser $T_{WH, inl.}$ which leads to a larger slope of m_d during 302-321 °C than 283-302 °C. Therefore it is being suggested that prefer to use a high $T_{WH, inl.}$ to obtain a higher m_d . When the second governing factor i.e. H_{bw} varies from 0.06 m to 0.08 m, the production of m_d also increases but further increase in H_{bw} from 0.08 m to 0.10 m, the value of m_d largely decreases. The reason is that the waste heat pipe is not fully covered at 0.06 m of H_{bw} , however, the low volume of basin water attains high T_{bw} for a certain amount of heat input. This generates a significant amount of vapours and produces a certain amount of m_d . The waste heat pipe got fully covered when H_{bw} is further increased from 0.06 m to 0.08 m and generated a large amount of vapours. During this time, fins also provide additional heat to the surface water to produce more vapours that result in a high generation of m_d . The further increase in H_{bw} from 0.08 m to 0.10 m largely added to the volume of basin water and its temperature reaches a low value for a certain amount of heat input. This leads to a low generation of vapours and consequently generates a small amount of m_d . The least influence on

the m_d among all input factors is observed for θ_g . With an increase in θ_g from 30° to 45° , a slight variation in m_d is found but the value of m_d decreases during 45° to 60° of θ_g .

Table 5.1.6: Experimental outcomes for the mass of distilled water under the different design set of run

| Experiment run | $T_{WH, \text{inl.}}$ ($^\circ\text{C}$) | θ_g (degree) | H_{bw} (m) | m_d (kg) | Standard error |
|---------------------------|---|---|--------------------------------|------------------------------|---------------------------|
| 1 | 321 | 45 | 0.10 | 1.403 | 0.018 |
| 2 | 321 | 30 | 0.08 | 2.103 | 0.020 |
| 3 | 302 | 60 | 0.10 | 1.203 | 0.022 |
| 4 | 283 | 45 | 0.10 | 1.157 | 0.020 |
| 5 | 302 | 45 | 0.08 | 2.113 | 0.023 |
| 6 | 321 | 45 | 0.06 | 2.147 | 0.015 |
| 7 | 283 | 45 | 0.06 | 1.780 | 0.017 |
| 8 | 321 | 60 | 0.08 | 2.220 | 0.021 |
| 9 | 302 | 60 | 0.06 | 1.790 | 0.017 |
| 10 | 302 | 30 | 0.06 | 1.753 | 0.020 |
| 11 | 283 | 60 | 0.08 | 1.583 | 0.023 |
| 12 | 283 | 30 | 0.08 | 1.770 | 0.032 |
| 13 | 302 | 30 | 0.10 | 1.253 | 0.020 |

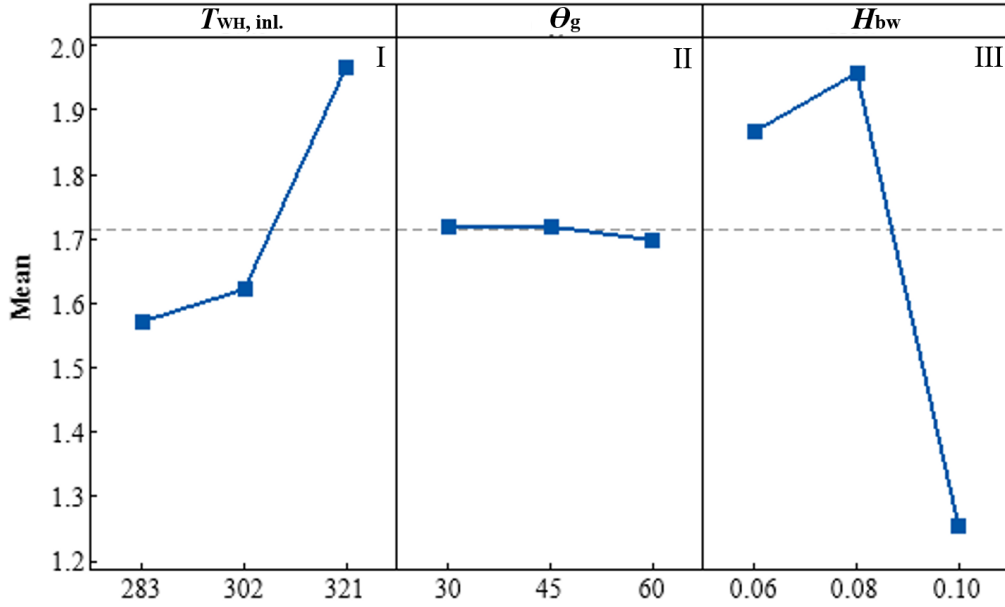


Figure 5.1.10: Main effects of individual input factors ($T_{WH, inl.}$, Θ_g and H_{bw}) on the experimental output (m_d)

The interaction effect of different input factors ($T_{WH, inl.}$, Θ_g and H_{bw}) on the experimental output (m_d) is presented in Figure 5.1.11. Interaction occurs when the influence of any input factor on performance output depends upon the level of other input factors. The interactions of $T_{WH, inl.}$ with Θ_g , $T_{WH, inl.}$ with H_{bw} and Θ_g with H_{bw} are represented by parts I, II and III of Figure 5.1.11 respectively. It can be observed from part I that at a low $T_{WH, inl.}$ (represented by a blue line), Θ_g of 30° is more desirable than 45° and 60° because a certain amount of vapours can be condensed fastly at 30° as the time to flow the vapours is very low. As the $T_{WH, inl.}$ increases at a moderate level (represented by a dark red dashed line), Θ_g of 45° is found to be more favourable than 30° and 60°. The reason is that the increased amount of vapours may overflow for 30° but all vapours can be handled by 45° of Θ_g . For high $T_{WH, inl.}$ (represented by a green dashed line), Θ_g of 60° is observed as dominant over 30° and 45° in the condensation of large vapours. It can be witnessed from part II that at a low $T_{WH, inl.}$ (represented by a blue line), H_{bw} of 0.06 m is found to be more favorable due to high generation of vapours as the low volume of basin water at 0.06 m of H_{bw} can achieve high T_{bw} . Although, some portion (0.01 m in height) of the waste heat pipe remains uncovered that leads to loss of heat energy and do not participate in heating the basin water. The further rise in $T_{WH, inl.}$ at a moderate (represented by a dark red dashed line) and high (represented by a green dashed line) levels, H_{bw} of 0.08 m is identified more attractive because the maximum heat is transferred from the waste heat pipe for a certain volume of basin water which leads to high

generation of vapours and fins boost the evaporation process by delivering the additional heat to the high energy water molecules at surface level. It has been observed from part III that for all levels of θ_g (at low, moderate and high represented by blue, dark red dashed and green dashed lines respectively), H_{bw} of 0.08 m always supports the large production of m_d but its highest value is obtained at θ_g of 45° compared to 30° and 60° . It is due to the fact that at 0.08 m of H_{bw} , the maximum possible heat transfer occurs and produces a large amount of vapours that can be condensed at θ_g of 45° .

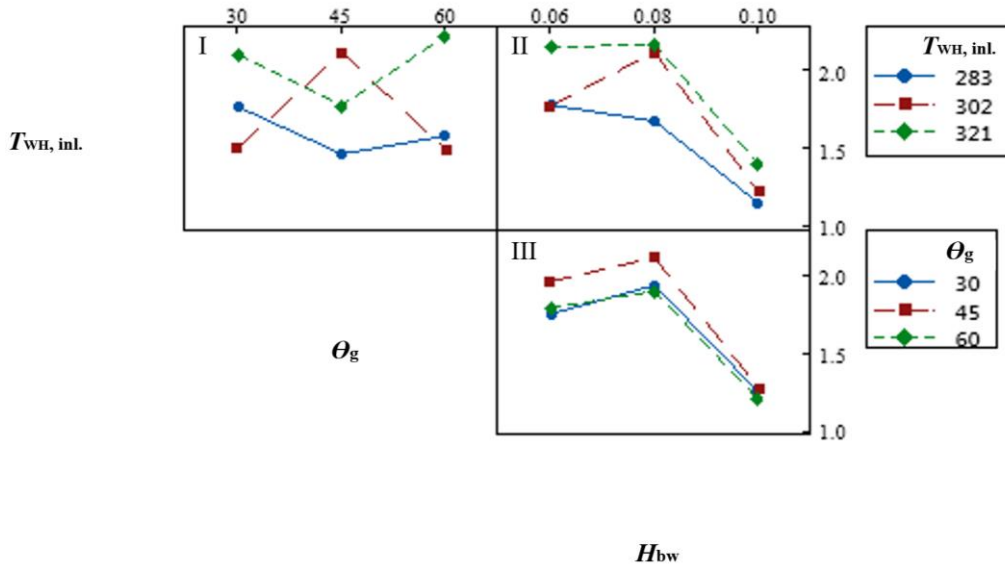


Figure 5.1.11: Interaction effect of various input factors ($T_{WH, inl.}$, θ_g and H_{bw}) on the experimental output (m_d)

The developed correlations (linear and quadratic) for the response parameter (m_d) are given below,

$$m_d = -0.17 + 0.01042 T_{WH, inl.} - 0.00069 \theta_g - 15.33 H_{bw} \quad (5.1.11a)$$

$$m_d = -16.2 + 0.065 T_{WH, inl.} - 0.0121 \theta_g + 193.9 H_{bw} - 0.0001 T_{WH, inl.}^2 - 0.000702 \theta_g^2 - 1139 H_{bw}^2 + 0.000266 T_{WH, inl.} \times \theta_g - 0.079 T_{WH, inl.} \times H_{bw} - 0.072 \theta_g \times H_{bw} \quad (5.1.11b)$$

$$m_d^* = -7.25 + 16.2 T^* - 0.0056 \theta_g + 12.83 H^* - 13.7 T^{*2} - 0.000316 \theta_g^2 - 11.26 H^{*2} + 0.0660 T^* \times \theta_g - 2.90 T^* \times H^* - 0.0048 \theta_g \times H^* \quad (5.1.11c)$$

The precision or goodness of developed correlations is determined by the coefficient of determination i.e. R^2 and it is presented in Table 5.1.7. It can be clearly recognized from the table that quadratic polynomial correlation can predict the response parameter with an accuracy of

98.43% whereas the linear correlation provides 64.01%. Therefore, the quadratic correlation is preferred to use in order to predict the value of response parameter by minimizing the error.

Table 5.1.7: Goodness of correlations for the mass of distilled water as response parameter

| Response parameter | Coefficient of determination or R^2 | |
|-------------------------------------|---------------------------------------|-----------|
| | Linear | Quadratic |
| Mass of distilled water, m_d (kg) | 0.6401 | 0.9843 |

The 3-D surface plots that display the combined effect of any two input factors (out of three i.e. $T_{WH, inl.}$, θ_g and H_{bw} with keeping one factor constant at centre level) on the predicted m_d are presented in Figure 5.1.12. In the first part (a) of Figure 5.1.12, the combined effect of $T_{WH, inl.}$ and θ_g is reported with keeping H_{bw} as a constant at the centre level of 0.08 m. It has been observed that the lowest level of $T_{WH, inl.}$ and the highest level of θ_g has a negative effect on m_d and produces its lowermost/minimum value. Corresponding to the highest level of $T_{WH, inl.}$ and moderate level of θ_g , a maximum value is observed for m_d . The combined effect of $T_{WH, inl.}$ and H_{bw} is analyzed in the second part (b) of Figure 5.1.12 with keeping θ_g as a constant at the centre level of 45° . It can be clearly seen that the better performance for m_d is always found to be at a moderate level of H_{bw} under all levels of $T_{WH, inl.}$, but its maximum value is obtained at the highest level of $T_{WH, inl.}$. In the third part (c) of Figure 5.1.12, the combined effect of θ_g and H_{bw} is reported with keeping $T_{WH, inl.}$ as a constant at the centre level of 302°C . It has been realized that the maximum value for m_d is achieved corresponding to the moderate levels of θ_g and H_{bw} . Therefore, it can be suggested that the highest level of $T_{WH, inl.}$ is always preferred to use to obtain maximum value for m_d but in the context of θ_g and H_{bw} , their moderate levels provide maximum performance for m_d .

The contour plots that show the different ranges of obtained m_d at various grouping of any two input factors are presented in Figure 5.1.13. In the first part (a) of Figure 5.1.13, the different ranges of obtained m_d at the combination of $T_{WH, inl.}$ and θ_g is specified with holding the $H_{bw} = 0.08$ m. It has been witnessed that the maximum range (> 2.2 kg or the area represented by purple colour) of m_d can be obtained at about $38-58^\circ$ of θ_g and $312-321^\circ\text{C}$ of $T_{WH, inl.}$. Further, it is also realized that as the $T_{WH, inl.}$ decreases from 321°C to 312°C , the range of θ_g goes narrow in order to obtain the same value of m_d but $\theta_g = 45^\circ$ is always desirable over the entire range ($312-321^\circ\text{C}$)

of $T_{WH, \text{inl.}}$. It means that the highest range of obtained m_d can be achieved at a lower $T_{WH, \text{inl.}}$ (312 °C) if $\theta_g = 45^\circ$ is selected but it requires a higher $T_{WH, \text{inl.}}$ to get the same m_d when θ_g is chosen

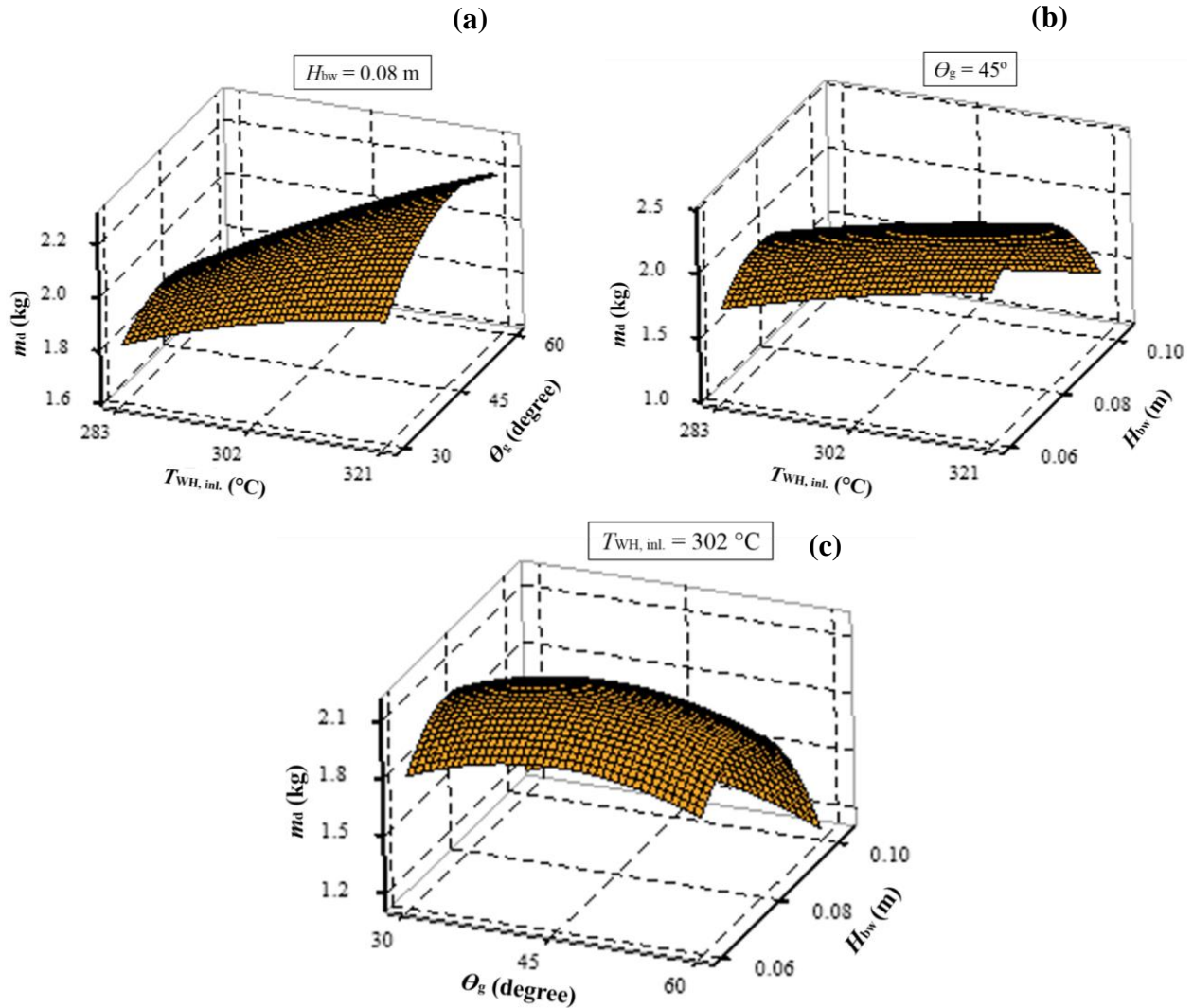


Figure 5.1.12: Surface plots that show the combined effect of any two input factors (a) $T_{WH, \text{inl.}}$ and θ_g , (b) $T_{WH, \text{inl.}}$ and H_{bw} and (c) θ_g and H_{bw} with keeping one factor constant (centre level) at a time on the predicted m_d

other than 45° . A similar behaviour can also be seen for the lower ranges of obtained m_d except that the desired value of θ_g slightly drops as the $T_{WH, \text{inl.}}$ is further lowered. In the second part (b) of Figure 5.1.13, the different ranges of obtained m_d at the arrangement of $T_{WH, \text{inl.}}$ and H_{bw} is stated with holding the $\theta_g = 45^\circ$. It has been observed that the maximum range (> 2.2 kg or the area represented by purple colour) of m_d can be attained at nearly 0.062-0.082 m of H_{bw} and 306-321

°C of $T_{WH, \text{inl.}}$ but that the range of H_{bw} goes contracted, as the $T_{WH, \text{inl.}}$ reduces from 321 °C to 306 °C. Moreover, it is also recognized that $H_{bw} = 0.075$ m is always preferable to get a maximum value of m_d over the entire range (306-321 °C) of $T_{WH, \text{inl.}}$. A similar action can also be realized for the lower ranges of obtained m_d . In the third part (c) of Figure 5.1.13, the different ranges of obtained m_d at the combination of H_{bw} and θ_g is indicated with holding the $T_{WH, \text{inl.}} = 302$ °C. It has been detected that the maximum range (> 2.0 kg or the area represented by purple colour) of m_d can be found at about 0.062-0.082 m of H_{bw} and 30-60° of θ_g but the range of H_{bw} goes slim when θ_g changes either lesser or greater than 45°. The desired values of θ_g and H_{bw} are found as 45° and 0.075 m respectively.

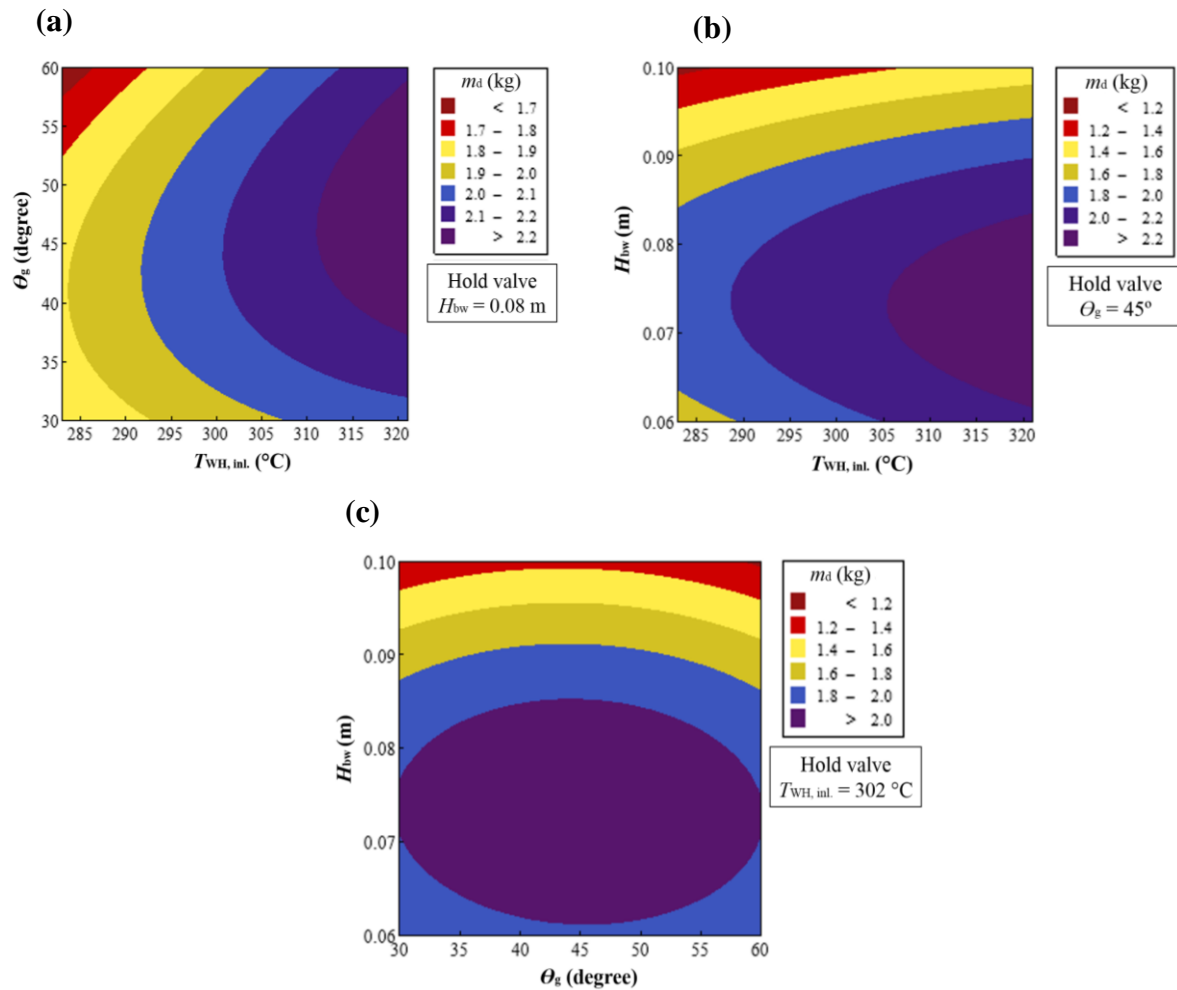


Figure 5.1.13: Contour plots that display the different ranges of obtained m_d at various the combination of any two input factors (a) $T_{WH, \text{inl.}}$ and θ_g , (b) $T_{WH, \text{inl.}}$ and H_{bw} and (c) θ_g and H_{bw} . The predicted value of m_d in correlation depends upon the linear, square and 2-way interaction of different input factors and their contributions are presented in Figure 5.1.14. The most sensitive

input factor in linear among all is recognized as H_{bw} followed by $T_{WH, inl.}$ and θ_g . The percentage contributions of H_{bw} , $T_{WH, inl.}$ and θ_g are realized as 45.15%, 18.81% and 0.05% respectively. In the contribution of square factors, H_{bw}^2 dominates (28.45%) the other two where $T_{WH, inl.}$ and θ_g contribute only 4.03% and 0.23% respectively. In the contribution of 2-way interaction factors, even though all interaction factors have a contribution below 2% but $T_{WH, inl.} * \theta_g$ found to be the most contributed factor with 1.38%. The error in the prediction of m_d is about 1.57%.

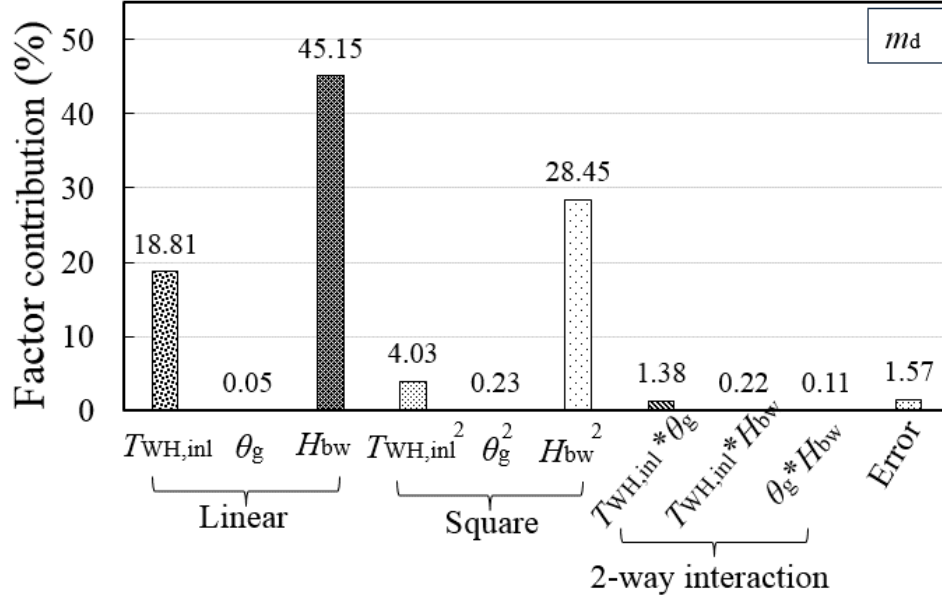


Figure 5.1.14: Contribution of various factors (linear, square and 2-way interaction of $T_{WH, inl.}$, θ_g and H_{bw}) in the predicted response parameter (m_d)

Based on the correlation, the values of m_d is predicted (a total number of 13 values) at the same design set conditions of different input factors and compared with the experimental outcomes of m_d along with the error between them as shown in Figure 5.1.15. The error (%) between the experimental and correlation values is calculated as follows,

$$\text{Error (\%)} = \frac{\text{Experimental value} - \text{Correlation value}}{\text{Experimental value}} \times 100 \quad (5.1.12)$$

It is observed that the present quadratic correlation has good agreement with the experimental results in the prediction of m_d and found the maximum error (acceptable) of 12.03%.

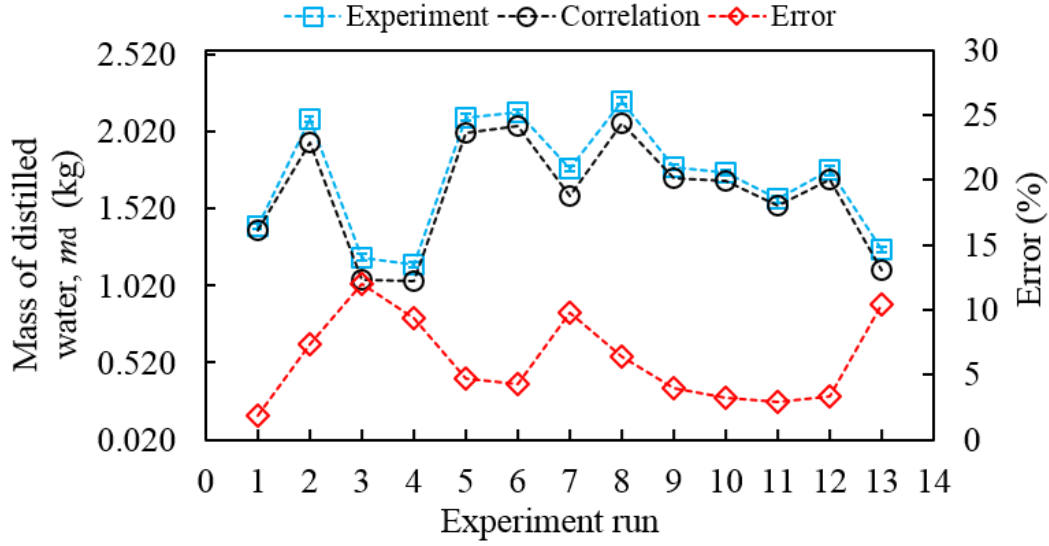


Figure 5.1.15: Comparison of correlation and experimental results for m_d along with error between them

5.1.3.7 Uncertainty analysis

Table 5.1.8 represents the uncertainties in the various measured values which are gauged by the method as mentioned in section 3.1.4.6.

Table 5.1.8: Uncertainty analysis of various measured values

| $T_{WH, inl.} = 321.53\text{ }^{\circ}\text{C}$, $\theta_g = 45^{\circ}$, $H_{bw} = 0.08\text{ m}$, Time = 100 minutes | | | | |
|---|--|--|--|------------------------------|
| | T_{fi} | T_{bw} | T_{ma} | m_d |
| Absolute | $3 \times 10^{-1}\text{ }^{\circ}\text{C}$ | $3 \times 10^{-1}\text{ }^{\circ}\text{C}$ | $3 \times 10^{-1}\text{ }^{\circ}\text{C}$ | $6 \times 10^{-3}\text{ kg}$ |
| Relative | 3×10^{-3} | 3×10^{-3} | 4×10^{-3} | 2×10^{-3} |

The expansion of technological development, different approaches to identifying and applications of distillation systems are prominent to be commercially realistic in the near future. Generally, the daily average productivity of the passive distillation system varies in the range of 0.4-1.9 kg/m²/day but if it is connected to the solar collector (active distillation system), the productivity increases to 2.9-4.6 kg/m²/day [Issa and Chang 2017]. However, the amount of distilled water produced varies from one study to another based on the design of the distillation system and working conditions such as wind speed, the intensity of solar radiation and ambient temperature. For example, the range of some distillation systems is reported as 3.60-16.70 kg/m²/day for certain designs as presented in Table 4. Due to the intermitted behaviour of solar

energy, only depending on it could not fulfill the demand of drinking pure water despite of accessible large amount of WH generated every year significantly at high temperatures. Also, there is no restriction for the location of distillation system if operated by WH and can work at night too. To produce 1000×10^3 kg of fresh water per day (365000×10^3 kg per year), about 10,000 tons of fossil fuel consumes every year [Methnani 2007]. If a single CFDS (with 1 m^2 of glass area) is applied for the recovery of available WH, it can produce about 14.05×10^3 kg per year over working 24 h for 365 days and save around 0.385 tons of fossil fuel per year. By applying more numbers of CFDS, a huge amount of fossil fuel may save for the next generation. The future is green with the high production CFDS through recovery of WH and possible to some extent the saving of fossil fuels along with the generation of drinking pure water.

5.1.4 Summary

The performance of the developed CFDS has been analyzed when operated by the WH and the key findings are given below,

- CFDS starts to produce m_d 20 minutes after the start of experiment and it increases almost linearly with time with a higher rate during the later period than earlier.
- The maximum value of m_d is obtained as 2.407 kg at optimal conditions of $T_{\text{WH, inl.}}$ (321.53°C), θ_g (45°) and H_{bw} (0.08 m). Corresponding to these conditions, the highest values of temperature for T_f (T_{f1} , T_{f3} and T_{f5}), T_{bw} and T_{ma} are found to be 86.33°C (T_{f1}), 84.0°C and 66.67°C respectively.
- The employment of wick and fins in the distillation system has increased its output from 2.054 kg to 2.407 kg with 17.18% improvement in the yield of m_d at the optimal conditions of input factors.
- The accuracy or goodness of the developed quadratic correlation for m_d is recognized as 98.43% with an error of 1.57%.
- The most governing input factors in the predicted response value of m_d are found to be H_{bw} and $T_{\text{WH, inl.}}$ which contribute 45.15% and 18.81% for linear respectively and 28.45% and 4.03% for quadratic respectively.
- It can be recommended from the surface plots that the highest level of $T_{\text{WH, inl.}}$ is always chosen to use to obtain a large value of m_d but the moderate levels of θ_g and H_{bw} provide maximum performance for m_d .

- The correlation has found good agreement with the experimental values and got a maximum error (acceptable) of 12.03%.

The above-mentioned outcomes provide guidelines for selecting the performance-driven factors in order to develop a high-production distillation system based on the availability of various heating resources.

CHAPTER 6

CONCLUSIONS AND FUTURE SCOPE

This thesis has covered the experimental investigation of a 10 kW biomass gasifier for useful energy production through optimizing the gasification process. Further, the potential of waste heat is analyzed for the effective power generation and desalination using various developed heat recovery systems as well as distillation system. This chapter presents the conclusions of performed work and the scope for the future work.

The inefficient use of biomass for energy production and dumping of WH to the ambient are major issues in the form of energy loss and environmental pollution. Therefore, the research work performed in this thesis has provided an optimistic solution in this regards. In order to address that the performance analysis of a downdraft biomass gasifier (10 kW capacity) is carried out for useful energy production through the optimization study using characterized sustainable waste/inefficiently used biomass and analyzed the feasibility of such plants having different capacities. Further, the WH of biomass energy-driven engine generator is applied to the developed HRSs (thermosyphon and array-based) for effective power generation. The potential of SGSP as a heat source has been also analyzed for the power generation when driven by solar energy as well as WH. Efforts have been made for charging the 12 V batteries (UPS and heavy-duty) from the output power of HRSs for end use. The potential of WH is further used for desalination to produce pure/distilled water by using a developed wick and copper-finned distillation system (CFDS) and developing the correlations for the response parameter. From this study, the following conclusions have been made,

- The various sustainable biomass (red mulberry, dried grass, leaves and dead branches) studied experimentally are found capable for useful energy production with a maximum HHV of 18.36 MJ/kg for red mulberry.
- The optimum value of ER is observed as 0.296 and found maximum values of CV as well η_{cg} as 5.846 MJ/m³ and 68.45% respectively. A blue colour flame is observed at the optimum ER.

- The economic investigation of different capacity plants (10 kW, 500 kW and 1000 kW) shows that a higher capacity plant is more favorable/economical as compared to a small capacity plant. Subsequently, the electricity production cost (Rs.4.34/kWh or 0.055 USD/kWh) and payback period (3.12 years) are found minimum for the largest capacity plant i.e., 1000 kW.
- An optimum ER of gasifier that results in the highest possible T_s (87 °C) is found to be 0.305 whereas the optimum TFR of thermosyphon is obtained as 0.496 for maximum performance.
- The maximum value of ΔT_{TEG} corresponding to 87 °C of T_s is found to be 39 °C where the maximum values of V (17.12 V) and I_s (0.152 A) are obtained from the TEGs-thermosyphon-based HRS. At these conditions, the maximum P_o and η_{TEG} are measured as 0.615 W and 2.218% respectively. Further, P_o is used for successfully charging a 12 V, 7 Ah UPS battery for end use and the minimum I_s required to charge this battery is realized as 0.118 A.
- The maximum relative error between the model and experimental values of ΔT_{TEG} is calculated as 14.91 %.
- The fabricated SGSP is capable of storing thermal energy with η_{SGSP} of 6.06% when driven by the solar energy under actual weather conditions.
- The maximum T_{LCZ} in SGSP is reached as 55.50 °C with a gain of 26.58 °C when working under S range of 26-976 W/m² over 40 days of operation.
- The TEGs-thermosyphon-based HRSs run by the SGSP (driven by solar energy) is not able to generate the enough output required to charge a 12 V, 7 Ah UPS battery at maximum achievable ΔT_{LU} (23.57 °C) due to the involvement of various thermal resistances (a total of nine) in the flow of heat transfer within the thermosyphon. The minimum required ΔT_{LU} for charging the UPS battery is experimentally determined as 45.62 °C.
- Further, it has been suggested that an external heat source is required to meet the same which can be fulfilled by the WH of biomass driven engine-generator. To charge a 12 V, 7 Ah UPS, The amount of required biomass i.e. m_b corresponding to a maximum achieved ΔT_{LU} of 23.57 °C is calculated as 10.11 kg.
- Then, the developed TEGs-array-based HRS run by the SGSP (driven by solar energy) has generated much higher (9.19 times) output compared to the TEGs-thermosyphon-based

and found a maximum V of 7.97 V corresponding to 43.36 °C of T_{LCZ} . But this output is still not enough and also it doesn't remain constant due to the intermittency of solar energy over the day and unavailability during the night.

- The experiments on the suggested requirement of an external heat source for the SGSP revealed that the SGSP is efficiently recovered the WH of biomass engine-generator with a significant range (0.75-0.77) of effectiveness and a high η_{SGSP} of 47.73%.
- The maximum values of V , I_s , P_o and η_{TEG} from the TEGs-array-based HRS are obtained as 81.62 V, 0.272 A, 7.483 W and 4.63% respectively at 68.04 °C (T_{LCZ}), 3 kW (W_L) and 51 Hz (f). This high performance is attained due to upgrading (array-based) in HRS where seven thermal resistances (out of total nine) have been totally eliminated and minimized the other two. Further, a 12 V, 80 Ah heavy-duty battery is successfully charged from the output power of upgrading HRS for end use.
- The proposed array-based HRS has produced 12-14 times more performance than the TEGs-thermosyphon-based HRS when operated directly by WH under similar temperature limit and obtained maximum V , I_s and P_o of 74.78 V, 0.261 A and 4.93 W respectively.
- The outcomes of the developed CFDS have explored that the maximum value of m_d (output/response parameter) is obtained as 2.407 kg at 321.53 °C, 45° and 0.08 m of $T_{WH, in}$, θ_g and H_{bw} respectively. Compared to a simple distillation system, the employment of wick and fins in CFDS has increased the productivity from 2.054 kg to 2.407 kg with a 17.18% improvement at the optimal conditions of input parameters.
- It has been realized that each factor has its certain influence on m_d , but H_{bw} and $T_{WH, in}$ are found to be the most dominant factors over θ_g .
- The quadratic correlation of the response parameter has been found to be in good agreement with the experimental values and found a maximum error of 12.03%.

It can be concluded from the outcomes of this study that the gasification process is an efficient way to produce useful energy (either thermal energy or power) from the biomass with almost zero waste production. Also, it is more economical for large capacities systems which could also be used for industrial purpose to reduce the load on grid electricity demand. Further, recovery of WH for power generation could produce more power due to enhancement of the system output towards fulfilling the electricity demand along with reduction in pollution. This study has also ensured that a large quantity of pure drinking water can be produced from the WH that could fulfill the demand

of pure water for any household along with power generation. Therefore, this research study provides useful guidelines in promoting as well as selecting gasification-based power plants and HRSs.

This study is experimentally carried out for end-use power generation using TEGs-based HRSs and pure drinking water production via distillation unit. Further, the blending of biomass (solid wood mixed with low-density biomass) can also be an appropriate feeding fuel for the biomass gasifier and the CO₂ exiting from the engine generator can be supplied as a gasifying agent along with air. The use of TEGs-thermosyphon-based HRS is limited for the high heat source temperatures (≥ 70 °C) which makes it unfavourable for low temperature heat sources such as solar thermal storage device i.e. SGSP. Further, it may be used for high temperature heat sources such as WH but the performance delivered by it would be low due to the involvement of various thermal resistances. However, there are future scope in the use of thermosyphon for more effective power generation from the WH without involvement of thermal resistances by applying it horizontally as a part of waste heat pipe and high temperature capacity TEGs can be imposed on the outer surface of thermosyphon. This part of waste heat pipe may be directly passed/immersed through the cold water tank of a tower for cooling system. The performance of the system can be maximized through the simulation technique via optimizing the heat transfer process. Further, research could be carried out on the recovery of surface heat loss from the gasifier for power generation. Since the shape of hopper is mostly circular, the new designed hemicircle-shaped TEGs can be directly imposed for power generation which opens up the opportunity to improve design structure of TEGs. Discounted cash flow technique can be also adopted for economic assessment of biomass-based energy generation. Further, research scopes exist towards the development of improved semiconductor materials in order to obtain high conversion efficiency. The present CFDS applied to WH is a single slope and further scope exists for double slope CFDS for a high production rate of distilled water. Instead of using steel-made heat exchanger, copper-made can be used for more effective heat transfer and high production of distilled water. This study also provides appropriate guidelines for the design of HRSs for power generation in order to harvest the WH available at different temperatures and sources. The above-mentioned outcomes also provide directions in selecting the performance-driven factors to develop high-production distillation systems.

REFERENCES

- Abdelgaied M, Harby K, Eisa A. Performance improvement of modified tubular solar still by employing vertical and inclined pin fins and external condenser: an experimental study. *Environmental Science and Pollution Research*. 2021; 28: 13504-14.
- Abdelkareem MA, Maghrabie HM, Sayed ET, Kais EC, Abo-Khalil AG, Al Radi M, Baroutaji A, Olabi AG. Heat pipe-based waste heat recovery systems: Background and applications. *Thermal Science and Engineering Progress*. 2022; 29: 101221.
- Aghaali H, Angstrom HE. A review of turbocompounding as a waste heat recovery system for internal combustion engines. *Renewable and Sustainable Energy Reviews*. 2015; 49: 813-24.
- Ahmed FE, Khalil A, Hilal N. Emerging desalination technologies: Current status, challenges and future trends. *Desalination*. 2021; 517: 115183.
- Alatawi I, Subhani T, Ahmed MM, Alqsair UF, Abdullah AS, Elashmawy M. Experimental investigation of a developed tubular solar still with longitudinal wick fins. *Renewable Energy*. 2022; 193: 1074-81.
- Angeline AA, Jayakumar J, Asirvatham LG, Marshal JJ, Wongwises S. Power generation enhancement with hybrid thermoelectric generator using biomass waste heat energy. *Experimental Thermal and Fluid Science*. 2017; 85: 1-2.
- Antar M, Lyu D, Nazari M, Shah A, Zhou X, Smith DL. Biomass for a sustainable bioeconomy: An overview of world biomass production and utilization. *Renewable and Sustainable Energy Reviews*. 2021; 139: 110691.
- ASTM D 121-09a (2009), standard terminology of coal and coke, pennsylvania: American Society for Testing and Materials. <https://www.astm.org/Standards/D121.htm> (Accessed: 02.06.2018).
- Awais M, Li W, Munir A, Omar MM, Ajmal M. Experimental investigation of downdraft biomass gasifier fed by sugarcane bagasse and coconut shells. *Biomass Conversion and Biorefinery*. 2021; 11: 429-44.
- Awais M, Omar MM, Munir A, Ajmal M, Hussain S, Ahmad SA, Ali A. Co-gasification of different biomass feedstock in a pilot-scale (24 kWe) downdraft gasifier: An experimental approach. *Energy*. 2022; 238: 121821.

Ayyadurai S, Kandasamy VK. Performance investigation of an advanced robust biomass gasifier operation for drying process at hilly region in India. *Journal of Electrical and Electronic Systems*. 2017; 6(212): 2332-0796.

Babu BV, Sheth PN. Modeling & simulation of biomass gasifier: effect of oxygen enrichment and steam to air ratio. Chemical Engineering Group, Birla Institute of Technology & Science Rajasthan, India. 2005.

Balat M, Balat M, Kırtay E, Balat H. Main routes for the thermo-conversion of biomass into fuels and chemicals. Part 2: Gasification systems. *Energy Conversion and Management*. 2009; 50(12): 3158-68.

Bari S, Hossain SN. Waste heat recovery from a diesel engine using shell and tube heat exchanger. *Applied Thermal Engineering*. 2013; 61(2): 355-63.

Baruah D, Baruah DC. Modeling of biomass gasification: A review. *Renewable and Sustainable Energy Reviews*. 2014; 39: 806-15.

Basu P. Biomass gasification and pyrolysis: practical design and theory. Academic press; 2010:167-228.

Basu P. Combustion and gasification in fluidized beds. CRC press; Taylor & Francis, Boca Raton, 2006. <https://doi.org/10.1201/9781420005158>.

Bharath M, Raghavan V, Prasad BV, Chakravarthy SR. Co-gasification of Indian rice husk and Indian coal with high-ash in bubbling fluidized bed gasification reactor. *Applied Thermal Engineering*. 2018; 137: 608-15.

Bhattacharyya B, Mitra S, Boro AK. Electrochemical machining: new possibilities for micromachining. *Robotics and Computer-Integrated Manufacturing*. 2002; 18(3-4): 283-9.

Bhattacharya P, Dey S. An update technology for integrated biomass gasification combined cycle power plant. *Applied Solar Energy*. 2014; 50: 44-8.

Bhattacharya SC, Jana C. Renewable energy in India: historical developments and prospects. *Energy*. 2009; 34(8): 981-91.

Bhattacharya SC, Siddique AM, Pham HL. A study on wood gasification for low-tar gas production. *Energy*. 1999; 24(4): 285-96.

Bisht AS, Thakur NS. Identification & prioritisation of barriers in the growth of pine needle biomass gasification plants (< 250 kW) for electricity generation in the Western Himalayan Region: Uttarakhand, India. *Process Integration and Optimization for Sustainability*. 2022: 37-60.

Boyaghchi FA, Chavoshi M, Sabeti V. Multi-generation system incorporated with PEM electrolyzer and dual ORC based on biomass gasification waste heat recovery: Exergetic, economic and environmental impact optimizations. *Energy*. 2018; 145: 38-51.

Brown GW. Standard deviation, standard error: Which'standard'should we use?. *American Journal of Diseases of Children*. 1982; 136(10): 937-41.

Cabeza LF, Zsembinszki G, Martín M. Evaluation of volume change in phase change materials during their phase transition. *Journal of Energy Storage*. 2020; 28: 101206.

Campoy M, Gomez-Barea A, Fuentes-Cano D, Ollero P. Tar reduction by primary measures in an autothermal air-blown fluidized bed biomass gasifier. *Industrial & Engineering Chemistry Research*. 2010; 49(22): 11294-301.

Cao Y, Mihardjo LW, Dahari M, Tlili I. Waste heat from a biomass fueled gas turbine for power generation via an ORC or compressor inlet cooling via an absorption refrigeration cycle: A thermoeconomic comparison. *Applied Thermal Engineering*. 2021; 182: 116117.

Chattopadhyay S, Ghosh S. Techno-economic analysis of biomass-fuelled indirectly-heated combined cogeneration plant for power and cooling. *AIP Conference Proceedings* 2020; 1: 2273.

Chattopadhyay S, Ghosh S. Techno-economic assessment of a biomass-based combined power and cooling plant for rural application. *Clean Technologies and Environmental Policy*. 2020; 22: 907-22.

Chattopadhyay S, Mondal P, Ghosh S. Simulated performance of biomass gasification based combined power and refrigeration plant for community scale application. *AIP Conference Proceedings* 2016; 1: 1754.

Cehade A, Louahlia-Gualous H, Le Masson S, Victor I, Abouzahab-Damaj N. Experimental investigation of thermosyphon loop thermal performance. *Energy Conversion and Management*. 2014; 84: 671-80.

Chen K, Guo S, Lin Y, Ying Z. Least absolute relative error estimation. *Journal of the American Statistical Association*. 2010; 105(491): 1104-12.

Chutichai B, Arpornwichanop A. Performance improvement of biomass gasification and PEMFC integrated system—design consideration for achieving high overall energy efficiency and power-to-heat ratio variation. *Chemical Engineering Transactions*. 2015; 43: 1501-6.

Chutichai B, Authayanun S, Assabumrungrat S, Arpornwichanop A. Performance analysis of an integrated biomass gasification and PEMFC (proton exchange membrane fuel cell) system: Hydrogen and power generation. *Energy*. 2013; 55: 98-106.

Currency, your UK currency and exchange rates resource, www.currency.me.uk/convert/usd/inr?ref=driverlayer.com/, Accessed: September 10, 2022.

Dasappa S, Subbukrishna DN, Suresh KC, Paul PJ, Prabhu GS. Operational experience on a grid connected 100 kWe biomass gasification power plant in Karnataka, India. *Energy for Sustainable Development*. 2011; 15(3): 231-9.

Dehkhoda AM, Ellis N. Biochar-based catalyst for simultaneous reactions of esterification and transesterification. *Catalysis Today*. 2013; 207: 86-92.

Demirbas A. New opportunities resulting from cogeneration systems based on biomass gasification. *Energy Sources*. 2005; 27(10): 941-8.

Deng Y, Zhu W, Wang Y, Shi Y. Enhanced performance of solar-driven photovoltaic–thermoelectric hybrid system in an integrated design. *Solar Energy*. 2013; 88: 182-91.

DeVilliers S. Seawater strontium and Sr/Ca variability in the Atlantic and Pacific oceans. *Earth and Planetary Science Letters*. 1999; 171(4): 623-34.

Dion LM, Lefsrud M, Orsat V, Cimon C. Biomass gasification and syngas combustion for greenhouse CO₂ enrichment. *Bioresources*. 2013; 8(2): 1520-38.

Diyoke C, Gao N, Aneke M, Wang M, Wu C. Modelling of down-draft gasification of biomass—An integrated pyrolysis, combustion and reduction process. *Applied Thermal Engineering*. 2018; 142: 444-56.

Dogru M, Howarth CR, Akay G, Keskinler B, Malik AA. Gasification of hazelnut shells in a downdraft gasifier. *Energy*. 2002; 27(5): 415-27.

Dutta A, Das SK, Roy PC. Experimental investigation on a downdraft biomass gasifier using tree waste and sawdust pellet. *IOP Conference Series: Materials Science and Engineering* 2021; 1080: 012033.

Dutta PP, Baruah DC. Gasification of tea (*Camellia sinensis* (L.) O. Kuntze) shrubs for black tea manufacturing process heat generation in Assam, India. *Biomass and Bioenergy*. 2014; 66: 27-38.

Elsaid K, Sayed ET, Yousef BA, Rabaia MK, Abdelkareem MA, Olabi AA. Recent progress on the utilization of waste heat for desalination: A review. *Energy Conversion and Management*. 2020; 221: 113105.

Elsner W, Wysocki M, Niegodajew P, Borecki R. Experimental and economic study of small-scale CHP installation equipped with downdraft gasifier and internal combustion engine. *Applied Energy*. 2017; 202: 213-27.

Enersol Biopower Pvt. Ltd., Quotation no: ESB-R49/500kW biomass gasifier set for power production/Accessed: 03 August 2022.

Enersol Biopower Pvt. Ltd., Quotation no: ESB-R50/1000kW biomass gasifier set for power production/ Accessed: 03 August 2022.

Fadhl B. Modelling of the thermal behaviour of a two-phase closed thermosyphon, PhD Thesis. Brunel University, London, UK. 2015.

Faraj K, Khaled M, Faraj J, Hachem F, Castelain C. Phase change material thermal energy storage systems for cooling applications in buildings: A review. *Renewable and Sustainable Energy Reviews*. 2020; 119: 109579.

Fathurrohman MI, Maspanger DR, Sutrisno S. Vulcanization kinetics and mechanical properties of ethylene propylene diene monomer thermal insulation. *Bulletin of Chemical Reaction Engineering & Catalysis*. 2015; 10(2): 104-110.

Fletcher DF, Haynes BS, Chen J, Joseph SD. Computational fluid dynamics modelling of an entrained flow biomass gasifier. *Applied Mathematical Modelling*. 1998; 22(10): 747-57.

Forgan BW. A new method for calibrating reference and field pyranometers. *Journal of Atmospheric and Oceanic Technology*. 1996; 13(3): 638-45.

Forman C, Muritala IK, Pardemann R, Meyer B. Estimating the global waste heat potential. *Renewable and Sustainable Energy Reviews*. 2016; 57:1568-79.

Fracaro GP, Souza SM, Medeiros M, Formentini DF, Marques CA, World Renewable Energy Congress, Sweden. 2011; 295-302.

Ganesh A, Grover PD. Combustion and gasification characteristics of rice husk. *Fuel*. 1992; 71(8): 889-94.

Ganguly S, Date A, Akbarzadeh A. On increasing the thermal mass of a salinity gradient solar pond with external heat addition: A transient study. *Energy*. 2019; 168: 43-56.

Ganguly S, Jain R, Date A, Akbarzadeh A. On the addition of heat to solar pond from external sources. *Solar Energy*. 2017; 144: 111-6.

Gao N, Li A. Modeling and simulation of combined pyrolysis and reduction zone for a downdraft biomass gasifier. *Energy Conversion and Management*. 2008; 49(12): 3483-90.

Gedik E. Experimental investigation of the thermal performance of a two-phase closed thermosyphon at different operating conditions. *Energy and Buildings*. 2016; 127: 1096-107.

Georgousopoulos S, Braimakis K, Grimekis D, Karellas S. Thermodynamic and techno-economic assessment of pure and zeotropic fluid ORCs for waste heat recovery in a biomass IGCC plant. *Applied Thermal Engineering*. 2021; 183: 116202.

Ghosh S, Das TK, Jash T. Sustainability of decentralized woodfuel-based power plant: an experience in India. *Energy*. 2004; 29(1): 155-66.

Gnanaraj SJ, Velmurugan V. An experimental study on the efficacy of modifications in enhancing the performance of single basin double slope solar still. *Desalination*. 2019; 467: 12-28.

Gonzalez AS, Plaza MG, Rubiera F, Pevida C. Sustainable biomass-based carbon adsorbents for post-combustion CO₂ capture. *Chemical Engineering Journal*. 2013; 230: 456-65.

Gu L, Guo M, He J, Yang Z. Experimental study on hydrogen production characteristics of kaolin supported Ni catalyzed by steam gasification of citrus peel. *Fuel*. 2023; 340: 127431.

Gunarathne DS, Mellin P, Yang W, Pettersson M, Ljunggren R. Performance of an effectively integrated biomass multi-stage gasification system and a steel industry heat treatment furnace. *Applied Energy*. 2016; 170: 353-61.

Guo F, Dong Y, Zhang T, Dong L, Guo C, Rao Z. Experimental study on herb residue gasification in an air-blown circulating fluidized bed gasifier. *Industrial & Engineering Chemistry Research*. 2014; 53(34): 13264-73.

HajiHashemi M, Mazhkoo S, Dadfar H, Livani E, Varnosefaderani AN, Pourali O, Nobar SN, Dutta A. Combined heat and power production in a pilot-scale biomass gasification system: Experimental study and kinetic simulation using ASPEN Plus. *Energy*. 2023; 276: 127506.

Hanaoka T, Inoue S, Uno S, Ogi T, Minowa T. Effect of woody biomass components on air-steam gasification. *Biomass and Bioenergy*. 2005; 28(1): 69-76.

Hanchate N, Ramani S, Mathpati CS, Dalvi VH. Biomass gasification using dual fluidized bed gasification systems: A review. *Journal of Cleaner Production*. 2021; 280: 123148.

Harbeck GE. The effect of salinity on evaporation. US Government Printing Office, Washington. 1955.

Hayashi M. Temperature-electrical conductivity relation of water for environmental monitoring and geophysical data inversion. *Environmental Monitoring and Assessment*. 2004; 96: 119-28.

He J, Yang Z, Guo M, Gu L, Zhang L, Yan Y, Ran J. Experimental study on the key factors affecting the gasification performance between different biomass: Compare citrus peel with pine sawdust. *International Journal of Hydrogen Energy*. 2022; 47(71): 30428-39.

Hernandez JJ, Barba J, Aranda G. Combustion characterization of producer gas from biomass gasification. *Global NEST Journal*. 2012; 14(2): 125-32.

Hofbauer H, Materazzi M. Waste gasification processes for SNG production in substitute natural gas from waste: Technical assessment and industrial applications of biochemical and thermochemical processes. Academic Press. 2019; 105-160.

https://chandigarhmetro.com/punjab_electricity-tariff-unit-price-hike-domestic-from-april-2017/, Chandigarhmetro.com Accessed: 18 June 2022.

Huang X, Yin T, Li G, Ma X, Wang Y, Li Z, Liu L, Liu X. Experimental study on drying biomass with a spherical heat carrier. *ACS Omega*. 2023; 8(30): 27482-7.

Huang Y, McIlveen-Wright DR, Rezvani SH, Huang MJ, Wang YD, Roskilly AP, Hewitt NJ. Comparative techno-economic analysis of biomass fuelled combined heat and power for commercial buildings. *Applied Energy*. 2013; 112: 518-25.

Ishaq H, Islam S, Dincer I, Yilbas BS. Development and performance investigation of a biomass gasification based integrated system with thermoelectric generators. *Journal of Cleaner Production*. 2020; 256: 120625.

Islam S, Dincer I. A comparative study of syngas production from two types of biomass feedstocks with waste heat recovery. *Journal of Energy Resources Technology*. 2018; 140(9):092002.

Issa RJ, Chang B. Performance study on evacuated tubular collector coupled solar still in West Texas climate. *International Journal of Green Energy*. 2017; 14(10):793-800.

Jadhao JS, Thombare DG. Review on exhaust gas heat recovery for IC engine. *International Journal of Engineering and Innovative Technology*. 2013; 2(12) 2:93-100.

Jaefarzadeh MR. Heat extraction from a salinity-gradient solar pond using in pond heat exchanger. *Applied Thermal Engineering*. 2006; 26(16): 1858-65.

James AM, Yuan W, Boyette MD, Wang D. The effect of air flow rate and biomass type on the performance of an updraft biomass gasifier. *BioResources*. 2015; 10(2): 3615-24.

Jangsawang W. Utilization of biomass gasifier system for drying applications. *Energy Procedia*. 2017; 138: 1041-7.

Jimenez O, Curbelo A, Suarez Y. Biomass based gasifier for providing electricity and thermal energy to off-grid locations in Cuba. Conceptual design. *Energy for Sustainable Development*. 2012; 16(1): 98-102.

Jouhara H, Khordehgah N, Almahmoud S, Delpech B, Chauhan A, Tassou SA. Waste heat recovery technologies and applications. *Thermal Science and Engineering Progress*. 2018; 6: 268-89.

Kalina J. Integrated biomass gasification combined cycle distributed generation plant with reciprocating gas engine and ORC. *Applied Thermal Engineering*. 2011; 31(14-15): 2829-40.

Karakilcik M, Dincer I, Bozkurt I, Atiz A. Performance assessment of a solar pond with and without shading effect. *Energy Conversion and Management*. 2013; 65: 98-107.

Karri M A. Thermoelectric power generation system optimization studies. PhD Dissertation, Clarkson University, Potsdam NY (USA). 2011.

Kaydouh MN, El Hassan N. Thermodynamic simulation of the co-gasification of biomass and plastic waste for hydrogen-rich syngas production. *Results in Engineering*. 2022; 16: 100771.

Khaleghi E, Torikachvili M, Meyers MA, Olevsky EA. Magnetic enhancement of thermal conductivity in copper-carbon nanotube composites produced by electroless plating, freeze drying, and spark plasma sintering. *Materials Letters*. 2012; 79: 256-8.

Khanmohammadi S, Saadat-Targhi M, Al-Rashed AA, Afrand M. Thermodynamic and economic analyses and multi-objective optimization of harvesting waste heat from a biomass gasifier integrated system by thermoelectric generator. *Energy Conversion and Management*. 2019; 195: 1022-34.

Kim KT, Kim KJ, Ha GH. Thermoelectric properties of P-type bismuth telluride powders synthesized by a mechano-chemical process. *Electronic Materials Letters*. 2010; 6: 177-80.

Kim Y, Shin DH, Kim JS, You SM, Lee J. Boiling and condensation heat transfer of inclined two-phase closed thermosyphon with various filling ratios. *Applied Thermal Engineering*. 2018; 145: 328-42.

Kim YD, Yang CW, Kim BJ, Kim KS, Lee JW, Moon JH, Yang W, Tae UY, Do Lee U. Air-blown gasification of woody biomass in a bubbling fluidized bed gasifier. *Applied Energy*. 2013; 112: 414-20.

Kirshenbaum, A.D. and Grosse, A.V. The combustion of carbon subnitride, C_4N_2 , and a chemical method for the production of continuous temperatures in the range of 5000-6000°K. *Journal of the American Chemical Society*. 1956; 78(9): 2020.

Kulkarni A, Saluja J. Coal conversion and biomass conversion: Volume 1: Final report on USAID (Agency for International Development)/GOI (Government of India) Alternate Energy Resources and Development Program. Viking Systems International, Pittsburgh, PA (USA); 1987.

Kumar A, Kumar K, Kaushik N, Sharma S, Mishra S. Renewable energy in India: current status and future potentials. *Renewable and Sustainable Energy Reviews*. 2010; 14(8): 2434-42.

Kumar A, Kumar N, Baredar P, Shukla A. A review on biomass energy resources, potential, conversion and policy in India. *Renewable and Sustainable Energy Reviews*. 2015; 45: 530-9.

Kumar A, Randa R. Experimental analysis of a producer gas generated by a chir pine needle (leaf) in a downdraft biomass gasifier. *International Journal of Engineering Research and Applications*. 2014; 4(10): 122-30.

Kumar A, Singh K, Das R. Response surface based experimental analysis and thermal resistance model of a thermoelectric power generation system. *Applied Thermal Engineering*. 2019; 159: 113935.

Kumar A, Singh K, Verma S, Das R. Inverse prediction and optimization analysis of a solar pond powering a thermoelectric generator. *Solar Energy*. 2018; 169: 658-72.

Kumar Tripathi A, Patra I, Bharath Kumar N, Majdi A, Muda I, Mahdavi A. Environmental and exergoeconomic assessments of a novel biomass gasification based solid oxide fuel cell and heat engine hybrid energy system. *Energy Sources, Part A: Recovery, Utilization, and Environmental Effects*. 2022; 44(4): 8490-511.

Kuo PC, Wu W. Thermodynamic analysis of a combined heat and power system with CO_2 utilization based on co-gasification of biomass and coal. *Chemical Engineering Science*. 2016; 142: 201-14.

Laha P, Chakraborty B, Ostergaard PA. Electricity system scenario development of India with import independence in 2030. *Renewable Energy*. 2020; 151: 627-39.

Laird DA, Brown RC, Amonette JE, Lehmann J. Review of the pyrolysis platform for coproducing bio-oil and biochar. *Biofuels, Bioproducts and Biorefining*. 2009; 3(5): 547-62.

- Lenka R. Characterization of the properties of some biomass species and estimation of their power generation potentials. PhD dissertation, NIT Rourkela, India, 2016. (<http://ethesis.nitrkl.ac.in/8386/>: Accessed: 01-06-2018).
- Leung DY, Yin XL, Wu CZ. A review on the development and commercialization of biomass gasification technologies in China. *Renewable and Sustainable Energy Reviews*. 2004; 8(6): 565-80.
- Lewandowski A, Szypłowska A, Kafarski M, Wilczek A, Szerement J, Barmuta P, Skierucha W. Wideband extraction of soil dielectric spectrum from vector-network-analyzer measurements. *IEEE MTT-S International Microwave Workshop Series on Advanced Materials and Processes for RF and THz Applications (IMWS-AMP)*, Pavia, Italy, 20-22 September, 2017; 1-3.
- Li CY, Shen Y, Wu JY, Dai YJ, Wang CH. Experimental and modeling investigation of an integrated biomass gasifier–engine–generator system for power generation and waste heat recovery. *Energy Conversion and Management*. 2019; 199: 112023.
- Liu MC, Kong LB, Zhang P, Luo YC, Kang L. Porous wood carbon monolith for high-performance supercapacitors. *Electrochimica Acta*. 2012; 60: 443-8.
- Loni R, Najafi G, Bellos E, Rajaei F, Said Z, Mazlan M. A review of industrial waste heat recovery system for power generation with Organic Rankine Cycle: Recent challenges and future outlook. *Journal of Cleaner Production*. 2021; 287: 125070.
- Louahlia-Gualous H, Le Masson S, Chahed A. An experimental study of evaporation and condensation heat transfer coefficients for looped thermosyphon. *Applied Thermal Engineering*. 2017; 110: 931-40.
- Lu H, Walton JC, Swift AH. Desalination coupled with salinity-gradient solar ponds. *Desalination*. 2001; 136(1-3): 13-23.
- Luo X, Wu T, Shi K, Song M, Rao Y. Biomass gasification: an overview of technological barriers and socio-environmental impact. *Gasification for Low-grade Feedstock (Book)*, London, United Kingdom. 2018:1-5.
- Lv PM, Xiong ZH, Chang J, Wu CZ, Chen Y, Zhu JX. An experimental study on biomass air–steam gasification in a fluidized bed. *Bioresource Technology*. 2004; 95(1): 95-101.
- Mahapatro A, Mahanta P. Gasification studies of low-grade Indian coal and biomass in a lab-scale pressurized circulating fluidized bed. *Renewable Energy*. 2020; 150: 1151-9.

Mahishi MR, Goswami DY. Thermodynamic optimization of biomass gasifier for hydrogen production. *International Journal of Hydrogen Energy*. 2007; 32(16): 3831-40.

Ma HK, Lin CP, Wu HP, Peng CH, Hsu CC. Waste heat recovery using a thermoelectric power generation system in a biomass gasifier. *Applied Thermal Engineering*. 2015; 88: 274-9.

Mamur H, Bhuiyan MR, Korkmaz F, Nil M. A review on bismuth telluride (Bi_2Te_3) nanostructure for thermoelectric applications. *Renewable and Sustainable Energy Reviews*. 2018; 82: 4159-69.

Martínez LV, Rubiano JE, Figueredo M, Gómez MF. Experimental study on the performance of gasification of corncobs in a downdraft fixed bed gasifier at various conditions. *Renewable Energy*. 2020; 148: 1216-26.

Mathieu P, Dubuisson R. Performance analysis of a biomass gasifier. *Energy Conversion and Management*. 2002; 43(9-12): 1291-9.

Mehrpooya M, Ghorbani A, Moosavian SA, Amirhaeri Y. Optimal design and economic analysis of a hybrid process of municipal solid waste plasma gasification, thermophotovoltaic power generation and hydrogen/liquid fuel production. *Sustainable Energy Technologies and Assessments*. 2022; 49: 101717.

Methnani M. Influence of fuel costs on seawater desalination options. *Desalination*. 2007; 205(1-3): 332-9.

Mohaisen HS, Esfahani JA, Ayani MB. Improvement in the performance and cost of passive solar stills using a finned-wall/built-in condenser: An experimental study. *Renewable Energy*. 2021; 168: 170-80.

Motta IL, Miranda NT, Maciel Filho R, Maciel MR. Biomass gasification in fluidized beds: A review of biomass moisture content and operating pressure effects. *Renewable and Sustainable Energy Reviews*. 2018; 94: 998-1023.

Mukunda HS, Paul PJ, Dasappa S, Shrinivasa U, Sharan H, Buehler R, Hasler P, Kaufmann H. Results of an Indo-Swiss programme for qualification and testing of a 300-kW IISc-Dasag gasifier. *Energy for Sustainable Development*. 1994; 1(4): 46-9.

Muniandy V, Aziz MS, Latip HF. Study on the improvement of heat recovery steam generator efficiency—A review. *Journal of Advanced Research in Fluid Mechanics and Thermal Sciences*. 2022; 94(2): 89-98.

Murugan PC, Raveendran PS, Glivin G, Kalaiselvan N, Sekhar SJ, Gayathri SN. Experimental investigation on downdraft biomass gasifier with leafy biomass available at educational institutions. *AIP Conference Proceedings* 2023; 2492: 020075.

Murugan PC, Sekhar SJ. Investigation on the yield of producer gas from tamarind shell (*Tamarindus Indica*) as feedstock in an Imbert type biomass gasifier. *Fuel*. 2021; 292: 120310.

Musharavati F, Khoshnevisan A, Alirahmi SM, Ahmadi P, Khanmohammadi S. Multi-objective optimization of a biomass gasification to generate electricity and desalinated water using Grey Wolf Optimizer and artificial neural network. *Chemosphere*. 2022; 287: 131980.

Myerson A. *Handbook of industrial crystallization*. Butterworth-Heinemann. Butterworth-Heinemann, Woburn, MA. 2002.

Nagy E. *Basic equations of mass transport through a membrane layer*. Elsevier. Veszprem, Hungary. 2018; 483–96.

Nakoa K, Rahaoui K, Date A, Akbarzadeh A. An experimental review on coupling of solar pond with membrane distillation. *Solar Energy*. 2015; 119: 319-31.

Naresh Y, Balaji C. Experimental investigations of heat transfer from an internally finned two phase closed thermosyphon. *Applied Thermal Engineering*. 2017; 112: 1658-66.

Narvaez I, Orio A, Aznar MP, Corella J. Biomass gasification with air in an atmospheric bubbling fluidized bed. Effect of six operational variables on the quality of the produced raw gas. *Industrial & Engineering Chemistry Research*. 1996; 35(7): 2110-20.

Nguyen NM, Alobaid F, May J, Peters J, Epple B. Experimental study on steam gasification of torrefied woodchips in a bubbling fluidized bed reactor. *Energy*. 2020; 202: 117744.

Nisamaneenate J, Atong D, Sornkade P, Sricharoenchaikul V. Fuel gas production from peanut shell waste using a modular downdraft gasifier with the thermal integrated unit. *Renewable Energy*. 2015; 79: 45-50.

Noie SH. Heat transfer characteristics of a two-phase closed thermosyphon. *Applied Thermal Engineering*. 2005; 25(4): 495-506.

Nougriaya SK, Chopra MK, Gupta B, Baredar P. Stepped solar still: A review on designs analysis. *Materials Today: Proceedings*. 2021; 46: 5647-60.

Nuwayhid RY, Shihadeh A, Ghaddar N. Development and testing of a domestic woodstove thermoelectric generator with natural convection cooling. *Energy Conversion and Management*. 2005; 46(9-10): 1631-43.

- Nwokolo N, Mamphweli S, Makaka G. An investigation into heat recovery from the surface of a cyclone dust collector attached to a downdraft biomass gasifier. *Applied Thermal Engineering*. 2016; 98: 1158-64.
- Ojolo SJ, Orisaleye JI. Design and development of a laboratory scale biomass gasifier. *Journal of Energy and Power Engineering*. 2010; 4(8): 16-23.
- Olgun H, Ozdogan S, Yinesor G. Results with a bench scale downdraft biomass gasifier for agricultural and forestry residues. *Biomass and Bioenergy*. 2011; 35(1): 572-80.
- Omara AA. Phase change materials for waste heat recovery in internal combustion engines: A review. *Journal of Energy Storage*. 2021; 44: 103421.
- Omara ZM, Eltawil MA, ElNashar EA. A new hybrid desalination system using wicks/solar still and evacuated solar water heater. *Desalination*. 2013; 325: 56-64.
- Osat M, Shojaati F, Osat M. A solar-biomass system associated with CO₂ capture, power generation and waste heat recovery for syngas production from rice straw and microalgae: Technological, energy, exergy, exergoeconomic and environmental assessments. *Applied Energy*. 2023; 340: 120999.
- Ozbek H, Phillips SL. Thermal conductivity of aqueous NaCl solutions from 20 °C to 330 °C. Department of Energy, Lawrence Berkeley Laboratory, CA. 1979.
- Ozgoli HA. Simulation of integrated biomass gasification-gas turbine-air bottoming cycle as an energy efficient system. *International Journal of Renewable Energy Research*. 2017; 7(1): 275-84.
- Palliser C, McKibbin R. A model for deep geothermal brines, III: Thermodynamic properties—enthalpy and viscosity. *Transport in Porous Media*. 1998; 33: 155-71.
- Panwar NL, Rathore NS, Kurchania AK. Experimental investigation of open core downdraft biomass gasifier for food processing industry. *Mitigation and Adaptation Strategies for Global Change*. 2009; 14: 547-56.
- Panwar NL, Rathore NS. Potential of surplus biomass gasifier based power generation: A case study of an Indian state Rajasthan. *Mitigation and Adaptation Strategies for Global Change*. 2009; 14: 711-20.
- Pan YG, Velo E, Roca X, Manya JJ, Puigjaner L. Fluidized-bed co-gasification of residual biomass/poor coal blends for fuel gas production. *Fuel*. 2000; 79(11): 1317-26.

- Pandey B, Sheth PN, Prajapati YK. Air-CO₂ and oxygen-enriched air-CO₂ biomass gasification in an autothermal downdraft gasifier: Experimental studies. *Energy Conversion and Management*. 2022; 270: 116216.
- Parikh J, Channiwala SA, Ghosal GK. A correlation for calculating elemental composition from proximate analysis of biomass materials. *Fuel*. 2007; 86(12-13): 1710-9.
- Parikh PP, Bhawe AG, Kapse DV. Study of thermal and emission performance of small gasifier-dual-fuel engine systems. *Biomass*. 1989; 19(1-2): 75-97.
- Parvez M, Khan O, Howari H. Investigation of (3E) energy, exergy, and environmental analysis of syngas production for combined power and cooling plant by testing six different biomasses. *Biomass Conversion and Biorefinery*. 2023; 34:1-5.
- Parvez M. Thermodynamic analysis of a biomass gasifier driven combined power and ejector-absorption refrigeration (CPER) system. *International Journal of Exergy*. 2019; 29(1): 69-88.
- Pavlas M, Stehlik P, Oral J, Klemes J, Kim JK, Firth B. Heat integrated heat pumping for biomass gasification processing. *Applied Thermal Engineering*. 2010; 30(1): 30-5.
- Pawar A, Panwar NL. Analysis of biochar from carbonisation of wheat straw using continuous auger reactor. *International Journal of Environment and Sustainable Development*. 2022; 21 (1-2): 218-25.
- Perry DL. *Handbook of Inorganic Compounds*. 2nd Edition, CRC Press, Boca Raton, FL. 2016.
- Phillips J. Different types of gasifiers and their integration with gas turbines. In *The Gas Turbine Handbook*, edited by: Smith L, Karim H, Etemad S, Pfefferle WC, National Energy Technology Laboratory, DOE, Morgantown, WV. 2006, 67-77.
- Pissot S, Berdugo Vilches T, Thunman H, Seemann M. Dual fluidized bed gasification configurations for carbon recovery from biomass. *Energy & Fuels*. 2020; 34(12): 16187-200.
- Pourkiaei SM, Ahmadi MH, Sadeghzadeh M, Moosavi S, Pourfayaz F, Chen L, Yazdi MA, Kumar R. Thermoelectric cooler and thermoelectric generator devices: A review of present and potential applications, modeling and materials. *Energy*. 2019; 186: 115849.
- Puig-Arnabat M, Bruno JC, Coronas A. Modeling of trigeneration configurations based on biomass gasification and comparison of performance. *Applied Energy*. 2014; 114: 845-56.
- Puig-Arnabat M, Bruno JC, Coronas A. Review and analysis of biomass gasification models. *Renewable and Sustainable Energy Reviews*. 2010; 14(9): 2841-51.

Quintero-Coronel DA, Lenis-Rodas YA, Corredor L, Perreault P, Bula A, Gonzalez-Quiroga A. Co-gasification of biomass and coal in a top-lit updraft fixed bed gasifier: Syngas composition and its interchangeability with natural gas for combustion applications. *Fuel*. 2022; 316: 123394.

Rabl A, Nielsen CE. Solar ponds for space heating. *Solar Energy*. 1975; 17(1): 1-2.

Rajvanshi AK. Biomass gasification. *Alternative Energy in Agriculture*. 1986; 2(4): 82-102.

Raman P, Ram NK. Design improvements and performance testing of a biomass gasifier based electric power generation system. *Biomass and Bioenergy*. 2013; 56: 555-71.

Ram NK, Singh NR, Raman P, Kumar A, Kaushal P. A detailed experimental analysis of air–steam gasification in a dual fired downdraft biomass gasifier enabling hydrogen enrichment in the producer gas. *Energy*. 2019; 187: 115937.

Rashidi S, Shamsabadi H, Esfahani JA, Harmand S. A review on potentials of coupling PCM storage modules to heat pipes and heat pumps. *Journal of Thermal Analysis and Calorimetry*. 2020; 140: 1655-713.

Ratafia-Brown J, Manfredo L, Hoffmann J, Ramezan M. Major environmental aspects of gasification-based power generation technologies. Final Report to DOE of U.S., National Energy Technology Laboratory, WV. 2002

Rather NU, Sahoo U. Hybrid solar-biomass gasifier system for electricity and cold storage applications for rural areas of India. *Hybrid Renewable Energy Systems*. 2021: 199-246.

Rather NU, Tripathi A. Design of biomass gasifiers for power generation, cold storage and heating for Jammu and Kashmir state. *Journal Impact Factor*. 2018; 3: 86. <http://dx.doi.org/10.7324/IJASRE.32593>

Ravindranath NH, Balachandra P. Sustainable bioenergy for India: Technical, economic and policy analysis. *Energy*. 2009; 34(8): 1003-13.

Ray A, Jana K, De S. Polygeneration for an off-grid Indian village: Optimization by economic and reliability analysis. *Applied Thermal Engineering*. 2017; 116: 182-96.

Reed TB, Das A. Handbook of biomass downdraft gasifier engine systems. Biomass Energy Foundation. 1988.

Reif F. Fundamentals of statistical and thermal physics. *American Journal of Physics*. 1998; 66: 164–167.

Roy D, Samanta S, Ghosh S. Performance optimization through response surface methodology of an integrated biomass gasification based combined heat and power plant employing solid oxide fuel cell and externally fired gas turbine. *Energy Conversion and Management*. 2020; 222: 113182.

Roy D, Samanta S, Ghosh S. Thermodynamic analysis of a biomass based solid oxide fuel cell integrated advanced power generation system. *IOP Conference Series: Materials Science and Engineering* 2018; 377: 012210.

Roy D, Samanta S, Ghosh S. Thermo-economic assessment of biomass gasification-based power generation system consists of solid oxide fuel cell, supercritical carbon dioxide cycle and indirectly heated air turbine. *Clean Technologies and Environmental Policy*. 2019; 21: 827-45.

Roy PC, Datta A, Chakraborty N. Assessment of cow dung as a supplementary fuel in a downdraft biomass gasifier. *Renewable Energy*. 2010; 35(2): 379-86.

Rusydi AF. Correlation between conductivity and total dissolved solid in various type of water: A review. *IOP conference series: Earth and Environmental Science* 2018; 118: 012019.

Ruya PM, Lim SS, Purwadi R, Zunita M. Sustainable hydrogen production from oil palm derived wastes through autothermal operation of supercritical water gasification system. *Energy*. 2020; 208: 118280.

Samanta S, Roy D. Molten carbonate fuel cell integrated hybrid system for clean and efficient power generation. *Applied Thermal Engineering*. 2023; 226: 120294.

Sapariya D, Patdiwala U, Makwana J, Panchal H, Ramana PV, Alrubaie AJ. Experimental study on effect of temperature and equivalence ratio on biomass syngas generation for fluidized bed gasifier techniques. *Energy Sources, Part A: Recovery, Utilization, and Environmental Effects*. 2023; 45(2): 5848-63.

Saravanakumar A, Haridasan TM, Reed TB, Bai RK. Experimental investigations of long stick wood gasification in a bottom lit updraft fixed bed gasifier. *Fuel Processing Technology*. 2007; 88(6): 617-22.

Sarbu GC, Beniuga O. Evaluating measurement uncertainty of thermocouples calibration. *International Conference and Exposition on Electrical and Power Engineering, IEEE* 2018; 411-415.

Saxena RC, Adhikari DK, Goyal HB. Biomass-based energy fuel through biochemical routes: A review. *Renewable and Sustainable Energy Reviews*. 2009; 13(1): 167-78.

Sayer AH, Al-Hussaini H, Campbell AN. New theoretical modelling of heat transfer in solar ponds. *Solar Energy*. 2016; 125: 207-18.

Schoeters J, Maniatis K, Buekens A. The fluidized-bed gasification of biomass: experimental studies on a bench scale reactor. *Biomass*. 1989; 19(1-2): 129-43.

Senapati PK, Behera S. Experimental investigation on an entrained flow type biomass gasification system using coconut coir dust as powdery biomass feedstock. *Bioresource Technology*. 2012; 117: 99-106.

Sharqawy MH, Lienhard JH, Zubair SM. Thermophysical properties of seawater: a review of existing correlations and data. *Desalination and Water Treatment*. 2010; 16(1-3): 354-80.

Sheth PN, Babu BV. Experimental studies on producer gas generation from wood waste in a downdraft biomass gasifier. *Bioresource Technology*. 2009; 100(12): 3127-33.

Singh AK, Singh DB, Mallick A, Sharma SK, Kumar N, Dwivedi VK. Performance analysis of specially designed single basin passive solar distillers incorporated with novel solar desalting stills: a review. *Solar Energy*. 2019; 185: 146-64.

Singh B, Gomes J, Tan L, Date A, Akbarzadeh A. Small scale power generation using low grade heat from solar pond. *Procedia Engineering*. 2012; 49: 50-6.

Singh B, Tan L, Date A, Akbarzadeh A. Power generation from salinity gradient solar pond using thermoelectric generators for renewable energy application. *International Conference on Power and Energy (PECon), IEEE 2012*; 89-92.

Singh G, Das R. Experimental study on a new small-scale absorption system: response surface and inverse analyses. *Journal of Energy Resources Technology*. 2021; 143(9): 092103.

Singh H, Sapra PK, Sidhu BS. Evaluation and characterization of different biomass residues through proximate & ultimate analysis and heating value. *Asian Journal of Engineering and Applied Technology*. 2013; 2(2): 6-10.

Singh K, Das R. Exergy optimization of cooling tower for HGSHP and HVAC applications. *Energy Conversion and Management*. 2017; 136: 418-30.

Singh R, Tundee S, Akbarzadeh A. Electric power generation from solar pond using combined thermosyphon and thermoelectric modules. *Solar Energy*. 2011; 85(2): 371-8.

Singh SK, Kaushik SC, Tyagi VV, Tyagi SK. Comparative Performance and parametric study of solar still: A review. *Sustainable Energy Technologies and Assessments*. 2021; 47: 101541.

Singh VC, Sekhar SJ. Performance studies on a downdraft biomass gasifier with blends of coconut shell and rubber seed shell as feedstock. *Applied Thermal Engineering*. 2016; 97: 22-7.

Situmorang YA, Zhao Z, Yoshida A, Abudula A, Guan G. Small-scale biomass gasification systems for power generation (< 200 kW class): A review. *Renewable and Sustainable Energy reviews*. 2020; 117: 109486.

Siwal SS, Zhang Q, Sun C, Thakur S, Gupta VK, Thakur VK. Energy production from steam gasification processes and parameters that contemplate in biomass gasifier—A review. *Bioresource Technology*. 2020; 297: 122481.

Sivakumar D, Thiruvengadam M, Anand R, Ponpandian M. Suitability of groundwater around Pallavaram, Chennai, Tamil Nadu. *Pollution Research EM International*. 2014; 33(3): 43-8.

Sivakumar S, Pitchandi K, Natarajan E. Design and analysis of downdraft biomass gasifier using computational fluid dynamics. *International Conference on Computational Mechanics and Simulation*. Guwahati, India. 2006.

Skogtjarn P, Scania P, Ab C, Nr Lithisyex R, Elfvik SD, Ab SC, Msc JB. Modelling of the exhaust gas temperature for diesel engines. Master's Thesis, Avdelning Institution Division, Department of Electrical Engineering, linkoping University. 2002; 58183.

Sosso A, Cerri R. Calibration of multimeters as voltage ratio standards. *Conference on Precision Electromagnetic Measurements, CPEM, IEEE*. 2000; 375-376.

Srinivas T, Gupta AV, Reddy BV. Thermodynamic equilibrium model and exergy analysis of a biomass gasifier. *Journal of Energy Resources Technology*, 2009; 131(3): 031801.

Srinivas T, Reddy BV, Gupta AV. Biomass-fuelled integrated power and refrigeration system. *Proceedings of the Institution of Mechanical Engineers-A*. 2011; 225(3): 249-58.

Sun XY, Chen JL, Zhao Y, Li X, Ge TS, Wang CH, Dai YJ. Experimental investigation on a dehumidification unit with heat recovery using desiccant coated heat exchanger in waste to energy system. *Applied Thermal Engineering*. 2021; 185: 116342.

Susastriawan AA, Saptoadi H, Purnomo. Design and experimental study of pilot scale throat-less downdraft gasifier fed by rice husk and wood sawdust. *International Journal of Sustainable Energy*. 2018; 37(9): 873-85.

Suyambazhahan S. Experimental study of coconut shell fluidized bed gasification for production of fuel gas for end-use applications. *International Journal of Applied Engineering Research*. 2018; 3(20): 14682-8.

Taggar GK, Singh R, Kumar R, Pathania PC. First report of flower chafer beetle, *Oxycetonia versicolor*, on pigeonpea and mungbean from Punjab, India. *Phytoparasitica*. 2012; 40: 207-11.

Takashiri M, Takiishi M, Tanaka S, Miyazaki K, Tsukamoto H. Thermoelectric properties of n-type nanocrystalline bismuth-telluride-based thin films deposited by flash evaporation. *Journal of Applied Physics*. 2007; 101(7) 074301.

Tao J, Ge Y, Liang R, Sun Y, Cheng Z, Yan B, Chen G. Technologies integration towards bio-fuels production: A state-of-the-art review. *Applications in Energy and Combustion Science*. 2022; 10: 100070.

Tchanche BF, Lambrinos G, Frangoudakis A, Papadakis G. Low-grade heat conversion into power using organic Rankine cycles—A review of various applications. *Renewable and Sustainable Energy Reviews*. 2011; 15(8): 3963-79.

Tezer O, Karabag N, Ongen A, Çolpan CO, Ayol A. Biomass gasification for sustainable energy production: A review. *International Journal of Hydrogen Energy*. 2022; 47(34): 15419-33.

Tundee S, Srihajong N, Charmongkolpradit S. Electric power generation from solar pond using combination of thermosyphon and thermoelectric modules. *Energy Procedia*. 2014; 48: 453-63.

Umeki K, Namioka T, Yoshikawa K. Analysis of an updraft biomass gasifier with high temperature steam using a numerical model. *Applied Energy*. 2012; 90(1): 38-45.

Velez JF, Chejne F, Valdes CF, Emery EJ, Londono CA. Co-gasification of colombian coal and biomass in fluidized bed: An experimental study. *Fuel*. 2009; 88(3): 424-30.

Verma S, Das R. Transient study of a solar pond under heat extraction from non-convective and lower convective zones considering finite effectiveness of exchangers. *Solar Energy*. 2021; 223: 437-48.

Vivek M, Srividhya PK, Sujatha K. Portable biomass gasifier power generation using non edible seed cake. *Bulletin of Electrical Engineering and Informatics*. 2015; 4(4): 274-9.

Wakeland RS, Keolian RM. Effectiveness of parallel-plate heat exchangers in thermoacoustic devices. *The Journal of the Acoustical Society of America*. 2004; 115(6): 2873-86.

Wang JJ, Yang K, Xu ZL, Fu C. Energy and exergy analyses of an integrated CCHP system with biomass air gasification. *Applied Energy*. 2015; 142: 317-27.

Wang MY, Lin CP, Ma HK. Investigation of thermoelectric power generation module on waste heat recovery in a downdraft gasifier. *Advanced Materials Research*. 2014; 860: 437-40.

Wang Y, Huang Y, Roskilly AP. Trigeneration integrated with absorption enhanced reforming of lignite and biomass. *Fuel*. 2009; 88(10): 2004-10.

Wang Y, Kinoshita CM. Experimental analysis of biomass gasification with steam and oxygen. *Solar Energy*. 1992; 49(3): 153-8.

Wang Y, Yoshikawa K, Namioka T, Hashimoto Y. Performance optimization of two-staged gasification system for woody biomass. *Fuel Processing Technology*. 2007; 88(3): 243-50.

Weinberger H. The physics of the solar pond. *Solar Energy*. 1964; 8(2): 45-56.

Wong-Pinto LS, Milian Y, Ushak S. Progress on use of nanoparticles in salt hydrates as phase change materials. *Renewable and Sustainable Energy Reviews*. 2020; 122: 109727.

Wu CZ, Huang HA, Zheng SP, Yin XL. An economic analysis of biomass gasification and power generation in China. *Bioresource Technology*. 2002; 83(1): 65-70.

Wu Z, Zhu P, Yao J, Zhang S, Ren J, Yang F, Zhang Z. Combined biomass gasification, SOFC, IC engine, and waste heat recovery system for power and heat generation: Energy, exergy, exergoeconomic, environmental (4E) evaluations. *Applied Energy*. 2020; 279: 115794.

Xiong J, Xie G, Zheng H. Experimental and numerical study on a new multi-effect solar still with enhanced condensation surface. *Energy Conversion and Management*. 2013; 73: 176-85.

Yang W, Ponzio A, Lucas C, Blasiak W. Performance analysis of a fixed-bed biomass gasifier using high-temperature air. *Fuel Processing Technology*. 2006; 87(3): 235-45.

Yeo SD, Lim BJ, Lee GR, Park CD. Experimental study of effects of different heat sources on the performance of the hybrid multiple-effect diffusion solar still. *Solar Energy*. 2019; 193: 324-34.

Yin CY. Prediction of higher heating values of biomass from proximate and ultimate analyses. *Fuel*. 2011; 90(3): 1128-32.

Yoo BY, Huang CK, Lim JR, Herman J, Ryan MA, Fleurial JP, Myung NV. Electrochemically deposited thermoelectric n-type Bi₂Te₃ thin films. *Electrochimica Acta*. 2005; 50(22): 4371-7.

Yoon SJ, Son YI, Kim YK, Lee JG. Gasification and power generation characteristics of rice husk and rice husk pellet using a downdraft fixed-bed gasifier. *Renewable Energy*. 2012; 42: 163-7.

Yousef MS, Hassan H, Kodama S, Sekiguchi H. An experimental study on the performance of single slope solar still integrated with a PCM-based pin-finned heat sink. *Energy Procedia*. 2019; 156: 100-4.

Yuan Y, Yuan T, Wang D, Tang J, Zhou S. Sewage sludge biochar as an efficient catalyst for oxygen reduction reaction in an microbial fuel cell. *Bioresource Technology*. 2013; 144: 115-20.

- Yuksel YE, Ozturk M, Dincer I. Performance investigation of a combined biomass gasifier-SOFC plant for compressed hydrogen production. *International Journal of Hydrogen Energy*. 2020; 45(60): 34679-94.
- Zainal ZA, Ali R, Lean CH, Seetharamu KN. Prediction of performance of a downdraft gasifier using equilibrium modeling for different biomass materials. *Energy Conversion and Management*. 2001; 42(12): 1499-515.
- Zainal ZA, Rifau A, Quadir GA, Seetharamu KN. Experimental investigation of a downdraft biomass gasifier. *Biomass and Bioenergy*. 2002; 23(4): 283-9.
- Zhang J, Kan X, Shen Y, Loh KC, Wang CH, Dai Y, Tong YW. A hybrid biological and thermal waste-to-energy system with heat energy recovery and utilization for solid organic waste treatment. *Energy*. 2018; 152: 214-22.
- Zheng X, Chen C, Ying Z, Wang B. Experimental study on gasification performance of bamboo and PE from municipal solid waste in a bench-scale fixed bed reactor. *Energy Conversion and Management*. 2016; 117: 393-9.
- Zheng XF, Yan YY, Simpson K. A potential candidate for the sustainable and reliable domestic energy generation—Thermoelectric cogeneration system. *Applied Thermal Engineering*. 2013;53(2):305-11.
- Zhou C, Ge Z, Wang Y, Shang F, Guo L. Experimental study on supercritical carbon dioxide gasification of biomass. *Carbon Neutrality*. 2023; 2(1): 2.
- Zoghi M, Habibi H, Choubari AY, Ehyaei MA. Exergoeconomic and environmental analyses of a novel multi-generation system including five subsystems for efficient waste heat recovery of a regenerative gas turbine cycle with hybridization of solar power tower and biomass gasifier. *Energy Conversion and Management*. 2021; 228: 113702.